

Informatik

Dissertationsthema

„Thalamic neurons *in silico*“

Inaugural-Dissertation
zur Erlangung des Doktorgrades
der Naturwissenschaften im Fachbereich
Mathematik und Informatik
der Mathematisch-Naturwissenschaftlichen Fakultät
der Westfälischen Wilhelms-Universität Münster

vorgelegt von
Patrick Meuth
aus Bad Schwalbach
- 2011 -

Dekan: Prof. Dr. Matthias Löwe

Erster Gutachter: Prof. Dr. Martin Burger

Zweiter Gutachter: Prof. Dr. Thomas Budde

Tag der mündlichen Prüfung: 29.06.2011

Tag der Promotion: 29.06.2011

Post nubila Phoebus

Table of content

Overview	7
Introduction	9
1. Neuronal excitability	9
2. Thalamocortical system	10
3. Ionic currents of interest (I_{TASK} , I_h , I_T)	11
4. Mathematical background	12
4.1 Hodgkin-Huxley model	12
4.2 Neuronal equilibrium potential	14
4.3 Cable equation	16
5. NEURON simulation environment	18
5.1 Basic building blocks	18
5.2 HOC - Programming language	19
5.3 NMODL - Model description language	19
References	19
Methods	21
1. Implementing biophysical mechanisms with NMODL	21
1.1 The H current	21
1.2 The T current	25
1.3 The TASK current	27
2. TNT – an upgrade of the NEURON simulation environment	30
2.1 Why TNT?	31
2.2 How to define a set of simulations in TNT?	31
2.3 Automated mechanism compilation	35
2.4 TNT's program structure	36
References	46
Results	47
Project I (J Neurophysiol. 2006)	47
Project II (Neuropharmacology. 2007)	48
Project III (Mol Cell Neurosci. 2007)	48
Project IV (Pflugers Arch. 2008)	49
Project V (Mol Cell Neurosci. 2008)	50
Project VI (J Neurosci. 2009)	50
Scientific publications	53
Summary (English)	
Summary (German)	
Danksagung	
Tabellarischer Lebenslauf	

Overview

The presented work entitled “Thalamic neurons *in silico*” pursues two major goals. First of all it deals with the following more general physiological question:

In which way do ion channels exert influence on the firing behavior and network interactions of thalamic neurons?

and introduces computer modeling solutions for several of its dedicated practical subtasks. In a second glance this fruitful interdisciplinary approach is supposed to encourage others to look above the rim and foster the fusion of disciplines that are often mistaken as disjunctive.

While investigating network interaction and systemic function this work focuses on the thalamo-cortical system, an extensively and reciprocally connected neuronal network between thalamus and cortex. The function of that system is based on

- the intrinsic properties of the involved neurons (e.g. ion channels like I_{TASK} , I_h and I_T)
- the properties of the neuronal network (e.g. resonant behavior)
- the modulation of these properties by neurotransmitters (e.g. acetylcholine or serotonin)

Some of these aspects can be addressed by *in vivo* and *in situ* experimentations, but numerous experimental constraints thereby apply. Tasks like the voltage control in dendrites or the direct analysis of neuronal activity of multiple neurons are two examples where computer simulation *in silico* can help to overcome experimental limitations.

To increase the understanding of thalamic neuron function the following aspects were addressed:

- analysis of ion channel functions in case highly selective inhibitors or appropriate KO (genetic knock-out of specified ion channels) mice are not available.
- assessment of experimental procedures which are toxic to living cells.
- dissection of net effects induced by substances that modulate multiple ion channels.
- analysis of cell types which are due to cell size and infrequency experimentally difficult to target.
- assessment of compartmentalized expression of ion channels.
- analysis of the interaction of multiple ion channels in view of changing channel parameters e.g. during postnatal development.
- analysis of multiple directly interconnected neurons where double recordings represent the current experimental limit.

Taken together the development of a biologically realistic thalamic neuron model, reflecting the state-of-the-art literature knowledge and incorporating so far unimplemented ion channels, revealed the following new findings:

- (1) Multiple ion channels including I_{NaP} , I_h , I_{IR} , and non-inactivating I_{KV} channels contribute to the resting membrane potential of thalamocortical relay (TC) neurons.
- (2) Extracellular acidification blocks about 25% of I_h and 90% of I_{TASK} in TC neurons.
- (3) The functional interaction between the depolarizing I_h and the hyperpolarizing I_{TASK} most likely accounts for the TC cell's resistivity against extracellular acidification.
- (4) The inhalational anesthetic halothane functions via the specific modulation of I_h and I_{TASK} .

- (5) The voltage sags of TC neurons, caused by hyperpolarizing voltage steps, increase during the postnatal development and can be clearly attributed to the increasing I_h .
- (6) Thalamocortical oscillations stop in case the I_h density falls below a critical threshold.
- (7) Maturing animals compensate the initial lack of I_h by right-shifting the corresponding I/V relationship via high levels of cAMP.
- (8) The functional differences in the burst behavior of thalamic inter- and relay neurons cannot be explained by location-dependent differences in the I_T channel distribution, but are caused by differences in the T current density and I/V relationship.
- (9) Regarding the three different thalamic nuclei lateral geniculate nucleus, centrolateral nucleus and reticular nucleus, the LTS onset potential primarily depends on the I/V relationship of I_T , whereas the number of LTS associated action potentials as well as the minimum stimulation strength necessary for eliciting a LTS mainly depends on the T current density.
- (10) Clinically relevant concentrations of the anti-absence substance ethosuximide function via the parallel reduction of I_T , I_{KCa} and I_{NaP} .

In a next step the described thalamic model cell is planned to be part of a larger thalamocortical network model that possesses "small-world" properties. Those network topologies show an increased synchronizability and are thus ideal candidates for investigating the hypersynchronized thalamocortical activity occurring during absence epileptic seizures.

Besides providing so far unachievable answers to questions of the neuroscience sector, the presented work additionally includes improvements from the computer science point of view. Developing the software package TNT - text file based NEURON power transmission - from the scratch lead to the following upgrades of the original NEURON simulation environment:

- (1) Intuitive and compact simulation description of an arbitrary number of simulations
- (2) Extension of the modularization principle to network components and network connectivity
- (3) Powerful parser and error handling engine
- (4) Automated conversion to / build up of NEURON standard hoc simulations
- (5) Automated integration and compilation of all simulation required NMODL mechanisms
- (6) Unsupervised simulation execution and data recording

The conceptual design of the following chapters comprises a brief introduction into neuronal information processing as well as the functional context of the thalamocortical system. Thereof the three ionic currents I_{TASK} , I_h , and I_T are of greatest importance for the presented work and thus shortly introduced in the following section. The step from biology to virtual cells relies on various mathematical assumptions and models that are briefly summarized in section 4. Since all simulations are based on using the NEURON simulation environment the introduction closes by giving a short program overview including the presentation of NEURON's basic features.

The methods chapter comprises two parts. The first one gives a detailed explanation about how to implement biophysical mechanisms with the model description language NMODL on the basis of the current implementations I_h , I_T and I_{TASK} . The second part introduces the self-developed software package TNT upgrading the NEURON simulation environment.

Thereafter follows the results chapter summarizing the scientific question, the modeling approach and the gained findings for each of the six scientific projects presented at the end of this work.

Introduction

1. Neuronal excitability

Information exchange between neurons, e.g. in the CNS (central nervous system), is enabled by the ability to generate a brief but strong change in membrane potential (action potential), a feature that is only shared by a few other cell types (e.g. heart muscle cells). Connected through dendrites, axons, and synapses a complex neuronal network arises, capable of efficiently processing information.

The cytoplasm in a neuron's soma is separated from its environment by a semipermeable plasma membrane. Ions can pass this barrier through specific ion channels, which are macromolecular pores that are distributed over the entire cell surface. Of physiological importance are e.g. sodium (Na^+), potassium (K^+), calcium (Ca^{2+}) and chloride (Cl^-) channels [1]. Ion pumps, which are energy consuming membrane transport proteins, maintain an ion concentration gradient between the intracellular (cytosol) and extracellular space. Due to this gradient and the semipermeability of the plasma membrane, a potential difference between the cytosolic side and the extracellular side of the plasma membrane arises. This potential difference V_m typically reaches values of -50 to -70 mV (depending on species and cell type), and is called the resting membrane potential (RMP or V_{Rest}).

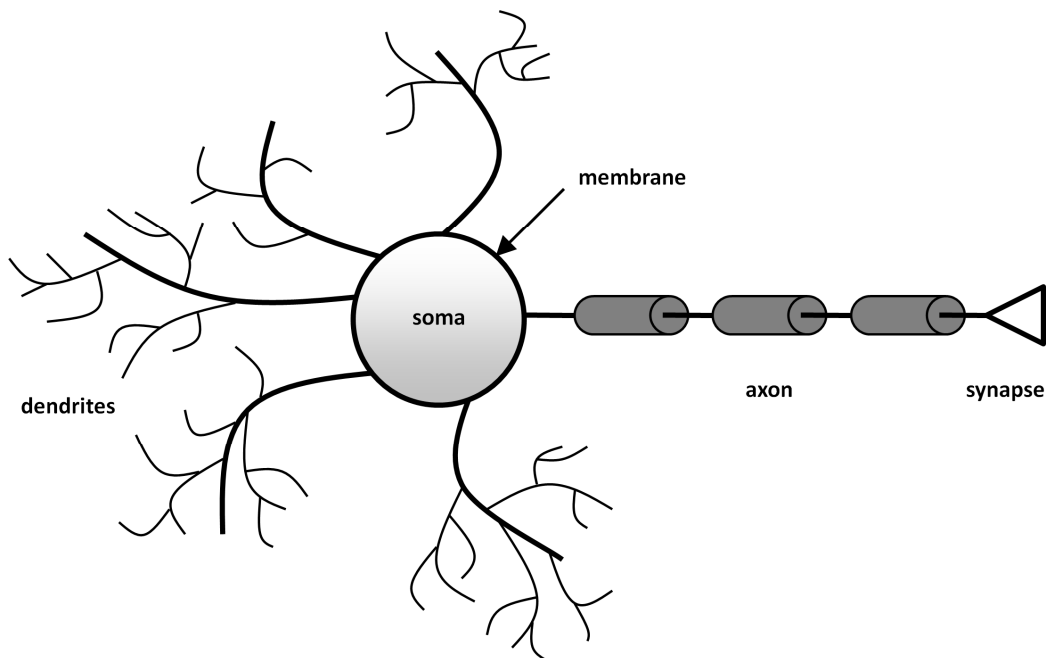


Fig. 1: Schematic figure describing the structure of a single neuron.

Excitatory and inhibitory signals from connected cells arrive via the dendrites or directly at the soma (see figure 1) and cause the potential difference between the cytosol and the extracellular matrix to decrease (V_m is shifted to higher values, depolarization) or to increase (V_m is shifted to lower values, hyperpolarization), respectively. Therefore, the signal processing of a neuron is mainly assigned to its soma and can be regarded as a summation of weighted input signals [2].

If summation causes V_m to depolarize over a specific threshold, the neuron generates a signal known as action potential. This travels along the axon, arrives at a synapse, and acts as an input to another connected cell either by direct electrical coupling or via a chemical transmission. The mechanism behind action potential generation is based on the voltage dependency of the respective ion channels. The open probability of some ion channels depends on the membrane potential. If membrane depolarization reaches the specific threshold of Na^+ -channels, they open and Na^+ -ions will flow along the electrical and chemical gradient into the cell. This leads to an additional depolarization

which, in turn, causes further sodium channels to open and the Na^+ -flow to increase. This regenerative process, known as “Hodgkin-Cycle”, would continue until the membrane potential reaches the sodium equilibrium potential (approx. +50 mV, depending on cell type).

However, Na^+ -channels close in a time-dependent manner (1-5 ms). Moreover, the potassium channels’ specific threshold is passed during the regenerative process. Potassium channels open with a delay (“delayed rectification”) and while K^+ -ions leave the cell through the open channels, they repolarize the membrane potential [2]. Since the potassium equilibrium potential is significantly lower than the neuron’s resting potential (approx. -80 mV) the cell thereby reaches values below the RMP (“afterhyperpolarization”). As K^+ -channels deactivate in a voltage-dependent manner, the membrane potential finally returns back to the RMP. Simplified, the time course of an action potential is characterized by an exponentially growing depolarization followed by a rapid hyperpolarization, which is illustrated in figure 2. Part A is a plot of three depolarizing current pulses of different strength (see inset) that are applied to a neuronal cell model. In contrast to stimulus one (dashed black line) and two (solid black line) the membrane depolarization of stimulus three (gray line) is strong enough to trigger action potential generation. Part B of this figure depicts the Na^+ - and K^+ -conductance changes during the occurrence of the first action potential.

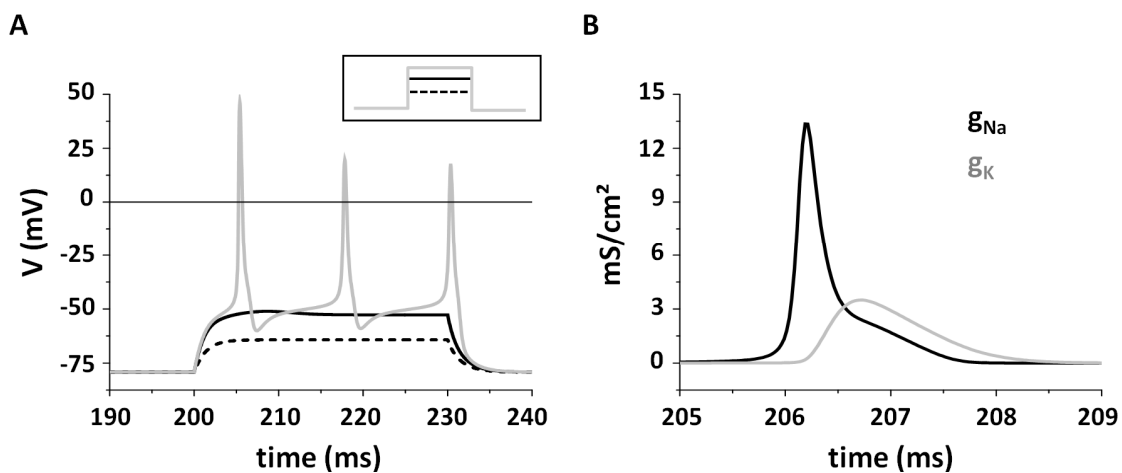


Fig. 2: Action potentials and ionic conductance [3].

A neuron’s firing frequency is limited due to a refractory period following each action potential. During the refractory period Na^+ -channels are in an inactive state. Reactivation and thus action potential generation is not possible before repolarization of the membrane potential (absolute refractory period). After the repolarization phase an action potential of reduced amplitude may be generated (relative refractory period) and the signal required for a subthreshold depolarization remains increased as long as the delayed-rectifier- K^+ -channels are active (subnormal period). It is only after the cell’s RMP has been reestablished that a subsequent action potential will be independent of the preceding one.

For representing biological nerve cells, a variety of models at any level of detail have been developed. A review regarding the biological plausibility and computational efficiency of the most popular ones is given in [4].

2. Thalamocortical system

The thalamus, also known as “the gate to consciousness”, is a brain structure that controls, whether or not information from the sensory periphery (with the exception of the sense of smell) will be transmitted to the cortex for further processing. In this context information can be represented by a

single action potential as well as a cascade of multiple action potentials. During wakefulness thalamic relay neurons show tonic action potential generation (see figure 2 A, gray trace), an activity mode that is dominated by relatively low frequencies and relatively large activity breaks between two consecutive action potentials respectively. These gaps allow stimuli from the periphery to evoke additional action potentials on top of the basic frequency and thereby to transfer the information faithfully to the cortex. The opposite is true during sleep. In this state the same set of neurons show high frequency bursts of action potentials (see figure 4) which in combination with the relative and absolute refractory period hardly leaves space for additional action potentials and thus closes “the gate”.

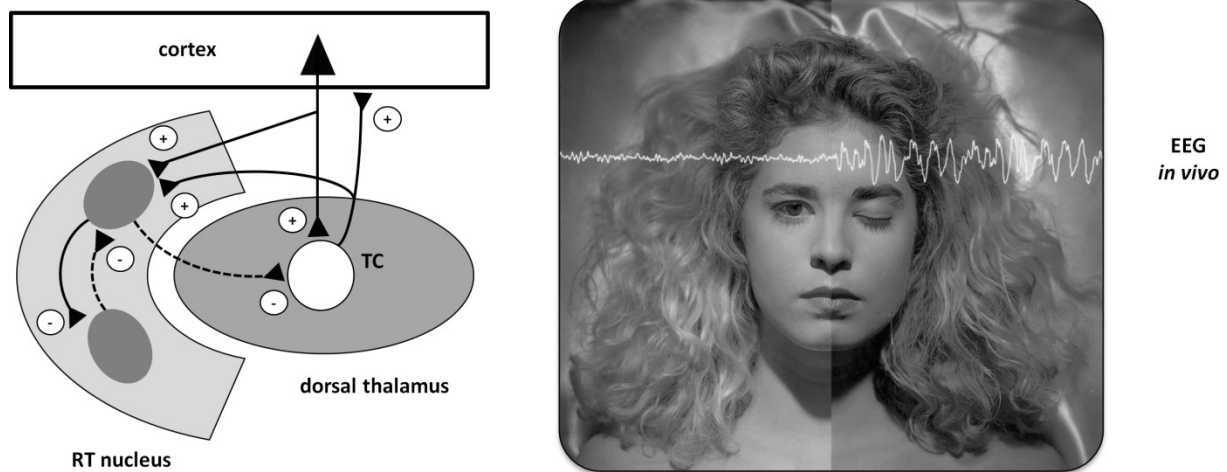


Fig. 3: Thalamocortical information flow [5].

Information flow between thalamus and cortex resembles a positive feedback loop that is counter-regulated by the nucleus reticularis thalami (NRT). The interneurons of the NRT receive excitatory cortical as well as thalamic inputs and in turn exert inhibitory influence on thalamic relay neurons. Additionally there is a reciprocal inhibition between the NRT neurons (see figure 3).

Recording the cortical electroencephalogram (EEG) allows the visualization of the thalamocortical activity states. The EEG in the awake state is characterized by relatively small amplitudes and a variety of different frequencies whereas during sleep relatively high amplitudes and low frequencies are dominating. Highly synchronized thalamic and cortical activity is termed thalamocortical oscillation, which can occur during wakefulness but is primarily associated to sleep.

3. Ionic currents of interest (I_{TASK} , I_h , I_T)

In thalamic relay neurons the currents I_{TASK} , I_h and I_T are of greatest importance. First of all, the switch from tonic to burst activity or vice versa gets initiated by changing the resting membrane potential via the modulation of I_{TASK} and I_h (see Project I, results section). Secondly, the high frequency action potentials generated during burst mode (see figure 4) ride on top of so called low-threshold calcium spikes (LTS), which are carried by I_T .

I_{TASK} is a potassium leak current that shows outward rectification and a current reversal at the K^+ equilibrium potential. The abbreviation TASK stands for TWIK related acid-sensitive potassium channel, meaning that there is a phylogenetic relationship to another branch (TWIK) of the family of two pore domain building potassium channels and a sensitivity to changes in pH. Increasing the I_{TASK} amplitude leads to a membrane hyperpolarization.

The H current (I_h) is a hyperpolarization-activated cyclic nucleotide-gated mixed cation current. Its sensitivity to cyclic adenosine monophosphate (cAMP), a second messenger molecule of the cellular signal transduction, gets expressed by the term “cyclic nucleotide-gated”. By adding cAMP the H current increases in a dose-dependent manner. Increasing the I_h amplitude leads to a depolarization of the membrane.

As mentioned before the T-type calcium current (I_T) is responsible for LTS generation. In this context the term “low-threshold” means that I_T activates well below the threshold of action potential generation. By modulating this depolarizing current component one influences the onset of the LTS and in consequence gets control over the occurrence and frequency of thalamocortical oscillations. Therefore substances modulating the T current are clinically used for e.g. dampening epileptic seizures.

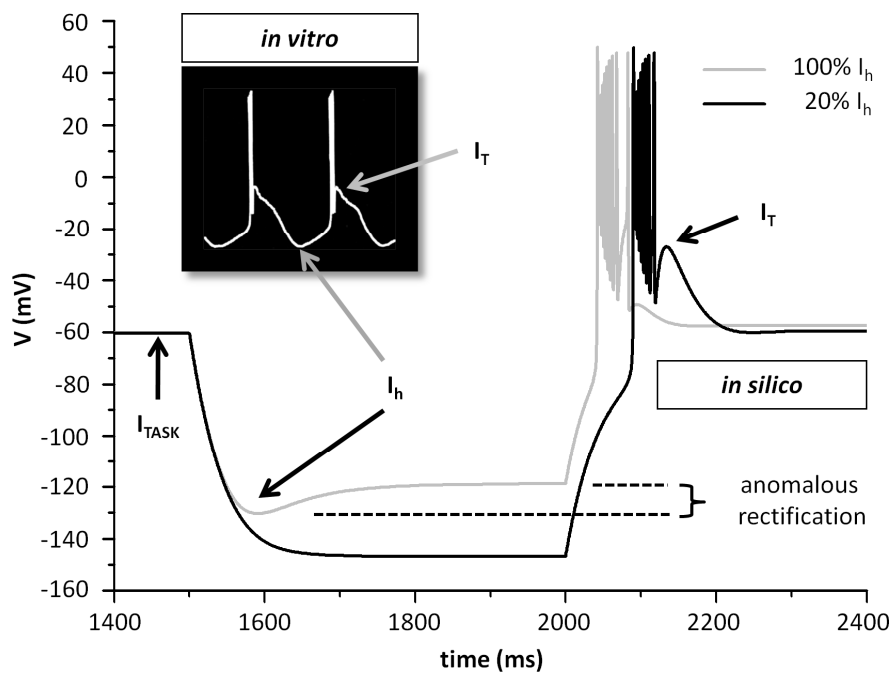


Fig. 4: Burst mode of a thalamic relay neuron.

Figure 4 exemplifies the interplay of I_{TASK} , I_h and I_T in thalamic relay neurons which is best visible during the burst mode (*in silico* vs. *in vitro*). After establishing a stable membrane voltage with the contribution of I_{TASK} a hyperpolarizing voltage step activates the H current which then pushes the cell back to a higher potential above the I_T threshold. The activated I_T current leads to a LTS which is crowned by a burst of action potentials. A succeeding hyperpolarization triggers the whole process again (see *in vitro* inset). Please note that simulating the burst mode with reduced H current amplitude (20%, black trace) almost completely stops anomalous rectification, one hallmark of I_h , and consequently delays the burst occurrence.

4. Mathematical background

4.1 Hodgkin-Huxley model

In 1952 Alan Lloyd Hodgkin and Andrew Fielding Huxley developed a model for describing the action potential generation in the giant axons of squids. After discovering that the Hodgkin-Huxley model is also adaptable to the neurons of all other species they were awarded the Nobel Prize in medicine together with Sir John Carew Eccles in 1963.

As depicted in figure 5 the Hodgkin-Huxley model comprises a capacitor (C_m) for the membrane capacitance, a resistance (R_m) implementing a voltage-dependent leak current, a variable conductance (g_x) for representing additional ion channels and a current source (I_{inject}) for the application of external stimuli with all of them connected in parallel. The equilibrium potentials (E_m , E_x) thereby declare that membrane voltage at which the corresponding current reaches its ionic equilibrium and reverses direction if passing it (see equation 2). Dividing a neuron's total membrane area into smaller compartments (see figure 5) accounts for differently equipped membrane sections. Two neighboring compartments are connected via an axial resistance (R_a) which ensures two independent membrane voltages (V_m).

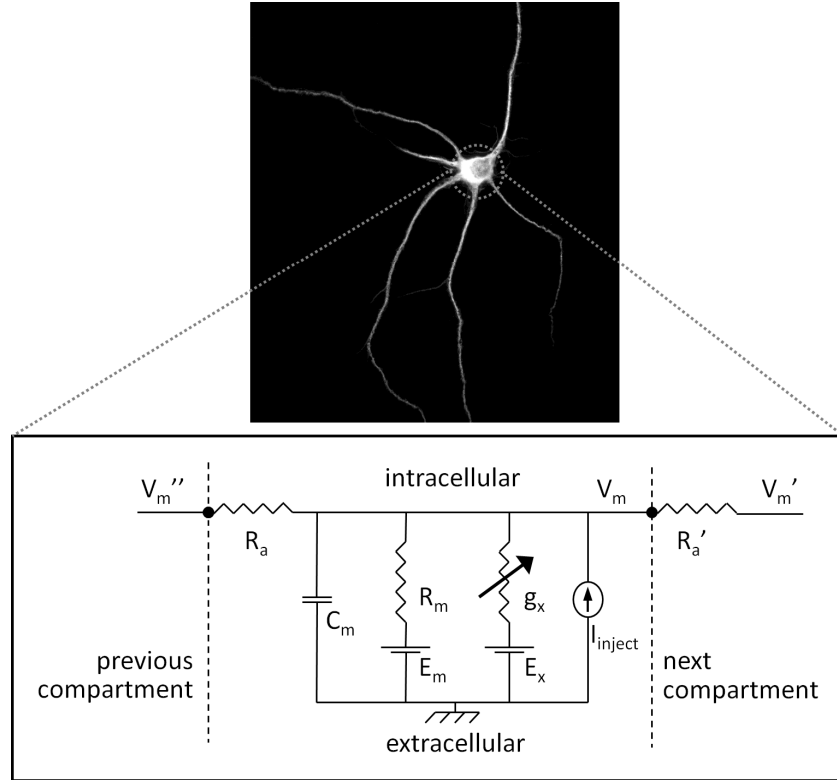


Fig. 5: Hodgkin-Huxley circuit diagram [3].

In contrast to this via g_x and R_a freely expandable circuit version, the original Hodgkin-Huxley model solely comprised a single compartment equipped with one potassium (K^+), sodium (Na^+) and leak current. According to Kirchoff's current law the sum of all currents running into and out of a junction of an electrical circuit equals zero. Consequently the capacitor charging current of the original Hodgkin-Huxley model can be calculated by subtracting the potassium, sodium and leak current from the current source I_{inject} (see equation 1).

$$C * \frac{dV}{dt} = I_{inject} - I_K - I_{Na} - I_{leak} \quad (1)$$

In case one of the ion channels opens, the intra- and extracellular milieu starts to equilibrate existing ion gradients. The corresponding ion flow results in a current I_x (with x specifying the passing sort of ions) which is proportional to the potential difference (also called "driving force") of the membrane voltage V_m and the equilibrium potential E_x . Limited by the maximum conductance $\bar{g}_x < 1$ the ionic current I_x can be calculated according to equation 2.

$$I_x = \bar{g}_x * (V_m - E_x) \quad (2)$$

When Hodgkin and Huxley revealed that \bar{g}_{Na} and \bar{g}_K are time-dependent, they expanded their previous current definition (see equation 2) by so-called gating variables ranging between 0 and 1. The probabilistic dynamic of the sodium and potassium channel was best approximated with three different variables named m , h and n leading to the following clearly more accurate current equations.

$$\begin{aligned} I_{Na} &= \bar{g}_{Na} * m^3 * h * (V_m - E_{Na}) \\ I_K &= \bar{g}_K * n^4 * (V_m - E_K) \end{aligned} \quad (3)$$

Thereby m and h account for the fast activation (channel opening) and the delayed inactivation (channel closing) of the sodium current. In contrast the potassium current shows no inactivation and activation occurs much slower (see figure 2 B), so that a single gating variable named n sufficed for an accurate current description. All gating variables are calculated according to the following system of differential equations, where the voltage-dependent exponential functions α_x and β_x are specifically adjusted to experimentally derived, electrophysiological findings.

$$\begin{aligned} \frac{dn}{dt} &= \alpha_n(V) * (1 - n) - \beta_n(V) * n \\ \frac{dm}{dt} &= \alpha_m(V) * (1 - m) - \beta_m(V) * m \\ \frac{dh}{dt} &= \alpha_h(V) * (1 - h) - \beta_h(V) * h \end{aligned} \quad (4)$$

4.2 Neuronal equilibrium potential

For each single sort of ions there are two major forces determining the corresponding trans-membrane influx or efflux, respectively. One force is the chemical gradient that tries to equilibrate the different intra- and extracellular ionic concentrations ($[x]_i / [x]_o$, see table 1) based on the Brownian motion. The second one is the electrical gradient or membrane potential respectively that aims the balanced distribution of positively and negatively charged ions on both sides of the membrane. Since both forces compete each other the cell's equilibrium potential matches neither a chemical nor an electrical equilibrium but lies somewhere in between.

x	$[x]_i$	$[x]_o$
Na ⁺	5 - 15	140 - 150
K ⁺	120 - 150	4 - 5
Cl ⁻	4 - 5	120 - 150

Tab. 1: Typical ion concentrations (in mmol/l) of a neuron [6].

Estimating this intermediate state consequently requires the relation of chemical concentrations and electrical potentials via a term that is common to both worlds. This term can be derived from thermodynamics, a discipline describing the relationship and transformation between different forms of energy, and is known as free enthalpy or Gibbs energy G , respectively.

In chemistry the change ΔG determines whether or not and in case under which circumstances a reaction takes place. Thereby a positive ΔG denotes the reaction requiring the supply of external

starting energy whereas a reaction with negative ΔG can occur spontaneously and releases energy. In case ΔG equals zero all reagents are in an energetic equilibrium (concentration ratio K) and the following equation holds for standard conditions (indicated by the zero in the exponent).

$$\Delta G^0 = -RT * \ln K \tag{5}$$

- G^0 standard Gibbs energy ($J * mol^{-1}$)
- R general gas constant ($8.31 J * mol^{-1} * K^{-1}$)
- T temperature (K)
- K equilibrium constant

Electrochemistry is a discipline that deals with the gain of electrical energy from chemical reactions. The most prominent way of doing so is the galvanic cell which one meets in form of batteries or accumulators in the everyday life. These simple devices solely comprise two electrically connected electrodes that reside in two separated basins of electrolyte solutions. By enabling an electron back transfer via a salt bridge or porous disc between both basins the electrical loop gets closed and current starts to flow. The thereby measurable voltage drop depends on the participating reagents and gets expressed relative to the standard hydrogen electrode as so-called standard electrode potential E^0 . This potential can be used to calculate the corresponding Gibbs energy under standard conditions according to equation 6.

$$\Delta G^0 = -zF * \Delta E^0 \tag{6}$$

- G^0 standard Gibbs energy ($J * mol^{-1}$)
- z number of exchanged electrons
- F Faraday constant ($9.65 * 10^4 * C * mol^{-1}$)
- E^0 standard electrode potential (V)

Equalizing and rearranging equation 5 and 6 leads to the Nernst equation (7). Named after the German Nobel Prize laureate Walther Hermann Nernst the homonymous equation allows calculating the cell's equilibrium potential E_x in dependence to the transmembrane gradient of ion x , the corresponding ion charge z and the temperature [7].

$$E_x = \frac{R * T}{z * F} * \ln \left(\frac{[x]_o}{[x]_i} \right) \tag{7}$$

- E_x equilibrium potential of ion x (V)
- R general gas constant ($8.31 J * mol^{-1} * K^{-1}$)
- T temperature (K)
- z ion charge
- F Faraday constant ($9.65 * 10^4 * C * mol^{-1}$)
- $[x]_o$ concentration of ion x outside the cell
- $[x]_i$ concentration of ion x inside the cell

Later on this fundamental estimate has been expanded by David Eliot Goldman, Alan Lloyd Hodgkin and Bernard Katz to the Goldman-Hodgkin-Katz voltage equation (GHK) in order to account for the fact that the cell's membrane is permeable to more than one sort of ions. Their experiments revealed a cell's equilibrium potential E_m to be best approximated by replacing the logarithm term of the Nernst equation by the sum of all included ionic transmembrane gradients multiplied with the corresponding ion permeability.

Exemplarily assuming that solely sodium, potassium and chloride ions can pass the membrane would lead to the GHK equation given in (8). Please note that for the negatively charged chloride ion the numerator and denominator have to be flipped.

$$E_m = \frac{R * T}{F} * \ln \left(\frac{p_{Na} * [Na^+]_o + p_K * [K^+]_o + p_{Cl} * [Cl^-]_i}{p_{Na} * [Na^+]_i + p_K * [K^+]_i + p_{Cl} * [Cl^-]_o} \right) \quad (8)$$

E_m	membrane equilibrium potential (V)
R	general gas constant ($8.31 \text{ J} * \text{mol}^{-1} * \text{K}^{-1}$)
T	temperature (K)
p_x	permeability of ion x
F	Faraday constant ($9.65 * 10^4 * \text{C} * \text{mol}^{-1}$)
$[x]_o$	concentration of ion x outside the cell
$[x]_i$	concentration of ion x inside the cell

4.3 Cable equation

The applicability of the cable theory to current flowing along a neuronal membrane gets most obvious while focusing on the cylindrical axons or dendrites but holds likewise for the soma (see figure 1). In order to derive the underlying cable equation the previously introduced Hodgkin-Huxley circuit (see figure 5) has to be simplified to the passive cable depicted in figure 6.

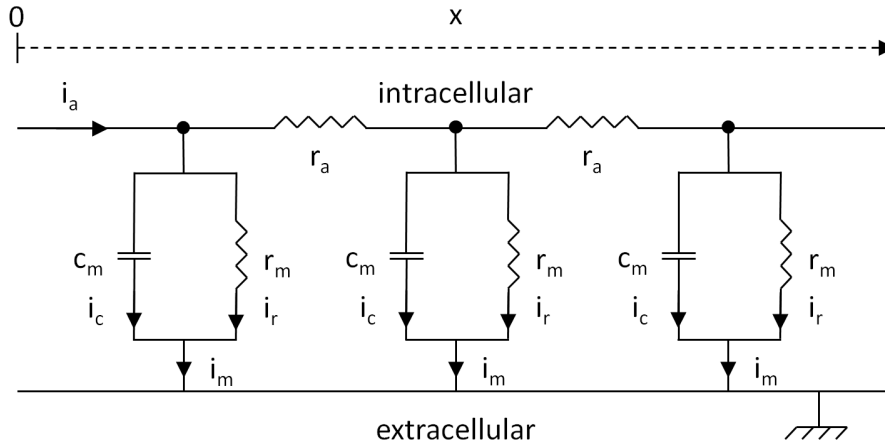


Fig. 6: Passive cable with three compartments.

Conversion from the specific membrane resistance R_m ($\Omega * \text{cm}^2$) and capacitance C_m ($\mu\text{F}/\text{cm}^2$) measured per unit area to the individual compartment resistance r_m ($\Omega * \text{cm}$) and capacitance c_m ($\mu\text{F}/\text{cm}$) measured per compartment length takes place by division and multiplication with the cable circumference respectively. Thereby the cable radius z is given in cm. Dividing the specific cytosol resistance R_a ($\Omega * \text{cm}$) by the cable cross section delivers the axial resistance r_a (Ω/cm).

$$r_m = \frac{R_m}{2\pi z} \quad c_m = C_m * 2\pi z \quad r_a = \frac{R_a}{\pi z^2} \quad (9)$$

A current i_a injected at position $x = 0$ will generally split in two components every time it passes a compartment junction (see figure 6, filled black circles). Thereby one component continues its way along the axial resistance r_a while the other component drains to the outside.

By assuming a perfectly sealed membrane ($r_m = \infty$, $c_m = 0$) the drain component gets zero and the injected current solely travels along the axial resistances. According to Ohm's law the current i_a then

results in a voltage drop equal to the product of i_a and r_a at each passed axial resistance so that the voltage difference between the injection origin and all other positions x increases proportional to the number of passed axial resistances Δx as stated in equation 10.

$$\Delta V = i_a * r_a * \Delta x \quad (10)$$

Assuming continuous and infinitely small increments of x equation 10 can be written as partial differential equation 11.

$$\frac{1}{r_a} \frac{\partial V}{\partial x} = i_a \quad (11)$$

This ideal situation gets left by bringing back finite and unitary membrane resistances r_m as well as unitary membrane conductances $c_m > 0$. If i_m equals the overall current that drains to the outside per membrane compartment the change in i_a at position x can be calculated as the product of i_m and the number of passed compartments Δx (see equation 12).

$$\Delta i_a = i_m * \Delta x \quad (12)$$

By using continuous, infinitesimally small increments equation 12 delivers the partial differential equation 13.

$$\frac{\partial i_a}{\partial x} = i_m \quad (13)$$

As long as the capacitors are not fully charged the overall current i_m gets split into a current i_c flowing through the capacitances c_m and a current i_r flowing through the resistances r_m .

$$i_c = c_m * \frac{\partial V}{\partial t} \quad i_r = \frac{V}{r_m} \quad (14)$$

Substituting the terms of equation 15 with equation 13 and 14 delivers the partial differential equation 16.

$$i_m = i_c + i_r \quad (15)$$

$$\frac{\partial i_a}{\partial x} = c_m * \frac{\partial V}{\partial t} + \frac{V}{r_m} \quad (16)$$

From there a last substitution of the term i_a according to equation 11 suffices to finally derive the cable equation (17).

$$\frac{1}{r_a} \frac{\partial^2 V}{\partial x^2} = c_m * \frac{\partial V}{\partial t} + \frac{V}{r_m} \quad (17)$$

This second-order ordinary differential equation describes the membrane potential in a one-dimensional cable structure with an ohmic intracellular cytoplasm. Given appropriate boundary conditions it holds regardless of the exact nature of the neuronal membrane [8]. Consequently almost every nerve simulation program operates with this compartment concept and the cable equation [9].

5. NEURON simulation environment

Developed by Michael Hines and John W. Moore the NEURON simulation environment became one of the most popular programs for simulating neuronal activity. Its wide spread in the neuroscience sector might be attributed the convincing combination of a computationally efficient and accurate solver of the cable equation and a simple interface for incorporating additional mechanisms that are newly discovered or representing a theoretical test approach. Besides simulating individual cells, NEURON is also capable of dealing with networks of neurons that may include several types of ion channels or possess complex branching morphologies. Due to the unitized operating mode global constraints, mechanism compatibility and processing efficiency is always ensured by the simulator itself. The built-in graphical user interface (GUI) enables the user to interact with running simulations at any point of time and allows testing a multitude of different parameter settings with just a few mouse clicks [10-14].

5.1 Basic building blocks

The first step in modeling a nerve cell is to specify its morphology. In general structures of any complexity can be described by sequences of cylindrical sections, which are NEURON's basic building blocks. The body structure of a section is determined by setting the parameters *length* and *diam* (diameter). By default each section consists of a single segment but can be further subdivided by increasing the parameter *nseg*. Consequently a section of length L gets partitioned into a corresponding number of segments, each having a length of $L/nseg$. Since the center of each segment represents one of NEURON's calculation points (see figure 7, filled black circles), the overall number of segments per section determines its spatial resolution.

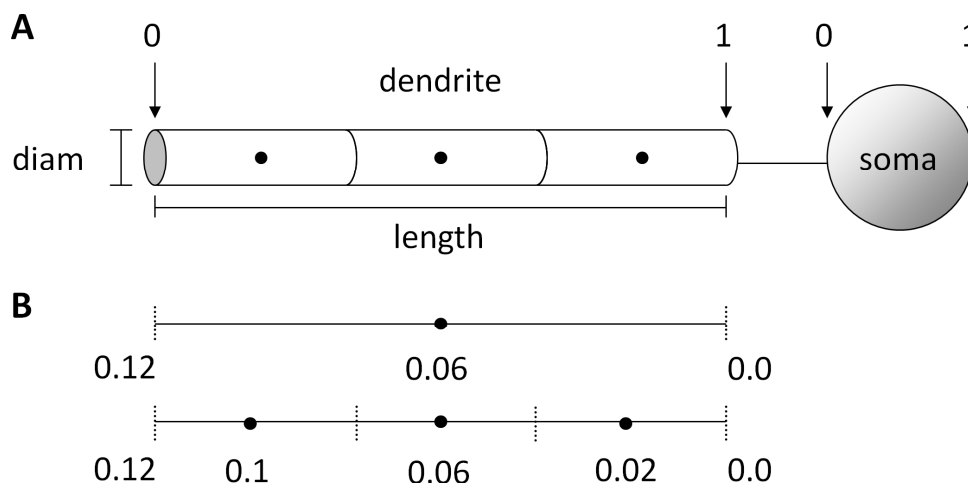


Fig. 7: Morphology specification using sections and segments.

A corresponding example is illustrated in figure 7 B. Assigning an ion channel distribution, that is supposed to be linearly decreasing from its maximum of 0.12 S/cm^2 at the distal part to 0 S/cm^2 at the proximal part, to the dendritic section of part A will result in a three times higher spatial resolution in the lower case ($nseg=3$) in comparison to the upper case ($nseg=1$). On the other hand each additional calculation point heightens the overall work load and potentially slows-down large-scale simulations. Therefore one has to weigh up thoroughly how many segments are reasonably required for each particular modeling approach.

Bringing "life" into these so far empty hulls happens via biophysical mechanisms defined in NMODL (see section 5.3) and so-called point processes. The latter are NEURON's built-in tools for simulating a current or voltage clamp aperture but can be also used for implementing e.g. ionic leak channels.

Since point processes are assigned to a specific section position, they conceptually differ from mechanisms which are distributed over the entire section (so-called range variables). The amount of mechanisms and point processes assigned to a single section is generally unlimited and thus allows multifaceted simulations of arbitrary complexity.

5.2 HOC - Programming language

NEURON uses a C-like programming language, which is based on hoc (high order calculator), a floating point calculator described by Kernighan and Pike [15]. Excluding polymorphism and inheritance it supports the common principles of object-oriented programming like data encapsulation or the definition of abstract data types for instance. Hoc commands are multi-purpose since they can be used to control simulations, generate and customize the GUI as well as access any kind of NEURON's parameters. A more detailed description including the modeling of an example cell is given in [9].

5.3 NMODL - Model description language

NMODL, which stands for NEURON model description language, is the appropriate tool in order to expand the repertoire of NEURON's biophysical mechanisms. It can be used to specify physical models in terms of simultaneous nonlinear algebraic equations, differential equations or kinetic schemes and originates from MODL, a development at the NBSR (National Biomedical Simulation Resource). Specifications are translated into C statements, compiled for computational efficiency and linked to the NEURON simulation environment afterwards. This procedure allows the user to exclusively work with compact and easy to understand high-level mechanism descriptions and keeps him away from any low-level program compatibility or efficiency concerns [16].

References

- [1] JG Nicholls, AR Martin, BG Wallace, and PA Fuchs. *From Neuron to Brain*. Sinauer Associates, 4th edition, 2001.
- [2] ER Kandel. *Principles of Neural Science*. McGraw-Hill Publishing, 4th edition, 2000.
- [3] P Meuth, SG Meuth, D Jacobi, T Broicher, HC Pape, and T Budde. *Get the Rhythm: Modeling Neuronal Activity*. Journal of Undergraduate Neuroscience Education (JUNE), 4(1):A1–11, 2005.
- [4] EM Izhikevich. *Which Model to Use for Cortical Spiking Neurons?* IEEE Transactions on Neural Networks, 15(5):1063–1070, 2004.
- [5] JA Hobson. *Schlaf. Gehirnaktivität im Ruhezustand*. Spektrum Akad. Vlg., 1990.
- [6] EJ Speckmann, J Hescheler, R Köhling. *Physiologie*. Elsevier Urban & Fischer Verlag, 5. Auflage, 2008
- [7] G Adam, P Läuger, G Stark. *Physikalische Chemie und Biophysik*. Springer-Verlag Berlin Heidelberg New York, 1977.
- [8] C Koch. *Biophysics of Computation, Information Processing in Single Neurons*. Oxford University Press, 1st edition, 1998.

- [9] ML Hines and NT Carnevale. *The NEURON Simulation Environment*. *Neural Comput.*, 9(6): 1179–1209, 1997.
- [10] M Hines. *NEURON - A program for simulation of nerve equations*. *Neural Systems: Analysis and Modeling*, pages 127–136, 1993.
- [11] M Hines. *The NEURON Simulation Program*. *Neural Network Simulation Environments*, pages 1–14, 1993.
- [12] M Hines and NT Carnevale. *Computer modeling methods for neurons*, pages 226–230. *The Handbook of Brain Theory and Neural Networks*. MIT Press, Cambridge, MA, 1995.
- [13] ML Hines and NT Carnevale. *NEURON: a Tool for Neuroscientists*. *The Neuroscientist*, 7:123–135, 2001.
- [14] ML Hines and NT Carnevale. *Recent Developments in NEURON*. *Brains, Minds and Media*, 1:221, 2005.
- [15] BW Kernighan and R Pike. *Appendix 2: Hoc manual.*, pages 329–333. *The UNIX Programming Environment*. Prentice Hall, 1984.
- [16] ML Hines and NT Carnevale. *Expanding NEURON's repertoire of mechanisms with NMODL*. *Neural Comput.*, 12:839–851, 2000.

Methods

1. Implementing biophysical mechanisms with NMODL

The methodological progress and growing acceptance of neuronal modeling within the last 10-15 years led to a remarkable amount of simulation projects that covered almost all regions and sub-regions of the human and vertebrate brain including a multitude of different cell types, ion channels and their specific features. Following the reusability principle the neuronal modeling community started several projects to collect, unitize and redistribute already existing models for the sake of effectiveness. One of the oldest and most common data bases thereof is the “ModelDB” from the “SenseLab Project” (<https://senselab.med.yale.edu>) at Yale University. My very first TC neuron model published in 2005 [1] is already incorporated there and builds the basis for all succeeding and in this work presented neuronal cell models.

In a first step topology and geometry of a cell model are determined as mentioned in section 5 of the introduction resulting in an empty hull that has to be equipped with biophysical mechanisms in order to be functional. Those mechanisms are defined in NMODL (NEURON modeling language, see section 5.3, introduction) and exemplarily presented for the in this work most important ionic currents I_h , I_T and I_{TASK} . The first two current implementations were derived from the “ModelDB” (model 3808, Houweling and Sejnowski, 1997), whereas the TASK current was implemented for the first time in the context of this work.

1.1 The H current (I_h , File: ih.mod, [2])

TITLE, COMMENT and ENDCOMMENT tags are used to hold explanatory information and references for the modeler but are of no functional meaning.

```
TITLE hyperpolarization-activated current (H-current)

COMMENT
*****
reference:      Destexhe, Babloyantz & Sejnowski (1993)
                Biophys.J. 65, 1538-1552
found in:      thalamocortical neurons
*****
Maxim Bazhenov's first mod file
Rewritten for MyFirstNEURON by Arthur Houweling
ENDCOMMENT
```

Mathematically independent variables are defined by following the INDEPENDENT tag which usually solely holds the simulation time t .

```
INDEPENDENT {t FROM 0 TO 1 WITH 1 (ms)}
```

The NEURON section declares variables and their accessibility at the user level. In this case the variables $ghbar$, tau_s , tau_f , tau_c and ih are defined as RANGE variables (see section 5.1, introduction) and will be visible to the user via their variable name extended by an underscore and the SUFFIX “iH”. According to the WRITE command this mechanism is supposed to evaluate and output the current amplitude ih that relies on the ions h and ca (USEION) as well as on the equilibrium potential eh and the intracellular calcium concentration cai (READ). In case none of the default ions Na^+ , K^+ or Ca^{2+} is supposed to be used one has to explicitly specify the ion charge via the VALENCE command for the automatically evaluated Nernst equation (see section 4.2, introduction). Here

VALENCE 1 accounts for the H current's mixed cation permeability (e.g. $\text{Na}^+ = 1$, $\text{K}^+ = 1$ but not $\text{Ca}^{2+} = 2$ or $\text{Cl}^- = -1$). The parameter *cac* holds the value at which calcium binding is assumed to be half-activated. It has to be defined as GLOBAL in order to allow the user to access this crucial functional parameter.

```
NEURON {
    SUFFIX ih
    USEION h READ eh WRITE ih VALENCE 1
    USEION ca READ cai
    RANGE ghbar, tau_s, tau_f, tau_c, ih
    GLOBAL cac
}
```

In comparison to previous modeling languages NMODL ensures unit consistency by automatically checking all equations according to the unit information given in parenthesis. Within the UNITS section one can define unit aliases for a more compact scripting.

```
UNITS {
    (mA)      = (milliamp)
    (mV)      = (millivolt)
    (molar)   = (1/liter)
    (mM)      = (millimolar)
}
```

The PARAMETER block declares variables that are not changed by the mechanism itself, but are set by the user or controlled by the simulation environment. The opposite is true for STATE variables, which are the unknowns in differential and algebraic equations, and ASSIGNED variables.

```
PARAMETER {
    v                (mV)
    cai              (mM)
    celsius          (degC)
    eh               = -43 (mV)
    ghbar            = 4e-5 (mho/cm2)
    cac              = 5e-4 (mM)
}

STATE {
    s1               : fraction of open unbound slow gates
    s2               : fraction of open calcium-bound slow gates
    f1               : fraction of open unbound fast gates
    f2               : fraction of open calcium-bound fast gates
}

ASSIGNED {
    ih               (mA/cm2)
    h_inf
    tau_s            (ms)      : time constant slow gate
    tau_f            (ms)      : time constant fast gate
    tau_c            (ms)      : time constant calcium binding
    alpha_s          (1/ms)
    alpha_f          (1/ms)
    beta_s           (1/ms)
    beta_f           (1/ms)
    C
    k2               (1/ms)
}
```

```

tadj
s0          : fraction of closed slow gates
f0          : fraction of closed fast gates
}

```

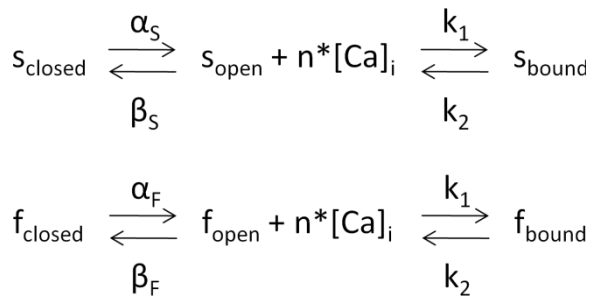
Whenever an ongoing simulation reaches a state that requires the mechanism to be updated (e.g. the membrane voltage v switches from the resting potential to action potential generation), the corresponding BREAKPOINT statements are executed. These usually include the integration of all state variables via the SOLVE command as well as assignments for updating the implemented currents. METHOD specifies one of the four built-in numerical integration methods in NEURON. One can select between the backward Euler, Crank-Nicholson, CVODE and DASPK method which differ in accuracy, stability and computational speed [3].

```

BREAKPOINT {
  SOLVE states METHOD euler
  ih = ghbar * (s1+s2) * (f1+f2) * (v-eh)
}

```

In order to account for the observation that the increase of intracellular calcium is accompanied by an increase in current amplitude, the presented H current implementation includes a kinetic scheme for intracellular calcium binding to the channel.



It assumes a slow (s) and fast (f) activation gate that change from the closed to the open state and vice versa based on the voltage-dependent rate constants α_s , β_s , α_f and β_f . Both gates are defined to possess $n = 2$ calcium binding sites, which when occupied lead from s_{open} and f_{open} to the second open states, s_{bound} and f_{bound} . In this context k_1 and k_2 represent the forward and backward rate constants for the calcium binding.

All six state variables are governed by differential equations and implemented as s0 (s_{closed}), s1 (s_{open}), s2 (s_{bound}), f0 (f_{closed}), f1 (f_{open}) and f2 (f_{bound}) in the corresponding DERIVATIVE block. The DERIVATIVE block and the remaining source code passages are framed by UNITSOFF and UNITSON in order to exclude them from the automatic unit consistency check. This is applicable in case unit consistency can be ensured manually and prevents from explicit unit statements like $x = (v + 15 \text{ (mV)}) / (10 \text{ (mV)})$ for the sake of legibility.

```

UNITSOFF
DERIVATIVE states {
  evaluate_fct(v,cai)

  s1' = alpha_s*s0 - beta_s*s1 + k2*(s2-C*s1)
  f1' = alpha_f*f0 - beta_f*f1 + k2*(f2-C*f1)
  s2' = -k2*(s2-C*s1)
  f2' = -k2*(f2-C*f1)
}
UNITSON

```

```

        s0 = 1-s1-s2
        f0 = 1-f1-f2
    }

```

The mechanism gets initialized by executing the assignments of the INITIAL block, which in this case starts with a comment about the term Q_{10} . This unitless temperature coefficient is a common way to describe the increase in reaction speed of biological or chemical processes while increasing the temperature by 10 K.

All rate constants are evaluated by a separate PROCEDURE called “evaluate_fct()”. This procedure is parameterized by the membrane voltage v and the intracellular calcium concentration cai in order to account for the rate constants’ dependencies. Core of the overall calculation are the voltage-dependent variables h_{inf} , tau_s and tau_f which have been adapted to previous *in vitro* measurements.

```

INITIAL {
    : Q10 assumed to be 3
    tadj = 3^((celsius-35.5)/10)
    evaluate_fct(v,cai)

    s1 = alpha_s / (beta_s+alpha_s*(1+C))
    s2 = alpha_s*C / (beta_s+alpha_s*(1+C))
    s0 = 1-s1-s2
    f1 = alpha_f / (beta_f+alpha_f*(1+C))
    f2 = alpha_f*C / (beta_f+alpha_f*(1+C))
    f0 = 1-f1-f2

    tau_c = 1 / (1+C) / k2    : for plotting purposes
}

PROCEDURE evaluate_fct( v(mV), cai(mM)) {
    h_inf = 1 / (1+exp((v+68.9)/6.5))
    tau_s = exp((v+183.6)/15.24) / tadj
    tau_f = exp((v+158.6)/11.2) / (1+exp((v+75)/5.5)) / tadj

    alpha_s = h_inf / tau_s
    alpha_f = h_inf / tau_f
    beta_s = (1-h_inf) / tau_s
    beta_f = (1-h_inf) / tau_f
    C = cai*cai/(cac*cac)
    k2 = 4e-4 * tadj
}

UNITSON

```

Taken together the I_h current is calculated according to the following equation comprising a direct voltage-dependence via the last product term as well as an indirect dependence on the membrane voltage and the intracellular calcium concentration via the states of the kinetic scheme.

$$I_h = \bar{g}_h * (s_{open} + s_{bound}) * (f_{open} + f_{bound}) * (V - E_h)$$

\bar{g}_h maximum I_h conductance (S/cm² = mho/cm²)
 E_h equilibrium potential of I_h (mV)

1.2 The T current (I_T , File: it.mod, [4])

Likewise ih.mod the T current implementation starts with the informational part (TITLE, COMMENT) and the declaration of the simulation time t as mathematically INDEPENDENT variable.

```
TITLE transient and low threshold calcium current (T-current)

COMMENT
*****
reference:      Huguenard & McCormick (1992)
                J.Neurophysiology 68(4), 1373-1383
found in:      thalamic relay neurons
*****
Assembled for MyFirstNEURON by Arthur Houweling
ENDCOMMENT

INDEPENDENT {t FROM 0 TO 1 WITH 1 (ms)}
```

Besides the already introduced ion ca and the corresponding intracellular concentration (cai) and extracellular concentration (cao) the NEURON block of the T current additionally specifies a similar looking but due to NEURON's case sensitivity new ion Ca . The Ca ion is supposed to be two times positively charged (VALENCE) and serves as "dummy" while determining the current amplitude iCa via the WRITE command. In other words the Ca^{2+} flow through T channels will change the intracellular ion concentration Ca_i but not cai upon which all other currents rely. This construction accounts for the electrophysiological finding that the T current does not activate calcium-dependent currents.

```
NEURON {
    SUFFIX iT
    USEION ca READ cai,cao
    USEION Ca WRITE iCa VALENCE 2
    RANGE pcabar, m_inf, h_inf, tau_m, tau_h, iCa
}

UNITS {
    (mA)      = (milliamp)
    (mV)      = (millivolt)
    (mM)      = (milli/liter)
    FARADAY   = 96480 (coul)
    R         = 8.314 (volt-coul/degC)
}

PARAMETER {
    v          (mV)
    celsius    (degC)
    dt         (ms)
    cai        (mM)
    cao        (mM)
    pcabar= 0.0001 (cm/s)
}
```

The STATE variables m and h refer to the Hodgkin-Huxley model (see section 4.1, introduction) and are fine-tuned in terms of course, speed and temperature adjustment via x_inf , tau_x and $tadjx$ of the ASSIGNED block.

```

STATE {
    m h
}

ASSIGNED {
    iCa          (mA/cm2)
    tau_m        (ms)
    tau_h        (ms)
    m_inf
    h_inf
    tadjm
    tadjh
}

```

As described before the BREAKPOINT block initiates the integration of all state variables and finally executes the current assignments. In this case the current assignment to iCa holds two new aspects that slightly differ from the previously used Hodgkin-Huxley current calculation. First of all the maximum conductance \bar{g} defined in mS/cm^2 is replaced by the maximum permeability \bar{p} defined in cm/s . Secondly the current's "driving force" term is substituted by a function named "ghk()" that implements the Goldman-Hodgkin-Katz equation (see section 4.2, introduction). Considering that the latter returns mC/cm^3 which multiplied with the unitless gating variables and the ion permeability given in cm/s results in $\text{mC}/\text{s}\cdot\text{cm}^2$ both terms equalize each other via the conversion $C = A\cdot s$ to the NMODL standard mA/cm^2 .

```

BREAKPOINT {
    SOLVE state
    iCa = pcabar * m*m*h * ghk(v,cai,cao,2)
}

PROCEDURE state() {
    rates(v)

    m = m + (1-exp(-dt/tau_m))*(m_inf-m)
    h = h + (1-exp(-dt/tau_h))*(h_inf-h)
}

UNITSOFF
INITIAL {
    tadjm = 3.55^((celsius-23.5)/10)
    tadjh = 2.8^((celsius-23.5)/10)
    rates(v)
    m = m_inf
    h = h_inf
}

FUNCTION ghk( v(mV), ci(mM), co(mM), z) (millicoul/cm3) { LOCAL e, w
    w = v * (.001) * z * FARADAY / (R*(celsius+273.16))
    if (fabs(w)>1e-4)
        { e = w / (exp(w)-1) }
    else : denominator is small -> Taylor series
        { e = 1-w/2 }
    ghk = - (.001) * z * FARADAY * (co-ci*exp(w)) * e
}

PROCEDURE rates(v(mV)) {
    tau_m = (1/(exp((v+131.6)/-16.7)+exp((v+16.8)/18.2)) + 0.612) / tadjm
    m_inf = 1 / (1+exp((v+60.5)/-6.2))
    if (v<-80)

```

```

    { tau_h = exp((v+467)/66.6) / tadjh }
  else
    { tau_h = (exp((v+21.88)/-10.52)+28) / tadjh }
    h_inf = 1 / (1+exp((v+84)/4.03))
  }
UNITSON

```

In conclusion the given NMODL mechanism implements the calcium-carried T current calculated by the following equation.

$$I_{Ca} = \bar{p}_{Ca} * m^2 * h * ghk(V, [Ca^{2+}]_i, [Ca^{2+}]_o, VALENCE)$$

1.3 The TASK current (I_{TASK} , File: TASK3.mod, [Project I, results section])

In contrast to the H- and T current ModelDB did not hold any TASK current implementation to be reused for Project I (see results section) in 2007. Therefore the NMODL mechanism TASK3.mod was developed from the scratch.

Implementing the voltage-dependent TASK current requires knowing the exact current voltage relationship (see figure 8). Likewise frequency scanning this relationship can be measured by a so-called ramp protocol successively clamping the cell membrane to as many potentials of interest as possible. After giving the cell enough time to adapt to each new membrane voltage the sum of all ionic currents gets measured. In order to separate the TASK component from the overall current a TASK-specific blocker gets applied before repeating the whole experiment series. Afterwards the TASK current can be calculated by subtracting the overall current under the blocker influence from the control current at each single membrane potential.

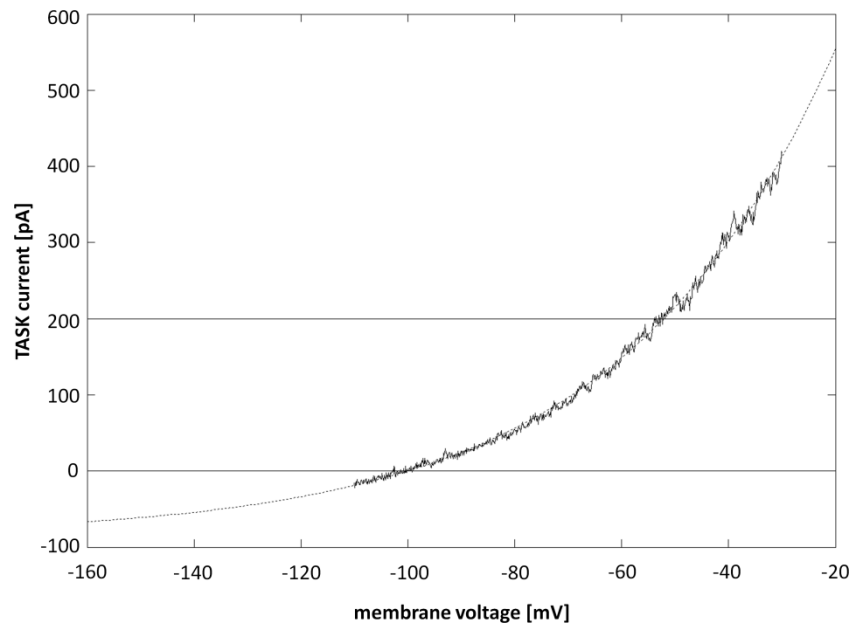


Fig. 8: Current voltage relationship of the thalamic TASK3 current.

State-of-the-art method for the parallel voltage clamp and current measurement of a cell membrane is called the patch-clamp technique. Initially published in 1976 by Erwin Neher and Bert Sakmann this single pipette approach was awarded the Nobel Prize for physiology or medicine in 1991. One generally distinguishes four different variations named cell-attached, inside-out, whole-cell and outside-out patch.

In the first step the glass pipette gets carefully pushed against the cell. Then a small negative pressure applied at the pipette end leads to a strong sealing between pipette tip and cell membrane separating the outer bath solution from the inner pipette solution. From an electrical point of view this separation represents a resistance in the giga ohm range once the separation is complete. After establishing this so-called gigaseal the cell-attached patch is achieved and any current running through the ion channels under the pipette tip will flow into the inner pipette solution where an electrode transfers the current to an amplifier for recording purposes. The advantage of the cell-attached mode is that the cell membrane remains intact.

A smooth withdrawing of the pipette would lead to the removal of the attached membrane patch from the cell. This configuration exposes the former inner part of the membrane to the outer bath solution and is therefore named inside-out patch. Consequently one gets control over the intracellular membrane processes by modifying the bath solution.

In contrast to all other variations the whole-cell patch allows measuring the complete cell membrane instead of solely a space-limited number of ion channels by removing the membrane patch after achieving the cell-attached mode. One way of doing so is the application of an additional negative pressure at the pipette end so that the membrane patch under the pipette tip gets sucked in. Alternatively one can fill the pipette with a small amount of an antibiotic (e.g. amphotericin-B or gramicidin) that diffuse into the membrane and form small perforations. Compared to the whole-cell patch this so-called perforated-patch reduces washing out the cell by the pipette solution but on the other hand increases the relative access resistance and thus the recording noise.

The outside-out patch starts in the whole-cell mode. By carefully withdrawing the pipette the cell membrane gets distended and finally ruptures. In case the resulting membrane fragments at the pipette tip reconnect the outer cell membrane is again exposed to the external bath solution and thus kept direction. This probably most difficult patch variation allows the control of the extracellular membrane processes via modifications of the bath solution.

After measuring the current voltage relationship of the TASK current (see figure 8) by the whole-cell patch-clamp technique the cell's morphology had to be determined in order to relate these absolute current values to the surface area. There are three good reasons to solely focus on the soma in this context. First of all the exploration of each single dendritic branch and axonal compartment of a neuron (see figure 1 and 7, introduction) is a quite complex task. Secondly, dendritic currents have to pass a number of axial resistances (see figure 5, introduction) in proportion to the distance resulting in a usually negligible net effect at the somatic measuring site. The third and most comprehensible argument is that a patchable neuronal slice has to have a limited thickness so that most of the dendritic tree is automatically truncated during the preparation process.

As discussed in section 5.1 of the introduction NEURON's basic building blocks are so-called sections. In case a single cell without dendrites or axons is supposed to be modeled a single section approach delivers a good approximation. Since the cylindrical shape of a section is solely determined by the parameters length and diameter the overall morphology measurement could be completed rapidly and revealed a median diameter of 20 μm and a median length of 30 μm resulting in an overall surface area of approximately 1885 μm^2 .

In the next step the measured current voltage relationship of the TASK current (see figure 8, solid line) was mathematically fitted by the single exponential function given in (1). Using the parameter values $A = 1054$, $t = 39.77$ and $y = -85.13$ revealed the best result (see figure 8, dotted line) with $r^2 = 0.99684$.

$$I_{fit} = A * e^{V/t} + y \quad (1)$$

Since NMODL requires a current that is relative to the cell surface, I_{rel} (in mA/cm²) satisfying equation 2 had to be determined.

$$I_{fit} \equiv I_{rel} * area \quad (2)$$

In order to ensure unit consistency the variables $area$ and I_{fit} had to be multiplied by the factor 10^{-8} leading from μm^2 to cm^2 and 10^9 leading from pA to mA respectively (3).

$$I_{fit} = I_{rel} * area * 10^{-8} * 10^9 \quad (3)$$

Rearranging the previous equation to (4) and substituting the $area$ term with (5) delivered the required Hodgkin-Huxley like current equation of I_{rel} (6).

$$I_{rel} = \frac{I_{fit}}{area * 10} \quad (4)$$

$$\bar{g}_k = \frac{1}{area * 10} = 5.305 * 10^{-5} \quad (5)$$

$$I_{rel} = \bar{g}_k * I_{fit} = \bar{g}_k * (1054 * e^{V/39.77} - 85.13) \quad (6)$$

Since neither gating variables nor any kinetic scheme had to be considered the TASK current implementation could be kept far more compact than those of I_h or I_T .

```

TITLE Task channel in TC neuron

COMMENT
  Assembled by Patrick Meuth
ENDCOMMENT

INDEPENDENT {t FROM 0 TO 1 WITH 1 (ms)}

UNITS {
  (mA) = (milliamp)
  (mV) = (millivolt)
}

NEURON {
  SUFFIX iTASK3
  USEION k READ ek WRITE ik
  RANGE ik, gkbar
}

PARAMETER {
  v                (mV)
  celsius          (degC)
  dt               (ms)
  ek               (mV)
  gkbar = 5.305e-5 (mho/cm2)
}

ASSIGNED {
  ik                (mA/cm2)
}

BREAKPOINT {
  ik = gkbar*(1054*exp(v/39.77)-85.13)
}

```

2. TNT – an upgrade of the NEURON simulation environment

In general there are three main reasons for the development of a virtual single cell or network model: verification, prediction and experimental limits.

The verification of measured results via a reductionist model can be crucial whenever side effects might impact the measurement or alternative modes of action could be causative as well. Within the presented work a model cell was exemplarily used to verify that the sequential application of several ion channel blockers did not impair the viability of the measured cell (see Project I, results section). Another example is the multi compartment cell model (see Project III, results section) used to disprove that the T current related, functional differences of thalamic interneurons and TC neurons are merely based on different somatic and dendritic T current densities instead of different current characteristics.

Model predictions are essential in case the experimental effort or cost for testing a single or several equivalent hypotheses limits the experimenter's number of trials. E.g. in order to ensure that the robustness of TC cells against extracellular acidification (see Project I, results section) is solely attributed to the interaction of I_h and I_{TASK} all other current combinations that could potentially interact in a similar way had to be excluded. Addressing this issue experimentally is definitely too laborious and was thus completely substituted by *in silico* simulations (see figure 9).

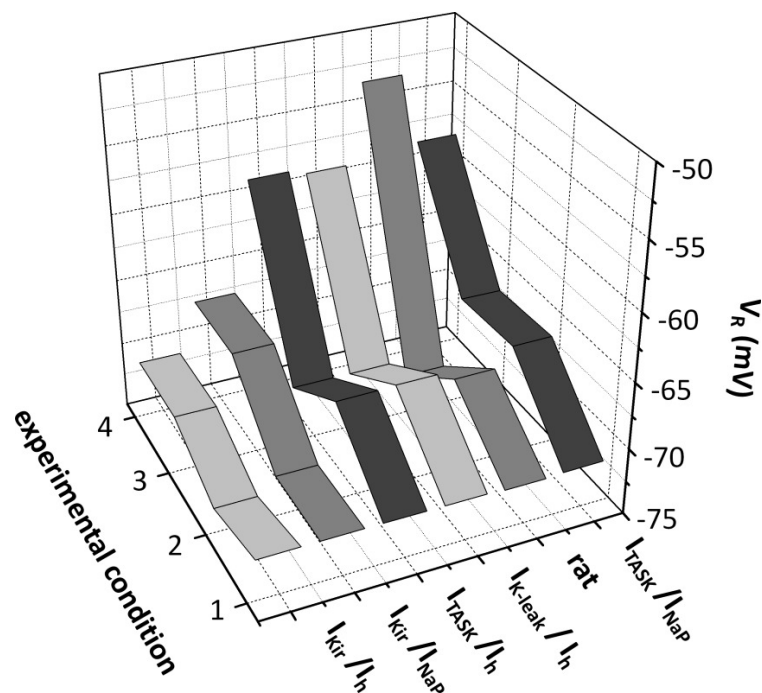


Fig. 9: Best match between *in silico* modeling of I_{TASK}/I_h and the *in vitro* observations (rat).

Besides limitations through effort and cost the experimenter usually faces technical or methodological problems more often. In these cases computer simulations can be a valuable tool to address the scientific question in another way. One apposite example is given in Project VI (see results section) where the influence of different H current characteristics on thalamocortical oscillations was supposed to be investigated. Since TC neurons require reciprocal feedback from the NRT (see section 2, introduction) in order to show oscillatory bursting the experimenter would have had to control at least one cell from both brain regions. Up to now the chance of successfully patching two interconnected cells in a slice preparation is rather low and doing so for four cells is almost impossible. Consequently all findings gained from the four cell neuronal network model build for that project are experimentally not to achieve.

On the other hand one has to admit that setting up a realistic simulation is not that easy and often requires a very fine-tuned parameter space in order to mimic the delicate interplay of multiple biophysical mechanisms. This is especially true whenever a model's predictive power is challenged in case detailed knowledge of one or more parameters simply can't be provided and a comprehensive parameter search is unavoidable.

2.1 Why TNT?

Repeatedly changing all user-accessible parameters (e.g. maximum ionic conductance, ion concentrations, cell size) and rerunning a simulation is well supported within the NEURON simulation environment and can be easily automated in the context of a parameter search. The opposite is true in case a mechanism is supposed to be substituted or a mechanism's internal realization has to be changed. Since membrane mechanisms have to be evaluated at every time step of a simulation the NEURON simulation environment demands them to be optimized in terms of processing speed. Therefore all NMODL files in the current simulation folder have to be converted into C-code and finally compiled into a new library named "nrnmech.dll" by manually calling the function "mknrndll" in the Microsoft Windows start menu. This obligatory library is automatically loaded whenever a simulation starts and determines the usable repertoire of mechanisms. In consequence the default procedure for preparing and running a simulation prevents any automated search that targets a mechanism's internal parameters or its replacement. At this point a program named TNT - text file based NEURON power transmission - was developed from the scratch. Besides providing the automated mechanism compilation (see section 2.3) TNT offers an easy and compact way of defining, executing and recording an unlimited series of unsupervised simulations within the NEURON simulation environment.

2.2 How to define a set of simulations in TNT?

TNT was completely written in NEURON's native programming language (hoc, see section 5.2, introduction) in order to offer it for a later integration into NEURON's standard distribution. As the abbreviation TNT already implies, the program operates on platform-independent, user-readable text files that are going to be introduced in the following.

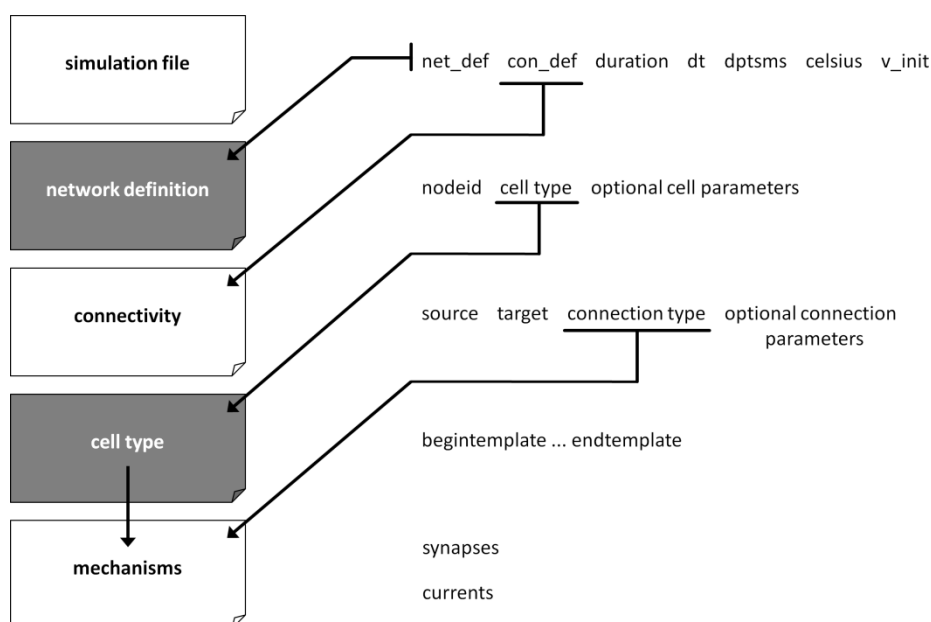


Fig. 10: File structure of a TNT simulation set.

According to the scheme given in figure 10 the definition of one or a set of different simulations follows a hierarchical modularization. On top of all stands the simulation file that holds the relative path to the network as well as connectivity definition file, the desired simulation duration (ms), integration time step (ms), number of recorded data points per millisecond (data plotting / writing to hard drive), temperature (°C) and initial membrane voltage (mV) for all incorporated cells.

Following this pattern an arbitrary number of simulations can be added to this file. The separation of network and connectivity definition in two files allows that testing the same set of cells with different connection patterns or the other way around can be defined in a very compact way. A corresponding simulation file is exemplarily given in the following.

```
// simulation 1-3
DB/net_defs/net_1.txt DB/connectivity/con_1.txt 40000 0.1 10 36 -70
DB/net_defs/net_1.txt DB/connectivity/con_2.txt 40000 0.1 10 36 -70
DB/net_defs/net_1.txt DB/connectivity/con_3.txt 40000 0.1 10 36 -70

// simulation 4-6
DB/net_defs/net_1.txt DB/connectivity/con_1.txt 40000 0.1 10 36 -70
DB/net_defs/net_2.txt DB/connectivity/con_1.txt 40000 0.1 10 36 -70
DB/net_defs/net_3.txt DB/connectivity/con_1.txt 40000 0.1 10 36 -70
```

The cell specification in the network definition file comprises a user-specified string serving as node identifier, the relative path to the desired cell template and optional parameter assignments enclosed in squared brackets that can be used for modifying the default template values. TNT thereby distinguishes three classes of variable assignments. Global variables are indicated by an asterisk (*) following the variable name (see *ginc_iar*). TNT counterchecks whether these variables are assigned multiple times and delivers a corresponding consistency warning if applicable. The second and third class distinguish default and non-default local variable assignments with the latter being indicated by the classic object-oriented dot (.) notation. Since many previous cell models from the “ModelDB” data base use the label “soma” for the default section TNT disburdens the user by automatically adding this prefix in case no other section name or object label is given (see *ghbar_iar*). Additionally TNT ensures that the closing squared bracket is present and delivers an error message otherwise.

External mechanisms or NMODL files (*.mod) respectively that are required for the simulation are usually listed in the network or connectivity definition file but can appear literally anywhere in the five classes of input text files. Whenever the TNT parser encounters the keyword “ex” the following list of mechanisms gets copied from the default mechanism folder (“DB/mechanisms”) into the temporary simulation folder (“DB/tmp_sim_folder”). Thereby TNT ensures every mechanism file to be copied only once in case a corresponding mechanism file could be found. A lacking mechanism file or the omitted closing keyword “endex” will lead to a meaningful error message.

```
ex
    HH2_Destexhe_96
    IT2_Destexhe_96
    cadecay_Destexhe_96
    kleak_Destexhe_96
    IT_Destexhe_96
    lh_Destexhe_96
endex

// delta oscillations
TC1    DB/cell_types/TC_Destexhe_96.hoc [ghbar_iar = 0 kl.gmax = 0.005 ginc_iar* = 1]
TC2    DB/cell_types/TC_Destexhe_96.hoc [ghbar_iar = 0 kl.gmax = 0.005]
```



```
RE1    DB/cell_types/RE_Destexhe_96.hoc
RE2    DB/cell_types/RE_Destexhe_96.hoc
```

Given the node identifiers from the network definition file a connection specification within the connectivity definition file has to satisfy the following pattern: source node identifier, target node identifier, type of connection and optional connection parameter assignments.

```
ex
    ampa_Destexhe_96
endex

// Glutamate AMPA receptors in synapses from TC to RE

TC1    RE1    AMPA_S    [Alpha* = 0.94 Beta* = 0.18 Cmax* = 0.5 Cdur* = 0.3 Erev* = 0 gmax=0.1]
TC1    RE2    AMPA_S    [gmax=0.1]
TC2    RE1    AMPA_S    [gmax=0.1]
TC2    RE2    AMPA_S    [gmax=0.1]
```

The above example defines a total of four directed connections between two TC neurons (TC1, TC2) and two NRT neurons (RE1, RE2) where each connection is realized as a point process named “AMPA_S”. In comparison to a biophysical mechanism the syntax for accessing variables of a point process is different. TNT automatically takes care of these differences and adds the name of the point process as suffix to all global variables (in this case “_AMPA_S”) while leaving the local variables unchanged.

Even the largest network simulations comprising an impressive amount of interacting cells are in most cases based on a limited number of different masters that are cloned and slightly modified for each new cell. For building such networks NEURON offers a convenient template construct (see figure 10, cell type). The following example template file originates from an early work of Alain Destexhe (ModelDB, accession number 3343, [5]) who is one of the most reputable scientists in the neuronal modeling sector. This NRT neuron implementation was used within Project VI (see results section) and additionally gives a good notion of the basic components necessary for defining a functional NEURON simulation.

```
begintemplate sRE                                // create a new template object
public soma

create soma                                     // one-compartment of 14260 um2
soma {
    diam = 70
    L = 64.86
    Ra = 100
}

proc init() { local v_potassium, v_sodium

    v_potassium = -100                          // potassium reversal potential
    v_sodium = 50                               // sodium reversal potential

    soma {
        insert pas                             // leak current
        e_pas = -90
        g_pas = 5e-5

        insert hh2                             // Hodgkin-Huxley INa and IK
        ek = v_potassium
        ena = v_sodium
    }
}
}
```

```

vtraub_hh2 = -55
gnabar_hh2 = 0.2
gkbar_hh2 = 0.02

insert it2          // reticular IT current
cai = 2.4e-4
cao = 2
eca = 120
shift_it2 = 2
qm_it2 = 2.5       // low q10
qh_it2 = 2.5
gcabar_it2 = 0.003 // strong

insert cad          // calcium decay
depth_cad = 1
taur_cad = 5
cainf_cad = 2.4e-4
kt_cad = 0         // no pump
}
endtemplate sRE

```

The first line of a template file holds the keyword “`begintemplate`” and a template identifier which is “`sRE`” in this case. Between that and the closing sequence “`endtemplate sRE`” any hoc code may appear. In contrast to e.g. dendrites modeling solely the soma of a cell usually requires only one section. Sections are generated with the “`create`” command that expects a list of comma-separated section names or array definitions to follow.

```
create soma, axon, dend[3]
```

The latter is also true for the keyword “`public`” which declares variables to be accessible from the outside. After generating the public section “`soma`” the example template continues by resetting some of this section’s default values. A sections default parameters comprise the earlier mentioned parameters (see section 5.1, introduction) number of segments (*nseg*), length (*L*) and diameter (*diam*) as well as the specific cytoplasmic resistivity *Ra* (default: 35.4 $\Omega \cdot \text{cm}$) and the specific membrane capacitance *cm* (default: 1 $\mu\text{F} / \text{cm}^2$). Grouping assignments in braces with a preceding section name prevents from using the explicit dot notation.

```
section.parameter
```

Braces are also used for enclosing the body of a function or procedure. The declaration of local variables has to appear as the first statement within the braces and on the same line as the function or procedure declaration, respectively.

```

func name() { local a, b, c          proc name() { local d, e
    ...                               ...
    return x                          }
}

```

Every template possesses one obligatory procedure named “`init()`” which is called whenever an instance of this template is generated via the “`new`” command. Referring to the example template the “`init()`” procedure is used to add some biophysical mechanisms to the so far empty cell hull and set their parameters. The associated keyword “`insert`” is thereby followed by the suffix (see section 1.1) of the desired mechanism. Consequently the instantiated NRT cell will be equipped with NEURON’s standard leak current *pas* (passive.mod, determining the resting membrane potential), the mechanism *hh2* (sodium and potassium current for action potential generation), a T current *it2* (for the generation of LTS; see section 3, introduction) and a calcium dynamic *cad* for updating the

intracellular calcium concentration in relation to the T current mediated calcium influx. Cell templates perfectly match the modularized concept of TNT simulations and have thus become an integral part of it.

The last class of TNT's input files (see figure 10) comprise the biophysical mechanisms written in NMODL. In contrast to the earlier introduced current implementations of I_h , I_T and I_{TASK} the realization of a synaptic connection is usually based on a point processes instead of a range variable.

```

NEURON {
    POINT_PROCESS AMPA_S
    POINTER pre
    RANGE C, R, R0, R1, g, gmax, lastrelease, TimeCount
    NONSPECIFIC_CURRENT i
    GLOBAL Cmax, Cdur, Alpha, Beta, Erev, Prethresh, Deadtime, Rinf, Rtau
}

```

Although functionally very different both NMODL implementations mainly differ in the NEURON block where the keyword "SUFFIX" is replaced by "POINT_PROCESS". An excerpt of the synapse implementation AMPA_S is exemplarily given.

2.3 Automated mechanism compilation

Mechanism files that are supposed to be used in a simulation have to be compiled into a C-code library named "nrnmech.dll" by manually calling the NEURON program link "mknrndll" in the Microsoft Windows start menu. Calling this function opens a graphical user interface that basically allows the selection of the current simulation folder and the compilation of all mechanism files therein. If the latter is started a new console opens that prints some user feedback about the ongoing compilation process. Finally a message indicating that the process did run into errors or that the file "nrnmech.dll" was built successfully gets presented. At this point the console waits for the user to acknowledge this information by pressing the return key before the console window closes.

One integral task of TNT was to deliver an alternative for this double user interaction. Tracing the process cascade called by "mknrndll" revealed the following components where "npf" stands for NEURON program folder.

1. The program link "mknrndll" executes "npf/bin/nrniv npf/lib/hoc/mknrndll.hoc" which calls the NEURON interpreter "nrniv.exe" to load and process the hoc file "mknrndll.hoc".
2. "mknrndll.hoc" generates the graphical user interface for selecting the current simulation folder and starting the compilation process by a button named "make nrnmech.dll".
3. Pressing that button executes "npf/bin/rxvt -e npf/bin/sh npf/lib/mknrndll.sh npf" in the selected simulation folder. Rxvt is a terminal emulator for the Unix X-Window system that was ported to the Microsoft Windows operating system by its embedding into a Cygwin environment. Calling rxvt with the option "-e" opens a terminal and executes the succeeding command with its arguments. In this case the shell script "mknrndll.sh" gets started.
4. The script basically deletes the previous "nrnmech.dll" if present and executes a second shell script named "mknrndll2.sh". Thereafter the existence of the new mechanism library gets checked and leads to a success or error message respectively. At this point the user finally gets requested to acknowledge the given information by pressing the return key.

5. "mknrndl2.sh" generates the obligatory file named "mod_func.c" that specifies which mechanism is supposed to be incorporated to the current simulation and finally executes the make file "mknrndll.mak".
6. The overall process cascade ends with that make file. It translates all specified NMODL mechanisms into C-code by "npf/bin/nocmodl.exe" and calls "npf/bin/gcc.exe" for the finishing compilation.

TNT's automated compilation concentrates on the integral parts of that process cascade starting at step 3. The associated procedure "compile()" thereby calls a slightly modified version of the above mentioned shell script which lacks the final request for user interaction (see step 4) but leaves step 5 to 6 unmodified. In order to indicate that difference TNT's alternative shell script was labeled "mknrndll-pm.sh".

2.4 TNT's program structure

The whole program comprises twelve different hoc files and one shell script ("mknrndll-pm.sh"). The latter and three of the hoc files ("compile.hoc", "help_sim.hoc", "trace.hoc") are solely required while running a simulation and thus not called by TNT itself. For each single simulation a temporary simulation folder ("DB/tmp_sim_folder") gets prepared that holds besides the previously mentioned software package all involved mechanism (*.mod) and cell template ("TNT_xxx.hoc") files. After compiling the NMODL mechanisms into C-code the simulation gets executed by calling a second instance of the NEURON interpreter "nrniv.exe".

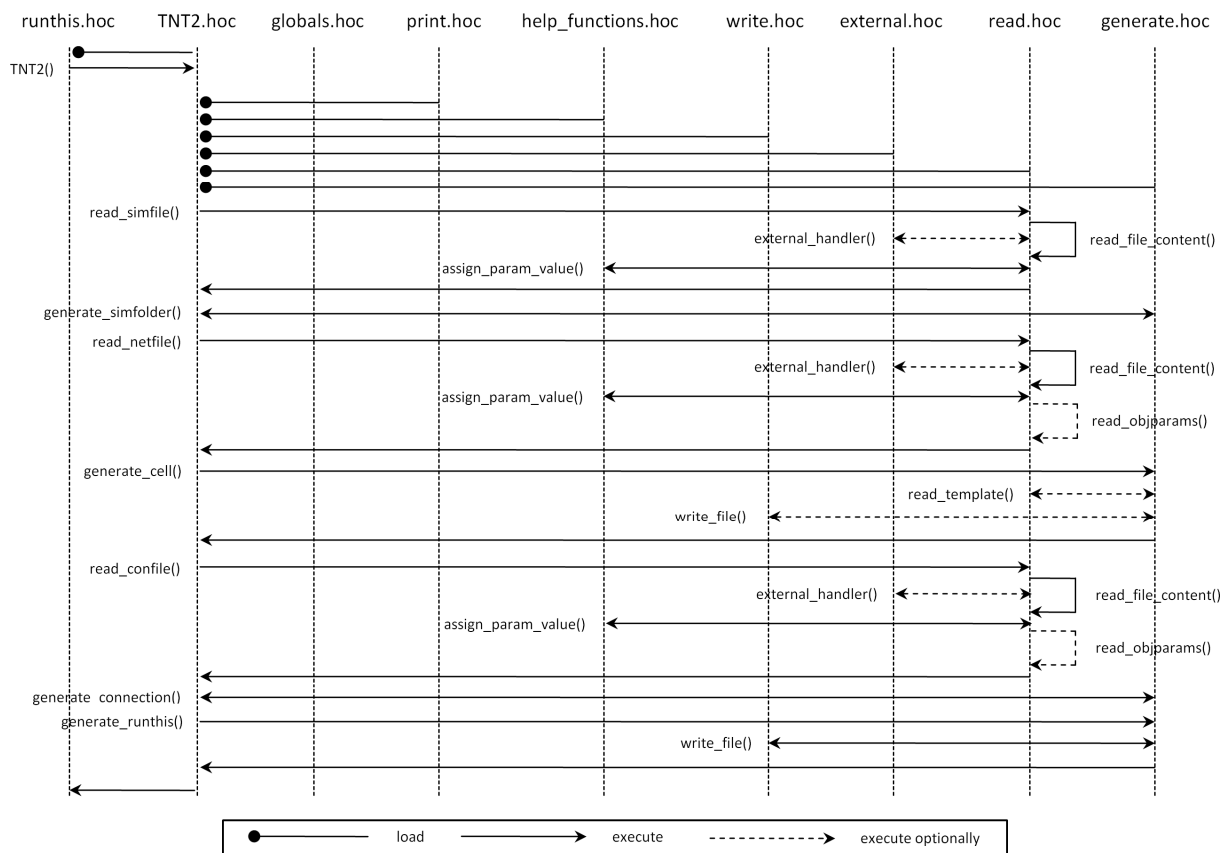


Fig. 11: TNT program flow.

TNT's core application includes the remaining nine hoc files given in the program flow of figure 11. Thereby the main procedure as well as the program folder is named "TNT2" indicating that version 2.0 is the latest release. Detailed descriptions about the purpose and characteristic of each single function and procedure of all twelve hoc files are given as lexicographically sorted listing in the following [sid = string identifier / cell identifier / node ID].

compile.hoc

compile() procedure

This procedure starts the compilation process for all mechanism files (*.mod) of the current folder. If the compilation ended without errors the resulting library "nrnmech.dll" gets loaded via the "nrn_load_dll()" command in order to prepare the simulation execution. Otherwise a corresponding error message will be send to the console window.

external.hoc

external_handler() procedure

Input to that procedure is the name of the desired mechanism file omitting the file extension. For the user's convenience and a compact simulation definition the default file extension ".mod" will be automatically added while this procedure tries to copy the specified mechanism file from "DB/mechanisms" to "DB/tmp_sim_folder". The copy process will be skipped if the specified mechanism file was already copied before. In case the specified mechanism is not part of the mechanism data base ("DB/mechanisms") a corresponding error message will be send to the console window. The procedure communicates via the global variable *comp*, which is set to 1 in case the specified mechanism was successfully copied and -1 otherwise.

generate.hoc

add_separators() procedure

Input to that procedure is a single numeric value that determines the number of repetitions of the string "-----" following "//". The resulting comment line is used to visually separate and structure the different parts of the simulation file "runthis.hoc" generated by the procedure "generate_runthis()".

generate_cell() procedure

Starts by calling the function "get_tablerow()" in order to determine whether current cell template is part of the list of already processed files. In case of a negative result it will be added to that list and read by the procedure "read_template()". If reading encountered no errors the buffered template content gets flushed to a new template file that is named like the source template but additionally holds the prefix "TNT_" in order to distinguish both. Thereafter this name will be added to the list of files that are going to be loaded via the "load_file()" command in the main script ("runthis.hoc") of the current simulation.

Independent of the cell template's processing history the buffer *cellconstructor* will be expanded by the commands necessary to generate the specified cell, add it to the list *cells* and assign its sid. Thereafter follows the processing of optional object parameter assignments if present. The

reserved symbol “*” indicates a global variable and may only appear as suffix. Its presence in front of or within the variable name will lead to an error message. The latter is also true in case global variables receive more than one value assignment. In contrast to global variable assignments which are buffered without the asterisk for a collective inclusion to the simulation’s main script later on, local variable assignments are immediately added there. Local variables will keep their obligatory prefix if explicitly specified via the dot notation or automatically receive the default “soma” prefix otherwise.

`generate_connection()` procedure

This procedure expands the buffer *conconstructor* by adding all commands necessary for generating an instance of the specified connection mechanism, attaching it to the target cell `sidB`, setting a pointer to the source cell `sidA` and attaching the associated object reference to the list *cons*. If optional parameter assignments are present, the procedure distinguishes local variable assignments which are immediately added to the simulation’s main script and assignments to global variables which are buffered for a collective inclusion later on. The latter are also checked for multiple value assignments and the incorrect position of the reserved symbol “*” which gets removed before buffering.

`generate_runthis()` procedure

Generates a hoc script named “runthis.hoc” that realizes the currently specified TNT simulation.

This script includes:

- definition and generation of the lists *cells* and *cons* holding the object references of all nodes and their connections
- “load_file()” commands for the inclusion of the necessary external functions (e.g. “nrngui.hoc” or “compile.hoc”)
- calling the procedure “compile()” for converting all NMODL mechanisms into C-code.
- “load_file()” commands for loading all TNT generated cell templates (indicated by the prefix “TNT_”)
- creating and setting up all cells by flushing the buffer *cellconstructor* which was filled by the procedure “generate_cell()”
- creating and setting up all connections by flushing the buffer *conconstructor* which was filled by the procedure “generate_connection()”
- assigning all global variables
- setting up all simulation parameters (e.g. simulation duration or initial membrane voltage)
- calling the procedures “print_all_sids()”, “print_all_cons()” and “print_sim_params()” in order to give a user feedback
- calling the procedure “trace_all_cells()” in order to record the membrane voltages of all cells during the simulation
- calling NEURON’s standard “RunControl” window
- commands for the initialization and execution of the simulation
- calling the procedure “write_traces()” for writing all recorded data to hard disk
- the command “quit()” which ends the overall processing by NEURON’s interpreter “nrniv.exe”

Data files are saved as user-readable text files to the folder of the currently executed simulation file. In order to indicate the affiliation to each other data files are named like the simulation file extended by the symbol "#", the current simulation number and the extension ".dat".

`generate_simfolder()` function

The function generates the temporary simulation folder "DB/tmp_sim_folder" after deleting the previous instance if present. Thereafter the simulation specific files "compile.hoc", "help_sim.hoc", "trace.hoc" and "mknrndll-pm.sh" are copied to the newly generated folder. In case an error occurs the function stops the further processing and returns 1 to the calling function. A successful execution will return 0.

globals.hoc

Defines and initializes all global numeric and string variables as well as objects.

help_functions.hoc

`assign_param_value()` procedure

The procedure receives three inputs comprising a list of variables separated by space characters, a numeric value indicating the affected variable and a binary switch that delivers information about the data type (0: string, 1: numeric) that is supposed to be assigned. After extracting the specified variable from the variable list the data type parameter determines which of the two global variables *nextstr* (string) or *nextnr* (numeric) gets assigned to it. Both global variables are used by the function "read_file_content()" in order to pass on the currently read token.

`calc_proc_time()` procedure

The procedure receives the amount of seconds elapsed since starting TNT and converts that value into a string representation of the form "w day(s) x hour(s) y min(s) z sec(s)". Thereby zero entries are omitted in order to return the shortest possible string.

`get_tablerow()` function

Inputs to that function are two strings. The first one represents a table where each row holds a single entry. The second one is the table entry whose position is supposed to be determined. In case the specified search string could be found the function returns its corresponding row number and -1 otherwise.

`isnumber()` function

Given a string as input the function determines whether this string might be a numeric value. In case the input equals one of the variable names in the working memory or its assignment to a numeric dummy variable fails the function returns 0. In case the numeric assignment succeeds the function returns 1.

`mod()` function

Inputs to that function are two numeric values *a* and *b*. The function returns *a* in case *b* equals 0 or the result of the modulo operation $\text{mod}(a,b) = a \text{ mod } b = a - [a/b] * b$.

str2num() function

Input to that function is a string. In case forwarding that input to “isnumber()” reveals a positive result the content of the associated numeric dummy variable gets returned and -1 otherwise.

help_sim.hoc

find_sid() function

Given a sid as search parameter the function returns the index of the first object in the cell list *cells* that matches the specified string. In case the cell list is empty or the requested sid could not be found the function returns -1.

print_all_cons() procedure

Sequentially determines the POINT_PROCESS label of each single connection object in the list *cons*. The output of that procedure is presented in a tabular form in the console window.

print_all_sids() procedure

This procedure sequentially goes through the complete cell list *cells* and outputs the sid of each single object therein in a tabular form in the console window.

print_sim_params() procedure

The procedure prints all simulation parameters (duration, integration time step, number of recorded data points per millisecond, temperature and initial membrane voltage) in a tabular form in the console window.

print.hoc

print_ascii_chars() procedure

Inputs to that procedure are two numeric variables *min* and *max*. In case *max* is lower than *min* their values get exchanged. For each integer of the interval [*min*, *max*] the procedure outputs one text line comprising the corresponding ASCII character in the console window.

print_con_header() procedure

Prints one text line in the console window that comprises the terms “sidA:”, “sidB:” and “mechanism:”. These column labels precede a list of triples (source cell sid, target cell sid, label of corresponding connection mechanism) received from the connectivity definition file.

print_dashed_line() procedure

The procedure generates a dashed line in the console window.

print_error_msg() procedure

Inputs to that procedure are the error type, the name of the function at which the error occurred and additional error information. Depending on the type of error a meaningful error

message will be printed in the console window. Thereby the output is cut into pieces smaller or equal to 68 characters in order to fit in one line of a non-resized, default console window.

Possible error types are:

- 0 file could not be opened
- 1 desired mechanism file is not part of the mechanism data base
- 2 wrong data type or incomplete variable sequence while reading simulation file
- 3 wrong data type or incomplete variable sequence while reading connectivity definition file
- 4 end of multiple line comment block (*/) is missing
- 5 template file contains commands outside the "begintemplate ... endtemplate" block
- 6 template file contains the keyword "endtemplate" but no preceding "begintemplate"
- 7 template file contains the keyword "begintemplate" two times
- 8 wrong data type or incomplete variable sequence while reading a network definition file
- 9 template file contains the keyword "begintemplate" but no closing "endtemplate"
- 10 "tmp_sim_folder" can't be prepared since files in there are blocked by another process
- 11 the closing symbol "]" is missing at the end of current parameter specification block
- 12 the closing symbol "]" is accidentally concatenated to the next token
- 13 the opening symbol "[" is accidentally concatenated to the preceding token
- 14 the reserved symbol "*" appeared without association to a variable name
- 15 multiple assignments to a global variable

print_line() procedure

A solid line will be printed in the console window.

print_msg() procedure

The single numeric input determines which of the different user feedback messages is going to be printed in the console window. Some of these messages are only available if TNT was started in the so called detail mode indicated by a 1 instead of a 0 as third parameter of the procedure call "TNT2()".

Possible message types are:

- 0 "Reading simulation file xxx ..."
- 1 call of "print_sim_header()" and "print_sim_params()"
- 2 "Reading network definition file xxx ..." [detail mode: call of "print_net_header()"]
- 3 [detail mode: current cell sid, corresponding cell template path and ">>> processed"]
- 4 [detail mode: current cell sid, corresponding cell template path and ">>> skipped"]
- Used in case template file was already processed before -
- 5 "Reading connectivity definition file xxx ..." [detail mode: call of "print_con_header()"]
- 6 [detail mode: source cell sid, target cell sid, connection type and ">>> addendum"]
- The latter is omitted in case the definition of the current connection does not include any connection parameter settings -
- 7 "Executing simulation ... " and call of "print_line()"
- 8 call of "print_line()" and "Simulation finished ..."

print_net_header() procedure

Output of that procedure is one text line comprising the terms "sid:" and "filename:" in the console window. This line represents the column labels for the following list of pairs (sid, path of corresponding cell template file) received from the current network definition file.

`print_sim_footer()` procedure

Given TNT's start time point the procedure calculates the elapsed amount of seconds. The result is then converted into a more readable format by calling "`calc_proc_time()`" and finally printed as part of a three lines comprising user feedback in the console window.

`print_sim_header()` procedure

Input to that procedure is the current simulation number. The procedure prints three lines in the console window that visually separate future from previous console outputs, announce the start of a new simulation and inform about the current simulation number.

`print_sim_params()` procedure

This procedure outputs all parameters of the currently processed simulation (current row in the simulation file) in a tabular form in the console window.

read.hoc

`read_confile()` function

Given are the path to the current connectivity definition file and a file position therein. The function defines a valid connectivity definition to require four consecutive strings (source sid, target sid, connection type and optional connection parameter assignments). Starting at the specified file position the function calls "`read_file_content()`" and "`assign_param_value()`" in case the read token satisfied the data type requirement. This sequence gets four times repeated if no errors occur. In case a fourth string was found it can either be the source sid of the next connectivity definition or the start of an optional parameter assignment block. The latter is indicated by the symbol "[" and results in calling "`read_objparams()`". If the first string character is unequal to that symbol the function read too far and the file position has to be reset in front of the last token. The function returns -1 in case of a wrong data type or incomplete variable sequence, 0 if no errors occurred but the end of file got reached and the current file position otherwise.

`read_file_content()` function

Inputs to that function are a file path, a file position therein and the desired data type. If the specified file does not exist or cannot be opened for reading a corresponding error message will be printed in the console window. Otherwise the function reads the next token at the specified position and calls "`isnumber()`" in order to check whether the data type requirement is fulfilled. Thereby the function supports five different modes.

Possible data type requests are:

- 0 explicit string request at the current position
- 1 explicit number request at the current position
- 2 find next string no matter at which position
- 3 find next number no matter at which position
- 4 just return the next token no matter what it is

After detecting a single-line (`//`) or multi-line (`/* ... */`) comment the following tokens are completely skipped until the end of the line or the closing character sequence "`*/`" got reached,

respectively. In case of an unclosed multi-line comment the function sends an error message to the console window. The keyword “ex” precedes a listing of external mechanisms that are supposed to be copied to the simulation folder. Consequently the function calls “external_handler()” for each succeeding token that is unequal to the closing keyword “endex”. If the latter does not appear before reaching the end of the file a corresponding error message will be outputted in the console window. The function returns -1 in case a wrong data type was found or other errors occurred, 0 if no errors occurred but the end of the file was reached and the current file position otherwise.

read_netfile() function

Inputs to this function are the path to the current network definition file and a file position therein. The function defines a valid cell definition to comprise three consecutive strings (sid, path to cell template, optional cell parameter assignments). Starting at the specified file position the called function “read_file_content()” determines whether the next token fulfills the required data type. If so, the corresponding parameter will be set by calling “assign_param_value()”. If a third string was found its first character determines whether it is the sid of the next cell definition or the start of an optional parameter assignment block. In the first case the file position has to be reset in front of the string since reading got too far. If the last string starts with “[“ the second case is true and the function “read_objparams()” gets called. The function returns -1 in case of a wrong data type or incomplete variable sequence, 0 if no errors occurred but the end of the file got reached and the current file position otherwise.

read_objparams() function

Given a file path and a file position therein this function repeatedly calls “read_file_content()” with the third parameter (data type) equal to four. This means that all tokens will be accepted without any data type limitation. If necessary the function truncates the opening (“[“) or closing (“]“) squared bracket from a succeeding variable name or preceding assignment value, respectively. While processing the optional parameter assignment block each parameter assignment gets unitized in that the left hand side of the equation is followed by a single space character, an equal sign, a single space character and the right hand side of the equation. Thereafter the unitized assignment is added to the buffer *objparams* which will be used by the functions “generate_cell()” or “generate_connection()” later on. The whole process stops if the closing squared bracket was read. In case an unclosed parameter assignment block gets detected, a corresponding error message will be send to the console window. The same is true if the opening squared bracket or closing squared bracket is accidentally concatenated to the previous or next token, respectively. The function returns -1 in case of an error, 0 if the end of the file was reached without errors and the current file position otherwise.

read_simfile() function

Given the path to a simulation file and a file position therein the function starts reading a predefined number of consecutive tokens at the specified location. A valid simulation definition requires two strings (path to network and connectivity definition file) followed by five numeric values (simulation duration, integration time step, number of data points recorded per millisecond, temperature and initial membrane voltage). For each of these parameters the function “read_file_content()” gets called. If the read token satisfied the required data type the procedure “assign_param_value()” finally sets the corresponding simulation parameter. The function returns -1 in case of a wrong data type or incomplete variable sequence, 0 if no errors occurred but the end of the file got reached and the current file position otherwise.

`read_template()` procedure

This procedure is parameterized with the path of a standard cell template that is supposed to be converted into a TNT cell template. The conversion comprises two major steps. At first the original template identifier (following the keywords “`begintemplate`” and “`endtemplate`”) gets substituted with a new unique template identifier (“Node” concatenated with a counter variable *x*) in order to prevent name collisions of templates from different sources. Secondly an additional public variable `sid` is added right behind the keyword “`begintemplate`” so that every instance of that template can be assigned a user-specified node identifier. In order to find a compromise between compactness and readability the procedure omits all comments, empty lines and tabulators of the original file but keeps its line breaks unchanged. All tokens are received by calling “`read_file_content()`” in a mode that does not apply any data type limitation. The conversion outputs a meaningful error message in the console window if a command outside the “`begintemplate ... endtemplate`” block was found, the keyword “`endtemplate`” is present but no preceding “`begintemplate`”, the keyword “`begintemplate`” occurs two times in a row, the closing keyword “`endtemplate`” is not present, the specified original template file does not exist or is unreadable.

runthis.hoc

This is the file that has to be executed in order to start TNT. After loading the TNT main script “`TNT2.hoc`” the procedure “`TNT2()`” gets executed with three parameters. These comprise the path to the TNT data base, the path to the desired simulation file and a binary switch determining whether (1) or not (0) detailed information about the ongoing simulations are printed in the console window.

TNT2.hoc

The TNT main script starts with a sequence of “`load_file()`” commands for the inclusion of all required external functions from NEURON (e.g. “`nrngui.hoc`”) as well as TNT (e.g. “`generate.hoc`”) and finally defines the main procedure “`TNT2()`”.

`TNT2()` procedure

Inputs to this procedure are the path of the TNT data base, the path of the desired simulation file and a binary value. The latter switches between TNT’s detailed (1) and standard (0) output behavior concerning information about the ongoing simulations.

TNT uses several global variables for sharing information about the currently defined simulation throughout all subfunctions. Consequently the buffers:

- *runthis* (all entries of the current simulation’s main script)
- *loadf* (list of cell templates to be loaded)
- *cellconstructor* (commands for generating all specified cells)
- *conconstructor* (commands for generating all specified connections)
- *processedfiles* (list of already processed template files)
- *globalparams* (list of global variables that have already been assigned a value)

have to be reset to empty strings before processing a new simulation.

After accomplishing this the procedure calls “read_simfile()” in order to read the first simulation definition. If this is valid the temporary simulation folder “DB/tmp_sim_folder” gets prepared (“generate_simfolder()”) and the processing of the network definition file follows. For each valid cell definition received via “read_netfile()” a corresponding cell will be generated (“generate_cell()”). Thereafter the generated cells are connected by successively reading the connectivity definition file (“read_confile()”) and generating a connection for each valid connection definition therein (“generate_connection()”). At this point all information required for executing the currently specified simulation are collected. Consequently the next two steps comprise writing a corresponding simulation script to a file named “runthis.hoc” in the temporary simulation folder (“generate_runthis()”) and calling NEURON’s interpreter “nrniv.exe” for its execution. The presence of the file “nrnmech.dll” within the temporary simulation folder indicates a successful compilation of all NMODL mechanisms involved in the current simulation. This in combination with the absence of other error messages will be judged as successful simulation execution. If this is the case, TNT repeats the whole process cascade until the last valid simulation definition got executed.

In case one of TNT’s called subfunctions encountered an error, the overall processing will be stopped. The procedure “TNT2()” itself releases only one error message in the console window, if the temporary simulation folder could not be prepared. After executing the last defined simulation without errors the user gets informed about the overall processing time according to an initially started stop watch.

trace.hoc

add_cell_trace procedure

Given a cell’s sid the procedure generates a new vector for recording its membrane voltage and adds that vector to the list of voltage traces.

trace_all_cells() procedure

Calls “add_cell_trace()” for all objects in the cell list *cells*.

write_traces() procedure

Input to that procedure are a file path and a numeric value that determines the desired number of data points written per row. According to the specified path a new file will be generated that starts with all information necessary to recover the time vector of the currently processed simulation later on.

These comprise the simulation duration *tstop* (ms), the integration time step *dt* (ms) and the number of recorded data points per millisecond *dptsms*. Thereafter all recorded voltage traces are successively supplemented. The data points of each trace are preceded by the corresponding cell sid, downsampled for the sake of smaller data files in case the number of recorded data points exceeds the desired number of written data points ($1/dt > dptsms$), separated by tabulators and portioned according to the specified number of written data points per row.

While being processed all voltage traces are summed up to an EEG-like signal. The corresponding vector will be written in the same format as before at the end of the file and receives the preceding term “EEG:” instead of a cell sid.

write.hoc

write_file() procedure

The two inputs to that procedure comprise the desired file path and file content. If executed it generates a new file on the hard disk according to the specified path and writes the given content into that file.

References

- [1] P Meuth, SG Meuth, D Jacobi, T Broicher, HC Pape, and T Budde. *Get the Rhythm: Modeling Neuronal Activity*. Journal of Undergraduate Neuroscience Education (JUNE), 4(1):A1–11, 2005.
- [2] A Destexhe, A Babloyantz, TJ Sejnowski. *Ionic mechanisms for intrinsic slow oscillations in thalamic relay neurons*. Biophys J., Oct;65(4):1538-52, 1993.
- [3] NT Carnevale and ML Hines. *The NEURON Book*. ISBN: 9780521843218, Cambridge University Press, 2006.
- [4] JR Huguenard, DA McCormick. *Simulation of the currents involved in rhythmic oscillations in thalamic relay neurons*. J Neurophysiol., Oct;68(4):1373-83, 1992.
- [5] A Destexhe, T Bal, DA McCormick, TJ Sejnowski. *Ionic mechanisms underlying synchronized oscillations and propagating waves in a model of ferret thalamic slices*. J Neurophysiol., Sep;76(3):2049-70, 1996.

Results

Project I (J Neurophysiol. 2006)

Membrane Resting Potential of Thalamocortical Relay Neurons Is Shaped by the Interaction Among TASK3 and HCN2 Channels

Sven G. Meuth*, Tatyana Kanyshkova*, Patrick Meuth*, Peter Landgraf, Thomas Munsch, Andreas Ludwig, Franz Hofmann, Hans-Christian Pape, and Thomas Budde (*equal contribution)

By combining molecular biological, electrophysiological, immunological, and computer modeling techniques, we here demonstrate a counterbalancing contribution of TASK channels, underlying hyperpolarizing K^+ leak currents, and HCN channels, underlying depolarizing I_h , to the resting membrane potential of thalamocortical relay (TC) neurons. RT-PCR experiments revealed the expression of TASK1, TASK3, and HCN1–4. Quantitative determination of mRNA expression levels and immunocytochemical staining demonstrated that TASK3 and HCN2 channels represent the dominant thalamic isoforms and are coexpressed in TC neurons. Extracellular acidification, a standard procedure to inhibit TASK channels, blocked a TASK current masked by additional action on HCN channels. Only in the presence of the HCN blocker ZD7288 was the pH-sensitive component typical for a TASK current, i.e., outward rectification and current reversal at the K^+ equilibrium potential. In a similar way extracellular acidification was able to shift the activity pattern of TC neurons from burst to tonic firing only during block of I_h or genetic knock out of HCN channels. A single compartmental computer model of TC neurons simulated the counterbalancing influence of TASK and HCN on the resting membrane potential. It is concluded that TASK3 and HCN2 channels stabilize the membrane potential by a mutual functional interaction, that the most efficient way to regulate the membrane potential of TC neurons is the converse modulation of TASK and HCN channels, and that TC neurons are potentially more resistant to insults accompanied by extracellular pH shifts in comparison to other CNS regions.

Modeling

The modeling contribution in this project comprised three tasks. The first task was to verify an electrophysiological experiment during which a series of different ion channel blockers were applied to a TC cell while recording the standing-outward current I_{SO} . This current is a mixture of different depolarizing and hyperpolarizing currents which are present while the cell is at rest and thus determine the RMP. Aim of this experiment was to identify the specific ion channels contributing to the I_{SO} by selective blockade. The cumulative application of in this case five ion channel blockers gave rise to the question whether the cells' viability might have been impaired by such a treatment. The single compartment model cell used in this project was able to mimic the electrophysiological data quite well and therefore successfully verified the experiment's plausibility.

The second task was to quantify the effects on I_h and I_{TASK} by extracellular acidification. This is the standard procedure to block the pH-sensitive TASK current. Since I_{TASK} is a hyperpolarizing component the TC cell was suggested to depolarize significantly upon acidification, but this was surprisingly not the case. It turned out that there is a counterregulating additional effect that partially blocks the depolarizing current I_h leading to a strongly reduced net effect. At this point the model cell was used to identify that parameter constellation for I_h and I_{TASK} that was among other possible solutions most accurate under extracellular acidification as well as control conditions.

Finally the question arose whether other combinations of depolarizing and hyperpolarizing currents were also able to interact likewise I_h and I_{TASK} in order to produce a similar effect. Since this testing would have been very time-consuming and costly in reality, computer modeling again demonstrated its general usability in the neuroscience sector.

Project II (Neuropharmacology. 2007)

T-current related effects of antiepileptic drugs and a Ca^{2+} channel antagonist on thalamic relay and local circuit interneurons in a rat model of absence epilepsy

Tilman Broicher, Thomas Seidenbecher, Patrick Meuth, Thomas Munsch, Sven G. Meuth, Tatyana Kanyshkova, Hans-Christian Pape, Thomas Budde

Channel blocking, anti-oscillatory, and anti-epileptic effects of clinically used anti-absence substances (ethosuximide, valproate) and the T-type Ca^{2+} current (I_T) blocker mibefradil were tested by analyzing membrane currents in acutely isolated local circuit interneurons and thalamocortical relay (TC) neurons, slow intrathalamic oscillations in brain slices, and spike and wave discharges (SWDs) occurring in vivo in Wistar Albino Glaxo rats from Rijswijk (WAG/Rij). Substance effects in vitro were compared between WAG/Rij and a non-epileptic control strain, the ACI rats. Ethosuximide (ETX) and valproate were found to block I_T in acutely isolated thalamic neurons. Block of I_T by therapeutically relevant ETX concentrations (0.25-0.75 mM) was stronger in WAG/Rij, although the maximal effect at saturating concentrations (≥ 10 mM) was stronger in ACI. Ethosuximide delayed the onset of the low threshold Ca^{2+} spike (LTS) of neurons recorded in slice preparations. Mibefradil (≥ 2 μM) completely blocked I_T and the LTS, dampened evoked thalamic oscillations, and attenuated SWDs in vivo. Computational modeling demonstrated that the complete effect of ETX can be replicated by a sole reduction of I_T . However, the necessary degree of I_T reduction was not induced by therapeutically relevant ETX concentrations. A combined reduction of I_T , the persistent sodium current, and the Ca^{2+} activated K^+ current resulted in an LTS alteration resembling the experimental observations. In summary, these results support the hypothesis of I_T reduction as part of the mechanism of action of anti-absence drugs and demonstrate the ability of a specific I_T antagonist to attenuate rhythmic burst firing and SWDs.

Modeling

One part of this study comprised the effect of ethosuximide, a clinically used drug against absence seizures, on the LTS of TC neurons. This substance has been reported to reduce the persistent sodium current I_{NaP} , the calcium-activated potassium channel I_{KCa} and I_T . Using an appropriate TC cell model enabled the stepwise and sole reduction of each of the three conductances, thereby emphasizing their specific LTS contribution. The model revealed that a strong modulation of I_T could theoretically mimic all experimentally observed LTS alterations, but under the prerequisite of clinically relevant ETX concentrations additional ETX action on I_{NaP} and I_{KCa} is indispensable.

Project III (Mol Cell Neurosci. 2007)

Specific expression of low-voltage-activated calcium channel isoforms and splice variants in thalamic local circuit interneurons

Tilman Broicher, Tatyana Kanyshkova, Peter Landgraf, Vladan Rankovic, Patrick Meuth, Sven G. Meuth, Hans-Christian Pape, and Thomas Budde

It has been suggested that the specific burst firing patterns of thalamic neurons reflect differential expression of low-voltage-activated (LVA) Ca^{2+} channel subtypes and their splice variants. By combining electrophysiological, molecular biological, immunological, and computational modeling techniques we here show that diverging LVA Ca^{2+} currents of thalamocortical relay (TC) and GABAergic interneurons of the dLGN correlate with a differential expression of LVA Ca^{2+} channel splice variations and isoforms ($\alpha 1\text{G-a}$ in TC; $\alpha 1\text{G-bc}$ and $\alpha 1\text{l}$ in interneurons). Implementation of the observed LVA Ca^{2+} current differences into a TC neuron model changed the burst firing from TC-like

to interneuron-like. We conclude that alternative splicing of the $\alpha 1G$ isoform in dLGN TC and interneurons, and the exclusive expression of the $\alpha 1I$ isoform in interneurons play a prominent role in setting the different LVA Ca^{2+} current properties of TC and interneurons, which critically contribute to the diverging burst firing behavior of these neurons.

Modeling

Thalamic interneurons and TC cells functionally differ in that the inhibitory interneurons show delayed LTS onsets, smaller LTS amplitudes and less action potentials riding on top of them during the burst mode. Experimentally evaluating I_T at the cells' soma revealed a more depolarized current-voltage-relationship and an overall slower current kinetic in interneurons compared to TC neurons.

Previous work suggested that these differences might be partially explained by a primary dendritic I_T expression. The multi compartment model used to test this hypothesis comprised three different sections, representing the soma, the proximal part and the distal part of a dendrite. By comparing the I/V relationship of a T current solely located in the distal part of the dendrite with a model possessing I_T only in the soma showed that a distal location leads to a hyperpolarized I/V relationship while measuring I_T at the soma. Therefore the model could exclude that location-dependent differences in the channel distribution account for the cell type specific functional differences.

At next, a single compartment TC model was used to test whether the previously measured right shift in the I/V relationship of I_T in combination with a reduced current density might match the experimentally found situation. By reducing I_T to 75% and right-shifting the corresponding I/V relationship by 10 mV (to more depolarized values) the original TC cell model started to burst like a thalamic interneuron. Therefore it could be concluded that different I_T properties mainly account for the different burst behaviors.

Project IV (Pflugers Arch. 2008)

Reciprocal modulation of I_h and I_{TASK} in thalamocortical relay neurons by halothane

Thomas Budde, Philippe Coulon, Matthias Pawlowski, Patrick Meuth, Tatyana Kanyshkova, Ansgar Japes, Sven G. Meuth, Hans-Christian Pape

By combining electrophysiological, immunohistochemical, and computer modeling techniques, we examined the effects of halothane on the standing outward current (I_{SO}) and the hyperpolarization-activated current (I_h) in rat thalamocortical relay (TC) neurons of the dorsal lateral geniculate nucleus (dLGN). Hyperpolarizing voltage steps elicited an instantaneous current component (I_i) followed by a slower time-dependent current that represented I_h . Halothane reduced I_h by shifting the voltage dependency of activation toward more negative potentials and by reducing the maximal conductance. Moreover, halothane augmented I_i and I_{SO} . During the blockade of I_h through Cs^+ , the current-voltage relationship of the halothane-sensitive current closely resembled the properties of a current through members of the TWIK-related acid-sensitive K^+ (TASK) channel family (I_{TASK}). Computer simulations in a single-compartment TC neuron model demonstrated that the modulation of I_h and I_{TASK} is sufficient to explain the halothane-induced hyperpolarization of the membrane potential observed in current clamp recordings. Immunohistochemical staining revealed protein expression of the hyperpolarization-activated cyclic nucleotide-gated (HCN) channel proteins HCN1, HCN2, and HCN4. Together with the dual effect of halothane on I_h properties, these results suggest that I_h in TC neurons critically depends on HCN1/HCN2 heterodimers. It is concluded that the reciprocal modulation of I_h and I_{TASK} is an important mechanism of halothane action in the thalamus.

Modeling

Halothane is an inhalational anesthetic that hyperpolarizes TC cells. In case this hyperpolarization is strong enough the TC neuron switches from tonic to burst activity like it would while falling asleep. Since the current project revealed that halothane modulates I_h as well as I_{TASK} , the question arose whether this modulation is strong enough to solely explain the hyperpolarization seen *in vitro*. An alternative scenario could have been that there is additional halothane action on other ion currents and that those mainly carry the change in membrane potential. Instead of testing all possible currents for a halothane effect, the computer model could efficiently demonstrate that the modulation of I_h and I_{TASK} totally suffices to induce a functional switch in TC neurons.

Project V (Mol Cell Neurosci. 2008)

Correlation of T-channel coding gene expression, I_T , and the low threshold Ca^{2+} spike in the thalamus of a rat model of absence epilepsy

Tilman Broicher, Tatyana Kanyshkova, Patrick Meuth, Hans-Christian Pape, Thomas Budde

T-type Ca^{2+} current-dependent burst firing of thalamic neurons is thought to be involved in the hyper-synchronous activity observed during absence seizures. Here we investigate the correlation between the expression of T-channel coding genes ($\alpha 1G$, $-H$, $-I$), T-type Ca^{2+} current, and the T-current-dependent low threshold Ca^{2+} spike in three functionally distinct thalamic nuclei (lateral geniculate nucleus; centrolateral nucleus; reticular nucleus) in a rat model of absence epilepsy, the WAG/Rij rats, and a non-epileptic control strain, the ACI rats. The lateral geniculate nucleus and centrolateral nucleus were found to primarily express $\alpha 1G$ and $\alpha 1I$, while the reticular thalamic nucleus expressed $\alpha 1H$ and $\alpha 1I$. Expression was higher in WAG/Rij when compared to ACI. The T-type Ca^{2+} current properties matched the predictions derived from the expression pattern analysis. Current density was larger in all nuclei of WAG/Rij rats when compared to ACI and correlated with LTS size and the minimum LTS generating slope, while T-type Ca^{2+} current voltage dependency correlated with the LTS onset potential.

Modeling

This comprehensive project compared three different thalamic nuclei in epileptic and non-epileptic rats in order to shed more light on new therapeutic targets. Before starting an overhasty search in this huge parameter space, computer modeling was used to validate the intuitively stated assumptions. The single compartment computer model used here predicted three findings: (1) The LTS onset potential primarily depends on the I/V relationship of I_T , whereas (2) the number of LTS associated action potentials as well as (3) the minimum stimulation strength necessary for eliciting a LTS mainly depends on the I_T density. All three predictions turned out to be consistent with the succeeding experiments.

Project VI (J Neurosci. 2009)

Postnatal Expression Pattern of HCN Channel Isoforms in Thalamic Neurons: Relationship to Maturation of Thalamocortical Oscillations

Tatyana Kanyshkova*, Matthias Pawlowski*, Patrick Meuth*, Celine Dubé, Roland A. Bender, Amy L. Brewster, Arnd Baumann, Tallie Z. Baram, Hans-Christian Pape, and Thomas Budde (*equal contribution)

Hyperpolarization-activated cyclic nucleotide-gated cation (HCN) channels are the molecular substrate of the hyperpolarization-activated inward current (I_h). Because the developmental profile of HCN channels in the thalamus is not well understood, we combined electrophysiological, molecular, immunohistochemical, EEG recordings *in vivo*, and computer modeling techniques to examine HCN gene expression and I_h properties in rat thalamocortical relay (TC) neurons in the dorsal part of the lateral geniculate nucleus and the functional consequence of this maturation. Recordings of TC neurons revealed an approximate six-fold increase in I_h density between postnatal day 3 (P3) and P106, which was accompanied by significantly altered current kinetics, cAMP sensitivity, and steady-state activation properties. Quantification on tissue levels revealed a significant developmental decrease in cAMP. Consequently the block of basal adenylyl cyclase activity was accompanied by a hyperpolarizing shift of the I_h activation curve in young but not adult rats. Quantitative analyses of HCN channel isoforms revealed a steady increase of mRNA and protein expression levels of HCN1, HCN2, and HCN4 with reduced relative abundance of HCN4. Computer modeling in a simplified thalamic network indicated that the occurrence of rhythmic delta activity, which was present in the EEG at P12, differentially depended on I_h conductance and modulation by cAMP at different developmental states. These data indicate that the developmental increase in I_h density results from increased expression of three HCN channel isoforms and that isoform composition and intracellular cAMP levels interact in determining I_h properties to enable progressive maturation of rhythmic slow-wave sleep activity patterns.

Modeling

Aim of this study was to investigate the functional consequences of the postnatal development of I_h concerning the single TC cell as well as the systemic thalamocortical oscillations during slow-wave sleep. The immanent difficulty was that a multitude of different ionic channels are modulated during cell maturation, so that the overall measured age-dependent changes can hardly be assigned to a single current experimentally.

Since computer modeling is free of such side effects, the model cell was able to demonstrate that the voltage sag upon hyperpolarizing voltage steps almost linearly increases while increasing the I_h current conductance. Additionally the simulations perfectly matched the very early postnatal situation with only about 20% I_h available and therefore almost no voltage sag. In summary the postnatal developing voltage sag could be clearly attributed to I_h .

The influence of I_h on thalamocortical oscillations were investigated by using a simplified four cell neuronal network. This network comprised two TC cells, both showing a certain amount of spontaneous activity in order to initiate oscillations without any external stimuli, and a second pair of interneurons from the nucleus reticularis thalami (NRT, RE cells). While reducing the I_h conductance from the adult situation of 100% I_h the oscillations between TC and RE cells slowed down and finally stopped at a level below 60% I_h . This clearly demonstrated the essential role of I_h in thalamocortical oscillations due to which it is also termed the “pacemaker channel”.

Given the findings that young animals possess less I_h and this current is very important for thalamocortical oscillations or sleep respectively, the final question of this project was whether there is any compensatory effect accounting for the lack of I_h in early postnatal stages. The experimental approach revealed a highly increased cAMP concentration in young animals. Since cAMP leads to a right shift in the current-voltage-relationship of I_h , meaning that there is more current while keeping the voltage unchanged, we used the network model to test whether this could be an appropriate explanation for the thalamocortical oscillations present in the rat EEG already at postnatal day 12. Indeed, shifting the I/V relationship of I_h in both TC cells according to the experimental data successfully evoked oscillations although the I_h conductance was even set to only 40%.

Scientific publications

Membrane Resting Potential of Thalamocortical Relay Neurons Is Shaped by the Interaction Among TASK3 and HCN2 Channels

Sven G. Meuth,^{1,*} Tatyana Kanyshkova,^{6,*} Patrick Meuth,^{6,*} Peter Landgraf,² Thomas Munsch,³ Andreas Ludwig,⁴ Franz Hofmann,⁵ Hans-Christian Pape,⁶ and Thomas Budde⁷

¹Neurologische Klinik, Bayerische Julius-Maximilians-Universität, Würzburg; ²Leibniz Institut für Neurobiologie, Magdeburg; ³Institut für Physiologie, Otto-von-Guericke-Universität, Magdeburg; ⁴Institut für Experimentelle und Klinische Pharmakologie und Toxikologie, Uni Erlangen-Nürnberg, Erlangen; ⁵Institut für Pharmakologie und Toxikologie, Technische Universität, München; and ⁶Institut für Physiologie I and ⁷Institut für Experimentelle Epilepsieforschung, Westfälische Wilhelms-Universität, Münster, Germany

Submitted 16 November 2005; accepted in final form 1 June 2006

Meuth, Sven G., Tatyana Kanyshkova, Patrick Meuth, Peter Landgraf, Thomas Munsch, Andreas Ludwig, Franz Hofmann, Hans-Christian Pape, and Thomas Budde. Membrane resting potential of thalamocortical relay neurons is shaped by the interaction among TASK3 and HCN2 channels. *J Neurophysiol* 96: 1517–1529, 2006. First published June 7, 2006; doi:10.1152/jn.01212.2005. By combining molecular biological, electrophysiological, immunological, and computer modeling techniques, we here demonstrate a counterbalancing contribution of TASK channels, underlying hyperpolarizing K⁺ leak currents, and HCN channels, underlying depolarizing I_h, to the resting membrane potential of thalamocortical relay (TC) neurons. RT-PCR experiments revealed the expression of TASK1, TASK3, and HCN1–4. Quantitative determination of mRNA expression levels and immunocytochemical staining demonstrated that TASK3 and HCN2 channels represent the dominant thalamic isoforms and are coexpressed in TC neurons. Extracellular acidification, a standard procedure to inhibit TASK channels, blocked a TASK current masked by additional action on HCN channels. Only in the presence of the HCN blocker ZD7288 was the pH-sensitive component typical for a TASK current, i.e., outward rectification and current reversal at the K⁺ equilibrium potential. In a similar way extracellular acidification was able to shift the activity pattern of TC neurons from burst to tonic firing only during block of I_h or genetic knock out of HCN channels. A single compartmental computer model of TC neurons simulated the counterbalancing influence of TASK and HCN on the resting membrane potential. It is concluded that TASK3 and HCN2 channels stabilize the membrane potential by a mutual functional interaction, that the most efficient way to regulate the membrane potential of TC neurons is the converse modulation of TASK and HCN channels, and that TC neurons are potentially more resistant to insults accompanied by extracellular pH shifts in comparison to other CNS regions.

INTRODUCTION

Despite its fundamental importance, rather little is known about the ionic conductances underlying the resting membrane potential of central neurons. In general, the resting potential is assumed to be determined by channels active below firing threshold, with I_h (Pape 1996) and I_{K-leak} (Jones 1989) playing major roles. Modulation of currents active below threshold is of particular interest because neuronal

excitability is regulated in this manner. Recently the molecular nature of I_h and I_{K-leak} was illuminated by the cloning of four members of the HCN channel family giving rise to native I_h currents in neurons and heart cells (Craven and Zagotta 2006) and five members of the TASK channel family, typically giving rise to highly regulated time- and voltage-independent K⁺ background currents (Patel and Lazdunski 2004). Depending on their sensitivity to changes in extracellular pH and based on sequence homologies TASK1, TASK3, and TASK5 channels constitute one subclass (Lesage 2003). Despite this progress in understanding, the molecular constituents and functional interaction of I_{K-leak} and I_h in specific cell types are yet not well understood.

Thalamocortical relay (TC) neurons offer a model system to gain our understanding of membrane currents that constitute the resting membrane potential for the following reasons. 1) TC neurons display large state-dependent shifts in membrane potential that are associated with a change from rhythmic burst firing at hyperpolarized potentials during slow-wave sleep to tonic single-spike activity at depolarized potentials during wakefulness (Steriade et al. 1997). Most important, the depolarization-induced cessation of burst activity depends on the downregulation of I_{K-leak} and the upregulation of I_h by a number of transmitters of the ascending arousal system of the brain stem (McCormick 1992). Because of their important function as targets of multiple regulatory pathways, I_{K-leak} and I_h are in the main focus of the present study. 2) Previous studies have begun to unravel the functional roles of HCN and TASK channels in TC neurons. Although it was shown that inhibition of TASK1 and TASK3 channels depolarize TC neurons, thereby preferring tonic single spike activity (Meuth et al. 2003, 2006), the genetic knock out or block of the HCN2 channels hyperpolarizes TC neurons, thereby preferring burst firing (Ludwig et al. 2003). 3) The pH dependency of HCN (Zong et al. 2001) and TASK (Rajan et al. 2000) channels and their corresponding membrane currents (Meuth et al. 2003; Munsch and Pape 1999) offer an experimental tool to probe this mutual functional interaction. Therefore we used extracellular acidification, molecular biological, electrophysiological, and computer modeling techniques to demonstrate the contri-

* S. G. Meuth, T. Kanyshkova, and P. Meuth contributed equally to this work.

Address for reprint requests and other correspondence: T. Budde, Westfälische Wilhelms-Universität, Medizinische Fakultät, Institut für Experimentelle Epilepsieforschung, Hüfferstr. 68, D-48149 Münster, Germany (E-mail: tbudde@uni-muenster.de).

The costs of publication of this article were defrayed in part by the payment of page charges. The article must therefore be hereby marked "advertisement" in accordance with 18 U.S.C. Section 1734 solely to indicate this fact.

bution of HCN2 and TASK3/TASK1 channels to the regulation of the resting membrane potential in TC neurons.

METHODS

Preparation

Rats and mice (postnatal days 12–29) were anesthetized with halothane, decapitated, and used for electrophysiological, immunohistochemical, and molecular biological analysis. A block of tissue containing the thalamus was removed and placed in ice-cold saline, containing (in mM): Sucrose, 200; PIPES, 20; KCl, 2.5; NaH_2PO_4 , 1.25; MgSO_4 , 10; CaCl_2 , 0.5; and dextrose, 10; pH 7.35 with NaOH. Thalamic slices were prepared as coronal sections on a vibratome. Before recording, slices were kept submerged in standard artificial cerebrospinal fluid (ACSF) containing (in mM): NaCl, 125; KCl, 2.5; NaH_2PO_4 , 1.25; NaHCO_3 , 24; MgSO_4 , 2; CaCl_2 , 2; and dextrose, 10; pH adjusted to 7.35 by bubbling with a mixture of 95% O_2 –5% CO_2 .

Whole cell patch-clamp recordings

Recordings were performed on visually identified TC neurons of the dorsal lateral geniculate nucleus (dLGN) at room temperature. Slices were recorded in a solution containing (in mM): NaCl, 120; KCl, 2.5; NaH_2PO_4 , 1.25; HEPES, 30; MgSO_4 , 2; CaCl_2 , 2; and dextrose, 10; pH 7.3 or 6.3 was adjusted with HCl. Electrical activity was measured with pipettes pulled from borosilicate glass (GC150T-10, Clark Electromedical Instruments, Pangbourne, UK), connected to an EPC-10 amplifier (HEKA Elektronik, Lamprecht, Germany), and filled with (in mM): K-gluconate, 95; K_3 -citrate, 20; NaCl, 10; HEPES, 10; MgCl_2 , 1; CaCl_2 , 0.5; BAPTA, 3; Mg-ATP, 3; and Na-GTP, 0.5. The internal solution was set to a pH of 7.25 with KOH and an osmolality of 295 mOsm/kg. Typical electrode resistance was 2–3 M Ω , with an access resistance in the range of 5–15 M Ω . Series resistance compensation of >40% was routinely used. Electrophysiological experiments were governed by Pulse software (HEKA Elektronik) operating on an IBM-compatible PC. A liquid junction potential of 8 ± 1 mV ($n = 6$) was taken into account.

I_h was activated using hyperpolarizing voltage steps from a holding potential of –43 to –133 mV in 10-mV increments. To increase stability of whole cell recordings the pulse length was decreased by 1,500 ms with increasing depth of the hyperpolarization (3.5-s pulse length at –130 mV). Steady-state activation of I_h activation, $p(V)$, was estimated by normalizing the tail current amplitudes (I), 50 ms after stepping to a constant potential from a variable amplitude step using the following equation

$$p(V) = (I - I_{\min}) / (I_{\max} - I_{\min})$$

where I_{\max} is the tail current amplitude for the voltage step from –133 to –98 mV and I_{\min} is the voltage step from –43 to –98 mV, respectively. I_h activation was usually well accounted for a Boltzmann distribution of the following form

$$p(V) = 1 / \{1 + \exp[(V - V_h)/k]\}$$

where V_h is the voltage of half-maximal activation and k is the slope factor.

During current-clamp recordings the instantaneous frequency (f) of action potential generation was determined by analyzing the first two action potentials elicited by a depolarizing current pulse.

All results are presented as means \pm SE. Substance effects were tested for statistical significance using the nonparametric Mann–Whitney test. Where applicable (Gaussian distribution of measured values), a parametric t -test modified for small samples was used. Differences were considered statistically significant at $P < 0.05$.

Drugs

ZD7288 [4-(*N*-ethyl-*N*-phenylamino)-1,2-dimethyl-6-(methylamino) pyridinium chloride; Biotrend, Cologne, Germany] was directly dissolved in the external recording solution.

Computer simulations with NEURON

For computer simulations, a previously described single-compartment TC neuron model (Huguenard and McCormick 1992; McCormick and Huguenard 1992) was adapted to NEURON (Hines and Carnevale 2001; Meuth et al. 2005). The model is based on the mathematical description of I_A , I_{K2} , I_C , I_L , I_T , I_{NaP} , and I_h and displays the two typical modes of action potential generation in thalamic cells: burst firing with two to six action potentials riding on a low-threshold Ca^{2+} spike (LTS) and single-spike activity with tonic trains of action potentials. This well-established model was extended by incorporating the inward rectifying current I_{Kir} of the Hodgkin–Huxley form (Williams et al. 1997) and the background potassium current I_{TASK} . The general equation describing the membrane potential over the time is

$$C_m(dV/dt) = -(I_{\text{leak}} + I_{\text{TASK}} + I_{\text{Kir}} + I_h) + I_{\text{inject}}$$

where C_m is the membrane capacitance and I_{inject} is the injection current. The noninactivating current I_{Kir} was modeled as previously described (Williams et al. 1997)

$$I_{\text{Kir}} = g_{\text{Kir}}m^a(V - E_{\text{Kir}})$$

where g_{Kir} is the maximal conductance of the current I_{Kir} , whereas m is the activation variable, and a is its exponent ($=3$). E_{Kir} is the reversal potential of the current I_{Kir} . The outwardly rectifying pH-sensitive leak current I_{TASK} was modeled as a mathematical fit through the currents measured in the current publication

$$I_{\text{TASK}} = g_{\text{TASK}}m(V - E_{\text{TASK}})$$

where g_{TASK} is the maximal conductance of the current I_{TASK} , whereas the driving force is defined as reversal potential E_{TASK} subtracted from the membrane potential V . The activation variable m is defined as

$$m = y_0 + A_1 e^{(x/t_1)} / (V - E_{\text{TASK}})$$

All values were assumed for maximal conductances and fixed reversal potentials and were systematically varied in some simulations. To demonstrate the contribution of the leak potassium current I_{TASK} to the total leak of TC neurons, we calculated a pH-insensitive (g_{leak}) and a pH-sensitive leak (g_{TASK}) conductance, respectively. The proportion of both leaks was changed systematically to achieve a model that simulates the pH effect in rat TC neurons. All computer modeling was carried out at 35°C.

The magnitude of pH-dependent effects on TASK (90% reduction) and HCN (25% reduction) channels used in computer modeling were estimated from previously published data. The reduction of I_h resulting from an intracellular shift of 0.8 pH units is roughly 25% (Munsch and Pape 1999). Both, TASK1 and TASK3 channels are inhibited by acidification, although over different pH ranges (pK values ≈ 7.5 and ≈ 6.7 for TASK1 and TASK3, respectively) (Duprat et al. 1997; Kim et al. 2000; Rajan et al. 2000). Tandem-linked heterodimeric TASK channel constructs displayed pH sensitivity ($pK \approx 7.3$) closer to that of TASK1 than to TASK3 (Berg et al. 2004; Czirjak and Enyedi 2002). Therefore TASK1 and TASK3 channels reveal 95 and 75% inhibition at pH 6.4, respectively, and an intermediate value of 90% was used for modeling.

Preparation of dissociated cell cultures from the dorsal thalamus

Dorsal thalami were prepared from embryos (Long–Evans rats) at stage E 19 and subsequently transferred into ice-cold Hanks balanced

salt solution (HBSS, without Ca/Mg). After triple washing with 5 ml HBSS each, 2.0 ml HBSS, containing 0.5% trypsin, was added to the tissue, followed by incubation at 37°C for 20 min. Tissue was washed again five times with 5 ml HBSS each and finally transferred into 2-ml tubes with HBSS, containing 0.01% DNaseI. To dissociate thalamic tissue, it was pressed slowly three times through a 0.9-mm-gauge needle followed by three passages through a 0.45-mm-gauge needle. The remaining cell suspension was poured through a nylon tissue (mesh aperture 125 μ m) into a 50-ml tube and filled up with 18 ml Dulbecco's modified Eagle medium (DMEM; Gibco, Eggenstein, Germany). After estimating cell quantity, the suspension was diluted with DMEM in accordance to the required density of 16,000 cells/ml. A 500- μ l aliquot of this suspension was placed on each well of a 24-well plate, containing defatted, baked, and poly-D-lysine-coated coverslips. The cell cultures were incubated at 37.0°C and 5% CO₂ up to the appropriate time points and finally fixed with 4% perfluoroalkoxy polymer resin (PFA) for 10 min.

Immunocytochemistry

After 21 days in vitro (DIV 21) PFA-fixed cells were washed three times with 10 mM PBS and subsequently preincubated at 4°C in blocking solution [10 mM PBS, 10% horse normal serum (NHS), 2% bovine serum albumin (BSA), 5% sucrose, 0.3% Triton X-100]. After 1 h, primary antibodies (rabbit anti-HCN2, 1:500, Alomone Labs, Jerusalem, Israel; goat anti-TASK3, 1:300, Santa Cruz Biotechnology, Heidelberg, Germany; rabbit anti-parvalbumin, 1:500, Swant, Bellinzona, Switzerland; mouse anti-MAP2 1:1,000, Sigma, Deisenhofen, Germany) were added to the blocking solution and incubated overnight. Thereafter cultures were washed with 10 mM PBS including 0.3% Triton X-100 and incubated with secondary antibodies (Cy5-conjugated rabbit-anti-mouse IgG, 1:1,000, Sigma; Cy3-conjugated goat-anti-rabbit IgG, 1:1,000; Dianova, Hamburg, Germany, Alexa-Fluor-488 conjugated donkey-anti-goat, 1:1,000; Molecular Probes; in blocking solution) for 2 h, washed, and coverslipped with Moviol. Omission of primary and secondary antibodies resulted in lack of fluorescent signals.

Reverse transcription-polymerase chain reaction (RT-PCR) assays

Poly(A) mRNA was prepared from freshly dissected tissue by extraction with Trizol reagent according to the manufacturer's instructions (Oligotex, Qiagen, Hilden, Germany). First-strand cDNA was primed with oligo(dT) from 0.5–1 μ g of mRNA and synthesized using the SuperScript II enzyme (Invitrogen Life Technologies) at 42°C for 50 min. PCR was performed in a 30- μ l reaction mixture using 0.75 U *Taq* polymerase (Qiagen) for HCN templates or 0.75 U HotStar*Taq* polymerase (Qiagen) for amplification of TASK templates; mixture in both cases contained 1.5 mM MgCl₂, 0.2 mM of each dNTP, and 50 pmol of each primer. Cycling protocols were: 3 min at 94°C, 35 cycles: 30 s at 94°C, 1 min at 58°C, 1 min at 72°C, 7 min at 72°C for HCNs; and 15 min at 95°C, 35 cycles: 30 s at 94°C, 1 min at 58°C, 1 min at 72°C, 10 min at 72°C for TASK amplification. The following primers were used

HCN1 (nucleotides 1462–1750) Accession No. AF247450

forward: CTC TCT TTG CTA ACG CGG AT
reverse: TTG AAA TTG TCC ACC GAA

HCN2 (nucleotides 1059–1428) Accession No. AF247451

forward: GTG GAG CGA ACT CTA TTC GT
reverse: GTT CAC AAT CTC CTC ACG CA

HCN3 (nucleotides 1713–1945) Accession No. AF247452

forward: GCA GCA TTT GGT ACA ACA CG
reverse: AGC GTC TAG CAG ATC GAG C

HCN4 (nucleotides 1871–2042) Accession No. AF247453

forward: GCA GCG CAT CCA CGA CTA C
reverse: CGT CAC AAA GTT GGG GTC TGC

TASK1 (nucleotides 220–735) Accession No. AB048823

forward: CAC CGT CAT CAC CAC AAT CG
reverse: TGC TCT GCA TCA CGC TTC TC

TASK2 (nucleotides 330–959) Accession No. AF259395

forward: TGG GCG CCT CTT CTG TGT CTT CTA
reverse: TCC CCT CCC CCA CTT GTT TTC ATT

TASK3 (nucleotides 188–602) Accession No. AF192366

forward: ATG AGA TGC GCG AGG AGG AGA AAC
reverse: ACG AGG CCC ATG CAA GAA AAG AAG

TASK5 (nucleotides 137–700) Accession No. AF294353

forward: GAG CCT GGG CGA GCG TCT GAA C
reverse: CGG GCC CGG AGT CTG TCT GG

TREK1 (nucleotides 447–1119) Accession No. NM_172041

forward: ACA GAA CTT CAT AGC CCA GCA T
reverse: TCC CAC CTC TTC CTT CGT CT

TREK2 (nucleotides 1192–1639) Accession No. NM_023096

forward: CAG TGG GCT TTG GTG ATT TTG T
reverse: AGG CGT AGG TTA TTG GGT CTG TT

TRAAK (nucleotides 766–1143) Accession No. NM_053804

forward: AAC TGG TTG CGA GCG GTG TC
reverse: GGG CTT CTT CGT TGG GTT GG

THIK1 (nucleotides 404–805) Accession No. NM_022293

forward: CGT GGG CAC AGT GGT AAC TA
reverse: GCT CCA CAG GAG ATG GCT AC

THIK2 (nucleotides 764–1013) Accession No. NM_022292

forward: CCT TCC TCC GGC ACT ACG AG
reverse: ATG AAG GCC AGC AGC GAG AT

Multiplex and nested PCR in isolated neurons

mRNAs from 10 identified TC neurons were collected using the Dynabeads mRNA direct micro kit (Dyna, Oslo, Norway). First cDNA was primed with oligo(dT)₂₅, immobilized on the beads, and synthesized using the Sensiscript reverse transcriptase (Qiagen) at 37°C for 1 h.

After reverse transcription, the cDNAs for TASK3 and HCN2 were amplified simultaneously as a multiplex PCR. For the amplification of TASK3 the primers described above were used; for HCN2 (nucleotides 688–1652) the multiplex primers were as follows: forward, TAC CTG CGT ACG TGG TTC GT, reverse, AAA TAG GAG CCA TCT GAC A. First multiplex amplification was performed in 50 μ l containing 50 pmol of each primer, 5 U Platinum *Taq* polymerase (Invitrogen) by using the following cycling program: 4 min at 95°C,

2 cycles: 30 s at 94°C, 1 min at 58°C, 5 min at 72°C, then cDNA library was removed and amplification proceeded with an additional 35 cycles: 30 s at 94°C, 1 min at 58°C, 1 min at 72°C, 7 min at 72°C. Nested amplification was carried out individually for each target in 50 μ l reaction mix using 5 μ l from the first amplification product, 10 pmol of correspondent primers, and 2.5 U Platinum *Taq* polymerase. Cycling protocol was: 4 min at 95°C, 30 cycles: 30 s at 94°C, 1 min at 58°C, 1 min at 72°C, 7 min at 72°C.

The efficiency of cDNA synthesis was controlled by single PCR amplification of glyceraldehyde-3-phosphate dehydrogenase (GAPDH) from the cDNA libraries using the primers mentioned above. PCR amplification was performed in 50 μ l containing 10 pmol of each primer, 2.5 U Platinum *Taq* polymerase; the cycling protocol was: 3 min at 95°C, 2 cycles: 30 s at 94°C, 1 min at 58°C, 5 min at 72°C, then cDNA library was removed and amplification proceeded with another 37 cycles: 30 s at 94°C, 1 min at 58°C, 1 min at 72°C, 7 min at 72°C.

Quantitative real-time PCR

The hybridization primer/probe assays for real-time PCR detection were purchased from Applied Biosystems. The following assay-on-demand probes were used: GAPDH: P/N 4308313, β_2 -microglobulin: Rn00560865_m1, TASK1: Rn00583727_m1, HCN1: Rn00584498_m1, HCN3: Rn00586666_m1, HCN4: Rn00572232_m1. The designed probes were: TASK3, forward: TCC TTC TAC TTC GCT ATC ACT GTC A, reverse: TTG CCA GCA TCG GTT CCA, reporter: CAT GTC CAT ATC CGA TAG TTG; HCN2, forward: ACA AGG AGA TGA AGC TGT CAG ATG, reverse: TGT CAG CCC GCA CAC T, reporter: CAG ATC TCC CCA AAA TAG. Real-time PCR was performed using the ABI Prism 7000 Sequence Detection System (Applied Biosystems, Darmstadt, Germany); PCR program was: 2 min at 50°C, 10 min at 95°C, 40 cycles: 15 s at 95°C and 1 min at

60°C. Results were analyzed with the ABI Prism 7000 SDS software. The efficiency of real-time primers was assessed by plotting Ct values versus corresponding dilution factor of total thalamic cDNA. Linear regression revealed slope factors that were maximally 8% different between β_2 -microglobulin, TASK1, TASK3, and HCN2.

RESULTS

Expression of HCN and TASK channel isoforms in rat dLGN

In a first experimental step, the expression of different HCN and TASK channel isoforms was determined through RT-PCR analysis on dLGN tissue. Strong signals for TASK1 and TASK3 were found, whereas TASK2 was less expressed and TASK5 was not detectable (Fig. 1A, left). To determine the expression of TASK isoforms on a more quantitative level, we subjected TASK1 and TASK3 mRNAs to a real-time PCR approach. Expression levels of TASK3 were 4.4 ± 0.2 -fold ($n = 3$) higher compared with TASK1 (Fig. 1D, left) after normalization to the constitutively expressed housekeeping gene β_2 -microglobulin. Similar expression ratios were found for cortical (3.6 ± 0.1 ; $n = 3$) and hippocampal (3.5 ± 0.1 ; $n = 3$) tissues that were used for comparison (data not shown). When cerebellar tissue, known to express high levels of TASK1, was tested, the TASK3/TASK1 expression ratio was 0.7 ± 0.1 ($n = 3$). Expression of HCN channels was assessed in a similar way. Standard PCR protocols revealed the expression of all four HCN isoforms (Fig. 1A, right). Real-time PCR was used to attain more quantitative results of isoform expression. The expression level of HCN2 could be assessed to be

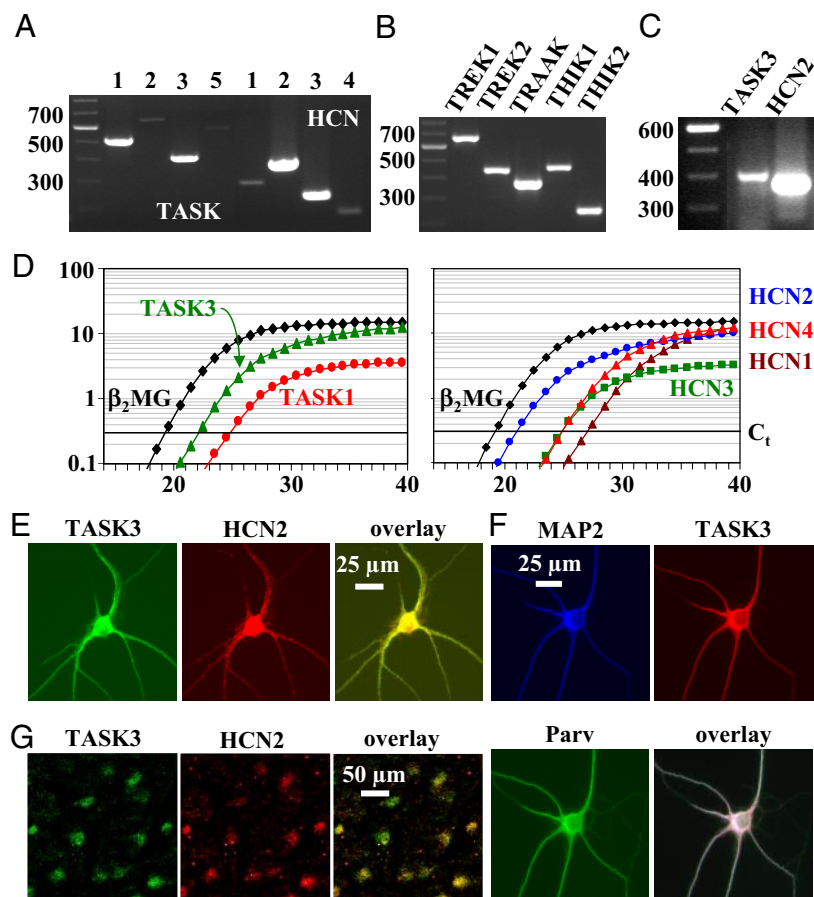


FIG. 1. Reverse transcription-polymerase chain reaction (RT-PCR) and immunological analysis of rat thalamic tissue. **A**: expression of TASK1–5 and HCN1–4 channels in dorsal lateral geniculate nucleus (dLGN) revealed by standard RT-PCR. **B**: expression of K_{2P} channels in dLGN revealed by standard RT-PCR. **C**: coexpression of HCN2 and TASK3 in identified thalamocortical relay (TC) neurons revealed by standard RT-PCR. **D**: quantitative real-time RT-PCR analysis of TASK1 and TASK3 and HCN1–4 expression in comparison to β_2 -microglobulin (β_2 -MG) in dLGN tissue. Number of cycles is plotted vs. normalized and baseline corrected fluorescence (ΔR_n). **E** and **F**: immunohistochemical localization of TASK3 (green fluorescence) and HCN2 (red fluorescence) in cell culture (**E**) and brain slices (**F**). Overlay (right) reveals coexpression of both ion channel proteins. **G**: immunohistochemical localization of microtubule associated protein 2 (MAP2; blue fluorescence), a neuron-specific marker, parvalbumin (green fluorescence), a TC neuron-specific marker, and TASK3 (red fluorescence) in thalamic neurons in cell culture. Overlay (right) reveals the coexpression of all 3 proteins.

7.5 ± 0.1-fold higher compared with HCN3 and HCN4, and 12 ± 0.1-fold (*n* = 3) higher compared with HCN1 (Fig. 1*D*, *right*). Together with earlier results obtained from HCN2-deficient mice (Ludwig et al. 2003), TASK1-deficient mice (Meuth et al. 2006), and Long-Evans rats (Meuth et al. 2003) we concluded that HCN2 and TASK3 are the dominant isoforms in dLGN.

The expression of other members of the K_{2P} family of ion channels (Patel and Lazdunski 2004) was probed by RT-PCR on the tissue level. The use of specific primer pairs revealed the presence of TREK-1, TREK-2, TRAAK, THIK-1, and THIK-2 mRNA in dLGN tissue (Fig. 1*B*).

Next, the cellular localization of HCN2 and TASK3 channels was determined. Neurons were acutely isolated from the dLGN, TC neurons were identified in populations of neurons using established criteria (Pape et al. 1994), and groups of 10 TC neurons were harvested for RT-PCR analysis. The use of HCN2- and TASK3-specific primer pairs revealed detectable PCR signals for the two ion channels (Fig. 1*C*). Furthermore, TASK3- and HCN2-specific antibodies revealed a dense population of HCN2 (716 ± 17 cells/mm²; Fig. 1*G*, *middle image*) and TASK3 (607 ± 29 cells/mm²; Fig. 1*G*, *left image*) expressing cells in dLGN slices (five independent preparations). Furthermore the overlap of images revealed 604 ± 26 cells/mm² (Fig. 1*G*, *right image*) with co-localization of both channels. The average cell density in Nissl staining was 808 ± 31 cells/mm² (*n* = 6; coronal sections of 14 μm thickness), indicating that 89, 75, and 75% of the cells express HCN2, TASK3, and HCN2/TASK3, respectively, thereby providing evidence for largely overlapping expression. In thalamic cell cultures (DIV 21), 100% of TC neurons (a total of 30 TC neurons were identified in 10 different cultures from three independent preparations) were positive for TASK3 (Fig. 1*E*, *left image*) and HCN2 (Fig. 1*E*, *middle image*). Their localization in TC neurons (a total of 24 cells were identified in eight

different cultures from three independent preparations) was further demonstrated by the finding that parvalbumin (Fig. 1*F*, *bottom left image*), a specific marker protein of TC neurons (Jones and Hendry 1989; Meuth et al. 2005; Sieg et al. 1998), was expressed in TASK3- (Fig. 1*F*, *top right image*) and MAP2-positive neurons (Fig. 1*E*, *top left image*).

Characterization of pH-sensitive ramp currents

In the following extracellular pH changes from a physiological value of 7.3 (control) to 6.3, a value that is reached during ischemic insults (Siemkowicz and Hansen 1981) were used to demonstrate the functional interaction of HCN and TASK channels in TC neurons. Because currents through HCN and TASK channels are sensitive to extracellular acidification (Malcolm et al. 2003; Meuth et al. 2003; Stevens et al. 2001), this experimental paradigm results in a concomitant downregulation of both I_{K-leak} and I_h . Currents through TASK channels were evoked by holding TC neurons at -30 mV and ramping the potential in 800 ms to -120 mV once every 20 s (Fig. 2*A*, *inset*). The rate of hyperpolarization 0.11 mV/ms is sufficiently slow to allow the membrane current to reach steady state at each potential and it is expected that only constitutively open channels can follow the ramp (Millar et al. 2000; Watkins and Mathie 1996). The current-voltage (*I-V*) relationship of the pH-sensitive current was obtained by subtracting currents recorded at pH 6.3 from control currents (i.e., pH 7.3 - pH 6.3). The *I-V* relationship of the pH-sensitive currents (about 10 min after extracellular acidification) was characterized by outward rectification (Fig. 2*A*, *gray trace*) and a reversal potential of -90 ± 2 mV (*n* = 10; Fig. 2*B*, *gray circle*), i.e., some 14 mV positive to the expected K^+ equilibrium potential ($E_K = -104$ mV). To demonstrate that pH-dependent regulation of I_h contributed to the deviation the HCN channel blocker ZD7288 was used. Incubation of TC neurons with 100 μM ZD7288 before

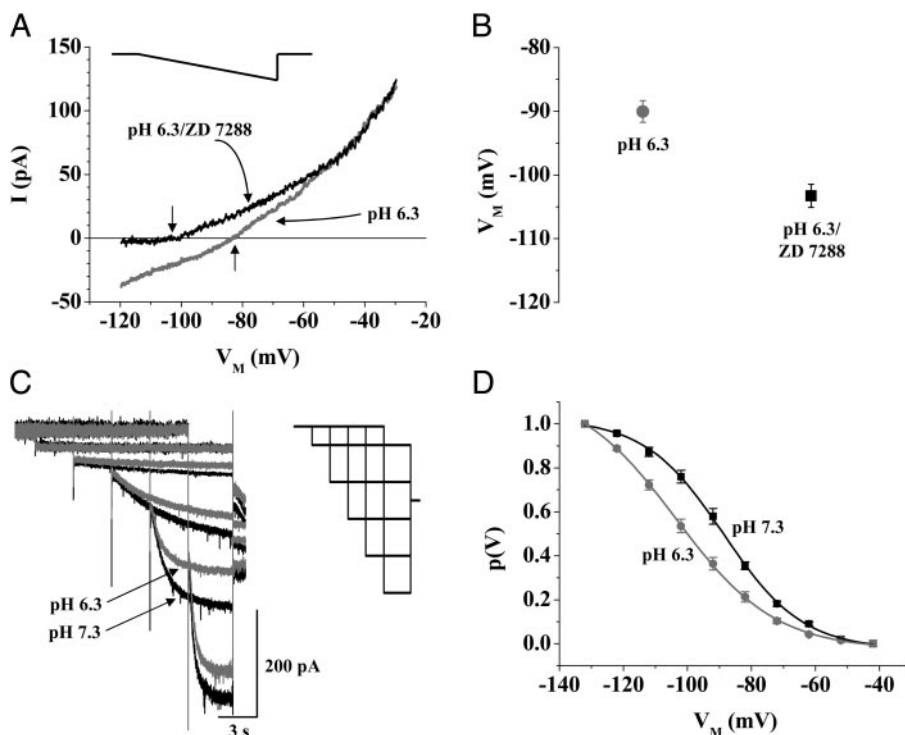


FIG. 2. Current components sensitive to extracellular acidification in TC neurons. *A*: current-to-voltage relationship (*I-V*) of the pH-sensitive current obtained by graphical subtraction (pH 7.3 - pH 6.3) in the presence (*black trace*) and absence (*gray trace*) of ZD7288 (100 μM). Currents were evoked by ramping the membrane from -30 to -120 mV over 800 ms (see *inset*). *B*: mean values of the reversal potential of pH-sensitive ramp current in the presence (*black square*) and absence (*gray circle*) of ZD7288. *C*: superimposed families of current traces recorded at pH 7.3 (*black traces*) and 6.3 (*gray traces*) in a rat TC neuron. Current traces at -53, -73, -93, -113, and -133 mV are shown. *Inset*: clarifies the voltage protocol. *D*: mean steady-state activation curves of I_h at pH 7.3 (*black squares*; *n* = 7) and pH 6.3 (*gray circles*; *n* = 7). Continuous lines represent best fits of a Boltzmann equation to the data points.

extracellular acidification was performed resulted in an I - V relationship of pH-sensitive ramps that revealed the typical features of a current carried by TASK channels (Meuth et al. 2003), including pronounced outward rectification (Fig. 2A, black trace) and a significantly ($P < 0.0001$) more hyperpolarized reversal potential of -103 ± 2 mV ($n = 8$; Fig. 2B, black square), i.e., close to the expected K^+ equilibrium potential.

To directly prove the modulation of HCN channels by extracellular acidification, we activated I_h from a holding potential of -43 mV by using hyperpolarizing voltage steps of increasing ($\Delta V = -10$ mV) amplitude and decreasing ($\Delta t = -1,500$ ms) duration (15.5 s at -53 mV to 3.5 s at -133 mV) followed by a constant step to -98 mV (Fig. 2C, inset). Recordings were performed in the presence of $150 \mu\text{M}$ Ba^{2+} to block TASK and inward rectifier channels (Meuth et al. 2003). An analysis of deactivating currents revealed a half-maximal value of I_h activation at a membrane potential of -87 ± 2 mV ($n = 7$) at pH 7.3 (Fig. 2D, black squares). Ten minutes after switching the extracellular solution from pH 7.3 to pH 6.3, half-maximal activation of I_h was significantly ($P = 0.00001$) shifted to -100 ± 1 mV ($n = 7$; Fig. 2D, gray circles). To ensure that this effect was not a result of run-down phenomena, I_h protocols were delivered in 10-min intervals under control conditions in a different set of experiments. No significant ($P = 0.153$) differences could be found under these recording conditions (first protocol: -86 ± 3 mV; second protocol: -84 ± 3 mV; $n = 4$; data not shown). In conclusion these findings indicated a contribution of both HCN and TASK channels to the pH-sensitive current component in dLGN TC neurons and point to an opposing functional influence on membrane excitability.

Effect of extracellular acidification on thalamic activity modes

The functional consequence of concomitant modulation of HCN and TASK channels by acidification was probed under current-clamp conditions. To ensure robust burst responses, recordings were obtained at slightly hyperpolarized values ($V_H = -73 \pm 1$ mV, $n = 12$; Fig. 3A) of the membrane potential with respect to the resting value (V_R) of -71 ± 1 mV ($n = 25$; Fig. 3A) using DC injection. Under these conditions, depolarizing current steps elicited high-frequency ($f_H = 134 \pm 10$ Hz, $n = 6$; Fig. 3B) bursts with two to five action potentials riding on top of a low-threshold Ca^{2+} spike (Fig. 3C). Changing the extracellular pH from 7.3 to 6.3 resulted in a nonsignificant depolarization of the membrane potential to $V_{pH6.3} = -68 \pm 1$ mV (Fig. 3A), during which burst firing ($f_{pH6.3} = 113 \pm 1$ Hz; Fig. 3B) was preserved (Fig. 3D; $n = 5$). Different results were obtained in the presence of ZD7288. Application of ZD7288 resulted in a significant ($P < 0.01$) hyperpolarization of the resting membrane potential (V_{ZD}) to -79 ± 2 mV ($n = 7$; Fig. 3A). After bringing the membrane potential back to the control level of about -72 mV using DC current injection, a step depolarization revealed that burst firing ($f_{ZD/H} = 136 \pm 11$ Hz; $n = 6$; Fig. 3B) persisted (Fig. 3E). Subsequent extracellular acidification resulted in a strong depolarization of the membrane potential ($V_{ZD/pH6.3}$) to -52 ± 3 mV ($n = 6$; Fig. 3A) accompanied by a change in firing mode from burst to tonic ($f_{ZD/pH6.3} = 32 \pm$ Hz, $n = 6$; Fig. 3, B and F). These findings show that extracellular acidification results in a net depolarization of TC neurons. The magnitude and, in consequence, the functional relevance of this depolarization is controlled by an interplay between TASK and HCN channels. The

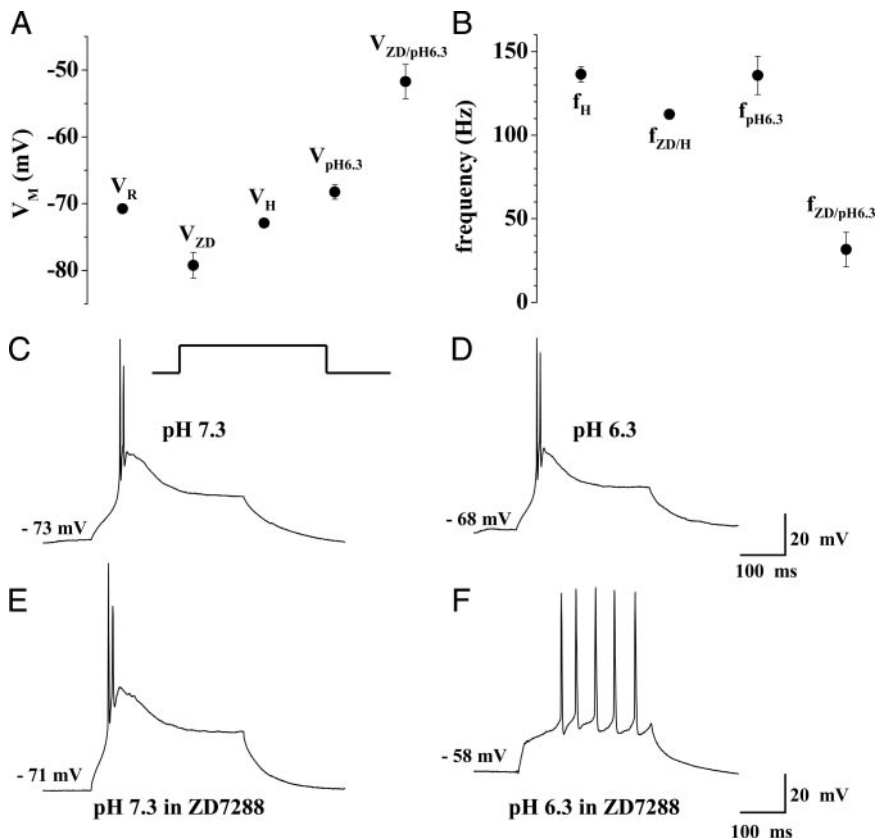


FIG. 3. Effect of extracellular acidification on thalamic activity modes in rat TC neurons recorded under current-clamp conditions. A: mean values of resting membrane potentials under different recording conditions. V_R , resting potential under control conditions; V_{ZD} , resting potential in the presence of $100 \mu\text{M}$ ZD7288; V_H , holding level of the membrane potential achieved by DC current injection; $V_{pH6.3}$, resting potential at pH 6.3; $V_{ZD/pH6.3}$, resting potential at pH 6.3 in the presence of ZD7288. B: mean firing frequencies under different recording conditions. Firing frequency was determined for the first 2 action potentials elicited by the depolarizing pulse. f_H , firing frequency at V_H ; $f_{ZD/H}$, firing frequency at V_H in the presence of ZD7288; $f_{pH6.3}$, firing frequency at pH 6.3; $f_{ZD/pH6.3}$, firing frequency at pH 6.3 in the presence of ZD7288. C–F: depolarizing current pulses (300-ms duration, 100–200 pA) from a control potential (V_H) of about -73 mV elicited robust burst responses in the absence (C) and presence (E) of ZD7288. Extracellular acidification results in a depolarizing shift of the membrane potential and generation of tonic trains of action potentials in response to the same depolarizing current pulse in the presence (F), but not in the absence (D), of ZD7288.

main characteristics of the two thalamic activity modes with high-frequency burst firing at hyperpolarized potentials and low-frequency tonic firing at depolarized potentials were unchanged.

Next the role of the HCN2 isoform was assessed through the use of a mouse strain deficient of HCN2 channels (HCN2^{-/-}) (Ludwig et al. 2003). The resting membrane potentials of TC neurons in wild-type (HCN2^{+/+}) mice ($V_{R/HCN2+/+} = -69 \pm 1$ mV, $n = 22$; Fig. 4A) were significantly ($P < 0.01$) more positive compared with HCN2^{-/-} mice ($V_{R/HCN2-/-} = -81 \pm 1$ mV, $n = 21$; Fig. 4A), confirming previous findings (Ludwig et al. 2003). A change of extracellular pH from 7.3 to 6.3 in cells held at a potential (V_H) of -73 ± 1 mV using DC current injection ($n = 8$; Fig. 4, A and C) resulted in a nonsignificant hyperpolarization of the membrane potential ($V_{pH6.3/HCN2+/+}$) to -75 ± 1 mV in HCN2^{+/+} mice ($n = 6$; Fig. 4, A and D). At pH 7.3 and pH 6.3 cells fired high-frequency bursts of action potentials with intraburst frequencies of $f_{HCN2+/+} = 114 \pm 2$ Hz and $f_{pH6.3/HCN2+/+} = 111 \pm 6$ Hz, respectively ($n = 6$; Fig. 4B). In HCN2^{-/-} mice held at -73 mV under control conditions the intraburst frequency was $f_{HCN2-/-} = 111 \pm 2$ Hz ($n = 5$; Fig. 4, B and E). At pH 6.3 TC neurons were significantly ($P < 0.01$) more depolarized with $V_{pH6.3/HCN-/-} = -58 \pm 2$ mV ($n = 5$; Fig. 4, A and F) and revealed tonic firing ($f_{pH6.3/HCN2-/-} = 33 \pm 7$ Hz, $n = 5$; Fig. 4, B and F). These data indicate that HCN2 channels carry a major part of I_h function in TC neurons.

Steady-state current components in TC neurons

Ion channels suitable to determine V_R should be able to sustain a steady-state current. To determine the contribution of

different current components, cells were kept at a holding potential of -68 mV. Under these recording conditions TC neurons displayed a standing outward current (I_{SO}) with an amplitude of 71 ± 4 pA ($n = 10$). In a first experimental step, a pharmacological profile of this current was obtained by cumulative application of different ion channel modulators. Figure 5 shows the time course of a typical experiment (Fig. 5A, open squares). Washin of tetrodotoxin (TTX, $1 \mu\text{M}$) had no effect, application of the I_h channel blocker ZD7288 ($100 \mu\text{M}$) significantly increased, and lowering the extracellular pH from 7.3 to 6.3 significantly decreased I_{SO} . Addition of Ba^{2+} ($150 \mu\text{M}$) and tetraethylammonium (TEA, 20 mM)/4-aminopyridine (4-AP, 6 mM) resulted in a further significant reduction of the outward current.

To increase outward current amplitudes, recordings were obtained at more depolarized values of the membrane potential. At -28 mV (Fig. 5A, closed squares), I_{SO} averaged 343 ± 15 pA ($n = 51$). TTX ($1 \mu\text{M}$) resulted in an increase in current amplitude of $7 \pm 1\%$ ($n = 9$) and additional application of ZD7288 ($100 \mu\text{M}$) decreased the current ($6 \pm 2\%$, $n = 9$). Changing the external pH from 7.3 to 6.3 in the continuous presence of TTX and ZD7288 induced a further decrease by $42 \pm 3\%$ ($n = 5$). Addition of Ba^{2+} ($150 \mu\text{M}$) and TEA (20 mM)/4-AP (6 mM) led to a further decrease by 49 ± 6 and $82 \pm 5\%$ ($n = 5$), respectively. All drug effects were statistically significant with respect to current amplitudes under control conditions. In the presence of all blocking agents, the current was almost completely blocked (9 ± 5 pA residual current; $n = 5$). These results are consistent with the hypothesis that Na^+ channels, I_h channels, pH-sensitive TASK channels, Ba^{2+} -sensitive Kir and leak channels, and TEA/4AP-sensitive voltage-dependent K^+ channels

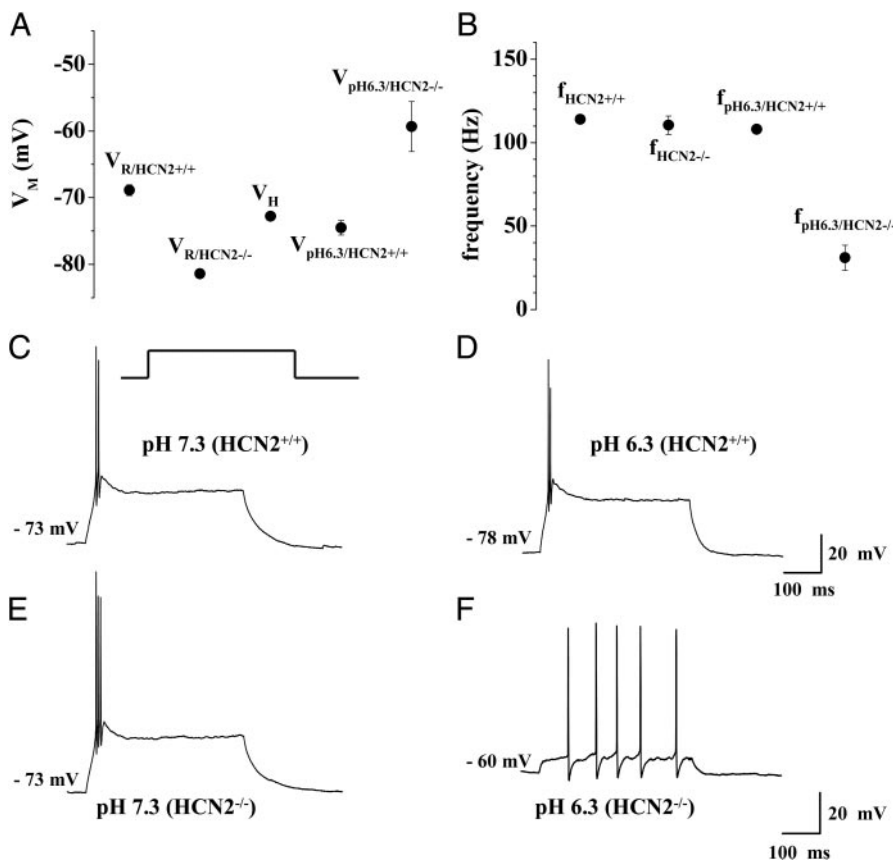


FIG. 4. Effect of extracellular acidification on thalamic activity modes in mice. A: mean values of resting membrane potentials under different recording conditions. $V_{R/HCN2+/+}$, resting potential under control conditions in HCN2^{+/+} mice; $V_{R/HCN2-/-}$, resting potential under control conditions in HCN2^{-/-} mice; V_H , holding level of the membrane potential achieved by DC current injection; $V_{pH6.3/HCN2+/+}$, resting potential at pH 6.3 in HCN2^{+/+} mice; $V_{pH6.3/HCN2-/-}$, resting potential at pH 6.3 in HCN2^{-/-} mice. B: mean firing frequencies under different recording conditions. Firing frequency was determined for the first 2 action potentials elicited by the depolarizing pulse. $f_{HCN2+/+}$, firing frequency at V_H in HCN2^{+/+} mice; $f_{HCN2-/-}$, firing frequency at V_H in HCN2^{-/-} mice; $f_{pH6.3/HCN2+/+}$, firing frequency at pH 6.3 in HCN2^{+/+} mice; $f_{pH6.3/HCN2-/-}$, firing frequency at pH 6.3 in HCN2^{-/-} mice. C and D: depolarizing current pulses (400-ms duration, 100–200 pA) were applied from a holding potential of about -73 mV. In TC neurons from HCN2^{+/+} mice pulse depolarization elicited a burst response at pH 7.3 (C) and pH 6.3 (D). E and F: in TC neurons from HCN2^{-/-} mice pulse depolarization elicited a burst response at pH 7.3 (E). Extracellular acidification resulted in a depolarizing shift of the membrane potential and generation of tonic trains of action potentials in response to the same depolarizing current pulse (F).

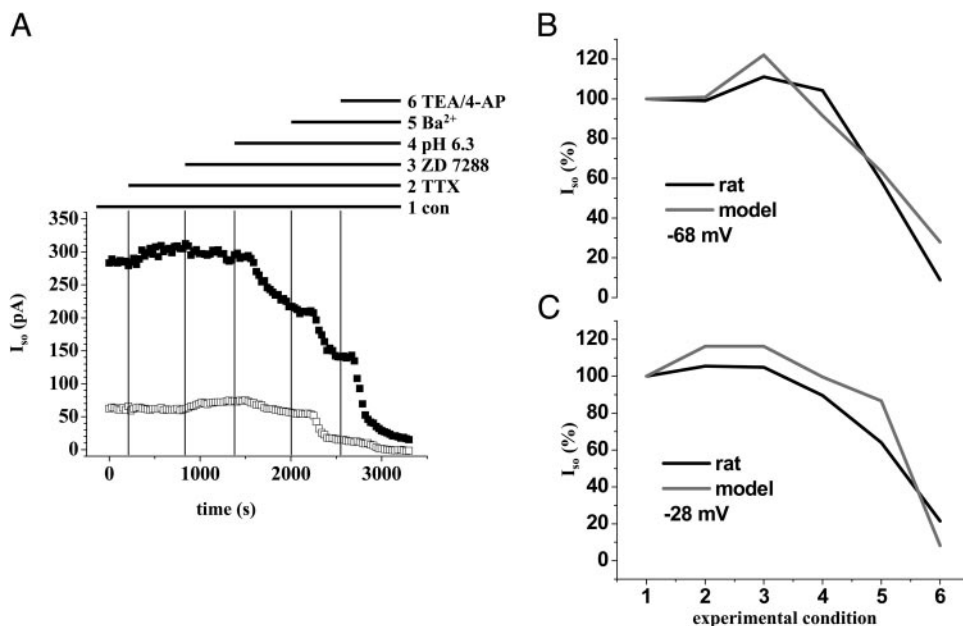


FIG. 5. Pharmacological profile of the standing outward current in thalamocortical relay neurons at different holding potentials. *A*: amplitude of the net outward current plotted against time in a relay neuron recorded under voltage-clamp conditions at -28 mV (black data points) and -68 mV (open data points) under the following experimental conditions (1–6): 1, control conditions; 2, during cumulative application of TTX ($1 \mu\text{M}$); 3, ZD7288 ($100 \mu\text{M}$); 4, H^+ (pH 7.3–6.3); 5, Ba^{2+} ($150 \mu\text{M}$); 6, TEA/4-AP ($20 \text{ mM}/6 \text{ mM}$), as indicated by horizontal lines. Holding current was recorded every 20 s for a duration of 800 ms. *B* and *C*: comparison of averaged data from recordings in 5 neurons (black traces) and computer modeling (gray traces) at -68 mV (*B*) and -28 mV (*C*). Normalized I_{SO} amplitudes are plotted vs. time. Recording conditions as in *A*. For reduction of currents in the model cell see text.

constitute I_{SO} in TC neurons with the degree of their contribution depending on the value of the holding potential.

Computer modeling of steady-state current in TC neurons

We modified an existing TC neuron model (Huguenard and McCormick 1992; McCormick and Huguenard 1992) by adding an inward rectifier K^+ current (Williams et al. 1997) and substituting the linear characteristic of $I_{\text{K-leak}}$ by a Goldman-Hodgkin-Katz (GHK) formalism (Meuth et al. 2005). Furthermore we made 49% of $I_{\text{K-leak}}$ (default value = 10 nS) sensitive to changes in pH and designated this component as the outwardly rectifying TASK current (I_{TASK}). This assumption was based on previous and above findings indicating that the current through TASK channels makes up about 38–59% of I_{SO} in rodent TC neurons (Meuth et al. 2003, 2006; Musset et al. 2006).

Next, the consecutive pharmacological manipulation of I_{SO} was analyzed using the model cell. Current changes at a holding potentials of -68 mV (Fig. 5*B*) and -28 mV (Fig. 5*C*) were compared with averaged experimental data (black lines, $n = 5$). Although a 90% reduction of I_{NaP} (TTX effect) resulted in a 16% increase in I_{SO} at -28 mV with no effect at -68 mV, 90% block of I_{h} (ZD7288 effect) had no effect at -28 mV but increased I_{SO} by 22% at -68 mV. Reduction (the remaining current is stated in %) of I_{TASK} , I_{Kir} , $I_{\text{K-leak}}$, and the delayed rectifier K^+ current (I_{DR}) was used to simulate extracellular acidification (I_{TASK} : 25%), block by Ba^{2+} (I_{TASK} : 0%; I_{Kir} : 10%; $I_{\text{K-leak}}$: 90%), and block by TEA/4-AP (I_{Kir} : 0%; $I_{\text{K-leak}}$: 70%; I_{DR} : 55%). In addition the transient K^+ outward current (I_{A}) was assumed to be completely 4-AP sensitive. As shown in Fig. 5, *B* and *C*, the model cell (gray lines) reliably describes the qualitative changes of I_{SO} in rats (black lines) with a mean deviation between modeled and measured current amplitudes of $12 \pm 2\%$ ($n = 10$; averaged over all experimental conditions at two holding potentials).

Next we used computer modeling techniques to assess the relative contribution of HCN and TASK channels to the pH effects. The resting membrane potential of the model cell was

$V_1 = -72$ mV (Fig. 6*A*). From this potential a step depolarization evoked a low-threshold Ca^{2+} spike and a high-frequency burst ($f_1 = 102$ Hz; Fig. 6*B*) of action potentials (Fig. 6*C*). The effect of extracellular acidification was simulated by simultaneously reducing the maximal conductance of I_{h} and I_{TASK} by 25% (Munsch and Pape 1999) and 90% (Meuth et al. 2003) of their initial values, respectively. As a result the membrane potential of the model cell depolarized to $V_2 = -68$ mV (Fig. 6*A*) with burst firing ($f_2 = 112$ Hz; Fig. 6*B*) being preserved (Fig. 6*D*). Next, the block of HCN channels by ZD7288 was simulated by removing I_{h} from the computer model, resulting in membrane hyperpolarization to $V_3 = -82$ mV (Fig. 6*A*). Using DC-current injection the membrane potential of the model cell was reset to $V_{3/\text{DC}} = -72$ mV (Fig. 6*A*) and a subsequent step depolarization elicited a burst response ($f_{3/\text{DC}} = 105$ Hz; Fig. 6, *B* and *E*). Next, extracellular acidification was simulated by removing 90% of I_{TASK} , thereby leading to a depolarization of the membrane potential to -58 mV (Fig. 6*A*) accompanied by tonic firing ($f_{4/\text{DC}} = 19$ Hz; Fig. 6, *B* and *F*). In an additional set of simulations the upregulation of I_{h} (e.g., by cAMP) was modeled by increasing the default value of I_{h} conductance by 25% (data not shown). As a consequence the resting membrane potential of the model cell was depolarized to $V_1 = -70$ mV. Simulation of extracellular acidification depolarized the membrane potential to $V_2 = -66$ mV, thereby shifting the model to an intermediate firing mode (LTS crowned by a single action potential and followed by tonic firing of three action potentials).

Taken together these findings indicate an opposing interaction of TASK3/TASK1 and HCN2 channels to stabilize the resting membrane potential of TC neurons.

Because a number of components contribute to I_{SO} we expanded our modeling approach. Different combinations of hyperpolarizing (I_{Kir} , $I_{\text{K-leak}}$, I_{TASK}) and depolarizing (I_{h} , I_{NaP}) currents were modulated and compared with the effect seen in rats (Fig. 7). The following experimental conditions were analyzed: 1) Control conditions represent V_{R} of the model cell (-72 mV) and mean V_{R} of rat TC neurons (-71 ± 1 mV, $n =$

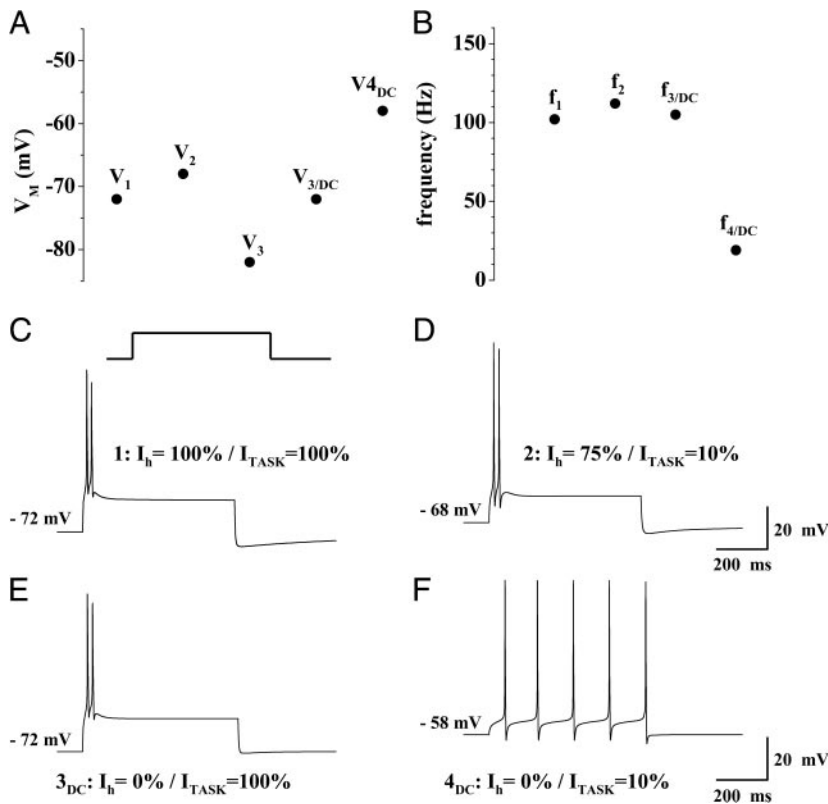


FIG. 6. Computer simulation of activity modes in rat TC neurons. *A* and *B*: resting membrane potentials and firing frequencies of the model cell under different conditions: Control conditions (V_1, f_1); with I_h (the current through HCN channels) and I_{TASK} (the current through TASK channels) reduced by 25 and 90%, respectively, (V_2, f_2); without I_h (V_3); without I_h and the membrane potential reset to the control level ($V_{3/DC}, f_{3/DC}$); without I_h , DC current injection, and 90% reduction of I_{TASK} ($V_{4/DC}, f_{4/DC}$). *C*: depolarizing current pulses (300-ms duration, 150 pA) were applied from a potential of -72 mV. With I_h and I_{TASK} set to 100%, the membrane resting potential settled at -72 mV. A step depolarization resulted in a burst response. *D*: setting I_h and I_{TASK} to 75 and 10%, respectively, resulted in a membrane depolarization to -68 mV and a burst of action potentials after a depolarizing current step. *E*: with I_h and I_{TASK} set to 0 and 100%, respectively, a DC current injection of 150 pA was necessary to set the resting potential to a value of -72 mV. A step depolarization resulted in a burst of action potentials. *F*: setting I_h and I_{TASK} to 0 and 10%, respectively, resulted in a membrane depolarization to -58 mV and a tonic train of action potentials following a depolarizing current step.

25) recorded in slices. 2) During extracellular acidification (pH 6.3) both 25 and 90% reductions of I_h and I_{TASK} were assumed in native cells, respectively. Therefore in the model cell the indicated depolarizing and hyperpolarizing current was reduced by 25 and 90%, respectively. The resulting changes in

V_R are shown. 3) The block of I_h hyperpolarizes native TC neurons and the model cell. To reach the control level of V_M (about -73 mV) positive DC currents of 100–200 and 150 pA were injected to native TC neurons and the model cell, respectively. Furthermore, the indicated depolarizing current was removed in the model cell. 4) The last experimental condition simulates the effect of reducing the indicated hyperpolarizing current by 90%, whereas the indicated depolarizing current was removed from the computer model and a positive current of +150 pA was injected. As shown in Fig. 7, only the combined modulation of I_{TASK}/I_h and I_{K-leak}/I_h closely matched the experimental data from rats. It is interesting to note that the use of a linear I_{K-leak} component was less effective in reproducing whole cell patch-clamp recordings (data not shown).

Taken together, these data show that the joined modulation of I_{TASK} and I_h is the most likely cellular action that account for the pH effect seen in native TC neurons.

DISCUSSION

The main results of the present paper can be summarized as follows. 1) All known pacemaker channels (HCN1–4), TASK1–3 channels, and at least five other members of the K_{2P} channel family (TREK1, TREK2, TRAAK, THIK1, THIK2) are expressed in rat dLGN. 2) The dominant isoforms, HCN2 and TASK3, are coexpressed in TC neurons. 3) Current components carried by HCN and TASK channels contribute to the pH-sensitive component elicited by hyperpolarizing ramp protocols in TC neurons. 4) Extracellular acidification leads to depolarization of TC neurons the magnitude of which critically depends on the availability of HCN and TASK channels. Current-clamp recordings in rats, HCN2^{-/-} mice, and computer modeling studies demonstrate that the counterbalancing

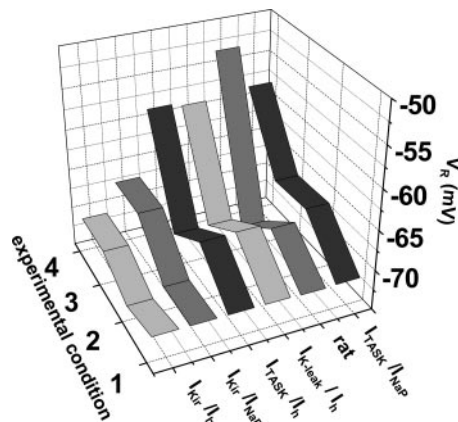


FIG. 7. Modeling the effect of hyperpolarizing (I_{Kir} , I_{K-leak} , I_{TASK}) and depolarizing (I_h , I_{NaP}) membrane currents on V_{rest} . Different pairs of currents (as indicated) were altered in a computer model to reproduce the results found in native rat TC neurons. Experimental conditions were as follows: 1, control condition: V_{rest} of the model cell and mean V_R of rat TC neurons. 2, pH 6.4: in native TC neurons a 25 and 90% reduction of I_h and I_{TASK} was assumed, respectively. Therefore in the model cell the indicated depolarizing and hyperpolarizing current was reduced by 25 and 90%, respectively. 3, block of I_h and injection of +150-pA DC current in native TC neurons. In the model cell the indicated depolarizing current was eliminated and +150-pA DC current was injected. 4, pH 6.4 and block of I_h during DC current injection. In the model cell the indicated depolarizing current was eliminated, the indicated hyperpolarizing current was reduced by 90% and +150-pA DC current was injected. Note that only the combination I_{TASK}/I_h and I_{K-leak}/I_h closely matches the native situation (rat).

effects of HCN2 and TASK3/TASK1 channels play an important role in setting the resting membrane potential of TC neurons. 5) Although modulation of TASK and/or HCN channels can effectively shift TC neurons between firing modes, the overall characteristics of the two forms of activity are rather unchanged.

pH-sensitive membrane currents in TC neurons

TASK1 and TASK3 channels, which are sensitive to changes in extracellular pH (Duprat et al. 1997; Kim et al. 2000; Rajan et al. 2000), are expressed in TC neurons (Meuth et al. 2003). Thus pH-sensitive currents evoked by hyperpolarizing voltage ramps revealed typical features of a current carried by TASK channels. However, the reversal potential deviated from that of a pure K^+ current. Even more surprising, in contrast to the inhibition of TASK channels by bupivacaine and muscarine (Meuth et al. 2003), the closure of TASK channels by external H^+ ions did not result in a strong depolarization of the membrane potential. Only after blocking I_h , pH-sensitive ramp currents reversed at the expected K^+ reversal potential and extracellular acidification induced a strong depolarization, thereby proving the contribution of both HCN and TASK channels to the pH-sensitive component.

The counterbalancing modulation of TASK and HCN channels restricts the net effect of acidification on the resting membrane potential. The experimental paradigm used to demonstrate this interaction included the use of DC current injection to achieve similar control values of the membrane potential (about -72 mV). This was done to exemplify the different effects of acidification with (no shift in activity mode) and without I_h (shift in activity mode), rather than to mimic a sequence of events in the brain. The scenario of interacting TASK and HCN channels is strengthened by the fact that V_R values of TASK1-deficient mice are significantly more depolarized compared with wild-type animals under control conditions and in the presence of ZD7288 (Meuth et al. 2006).

Based on results obtained from rat (Meuth et al. 2003; Musset et al. 2006), TASK1-KO mice (Meuth et al. 2006), and computer modeling (this study) it can be concluded that the pH-sensitive component (acidification to pH 6.3) makes up about 40% of I_{SO} (at -28 mV). However, at extracellular pH values exceeding the modulation range of TASK channels (i.e., pH <6.0) I_{SO} is further reduced, indicating the presence of additional pH-sensitive components. To assess whether other ion currents may mediate the pH effect seen in the present study, we used computer modeling. Not one combination, including I_{Kir} or I_{NaP} , was able to account for the result obtained from TC neurons. Nevertheless the contribution of more components cannot be fully excluded because changes in extracellular pH can modulate the activity of a variety of ion channels and receptors (for review see Kaila and Ransom 1998). Furthermore, subtle differences between cellular properties may account for differences in the pH effect under control conditions seen in rat (depolarization) and mice (hyperpolarization). This view is corroborated, for example, by the finding that TASK3 is clearly the dominant subtype in rat but TASK1 and TASK3 reveal roughly equal mRNA levels in mouse dLGN (Meuth et al. 2006). Similar considerations may apply to HCN channels that show functional expression of

HCN1 in rat (Budde et al. 2005) but not in mouse TC neurons (Franz et al. 2000).

Constituents of the resting membrane potential in TC neurons

The resting membrane potentials of TC neurons in different species and thalamic nuclei are reportedly in the range of -60 to -75 mV (McCormick and Pape 1990; Meuth et al. 2003; Porcello et al. 2003; Williams et al. 1997; Zhan et al. 1999), the evolution of which is ascribed to leak currents (I_{K-leak} , $I_{Na-leak}$), pacemaker currents (I_h), inwardly rectifying K^+ currents (I_{Kir}), voltage-dependent currents active below threshold (I_A , I_T), and any DC current experimentally injected to the cell (I_{inj}) (Williams et al. 1997; Zhan et al. 1999). In agreement with this assumption the standing outward current of TC neurons (Meuth et al. 2003) is composed of I_h , I_{Kir} , I_{TASK} , a persistent Na^+ current, and voltage-dependent K^+ currents. The results of the present study allow the assignment of most of the I_h component to HCN2 channels.

The evidence to support the hypothesis that I_h is active at the resting membrane potential of TC neurons under the present recording conditions (-71 mV) is as follows. I_h is a slow inward current activating at potentials negative to -55 mV (see Fig. 2D), shows no inactivation (McCormick and Pape 1990), and has a calculated reversal potential of about -35 mV (Budde et al. 1997). According to the approximation of a Boltzmann distribution to the data points a fraction of 18% of I_h is activated at -71 mV (see Fig. 2D), carrying an inward current of -34 ± 2 pA ($n = 28$). Block of I_h shifted the resting membrane potential of TC neurons by -8 mV, a value in close agreement with previously reported hyperpolarization (-5 to -9 mV) in a number of different neuronal cell types (Day et al. 2005; Doan and Kunze 1999; Lupica et al. 2001; Maccaferri and McBain 1996).

Based on our results on rodent TC neurons (Meuth et al. 2003, 2006; Musset et al. 2006) and computer modeling (this study) it can be assumed that the classical K^+ leak current is roughly equally composed of pH-sensitive current through TASK3/TASK1 channels (I_{TASK}) and other pH-insensitive leak channels (I_{K-leak}). Although quantitative PCR experiments, subtype-specific modulation, and gene knock out point to a domination of TASK3 over TASK1, the I_{K-leak} component may be carried by current through other members of the K_{2P} family. This conclusion is corroborated by the following findings. 1) I_{K-leak} revealing GHK rectification (Goldstein et al. 2001) is necessary to give closely matching modeling results. 2) THIK, TRAAK, and TREK channels are expressed in dLGN, although a consignment to defined cell types is still missing. The functional expression of TREK and TRAAK (Patel and Lazdunski 2004) channels in TC neurons is in agreement with the presence of a leak current inhibited by cAMP and Ba^{2+} (Budde et al. 1997, 2005) and an I_{SO} component enhanced by arachidonic acid (Meuth et al. 2006). 3) Modeling of the pH effect gives very similar results when both I_{TASK} and I_{K-leak} are assumed to be pH sensitive.

It is noticeable that HCN2 $^{-/-}$ mice show no plastic compensation for the loss of HCN2 channels. It has been noted before that, for example, cerebellar granule cells show a greater degree of plasticity in comparison with TC neurons in response

to TASK-1 deletion (Meuth et al. 2006). The reason for this difference is unknown.

Comparability between data obtained in vitro and in silico

The quantitative aspects of the complex relationship between current amplitudes in vitro, current amplitudes in the computer model, and their effect on the resting membrane potential depend on pharmacological tools, the large parameter space of the computer model, and experimental variations. Therefore it cannot be expected to achieve full match between experimental recordings and computer simulations. Still the following considerations reveal a reasonable degree of similarity between experiments and modeling. 1) Injection of small depolarizing and hyperpolarizing current pulses (from resting membrane potential) to the model cell under current-clamp conditions resulted in 1- to 3-mV voltage deflections and allowed the calculation of the input resistance under control conditions (43 M Ω) and after the block of I_h (90 M Ω). Multiplying the difference in input resistance (47 M Ω) by the amplitude of I_h at the resting membrane potential of the model cell under control conditions (-130 pA) results in a voltage deflection of -6 mV. In whole cell recordings that typically reveal higher membrane resistances (some hundred megaohms) smaller currents (some tens of picoamperes) are able to induce similar voltage shifts. 2) Absolute current values of I_h and I_{TASK} (amplitude of the pH-sensitive current in ZD7288) at -71 mV reveal very similar proportions in vitro ($I_h = 34 \pm 2$ pA, $n = 28$; $I_{TASK} = 31 \pm 2$ pA, $n = 25$) and in the computer model ($I_h = 131$ pA; $I_{TASK} = 137$ pA). Thus voltage changes induced by blocking/knocking out I_h in rats, mice, and the computer model ($V_{ZD} - V_R = -8$ mV; $V_{R/HCN2+/+} - V_{R/HCN2-/-} = -12$ mV; $V_3 - V_1 = -10$ mV; median = -10 mV) are in a range that has been described in several neuronal cell types (see above) and are comparable to the effects induced by blocking I_{TASK} ($V_R - V_{ZD/pH6.3} = 19$ mV; $V_{R/HCN2+/+} - V_{pH6.3/HCN-/-} = 11$ mV; $V_1 - V_{4DC} = 13$ mV; median = 14 mV). 3) The relationship between amplitudes measured in vitro (recording temperature $\approx 21^\circ\text{C}$) and the computer model (simulation temperature 35°C) is given by the Q_{10} value. Many enzyme reactions have a Q_{10} value near 3, as does the gating of many ion channels, including I_h (Hille 2001). Although values for absolute conductance of I_h seem to be <3 (Pena et al. 2006), the Q_{10} for I_h current amplitude in intracardiac neurons could be determined as 2.2 (Cuevas et al. 1997). Thus the amplitude of I_h at the resting membrane potential at 35°C can be expected to be -34 pA $\times 3.1$ ($Q_{\Delta T}$ for a temperature difference of 14°C) = -105 pA, which is close to the -130 pA generated by the computer model. The temperature dependency of TASK channels is less clear because some K_{2P} channels reveal a sevenfold increase in current amplitude for a 10°C increment in temperature (Maingret et al. 2000).

Functional implications

The dorsal thalamus has a key role in regulating the flow of sensory information from the periphery to the primary sensory cortical areas and participates in the generation of thalamocortical oscillations associated with different states of consciousness and the status of absence epilepsy (Steriade et al. 1997).

TC neurons are depolarized by neurotransmitters of the ascending brain stem system, including noradrenalin, serotonin, and acetylcholine (McCormick 1992). Whereas noradrenalin exerts this effect by the convergent modulation of I_{K-leak} (i.e., closure) and I_h (i.e., depolarizing shift in activation), acetylcholine depolarizes TC neurons by closing TASK and I_{KIR} channels (Meuth et al. 2003). This depolarization is responsible for the transition of sleep-related rhythmic burst activity to tonic activity associated with periods of wakefulness and REM sleep.

The view that the counterbalancing actions of TASK and HCN on the resting membrane potential constitute a more general motive in the CNS is in agreement with the broad expression of HCN (Monteggia et al. 2000) and TASK (Talley et al. 2001) channels in the brain, the reciprocal modulation of I_h and I_{TASK} by serotonin and halothane on hypoglossal motoneurons (Sirois et al. 2002), and the analysis of dendritic excitability in mouse frontal cortex pyramidal cells (Day et al. 2005).

Pathophysiological implications

Neuronal activity leads to transient extracellular alkalinization followed by a persistent extracellular acidification (Chesler and Kaila 1992). In dLGN synchronous afferent activation, tonic activity, and rhythmic burst discharges induce extracellular and intracellular increases in H^+ concentrations (Meyer et al. 2000; Tong and Chesler 1999). The data presented here suggest that pH shifts induced by different forms of activity in dLGN should have rather small effects on the overall firing pattern and resting membrane potential. This is of special interest for periods of generalized absence epilepsy, where the highly synchronous burst pattern of large populations of TC neurons is not expected to be altered by pH changes arising from rhythmic activity.

Periods of brain ischemia are characterized by a decrease in extracellular pH to values as low as 6.0 (Siemkiewicz and Hansen 1981; Simon et al. 1985). CNS neurons reveal extremely different sensitivity to ischemic insults (Centonze et al. 2001). The reason for this differential vulnerability is still largely unknown. Vulnerable neurons respond to ischemia with prolonged and strong membrane depolarization and subsequent cellular damage. Because of the joined modulation of TASK and HCN described here, it can be assumed that TC neurons show little depolarization in response to acidification during ischemic insults and thus a selective nonvulnerability. It seems, however, that other influences dominate the reaction of TC neurons to acute hypoxia (Erdemli and Crunelli 1998, 2000; Steinke et al. 1992; Szeliés et al. 1991). Under these conditions there is an enhanced release of monoamines and nitric oxide—substances known to strongly activate I_h —in the thalamus. Therefore acute hypoxia leads to membrane depolarization and altered electrical properties of TC neurons and makes the dLGN a part of a system-preferential, topographically organized brain injury after ischemia (Erdemli and Crunelli 1998, 2000; Steinke et al. 1992; Szeliés et al. 1991).

ACKNOWLEDGMENTS

Thanks to R. Ziegler and A. Jahn for excellent technical assistance.

GRANTS

This work was supported by Deutsche Forschungsgemeinschaft Grant BU 1019/5-2/7-1 (Leibniz-Program) to H.-C. Pape and Kommission Innovative Medizinische Forschung Grant BU 120501.

REFERENCES

- Berg AP, Talley EM, Manger JP, and Bayliss DA.** Motoneurons express heteromeric TWIK-related acid-sensitive K⁺ (TASK) channels containing TASK-1 (KCNK3) and TASK-3 (KCNK9) subunits. *J Neurosci* 24: 6693–6702, 2004.
- Budde T, Biella G, Munsch T, and Pape H-C.** Lack of regulation by intracellular Ca²⁺ of the hyperpolarization-activated cation current in rat thalamic neurons. *J Physiol* 503.1: 79–85, 1997.
- Budde T, Caputi L, Kanyshkova T, Staak R, Abrahamczik C, Munsch T, and Pape H-C.** Impaired regulation of thalamic pacemaker channels through an imbalance of subunit expression in absence epilepsy. *J Neurosci* 25: 9871–9882, 2005.
- Centonze D, Marfia GA, Pisani A, Picconi B, Giacomini P, Bernardi G, and Calabresi P.** Ionic mechanisms underlying differential vulnerability to ischemia in striatal neurons. *Prog Neurobiol* 63: 687–696, 2001.
- Chesler M and Kaila K.** Modulation of pH by neuronal activity. *Trends Neurosci* 15: 396–402, 1992.
- Craven KB and Zagotta WN.** CNG and HCN channels: two peas, one pod. *Annu Rev Physiol* 68: 375–401, 2006.
- Cuevas J, Harper AA, Trequatrini C, and Adams DJ.** Passive and active membrane properties of isolated rat intracardiac neurons: regulation by H- and M-currents. *J Neurophysiol* 78: 1890–1902, 1997.
- Czirjak G and Enyedi P.** Formation of functional heterodimers between the TASK-1 and TASK-3 two-pore domain potassium channel subunits. *J Biol Chem* 277: 5426–5432, 2002.
- Day M, Carr DB, Ulrich S, Ilijic E, Tkatch T, and Surmeier DJ.** Dendritic excitability of mouse frontal cortex pyramidal neurons is shaped by the interaction among HCN, Kir2, and K_{leak} channels. *J Neurosci* 25: 8776–8787, 2005.
- Doan TN and Kunze DL.** Contribution of the hyperpolarization-activated current to the resting membrane potential of rat nodose sensory neurons. *J Physiol* 514: 125–138, 1999.
- Duprat F, Lesage F, Fink M, Reyes R, Heurteaux C, and Lazdunski M.** TASK, a human background K⁺ channel to sense external pH variations near physiological pH. *EMBO J* 16: 5464–5471, 1997.
- Erdemli G and Crunelli V.** Response of thalamocortical neurons to hypoxia: a whole-cell patch-clamp study. *J Neurosci* 18: 5212–5224, 1998.
- Erdemli G and Crunelli V.** Release of monoamines and nitric oxide is involved in the modulation of hyperpolarization-activated inward current during acute thalamic hypoxia. *Neuroscience* 96: 565–574, 2000.
- Franz O, Liss B, Neu A, and Roeper J.** Single-cell mRNA expression of HCN1 correlates with a fast gating phenotype of hyperpolarization-activated cyclic nucleotide-gated ion channels (I_h) in central neurons. *Eur J Neurosci* 12: 2685–2693, 2000.
- Goldstein SA, Bockenhauer D, O’Kelly I, and Zilberberg N.** Potassium leak channels and the KCNK family of two-P-domain subunits. *Nat Rev Neurosci* 2: 175–184, 2001.
- Hille B.** *Ion Channels of Excitable Membranes*. Sunderland, MA: Sinauer, 2001.
- Hines ML and Carnevale NT.** NEURON: a tool for neuroscientists. *Neuroscientist* 7: 123–135, 2001.
- Huguenard JR and McCormick DA.** Simulation of the currents involved in rhythmic oscillations in thalamic relay neurons. *J Neurophysiol* 68: 1373–1383, 1992.
- Jones EG and Hendry SH.** Differential Calcium Binding Protein Immunoreactivity Distinguishes Classes of Relay Neurons in Monkey Thalamic Nuclei. *Eur J Neurosci* 1: 222–246, 1989.
- Jones SW.** On the resting potential of isolated frog sympathetic neurons. *Neuron* 3: 153–161, 1989.
- Kaila K and Ransom BR.** *pH and Brain Function*. New York: Wiley-Liss, 1998.
- Kim Y, Bang H, and Kim D.** TASK-3, a new member of the tandem pore K(+) channel family. *J Biol Chem* 275: 9340–9347, 2000.
- Lesage F.** Pharmacology of neuronal background potassium channels. *Neuropharmacology* 44: 1–7, 2003.
- Ludwig A, Budde T, Stieber J, Moosmang S, Wahl C, Holthoff K, Langebartels A, Wotjak C, Munsch T, Zong X, Feil S, Feil R, Lancel M, Chien KR, Konnerth A, Pape H-C, Biel M, and Hofmann F.** Absence epilepsy and sinus dysrhythmia in mice lacking the pacemaker channel HCN2. *EMBO J* 22: 216–224, 2003.
- Lupica CR, Bell JA, Hoffman AF, and Watson PL.** Contribution of the hyperpolarization-activated current (I_h) to membrane potential and GABA release in hippocampal interneurons. *J Neurophysiol* 86: 261–268, 2001.
- Maccaferri G and McBain CJ.** The hyperpolarization-activated current (I_h) and its contribution to pacemaker activity in rat CA1 hippocampal stratum oriens-alveus interneurons. *J Physiol* 497: 1: 119–130, 1996.
- Maignret F, Lauritzen I, Patel AJ, Heurteaux C, Reyes R, Lesage F, Lazdunski M, and Honore E.** TREK-1 is a heat-activated background K(+) channel. *EMBO J* 19: 2483–2491, 2000.
- Malcolm AT, Kourennyi DE, and Barnes S.** Protons and calcium alter gating of the hyperpolarization-activated cation current (I_h) in rod photoreceptors. *Biochem Biophys Acta* 1609: 183–192, 2003.
- McCormick DA.** Neurotransmitter actions in the thalamus and cerebral cortex and their role in neuromodulation of thalamocortical activity. *Prog Neurobiol* 39: 337–388, 1992.
- McCormick DA and Huguenard JR.** A model of the electrophysiological properties of thalamocortical relay neurons. *J Neurophysiol* 68: 1384–1400, 1992.
- McCormick DA and Pape H-C.** Properties of a hyperpolarization-activated cation current and its role in rhythmic oscillation in thalamic relay neurons. *J Physiol* 431: 291–318, 1990.
- Meuth P, Meuth SG, Jacobi D, Broicher T, Pape H-C, and Budde T.** Get the Rhythm: modeling of neuronal activity. *JUNE Fall 2005* 4: A1–A11, 2005.
- Meuth SG, Aller MI, Munsch T, Schuhmacher T, Seidenbecher T, Kleinschnitz C, Pape H-C, Wiendl H, Wisden W, and Budde T.** The contribution of TASK-1-containing channels to the function of dorsal lateral geniculate thalamocortical relay neurons. *Mol Pharmacol* 69: 1468–1476, 2006.
- Meuth SG, Budde T, Kanyshkova T, Broicher T, Munsch T, and Pape H-C.** Contribution of TWIK-related acid-sensitive K⁺ channel 1 (TASK1) and TASK3 channels to the control of activity modes in thalamocortical neurons. *J Neurosci* 23: 6460–6469, 2003.
- Meuth SG, Kanyshkova T, Landgraf P, Pape H-C, and Budde T.** Influence of Ca²⁺-binding proteins and the cytoskeleton on Ca²⁺-dependent inactivation of high-voltage activated Ca²⁺ currents in thalamocortical relay neurons. *Pfluegers Arch* 450: 111–122, 2005.
- Meyer TM, Munsch T, and Pape H-C.** Activity-related changes in intracellular pH in rat thalamic relay neurons. *Neuroreport* 11: 33–37, 2000.
- Millar JA, Barratt L, Southan AP, Page KM, Fyffe RE, Robertson B, and Mathie A.** A functional role for the two-pore domain potassium channel TASK-1 in cerebellar granule neurons. *Proc Natl Acad Sci USA* 97: 3614–3618, 2000.
- Monteggia LM, Eisch AJ, Tang MD, Kaczmarek LK, and Nestler EJ.** Cloning and localization of the hyperpolarization-activated cyclic nucleotide-gated channel family in rat brain. *Brain Res Mol Brain Res* 81: 129–139, 2000.
- Munsch T and Pape H-C.** Modulation of the hyperpolarization-activated cation current of rat thalamic relay neurons by intracellular pH. *J Physiol* 519: 493–504, 1999.
- Musset B, Meuth SG, Liu GX, Derst C, Wegner S, Pape H-C, Budde T, Preisig-Muller R, and Daut J.** Effects of divalent cations and spermine on the K⁺ channel TASK-3 and on the outward current in thalamic neurons. *J Physiol* 572: 639–657, 2006.
- Pape H-C.** Queer current and pacemaker: the hyperpolarization-activated cation current in neurons. *Annu Rev Physiol* 58: 299–327, 1996.
- Pape H-C, Budde T, Mager R, and Kisvarday Z.** Prevention of Ca²⁺-mediated action potentials in GABAergic local circuit neurons of the thalamus by a transient K⁺ current. *J Physiol* 478: 403–422, 1994.
- Patel AJ and Lazdunski M.** The 2P-domain K⁺ channels: role in apoptosis and tumorigenesis. *Pfluegers Arch* 448: 261–273, 2004.
- Pena F, Amuzescu B, Neaga E, and Flonta ML.** Thermodynamic properties of hyperpolarization-activated current (I_h) in a subgroup of primary sensory neurons. *Exp Brain Res* May 5, 2006, published online. DOI: 10.1007/s00221-006-0473-z.
- Porcello DM, Smith SD, and Huguenard JR.** Actions of U-92032, a T-type Ca²⁺ channel antagonist, support a functional linkage between I_T and slow intrathalamic rhythms. *J Neurophysiol* 89: 177–185, 2003.
- Rajan S, Wischmeyer E, Liu GX, Preisig-Muller R, Daut J, Karschin A, and Derst C.** TASK-3, a novel tandem pore domain acid-sensitive K⁺ channel. An extracellular histidine as pH sensor. *J Biol Chem* 275: 16650–16657, 2000.

- Sieg F, Obst K, Gorba T, Riederer B, Pape H-C, and Wahle P.** Postnatal expression pattern of calcium-binding proteins in organotypic thalamic cultures and in the dorsal thalamus in vivo. *Brain Res Dev Brain Res* 110: 83–95, 1998.
- Siemkowicz E and Hansen AJ.** Brain extracellular ion composition and EEG activity following 10 minutes ischemia in normo- and hyperglycemic rats. *Stroke* 12: 236–240, 1981.
- Simon RP, Benowitz N, Hedlund R, and Copeland J.** Influence of the blood-brain pH gradient on brain phenobarbital uptake during status epilepticus. *J Pharmacol Exp Ther* 234: 830–835, 1985.
- Sirois JE, Lynch C 3rd, and Bayliss DA.** Convergent and reciprocal modulation of a leak K^+ current and I_h by an inhalational anaesthetic and neurotransmitters in rat brainstem motoneurons. *J Physiol* 541: 717–729, 2002.
- Steinke W, Sacco RL, Mohr JP, Foulkes MA, Tatemichi TK, Wolf PA, Price TR, and Hier DB.** Thalamic stroke. Presentation and prognosis of infarcts and hemorrhages. *Arch Neurol* 49: 703–710, 1992.
- Steriade M, Jones EG, and McCormick DA.** *Thalamus*. Amsterdam: Elsevier, 1997.
- Stevens DR, Seifert R, Bufe B, Muller F, Kremmer E, Gauss R, Meyerhof W, Kaupp UB, and Lindemann B.** Hyperpolarization-activated channels HCN1 and HCN4 mediate responses to sour stimuli. *Nature* 413: 631–635, 2001.
- Szelies B, Herholz K, Pawlik G, Karbe H, Hebold I, and Heiss WD.** Widespread functional effects of discrete thalamic infarction. *Arch Neurol* 48: 178–182, 1991.
- Talley EM, Solorzano G, Lei Q, Kim D, and Bayliss DA.** CNS distribution of members of the two-pore-domain (KCNK) potassium channel family. *J Neurosci* 21: 7491–7505, 2001.
- Tong CK and Chesler M.** Activity-evoked extracellular pH shifts in slices of rat dorsal lateral geniculate nucleus. *Brain Res* 815: 373–381, 1999.
- Watkins CS and Mathie A.** A non-inactivating K^+ current sensitive to muscarinic receptor activation in rat cultured cerebellar granule neurons. *J Physiol* 491: 401–412, 1996.
- Williams SR, Turner JP, Hughes SW, and Crunelli V.** On the nature of anomalous rectification in thalamocortical neurones of the cat ventrobasal thalamus in vitro. *J Physiol* 505: 727–747, 1997.
- Zhan XJ, Cox CL, Rinzel J, and Sherman SM.** Current-clamp and modeling studies of low-threshold calcium spikes in cells of the cat's lateral geniculate nucleus. *J Neurophysiol* 81: 2360–2373, 1999.
- Zong X, Stieber J, Ludwig A, Hofmann F, and Biel M.** A single histidine residue determines the pH sensitivity of the pacemaker channel HCN2. *J Biol Chem* 276: 6313–6319, 2001.



ELSEVIER

Available online at www.sciencedirect.com

ScienceDirect

Neuropharmacology 53 (2007) 431–446

NEURO
PHARMACOLOGY

www.elsevier.com/locate/neuropharm

T-current related effects of antiepileptic drugs and a Ca^{2+} channel antagonist on thalamic relay and local circuit interneurons in a rat model of absence epilepsy

Tilman Broicher^a, Thomas Seidenbecher^a, Patrick Meuth^a, Thomas Munsch^d,
Sven G. Meuth^b, Tatyana Kanyshkova^a, Hans-Christian Pape^a, Thomas Budde^{a,c,*}

^a *Institut für Physiologie I, Westfälische Wilhelms-Universität Münster, Robert-Koch-Str. 27a, D-48149 Münster, Germany*

^b *Neurologische Klinik, Bayerische Julius-Maximilians-Universität, Josef-Schneider-Str. 11, D-97080 Würzburg, Germany*

^c *Institut für Experimentelle Epilepsieforschung, Hüfferstr. 68, D-48149 Münster, Germany*

^d *Institut für Physiologie, Otto-von-Guericke-Universität, Leipziger-Str. 44, 39120 Magdeburg, Germany*

Received 20 December 2006; received in revised form 29 May 2007; accepted 30 May 2007

Abstract

Channel blocking, anti-oscillatory, and anti-epileptic effects of clinically used anti-absence substances (ethosuximide, valproate) and the T-type Ca^{2+} current (I_T) blocker mibefradil were tested by analyzing membrane currents in acutely isolated local circuit interneurons and thalamocortical relay (TC) neurons, slow intrathalamic oscillations in brain slices, and spike and wave discharges (SWDs) occurring in vivo in Wistar Albino Glaxo rats from Rijswijk (WAG/Rij). Substance effects in vitro were compared between WAG/Rij and a non-epileptic control strain, the ACI rats. Ethosuximide (ETX) and valproate were found to block I_T in acutely isolated thalamic neurons. Block of I_T by therapeutically relevant ETX concentrations (0.25–0.75 mM) was stronger in WAG/Rij, although the maximal effect at saturating concentrations (≥ 10 mM) was stronger in ACI. Ethosuximide delayed the onset of the low threshold Ca^{2+} spike (LTS) of neurons recorded in slice preparations. Mibefradil (≥ 2 μM) completely blocked I_T and the LTS, dampened evoked thalamic oscillations, and attenuated SWDs in vivo. Computational modeling demonstrated that the complete effect of ETX can be replicated by a sole reduction of I_T . However, the necessary degree of I_T reduction was not induced by therapeutically relevant ETX concentrations. A combined reduction of I_T , the persistent sodium current, and the Ca^{2+} activated K^+ current resulted in an LTS alteration resembling the experimental observations. In summary, these results support the hypothesis of I_T reduction as part of the mechanism of action of anti-absence drugs and demonstrate the ability of a specific I_T antagonist to attenuate rhythmic burst firing and SWDs.

© 2007 Elsevier Ltd. All rights reserved.

Keywords: WAG/Rij; Thalamus; Absence epilepsy; T-type Ca^{2+} channel; LVA Ca^{2+} current; Ethosuximide; Valproate; Mibefradil; Patch-clamp; Spike and wave discharges

1. Introduction

Absence seizures are characterized by short lapses of consciousness with minimal motor and autonomic manifestations

* Corresponding author at: Institut für Experimentelle Epilepsieforschung, Hüfferstr. 68, D-48149 Münster, Germany. Tel.: +49 251 835 5531; fax: +49 251 835 5551.

E-mail address: tbudde@uni-muenster.de (T. Budde).

(Avoli et al., 2001). These seizures are accompanied by a highly stereotypical EEG pattern composed of spikes and waves at a frequency of ~ 3 Hz, which have been termed spike and wave discharges (SWD). Ample evidence suggests these seizures to be generated by the same network that generates slow wave sleep oscillations, which consists of cortical, reticular thalamic, and thalamocortical neurons (Avoli et al., 2001; Crunelli and Leresche, 2002b; Gloor, 1968; McCormick and Bal, 1997; Pace-Schott and Hobson, 2002; Williams, 1953).

Slow wave sleep rhythms in the thalamocortical system have been shown to depend on the action of I_T (Anderson et al., 2005; Lee et al., 2004), which generates a low threshold Ca^{2+} spike (LTS) in response to depolarization from hyperpolarized membrane potentials, and triggers high frequency bursts of action potentials (Perez-Reyes, 2003). Likewise, pathophysiological oscillations leading to absence seizures have been shown to be dependent on the action of I_T (Kim et al., 2001; Song et al., 2004). In line with the I_T dependence of thalamocortical slow oscillations, the mechanism of action of ETX, a prototypical anti-absence medication (Rogawski and Loscher, 2004), has been attributed to a reduction of this current in TC neurons in an initial series of studies (Coulter et al., 1989a,b, 1990). Subsequent work has failed to reproduce the finding of ETX induced I_T reduction by therapeutically relevant concentrations (0.25–0.75 mM). Instead, the mechanism of ETX action has been attributed to a reduction of the persistent Na^+ current (I_{NaP}) and the Ca^{2+} -activated K^+ current (I_{KCa}) (Leresche et al., 1998; Pfrieger et al., 1992; Sayer et al., 1993; Thompson and Wong, 1991). However, a systematic comparison of ETX effects between thalamic cell types from epileptic and non-epileptic rat strains has not been performed. Recently, the issue was readdressed by Porcello et al. (2003) showing that a specific I_T antagonist was able to inhibit thalamic oscillations *in vitro* and by Gomora et al. (2001) showing that ETX blocks cloned I_T channels expressed in HEK-293 cells. Similar to ETX, the mechanism of action of valproate, the first choice medication in absence epilepsy, is not fully understood. An increase in GABA turnover, as well as a blockade of transient and persistent voltage gated sodium currents and I_T have been suggested to underlie the anti-epileptic valproate effect (Posner et al., 2005; Rogawski and Loscher, 2004).

To further elucidate the role of I_T in drug action we addressed the following questions: (i) do anti-absence drugs block I_T ? To extend former investigations of TC neurons in laboratory rat strains (Coulter et al., 1989a,b, 1990; Leresche et al., 1998), we systematically compared Wistar Albino Glaxo rats from Rijswijk (WAG/Rij), a genetic model of absence epilepsy, and ACI rats, a non-epileptic control strain (Coenen and Van Luijtelaaar, 2003). Furthermore, we included local circuit interneurons in the analysis which are thought to synchronize thalamic activity (Contreras et al., 1993; Rinzel et al., 1998). We tested the effects of ETX, mibefradil, and valproate on isolated I_T and other voltage dependent membrane conductances of neurons from the dorsal lateral geniculate nucleus (LGN). The functional consequences of drug effects were assessed by current clamp recordings allowing the analysis of LTS properties. (ii) The initial observation that ETX blocks I_T led to the hypothesis that this effect is a mechanism of action of anti-absence medications (Crunelli and Leresche, 2002a; Huguenard, 2002). According to this hypothesis, a specific I_T antagonist should mimic network and systemic effects of anti-absence substances. To address this issue, we employed the I_T antagonist mibefradil (Bezprozvanny and Tsien, 1995; Mehrke et al., 1994; Mishra and Hermsmeyer, 1994) on different levels of experimental and biological complexity and analyzed

mibefradil's effect on I_T , the LTS, slow intrathalamic oscillations and SWDs.

2. Methods

2.1. Preparation for *in vitro* electrophysiology

All animal procedures were approved by local authorities. For patch-clamp experiments on acutely isolated neurons WAG/Rij and ACI rats (P15–P25) were deeply anaesthetized (halothane) and decapitated. Brains were removed and placed in cold, oxygenated artificial cerebrospinal fluid (ACSF) containing (mM): Sucrose, 210; PIPES, 20; KCl, 2.4; MgCl_2 , 10; CaCl_2 , 0.5; dextrose, 10; pH 7.25 with NaOH. Thalamic slices (500 μm) were obtained from coronal vibratome sections (Model 1000, Ted Pella, Redding, CA) and LGN tissue was transferred to a spinner flask and incubated for 25–30 min at 30 °C in an oxygenated solution containing trypsin (0.5–1 mg/ml, Sigma, Taufkirchen, Germany) and (mM): NaCl, 120; KCl, 5; MgCl_2 , 3; CaCl_2 , 1; PIPES, 20; dextrose, 25; pH adjusted to 7.35 with NaOH. For patch clamp recordings in brain slice preparations, rat brains (P20–25) were cut into 300 μm thick slices. Sections containing the LGN were transferred into a holding chamber containing a carbogenated solution composed of (mM): CaCl_2 , 3; KCl, 2.5; NaCl, 125; MgSO_4 , 4; NaH_2PO_4 , 1.25; NaHCO_3 , 22; dextrose, 10; pH \sim 7.4. Slices were heated for 20 min to 30 °C before being transferred to the holding chamber, and allowed to rest for 60–90 min afterwards. For multi-unit extracellular recordings, rat brains (P28–35) were cut into 500 μm thick horizontal slices and subjected to identical procedures as described for the patch clamp recordings in slice preparations, except that slices were continuously kept at a temperature of 30 °C in the holding as well as the recording chamber.

2.2. Electrophysiology

Single neurons were obtained after trituration with Pasteur pipettes of decreasing tip diameter. Whole-cell recordings were performed at room temperature using borosilicate glass pipettes (GC150TF-10, Clark Electromedical Instruments, Pangbourne, UK) connected to an EPC-7 amplifier (E.S.F. electronics, Friedland, Germany). The typical electrode resistance was 3–4.5 M Ω , while series resistance was in the range of 5–10 M Ω . Input resistances ranged from 0.5 to 5 G Ω . Voltage clamp experiments on dissociated neurons were controlled by pClamp6 software, operating via an interface (Digidata 1200, Axon Instruments, Foster City, CA). The following recording solutions were used: (i) extracellular solution (mM) for recordings of I_T and high voltage-activated (HVA) Ca^{2+} currents: NaCl, 112; CsCl, 4; KCl, 1; HEPES, 10; dextrose, 10; MgCl_2 , 0.5; CaCl_2 , 5.5; TTX, 0.001; TEA-Cl, 20; 4-aminopyridine, 6; pH 7.35 with NaOH. (ii) Extracellular solution (mM) for recordings of fast transient voltage gated sodium currents (mM): NaCl, 80; CsCl, 5; 4-aminopyridine, 5; TEA-Cl, 15; HEPES, 10; CaCl_2 , 1; MgCl_2 , 3; CdCl_2 , 0.15; KCl, 1; dextrose, 10; pH 7.35 with NaOH. (iii) Extracellular solution (mM) for recordings of the persistent sodium current: NaCl, 120; KCl, 1; HEPES, 10; CsCl, 4; 4-aminopyridine, 6; TEA-Cl, 20; BaCl_2 , 0.15; CdCl_2 , 0.15; NiCl, 0.05; dextrose, 10; CaCl_2 , 0.5; MgCl_2 , 5.5; pH 7.35 with NaOH. (iv) Intracellular solution (mM) for the recordings of Ca^{2+} and transient Na^+ currents: Cs-gluconate, 85; Cs_3 -citrate, 10; NaCl, 10; KCl, 1; EGTA, 5.5; CaCl_2 , 0.5; MgCl_2 , 0.25; HEPES, 10; TEA-Cl, 15; Mg-ATP, 3; Na_2 -GTP, 0.5; phosphocreatine, 15; pH 7.25 with KOH. (v) Intracellular solution (mM) for the recordings of the persistent sodium current: NaCl, 10; KCl, 1; HEPES, 10; Cs-Methansulfate, 100; TEA-Cl, 15; EGTA, 5.5; Mg-ATP, 3; Na_2 -GTP, 0.5; phosphocreatine, 15; CaCl_2 , 0.5; MgCl_2 , 0.25; pH 7.25 with CsOH. Test substances were solubilized in water and added to the standard extracellular solutions. A multi-barrel application pipette with a tip diameter of about 100 μm was used for test substance application. Recordings from acutely isolated neurons were analyzed using pClamp6 and Origin 5.0 software.

Whole cell recordings in brain slice preparations were done using glass pipettes (GC150T-10, Clark Electromedical Instruments, Pangbourne, UK) connected to an EPC-10 amplifier (HEKA Elektronik, Friedland, Germany). Electrode resistance ranged from 1.8 to 2.5 M Ω . Neuronal input resistance ranged from 200 to 800 M Ω , while series resistances ranged from 5 to 15 M Ω . The following recording solutions were used: (i) extracellular solution

(mM): CaCl₂, 3; KCl, 2.5; NaCl, 120; MgSO₄, 2; NaH₂PO₄, 1.25; HEPES, 30; dextrose, 10; pH 7.24 with NaOH. (ii) Intracellular solution (mM): CaCl₂, 0.5; NaCl, 10; MgCl₂, 1; HEPES, 10; K-BAPTA, 3; K-gluconate, 95; K-citrate, 20; phosphocreatine, 15; Na-GTP, 0.5; Mg-ATP, 3; pH 7.24 with KOH. The maximum voltage of the first LTS associated action potential was used as an index for the LTS onset latency. Action potential half width and amplitudes were measured using the Mini Analysis Program (Synaptosoft). Recordings from brain slice preparations were analyzed using Pulsefit (HEKA) and Origin 5.0 (OriginLab) software.

Extracellular multi-unit activities were recorded from horizontal brain slices in a submerged slice recording chamber with glass pipettes (0.5–8 MΩ electrode resistance) and an AC-coupled amplifier (custom-made) using a low pass filter of 3 kHz. Extracellular solution was composed of (mM): NaCl, 124; KCl, 4; NaH₂PO₄, 1.24; MgSO₄, 0.2; NaHCO₃, 26; dextrose, 10; CaCl₂, 3.1. Stimuli of 1 ms duration were delivered every 13 s through a bipolar tungsten electrode placed into the internal capsule. Data were sampled at 5 kHz, digitized and recorded with AxoScope software (Axon Instruments). Analysis was done on segments starting from 1.5 s until 11.5 s after the stimulation. Data were binned (50 or 100 ms) and action potentials were detected using a threshold based algorithm. Autocorrelations were calculated from the binned action potential counts. The positive half of the autocorrelograms were fitted with a Gabor function of the form: $f(x) = Ae^{(-x/\tau)} \cos(x\pi/T)^6$, where T is the period, τ is the decay time constant, and A is the amplitude of the Gabor function. In some cases an additional term was added to allow better fitting of the central peak. The modified Gabor function had the form: $f(x) = Ae^{(-x/\tau)} \cos(x\pi/T)^6 + Be^{(-x/\tau_2)}$, where B and τ_2 are the amplitude and the decay time constant of the central peak, respectively (Konig, 1994; Ulrich and Huguenard, 1995).

EEG recordings were performed as described previously (Seidenbecher and Pape, 2001; Seidenbecher et al., 1998; Staak and Pape, 2001). Briefly, WAG/Rij rats (between 6 and 10 months) were anaesthetized with pentobarbital (40 mg/kg, Sigma Aldrich) and positioned in a stereotaxic instrument. Small holes (~1 mm diameter) were drilled into the skull to allow access to cortical and thalamic sites. For bilateral EEG recordings, four silver electrodes were positioned on the dura of frontal and parietal cortices. Body temperature was monitored and maintained at 37 °C. Pentobarbital effect was allowed to decline for 2 h and recordings were done under fentanyl-droperidol neurolept anaesthesia. After stable generation of SWDs, infusion cannulae were positioned in the VB (coordinates: bregma: -3.3 mm, lateral: 2.5 mm, dorso-ventral: 5.8 mm from dura), causing a decline in EEG amplitude. After recovery of the EEG, mibefradil (2 μl, 20 or 200 mM) was administered into the VB at a flow rate of 0.5 μl/min using a microdialysis pump (CMA Microdialysis). Data were band-pass filtered at 0.3–100 Hz, digitized and stored on a personal computer and on a magnetic tape recorder. Analysis was done using Spike2 software (Science Products).

If not stated otherwise, all results are presented as mean ± SEM. Statistical significance was tested using Student's *t*-test. Differences were considered statistically significant if $p < 0.05$.

2.3. Modelling

For computer simulations a single compartment TC neuron model (Huguenard and McCormick, 1992; McCormick and Huguenard, 1992) was adapted as described previously (Hines and Carnevale, 2001; Meuth et al., 2006). The model was based on the mathematical description of $I_{K \text{ leak}}$, $I_{Na \text{ leak}}$, I_L , I_T , $I_{Na \text{ HH}}$, I_{NaP} , $I_{K \text{ HH}}$, I_A , and I_{KCa} . The persistent sodium current (I_{NaP}) was described by the following equation: $I_{NaP} = g * m_{inf} * (V - E_{Na})$, where $m_{inf} = 1/(1 + \exp(-(V + 50)/5))$, g is the maximum conductance, V is the membrane potential and E_{Na} is the sodium reversal potential. The half maximal activation was 10 mV more negative than that of the Hodgkin Huxley type Na⁺ currents. Maximum I_{NaP} conductance was set to ~0.2% of $I_{Na \text{ HH}}$ conductance (Crill, 1996). Neuronal membrane potential was described by the following equation: $C_M(dV/dt) = -I_M + I_{inject}$. I_M is the sum of all membrane currents, I_{inject} is the injected current, and C_M is the membrane capacitance. The model was capable of generating action potentials in both burst and tonic transmission modes. All simulations were carried out at 35 °C. To test for the effects of a reduction of available T-, persistent sodium and Ca²⁺ activated K⁺

currents, the maximum permeabilities of these currents were decreased in steps of 10%. For I_T , this was done in a model containing all currents and in a model without the Hodgkin Huxley and persistent Na⁺ conductances. The time to the maximum of the first burst associated action potential was taken as a measure of the LTS onset latency. In the absence of action potentials the maximum amplitude of LTS voltage deflection was used instead.

3. Results

3.1. Block of T-type Ca²⁺ currents by ethosuximide

To analyze the blocking effect of ETX on I_T , visually identified acutely isolated (Pape et al., 1994) TC neurons of the LGN were held at a potential of -50 mV under whole cell voltage-clamp conditions. To de-inactivate and activate T-type Ca²⁺ currents, cells were hyperpolarized to -100 mV for 720 ms and depolarized to -40 mV for 260 ms, respectively (0.1 Hz repetition frequency; standard stimulation). The elicited depolarization-induced transient inward currents were typical for I_T in TC neurons (Fig. 1A, upper panel) (Hernandez-Cruz and Pape, 1989; Huguenard, 1996; Perez-Reyes, 2003). The test potential was near to the maximum of the T-current I/V for LGN TC and interneurons (data not shown). Extracellular application of ETX resulted in a time- and concentration-dependent decrease in I_T amplitude in TC neurons of WAG/Rij and ACI rats. The ETX induced T-current reduction was partially or completely reversible (Fig. 1B), with no differences between the cell types or rat strains. However, distinct differences were found regarding efficacy and potency of block. Pooled data from 49 WAG/Rij and 40 ACI TC neurons recorded at different ETX concentrations revealed dose-response curves with a significantly lower EC₅₀ value in WAG/Rij (EC₅₀ = 0.21 mM) in comparison to ACI (EC₅₀ = 3.05 mM; Fig. 1C, upper panel). The blocking effects of therapeutically used ETX concentrations (0.25–0.75 mM) were higher in WAG/Rij than in ACI rats. At a concentration of 0.25 mM ETX blocked 14 ± 2% ($n = 4$) and 8 ± 3% ($n = 15$) of I_T in WAG/Rij and ACI TC neurons, respectively. An increase in concentration to 0.75 mM resulted in an increased I_T blockade of 19 ± 2% ($n = 20$) and 10 ± 2% ($n = 21$) in WAG/Rij and ACI TC neurons, respectively ($p = 0.0233$). I_T blockade was incomplete at the highest concentration tested (20 mM) and was greater in ACI than in WAG/Rij TC neurons. Ten millimolar ETX led to a current reduction of 52 ± 5% ($n = 30$) in ACI and 30 ± 3% ($n = 19$) in WAG/Rij TC neurons ($p = 0.0095$).

To test for changes in drug efficacy in TC neurons under conditions roughly resembling SWDs, we used a stimulation protocol of 20 pulses delivered at a frequency of 5 Hz (130 ms hyperpolarization to -100 mV followed by 60 ms to -40 mV), which was repeated every 30 s. As has been observed previously (Meuth et al., 2002), repetitive stimulation non-significantly increased T-type Ca²⁺ current amplitude from the 1st to the 20th pulse in 14 of 18 WAG/Rij (10th pulse: 5.8 ± 1.7%; 20th pulse: 5.7 ± 2.2%) and 10 of 15 ACI (10th pulse: 5.3 ± 2.1%; 20th pulse: 6.3 ± 2.5%; all cells recorded were included in the mean) neurons (Figs. 2A,C).

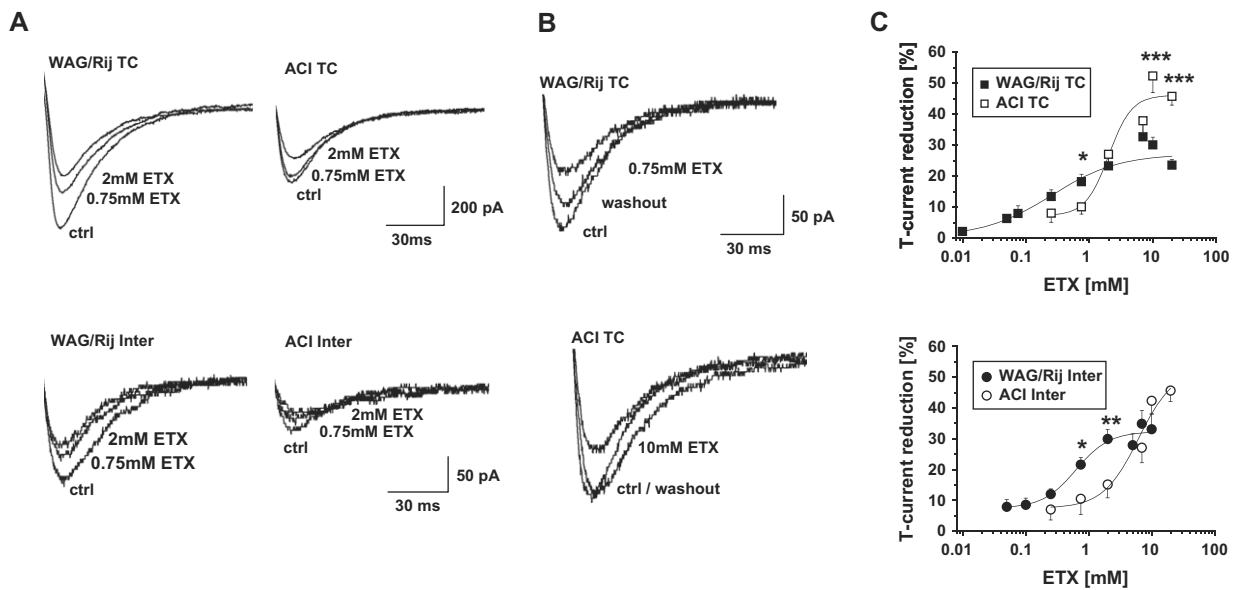


Fig. 1. Suppression of I_T by ETX in acutely isolated LGN TC neurons and interneurons of WAG/Rij and ACI. (A) Representative I_T traces of WAG/Rij and ACI TC neurons and interneurons, before (ctrl) and after application of the indicated ETX concentrations. Neurons were clamped to -100 mV for 720 ms before being stepped to -40 mV, with a repetition frequency of 0.1 Hz. (B) Examples of partial (upper panel) and complete (lower panel) reversibility of ethosuximide effects in representative recordings from a WAG/Rij TC (upper panel) and an ACI TC neuron (lower panel). Applied ETX concentrations are indicated. (C) Dose-response characteristics of ETX-induced reduction of I_T in TC neurons (upper panel) and interneurons (lower panel) of WAG/Rij and ACI rats. Solid line represents a Boltzmann fit to the data points. Dose-response curves are derived from pooled data obtained from 49 WAG/Rij TC, 40 ACI TC, 20 WAG/Rij interneurons, and 16 ACI interneurons. Differences in current blockade between the strains were significant for 0.75, 10, and 20 mM for TC neurons and for 0.75 and 2 mM in local circuit interneurons (see text). (* $p < 0.05$; ** $p < 0.01$; *** $p < 0.001$).

Maximal current facilitations in individual neurons were 17% in WAG/Rij and 21% in ACI.

The effect of 0.25 mM and 0.75 mM ETX was analyzed by comparing the 1st, the 10th, and the 20th pulse under control conditions to the corresponding pulse in the presence of the drug (Fig. 2B). The effect of 0.25 mM ethosuximide was not significantly different between ACI (I_T amplitude reduction: $15.8 \pm 5.6\%$, $19.4 \pm 4.3\%$, and $19.7 \pm 4.9\%$, $n = 12$) and WAG/Rij (I_T amplitude reduction: $13.9 \pm 3.3\%$, $16.9 \pm 3\%$, and $15.5 \pm 2.9\%$; $n = 17$). However the effect of 0.75 mM ETX was significantly (p values < 0.027) different between ACI (I_T amplitude reduction: $32.5 \pm 4.6\%$, $34 \pm 3.9\%$, and $34.2 \pm 5.3\%$, $n = 11$) and WAG/Rij (I_T amplitude reduction: $20.5 \pm 2.8\%$, $26.3 \pm 1.9\%$, and $22.8 \pm 1.5\%$, $n = 16$).

In addition to an increased overall effect, application of 0.25 mM ETX tended to decrease the T-type Ca^{2+} current facilitation for the 10th, and 20th pulse in ACI (I_T amplitude increase in 11 of 17 cells; 10th pulse: $2.3 \pm 2.9\%$; 20th pulse: $1.5 \pm 3.7\%$, all cells were included in the mean) and WAG/Rij (I_T amplitude increase in 6 of 12 cells; 10th pulse: $1.9 \pm 1.6\%$; 20th pulse: $3.1 \pm 2\%$; all cells were included in the mean, Fig. 2C). In the presence of 0.75 mM ethosuximide I_T amplitudes increased in ACI (I_T facilitation in 7 of 11 cells; 10th pulse: $2.3 \pm 2.4\%$; 20th pulse: $1.5 \pm 3\%$; all cells were included in the mean) and WAG/Rij (I_T facilitation in 9 of 16 cells; 20th pulse: $3.4 \pm 2.4\%$, all cells were included in the mean). Application of 0.75 mM ETX led to a decrease in I_T amplitude by $1 \pm 2\%$ for the 10th pulse.

The effects of 0.25 mM and 0.75 mM ETX were greater during 5 Hz stimulation than during low frequency stimulation

(analysis for the 10th and 20th pulse; ACI: 0.25 mM, $p < 0.046$; 0.75 mM $p < 0.00005$; WAG/Rij: 0.75 mM, $p < 0.02$; Fig. 2B).

Next, the effect of ETX on visually identified interneurons (Pape et al., 1994) was analyzed using standard stimulation protocols, as above (Fig. 1A, lower panel). The construction of dose-response curves from pooled data (ACI: $n = 16$; WAG/Rij: $n = 20$) revealed differences in EC_{50} values (ACI: 3.05 mM; WAG/Rij: 0.42 mM) and current reduction at 0.25 mM (ACI: $7 \pm 3\%$, $n = 6$; WAG: $12 \pm 2\%$, $n = 3$), 0.75 mM (ACI: $10 \pm 5\%$, $n = 6$; WAG: $21 \pm 2\%$, $n = 13$; $p = 0.037$), 2 mM (ACI: $15 \pm 4\%$, $n = 12$; WAG: $29 \pm 3\%$, $n = 15$; $p = 0.009$) and 10 mM (ACI: $42 \pm 4\%$, $n = 10$; WAG: $33 \pm 5\%$, $n = 8$; Fig. 1C, lower panel).

Overall, these results demonstrate similar effects of ETX on I_T of thalamic neurons of a given rat strain but differences in ETX effects between strains. Therapeutic ETX concentrations were more effective in WAG/Rij under low frequency stimulation (0.1 Hz), while higher concentrations were more effective in ACI. Five Hz stimulation increased ETX efficacy in both strains and resulted in a higher ETX effect in ACI compared to WAG/Rij.

3.2. Block of the persistent sodium current (I_{Nap}) by ethosuximide

In the following, the effects of ethosuximide on the persistent sodium current (I_{Nap}) were investigated in TC neurons of WAG/Rij and ACI rats. Neurons were held at -50 mV before being stepped to -90 mV for 1000 ms. From this potential

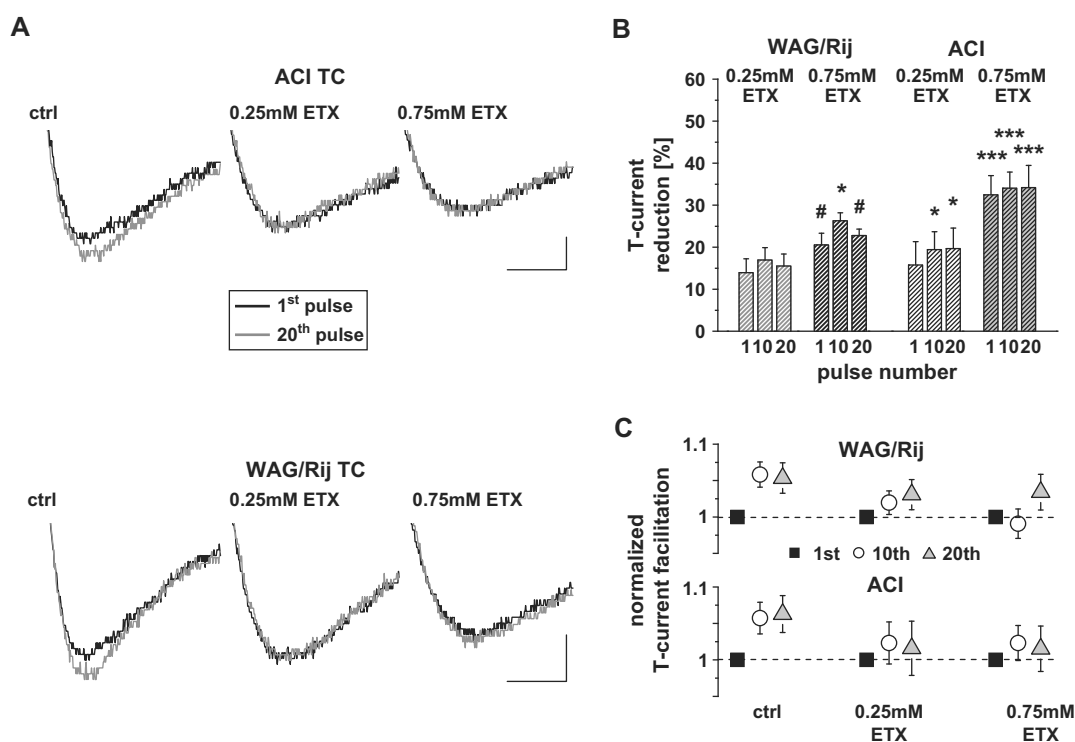


Fig. 2. Increased ethosuximide effect and I_T facilitation during 5 Hz stimulation. (A) Representative T-type Ca^{2+} currents recorded using a protocol that comprised of 20 pulses at a stimulation frequency of 5 Hz. Neurons were clamped to -100 mV for 130 ms before being clamped to -40 mV for 60 ms. The first and the 20th pulse are depicted in black and grey, respectively. An increase in I_T amplitude was observed from the first to the 20th stimulation under control conditions (1st and 20th pulses shown in the upper and lower left panels). During 5 Hz stimulation, application of therapeutically used ethosuximide concentrations (as indicated) induced a stronger block than observed during low frequency stimulation and diminished the facilitation of I_T . Scale represents 30 pA and 10 ms for the upper panel and 40 pA and 10 ms for the lower panel. (B) Quantification of the ETX induced I_T reduction during stimulation at a frequency of 5 Hz. The amplitude reductions of the 1st, 10th, and 20th pulses in the presence of the indicated ethosuximide concentrations are shown in relation to the amplitude of the corresponding current pulses under control conditions. Asterisks (*) indicate significant differences between the I_T reduction using low frequency stimulation and the I_T reduction using 5 Hz stimulation for the indicated ethosuximide concentrations. Hashes (#) indicate significant differences between the effect of ethosuximide between strains during 5 Hz stimulation. (C) Quantification of the I_T amplitude facilitation during stimulation with 20 pulses at a frequency of 5 Hz. Amplitudes of the 10th and 20th pulses are plotted after normalization to the amplitude of the 1st pulse. The T-type Ca^{2+} current facilitation was reduced after the application of the indicated ethosuximide concentrations. Graphs shown in (B) and (C) are derived from pooled data from recordings of 18 WAG/Rij TC and 15 ACI TC neurons. (*, # $p < 0.05$; ** $p < 0.01$; *** $p < 0.001$).

neurons were ramped to 0 mV in 1200 ms (0.075 mV/ms), eliciting TTX sensitive inward currents which were similar to I_{NaP} as described previously for TC neurons (Leresche et al., 1998; Parri and Crunelli, 1998). Application of 0.25 and 0.75 mM ETX resulted in measurable effects on the I_{NaP} amplitude only in 2 out of 10 neurons (WAG/Rij TC $n = 6$, ACI TC $n = 4$; data not shown), while a concentration of 10 mM ETX consistently induced a reversible reduction of I_{NaP} (shown for WAG/Rij in Fig. 3). On average, 10 mM ETX reduced the amplitude of I_{NaP} by $37 \pm 2\%$ and $24 \pm 1\%$ in WAG/Rij ($n = 3$) and ACI ($n = 3$) TC neurons, respectively (WAG/Rij TC vs. ACI TC, $p = 0.005$).

3.3. Block of I_T , HVA Ca^{2+} and Na^+ currents by mibefradil

Next, the effect of the I_T blocker mibefradil was analyzed using the standard stimulation protocol as above (-100 mV for 720 ms, -40 mV for 260 ms, 0.1 Hz repetition frequency). In both cell types from both rat strains, mibefradil completely blocked T-type Ca^{2+} currents at a concentration of $10 \mu\text{M}$ (Fig. 4). Pooled data revealed EC_{50} values of $0.07 \mu\text{M}$ (43

ACI TC neurons), $0.07 \mu\text{M}$ (28 WAG/Rij TC neurons), 0.08 (22 ACI interneurons), and $0.08 \mu\text{M}$ (14 WAG/Rij interneurons). Differences in current blockade were not significant.

To further investigate the blocking properties of mibefradil, high-voltage activated (HVA) Ca^{2+} currents (holding potential -40 mV, 50 ms depolarization to $+5$ mV) and fast transient Na^+ currents (holding potential -80 mV, 50 ms hyperpolarization to -120 mV, 50 ms depolarization to -30 mV) were analyzed in TC neurons (Fig. 5). At a concentration of $2 \mu\text{M}$, mibefradil blocked $95 \pm 3\%$ of T-type Ca^{2+} current ($n = 18$; Fig. 4A), $25 \pm 9\%$ of HVA Ca^{2+} current ($n = 6$; Fig. 5A), and $15 \pm 4\%$ of Na^+ current ($n = 5$; Fig. 5B) in ACI as well as 100% of T-type Ca^{2+} current ($n = 3$; Fig. 4A), $18 \pm 6\%$ HVA Ca^{2+} current ($n = 7$; Fig. 5A), and $28 \pm 9\%$ of Na^+ current ($n = 9$; Fig. 5B) in WAG/Rij. An increase of the mibefradil concentration to $20 \mu\text{M}$ induced stronger block of HVA Ca^{2+} current (ACI: $61 \pm 4\%$, $n = 7$; WAG/Rij: $62 \pm 5\%$, $n = 9$) and Na^+ current (ACI: 100% , $n = 6$; WAG/Rij: $94 \pm 4\%$, $n = 9$).

Taken together, these data characterize mibefradil as a potent blocker of T-type Ca^{2+} channels in thalamic neurons, which is about 10 times more efficient in blocking these channels than HVA Ca^{2+} or voltage gated Na^+ channels.

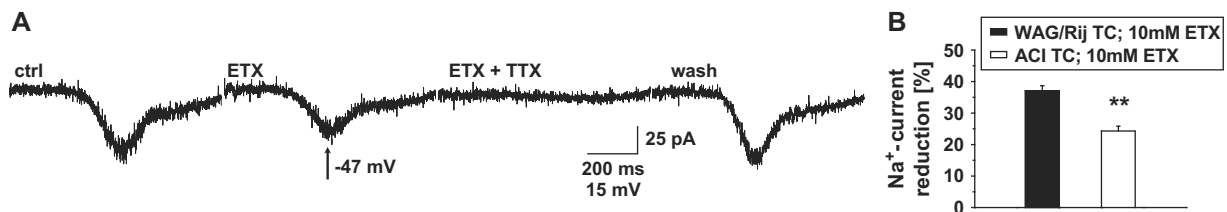


Fig. 3. Block of the persistent Na^+ current by ethosuximide. (A) Representative current traces evoked via current ramp stimulation (from -90 mV to 0 mV, 0.075 mV/ms) under control conditions (left panel), after application of 10 mM ethosuximide (2nd panel from the left), after wash in of 1 μM TTX and 10 mM ETX (3rd panel from the left), and after wash out of ETX and TTX (right panel). Depicted current traces derive from a WAG/Rij TC neuron. (B) Mean reduction of I_{NaP} by 10 mM ETX in WAG/Rij TC and ACI TC neurons (** $p < 0.01$).

3.4. Block of T-type Ca^{2+} and Na^+ currents by valproate

Since valproate is a first choice clinical absence-epilepsy medication, its effects on I_{T} and I_{Na} were analyzed using standard stimulation protocols as above. At a concentration of 1 mM, valproate reduced T-type Ca^{2+} currents in ACI and WAG/Rij TC neurons. A significant difference in drug effect was found for the I_{T} reduction between ACI TC ($20 \pm 3\%$, $n = 6$) and WAG/Rij TC neurons ($53 \pm 6\%$, $n = 8$; $p = 0.0008$; Fig. 6A). Voltage gated Na^+ currents were also affected by valproate. Application of 1 mM valproate led to a decrease of I_{Na} of $4 \pm 1\%$ ($n = 8$) and $9 \pm 3\%$ ($n = 11$) in ACI and WAG/Rij TC neurons, respectively (Fig. 6B).

In summary these data show a differential effect of valproate on T-type Ca^{2+} and voltage gated sodium currents of TC neurons of two different rat strains. Furthermore the results demonstrate that a first choice clinical absence-epilepsy medication effectively reduces T-type Ca^{2+} currents in these neurons.

3.5. Effect of ethosuximide on the low threshold Ca^{2+} spike and tonic action potential generation

To address the effect of ETX on the I_{T} -dependent LTS, TC neurons were analyzed through current clamp recordings in brain slice preparations in vitro. Resting membrane potentials and input resistances of ACI and WAG/Rij TC neurons were similar (data not shown). Using DC current injections, neurons were held at potentials around -60 mV. Via application of negative DC current pulses (-80 – -200 pA) cells were hyperpolarized to potentials around -100 mV for 800 ms to deactivate T-type Ca^{2+} currents. LTSs were elicited by depolarizing the neurons to approximately -60 mV from the hyperpolarized state (Fig. 7A, left panel). To approximate the effects of therapeutically used and saturating ETX concentrations we examined the influence of 1 mM and 10 mM ETX on the LTS. Application of 1 mM and 10 mM ETX resulted in a delay of the LTS onset in ACI TC (onset time under control conditions: 121.4 ± 11 ms, $n = 6$; ETX induced delay: 1 mM

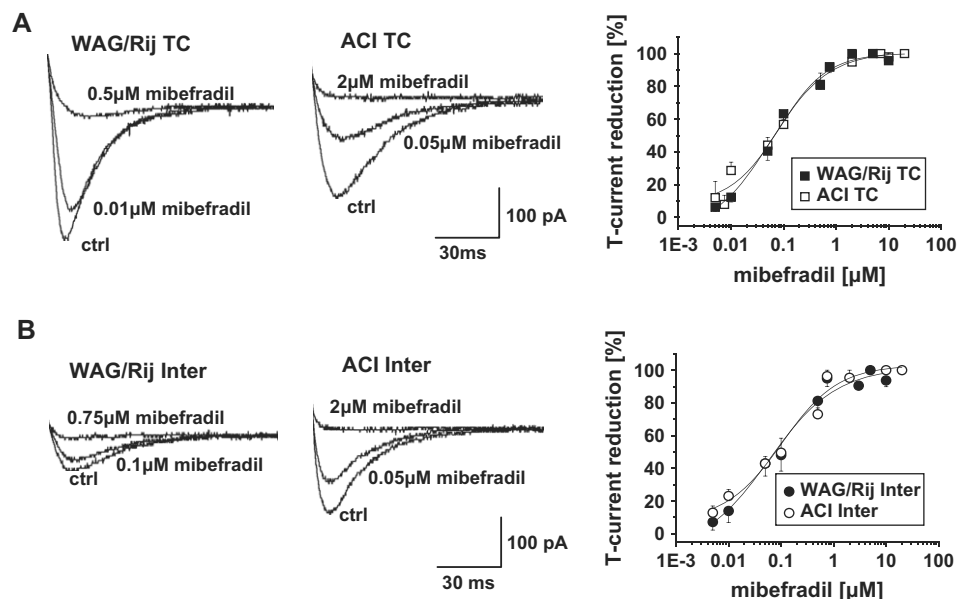


Fig. 4. Mibefradil induced I_{T} reduction in acutely isolated thalamic neurons. (A) I_{T} reduction in TC neurons of both strains. Representative current traces from WAG/Rij (left panel) and ACI (middle panel), before (ctrl) and after the application of the indicated mibefradil concentrations are shown. Right panel displays dose-response curves obtained through Boltzmann fits of pooled data from 28 WAG/Rij and 43 ACI TC neurons. (B) Mibefradil induced I_{T} reduction in interneurons. Conventions as in A. Right panel displays dose-response curves obtained through Boltzmann fits of pooled data from 14 WAG/Rij and 22 ACI interneurons.

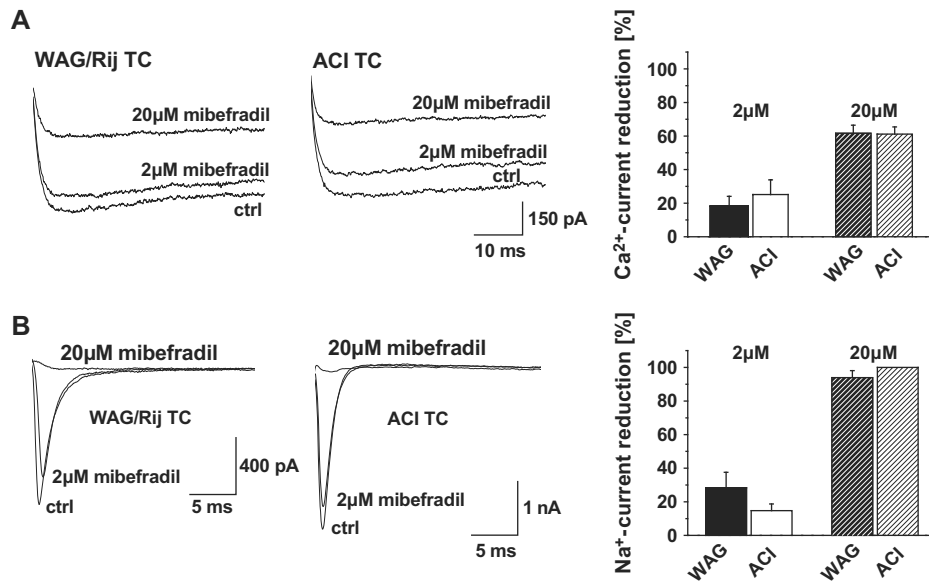


Fig. 5. Effect of mibefradil on I_{Na} and HVA Ca^{2+} currents. (A) Reduction of HVA Ca^{2+} currents after application of 2 and 20 μM mibefradil in WAG/Rij and ACI TC neurons. Representative current traces of HVA Ca^{2+} currents before (ctrl) and after the application of the indicated mibefradil concentrations in a WAG/Rij (left panel) and ACI (middle panel) are shown. Right panel displays mean current reduction obtained from 9 WAG/Rij and 7 ACI TC neurons. (B) Effect of 2 and 20 μM mibefradil on I_{Na} in WAG/Rij and ACI TC neurons. Representative current traces before (ctrl) and after the application of the indicated mibefradil concentrations in a WAG/Rij (left panel) and ACI (middle panel) TC neuron are shown. Right panel displays mean current reduction obtained from 10 WAG/Rij and 7 ACI TC neurons.

ETX: 26 ± 22 ms, $20 \pm 18\%$, $n = 5$; 10 mM ETX: 53 ± 20 ms, $42 \pm 16\%$, $n = 6$) and WAG/Rij TC neurons (onset time under control conditions: 103 ± 13 ms, $n = 7$; ETX induced delay: 1 mM ETX: 23 ± 19 ms, $20 \pm 18\%$, $n = 6$; 10 mM ETX: 52 ± 24 ms, $52 \pm 23\%$, $n = 6$; onset latencies were not significantly different between strains, $p = 0.32366$; Fig. 7A, left

panel). To obtain a further measure of T-type Ca^{2+} channel function, the voltage derivatives (dV/dt) of the LTS under control conditions and in the presence of ETX were calculated. As the slopes of action potentials generated by the LTS exceeded the slope of the LTS proper by more than an order of magnitude, the derivatives at -40 mV membrane potential were

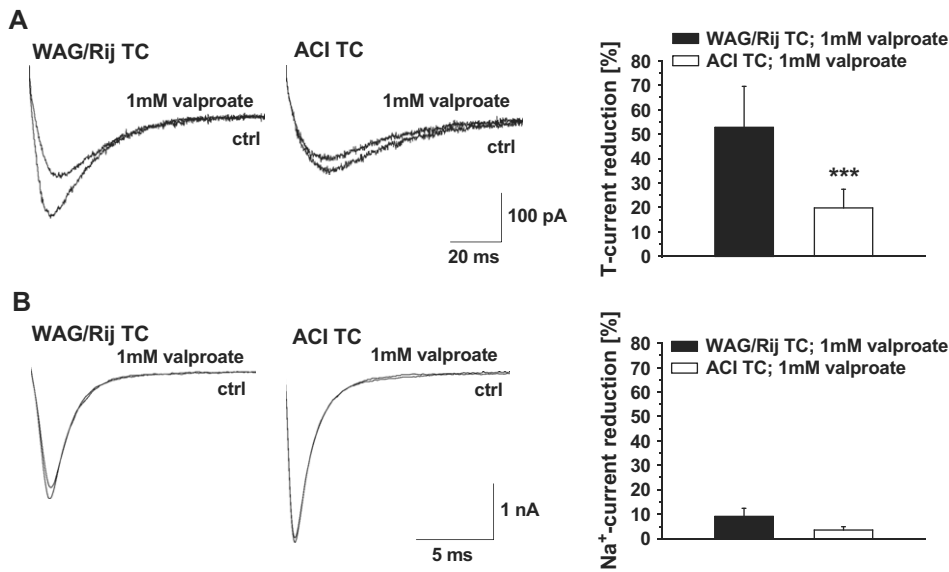


Fig. 6. Reduction of I_T and I_{Na} by 1 mM valproate. (A) Representative I_T traces in a WAG/Rij TC (left panel) and ACI TC (middle panel) neuron under control conditions (ctrl) and after application of 1 mM valproate. Neurons were clamped to -100 mV for 720 ms before being stepped to -40 mV at a frequency of 0.1 Hz. The right panel displays mean I_T reduction of recordings from 8 WAG/Rij TC and 6 ACI TC neurons. Valproate induced I_T reduction was significantly greater in WAG/Rij TC neurons when compared to current reduction in ACI TC neurons. (B) Representative I_{Na} traces in a WAG/Rij TC (left panel) and ACI TC (middle panel) neuron under control conditions (ctrl) and after application of 1 mM valproate. The right panel displays mean current reduction of recordings from 11 WAG/Rij TC and 8 ACI TC neurons (***) ($p < 0.001$).

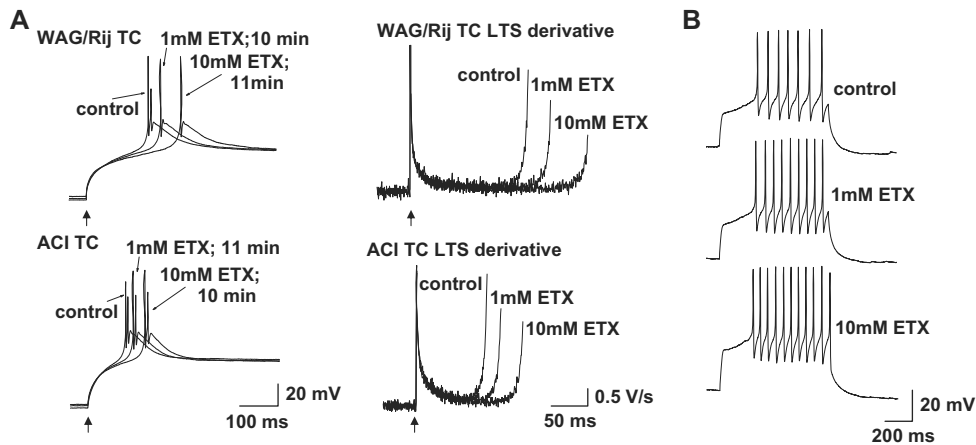


Fig. 7. Effect of 1 and 10 mM ethosuximide on the LTS and on tonic action potential generation. (A) Neurons were held at potentials around -60 mV via DC current injection. From this potential, neurons were hyperpolarized to about -100 mV for 800 ms to deactivate I_T , whereupon they were depolarized to the initial -60 mV. Application of ETX in 1 and 10 mM concentrations led to an increase in the LTS onset delay and to a reduction in LTS associated action potentials in WAG/Rij TC (upper left panel, $n = 7$) and ACI TC (lower left panel, $n = 6$) neurons (see text for details). To further quantify the effects of ethosuximide on the LTS, the derivatives (dV/dt) of the voltage traces were calculated (right panels). This was done until the membrane potential reached -40 mV, to avoid the confounding influence of the fast transient Na^+ current, see text. Black upward arrows mark the onset of the depolarizing stimulus in the voltage (left panels) and derivative (right panels) plots. Application of ethosuximide reduced the depolarization slopes at -40 mV membrane potential in WAG/Rij TC (right upper panel) and ACI TC neurons (lower right panel). (B) Effect of 1 and 10 mM ethosuximide on tonic action potentials. Neurons were held at about -60 mV and depolarized for 800 ms to generate a train of tonic action potentials. Recordings derived from a WAG/Rij rat are shown. ETX induced an increase in firing frequency, but left action potential half width and amplitude unchanged (WAG/Rij, $n = 4$; ACI, $n = 4$; see text for details).

analyzed. This was immediately prior to the onset of action potentials in our sample of neurons, and thus allowed the analysis of the depolarizing influence of I_T , while avoiding the confounding influence of the fast transient sodium current. Under control conditions, ACI TC neurons displayed derivatives of 3.1 ± 0.4 V/s ($n = 6$) at -40 mV, while in WAG/Rij TC neurons derivatives of 2.8 ± 0.5 V/s were found at -40 mV ($n = 6$; Fig. 7A, right panel). In ACI TC neurons application of 1 mM ETX led to a reduction of the derivatives at -40 mV to 2.4 ± 0.4 V/s ($74 \pm 4\%$ of control, $n = 5$), while a reduction to 2.1 ± 0.2 V/s ($79 \pm 7\%$ of control, $n = 6$) was observed in WAG/Rij TC neurons. An increase in ETX concentration to 10 mM induced a further decline in the derivatives at -40 mV to 2.1 ± 0.3 V/s ($68 \pm 6\%$ of control, $n = 6$) in ACI, while WAG/Rij TC neurons revealed derivatives of 1.9 ± 0.2 V/s ($71 \pm 5\%$ of control, $n = 6$). In about a third of the neurons the number of sodium-potassium action potentials riding the LTS was decreased after ETX application (2 of 6 ACI TC, control: 2.3 ± 0.5 APs, $n = 6$, 1 mM ETX: $78.5 \pm 20\%$ of control, $n = 6$, 10 mM ETX: $72.7 \pm 30\%$ of control, $n = 5$; 3 of 6 WAG/Rij TC, control: 2.0 ± 0.4 , $n = 6$ APs, 1 mM ETX: $80 \pm 20\%$ of control, $n = 6$, 10 mM ETX: $76.5 \pm 23\%$ of control, $n = 6$; some neurons of both strains generated only one LTS associated AP).

The effect of ETX on tonic action potentials was analyzed through application of depolarizing DC current pulses (between 50 and 150 pA; control frequencies ranged from 20 to 60 Hz) from holding potentials around -60 mV in TC neurons (Fig. 7B). ETX tended to increase action potential frequency (ACI TC, 1 mM ETX: $107 \pm 9\%$, $n = 3$; 10 mM ETX: $121 \pm 7\%$, $n = 4$; WAG/Rij, 1 mM ETX: $108 \pm 5\%$, $n = 4$; 10 mM ETX: $116 \pm 4\%$, $n = 3$), but left action potential half width and amplitude unchanged (half width: ACI control:

2.8 ± 0.2 ms, $n = 5$; 1 mM ETX: 2.7 ± 0.2 ms, $n = 3$; 10 mM ETX: 2.7 ± 0.3 ms, $n = 4$; WAG/Rij control: 2.8 ± 0.5 ms, $n = 4$; 1 mM ETX: 2.8 ± 0.4 ms, $n = 4$; 10 mM ETX: 2.7 ± 0.4 ms, $n = 4$; amplitude: ACI control: 48.5 ± 2 mV, $n = 5$; 1 mM ETX: 47.4 mV, $n = 3$; 10 mM ETX: 47 ± 2 mV, $n = 4$; WAG/Rij control: 52 ± 2 mV, $n = 4$; 1 mM ETX: 51 ± 1 mV, $n = 4$; 10 mM ETX: 50 ± 2 mV, $n = 4$).

Taken together, these results reveal that ETX delays the onset of the LTS, decreases the depolarization slope, reduces the number of LTS associated action potentials, and increases the frequency of tonic action potentials. Furthermore, the differences in ETX induced I_T blockade between WAG/Rij and ACI TC neurons did not translate into differences in LTS alteration.

3.6. Effect of mibefradil on the LTS and tonic action potential generation

In order to analyze mibefradil-induced changes of the LTS, current clamp experiments were conducted in TC neurons, as described above. The effects of 2 and 20 μ M mibefradil were examined. Application of 2 μ M mibefradil removed all LTS associated action potentials, reduced the LTS amplitude, delayed the onset of the LTS, and decreased the depolarization slope of the LTS (ACI TC, onset time under control conditions: 141 ± 12 ms, $n = 4$; 2 μ M mibefradil: 174 ± 38 ms, $123 \pm 27\%$ of control, $n = 4$; derivative at -40 mV under control conditions: 1.8 ± 0.3 V/s, $n = 4$; 2 μ M mibefradil (at LTS maximum): 0.15 ± 0.1 V/s, $n = 4$; Fig. 8A). The effect of 2 μ M mibefradil on tonic action potential generation was assessed by application of depolarizing DC current pulses (between 50 and 150 pA; control frequencies ranged from 15 to 25 Hz) from holding potentials around -60 mV. Two μ M

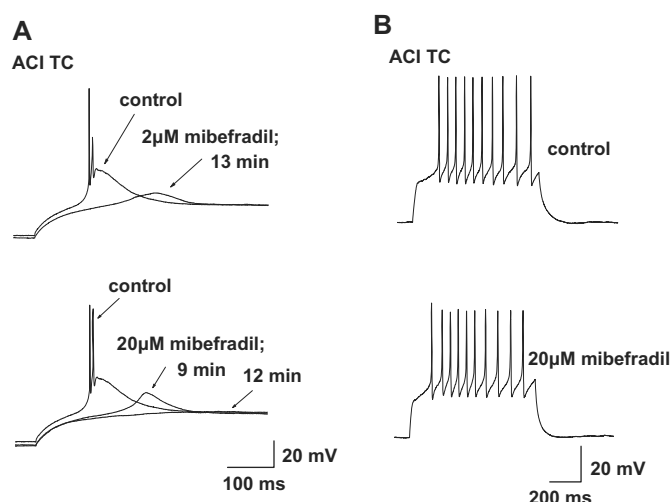


Fig. 8. Effect of mibefradil on the LTS and tonic action potential generation. (A) Application of 2 μM mibefradil led to the disappearance of all LTS associated action potentials and a reduction of the LTS amplitude, while application of 20 μM mibefradil resulted in a complete removal of the LTS in all neurons tested (WAG/Rij, $n = 5$; ACI, $n = 4$). (B) Effect of 20 μM mibefradil on tonic action potential generation (WAG/Rij, $n = 5$; ACI, $n = 4$; see text for details). Displayed recordings derive from an ACI rat.

mibefradil left tonic action potential frequency unchanged (ACI TC, 2 μM mibefradil: $99.5 \pm 5\%$ of control, $n = 4$), tended to decrease action potential amplitude (ACI TC control: 53.3 ± 1 mV, $n = 4$; 2 μM mibefradil: 49 ± 4 mV, $n = 4$), and did not affect action potential half width (ACI TC control: 3.7 ± 0.2 ms, $n = 4$; 2 μM mibefradil: 3.7 ± 0.2 ms, $n = 4$).

Application of 20 μM mibefradil completely removed the LTS and all associated action potentials in all tested neurons (ACI TC, $n = 4$; WAG/Rij TC, $n = 5$; Fig. 8A). Twenty μM mibefradil tended to reduce tonic action potential frequency (protocol as described above; 20–30 Hz under control conditions; ACI TC, 20 μM mibefradil: $89 \pm 6\%$ of control, $n = 4$; WAG/Rij TC, 20 μM mibefradil: $86 \pm 8\%$ of control, $n = 5$), slightly reduce action potential amplitude in ACI TC (ctrl: 52 ± 1 mV, $n = 4$; 20 μM mibefradil: 49 ± 4 mV, $n = 4$) and WAG/Rij TC neurons (ctrl: 46 ± 1 mV, $n = 5$; 20 μM mibefradil: 45 ± 4 mV, $n = 5$), while slightly increasing action potential half width in ACI TC (ctrl: 3.3 ± 0.3 ms, $n = 4$; 20 μM mibefradil: 3.6 ± 0.5 ms, $n = 4$) and WAG/Rij TC neurons (ctrl: 4.2 ± 0.5 ms, $n = 5$; 20 μM mibefradil: 4.4 ± 0.4 ms, $n = 5$; Fig. 8B).

These results show that 2 μM mibefradil severely inhibit LTS generation, while 20 μM completely block the LTS. Both mibefradil concentrations did not impair tonic action potential generation. No differences in mibefradil effects were observed between WAG/Rij and ACI.

3.7. Effect of I_T , I_{NaP} and I_{KCa} reduction on the LTS of a simulated neuron

The LTS generated by TC neurons is thought to arise from a complex interplay of I_T , the persistent sodium current (I_{NaP}),

the Ca^{2+} activated potassium current (I_{KCa}), the hyperpolarization activated cation current (I_h), and the transient potassium current I_A . Of these, ethosuximide has been reported to reduce I_T (Coulter et al., 1989a; Huguenard and Prince, 1994), I_{NaP} and I_{KCa} (Leresche et al., 1998). To identify the influence of an isolated reduction of each of these currents on the LTS and to relate this to the effect of ethosuximide on I_T and the LTS in native neurons, a TC neuron model was used (Hines and Carnevale, 2001). To analyze the effect of the different current components on the LTS, the model cell was hyperpolarized to -100 mV for 800 ms, and afterwards depolarized to -70 mV, whereupon a LTS was generated (Fig. 9A, upper panel). To assess the influence of an isolated reduction of I_T on the LTS, the maximal conductance of this current was reduced in steps of 10%. This led to an increase in LTS onset latency, a reduction of the depolarization slope (measured at -57 mV, just prior to AP onset in the model cell), and a reduction of the LTS associated action potentials, depending on the magnitude of I_T reduction (Table 1). A reduction of I_T conductance to 70% of control led to an increase of the LTS onset time by 15%, a decrease of the depolarization slope by 28%, and a reduction of the LTS associated action potentials from 4 to 3. A stronger reduction of the I_T conductance to 30% of control removed all LTS associated action potentials concomitant with a strong reduction of the LTS amplitude. A further decrease of I_T conductance led to the complete disappearance of the LTS. The effects of a reduction of the T-type Ca^{2+} current on the LTS was also investigated in a model without the fast transient sodium current ($I_{\text{Na HH}}$), to remove action potentials obscuring the shape of the LTS (Fig. 9A, lower panel). Removal of $I_{\text{Na HH}}$ had no substantial effect on the LTS alteration induced by T-current reduction. A complete list of the effects of the different current reductions on the LTS is given in Table 1.

Isolated reduction of the persistent sodium conductance in steps of 10% led to an increase in LTS onset latency, a decrease in depolarization slope, and a reduction of the LTS associated action potentials, depending on the magnitude of I_{NaP} reduction (Table 1). The effects of I_{NaP} reductions were smaller than those of a reduction of I_T , culminating in the reduction of LTS associated action potentials from 4 to 3, an increase in LTS onset latency of 8%, and a decrease in depolarization slope by 20% after the complete removal of the persistent sodium current.

Decrease of the maximum I_{KCa} conductance led to an increase in LTS associated action potentials, a reduction of LTS onset latency, and an increase in depolarization slope (at -57 mV; Table 1). Combined reduction of I_T to 80%, I_{NaP} to 40%, and of I_{KCa} to 80% of control led to a decrease in LTS associated action potentials from 4 to 3, an increase in LTS onset latency of 14%, and a decrease in depolarization slope by 31% (magnitude of I_{NaP} and I_{KCa} reductions were adopted from Leresche et al., 1998; Fig. 9B, Table 1). Further reduction of I_T (70% I_T , 40% I_{NaP} , 80% I_{KCa}) led to a reduction of LTS associated action potentials from 4 to 2, an increase in LTS onset latency of 22%, and a decrease of the depolarization slope at -57 mV of 41% (Table 1).

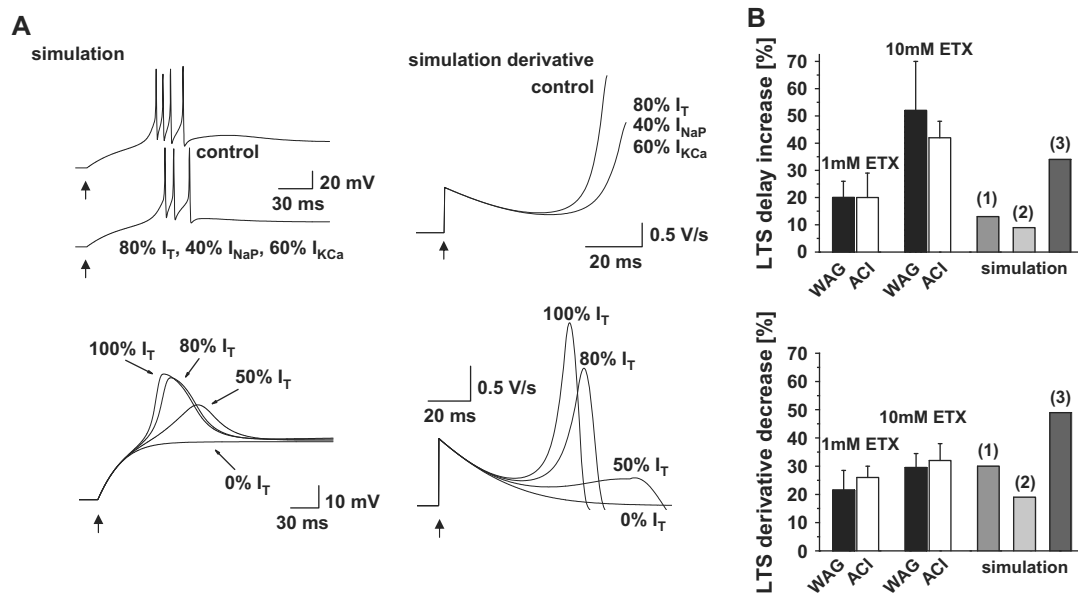


Fig. 9. (A) The effect of a reduction of I_T , I_{NaP} and I_{KCa} (to 80%, 40%, 60%, respectively) on LTS generation in a simulated neuron (upper panel). The model cell was hyperpolarized to -100 mV for 800 ms whereupon it was depolarized to -70 mV. As action potentials obscure the shape of the LTS, I_T was reduced in a model lacking voltage gated sodium currents (lower panel). Voltage traces for 100, 80, 50 and 0% availability of I_T are depicted. Refer to Table 1 for numerical analysis. The depolarization slopes (dV/dt) of the model cell were assessed as well (right panels). For the model including the fast transient sodium current, the derivatives were calculated until the membrane potential reached -57 mV, to avoid the influence of sodium-potassium action potentials (upper right panel), see text. In case of the model lacking fast transient sodium currents, the entire derivative of the LTS relates to the depolarizing influence of I_T (lower right panel). A combined reduction of I_T , I_{NaP} and I_{KCa} , as well as a sole reduction of I_T in the model lacking the fast transient Na^+ current led to a decrease of the depolarization slope, see Table 1 for quantification. Black arrows mark the onset of the depolarizing stimulation. (B) Quantification of the effects of ETX application on the LTS of WAG/Rij and ACI TC neurons and of current reductions on the LTS of a simulated neuron. The upper panel depicts a comparison of the LTS delay increase between WAG/Rij, ACI and modeled neurons. In both WAG/Rij and ACI TC neurons LTS onset delay increased by $\sim 20\%$ after the application of 1 mM ETX, while application of 10 mM resulted in an increase in LTS delay of 40% in ACI and 50% in WAG/Rij. For comparison, the delay increase after I_T , I_{NaP} and I_{KCa} reduction (to 80%, 40%, 60% of control, respectively), indicated by (1), as well as sole reduction of I_T to 80%, indicated by (2), and 50%, indicated by (3), in the model neuron are shown. I_T , I_{NaP} and I_{KCa} reduction (to 80%, 40%, 60% of control, respectively), caused a delay increase of 13%, while sole I_T reduction to 80% of control delayed the LTS by 9% and an I_T reduction of 50% caused a delay of 34%. The lower panel displays a comparison of the LTS derivative decrease between WAG/Rij, ACI and modeled neurons, same conventions as in the upper panel. In WAG/Rij and ACI 1 mM ETX reduced the depolarization slope by about 20%, while an increase in ETX concentration led to a further decrease to about 30%. In the model neuron the combined reduction of I_T , I_{NaP} and I_{KCa} led to a similar decrease of the depolarization slope by about 30%. A sole reduction of I_T in the model without the fast transient Na^+ current induced a depolarization slope decrease by 20% for an I_T reduction to 80% of control and by about 50% when I_T was reduced to 50% of control.

This data demonstrates that a sole reduction of I_T can replicate all major aspects of LTS alterations observed after application of ETX and mibefradil. However, this degree of reduction is not induced by therapeutically relevant ETX concentrations. The combined reduction of I_T , I_{NaP} and I_{KCa} resulted in an LTS alteration resembling those observed experimentally.

3.8. Effect of mibefradil on intrathalamic oscillations

To address the effect of mibefradil on evoked thalamic oscillations, extracellular multi-unit activity was recorded in the ventrobasal complex (VB) after stimulation of corticothalamic fibers running through the internal capsule (stimulation frequency 0.08 Hz). The VB rather than LGN was chosen for these experiments, in view of the more reliable appearance of evoked rhythmic burst discharges and SWDs (see below) under the present experimental conditions. Under control conditions, rhythmic burst activity (as identified by intra burst AP frequencies of >100 Hz) was observed in the VB of ACI and WAG/Rij rats. Application of 2 μ M mibefradil attenuated the oscillation (Fig. 10A), while application of 20 μ M led to the complete

cessation of rhythmic burst activity in the VB (data not shown). Effects of mibefradil were visible after ~ 15 – 20 min. Analysis was performed on recordings made after 20–25 min of wash in. Two μ M mibefradil reduced the number of action potentials during the oscillation to $61 \pm 2\%$ of control in ACI ($n = 3$, $p = 0.023$) and to $50 \pm 2\%$ of control in WAG/Rij rats ($n = 5$, $p = 0.043$). To further quantify the substance effect on rhythmicity and synchronicity of VB bursting, autocorrelograms were constructed, normalized and fitted with a Gabor function, (Fig. 10B; Konig, 1994; Ulrich and Huguenard, 1995). The amplitude, period, and decay time constant of the Gabor function relate to unit activity synchronicity, frequency and duration of burst activity, respectively. Under control conditions, Gabor fits had a period of 0.59 ± 0.03 s (1.7 Hz, $n = 6$) in ACI and 0.57 ± 0.03 s (1.8 Hz, $n = 5$) in WAG/Rij. Two μ M mibefradil tended to increase the period to $105 \pm 0.5\%$ of control in ACI ($n = 3$) and to $107 \pm 5\%$ of control in WAG/Rij ($n = 5$). Mean Gabor fit amplitudes under control conditions were 0.5 ± 0.08 in ACI ($n = 6$) and 0.7 ± 0.05 in WAG/Rij ($n = 5$). Application of 2 μ M mibefradil decreased Gabor fit amplitudes to $78 \pm 11\%$ of control in ACI ($n = 3$) and to $85 \pm 3\%$ of control

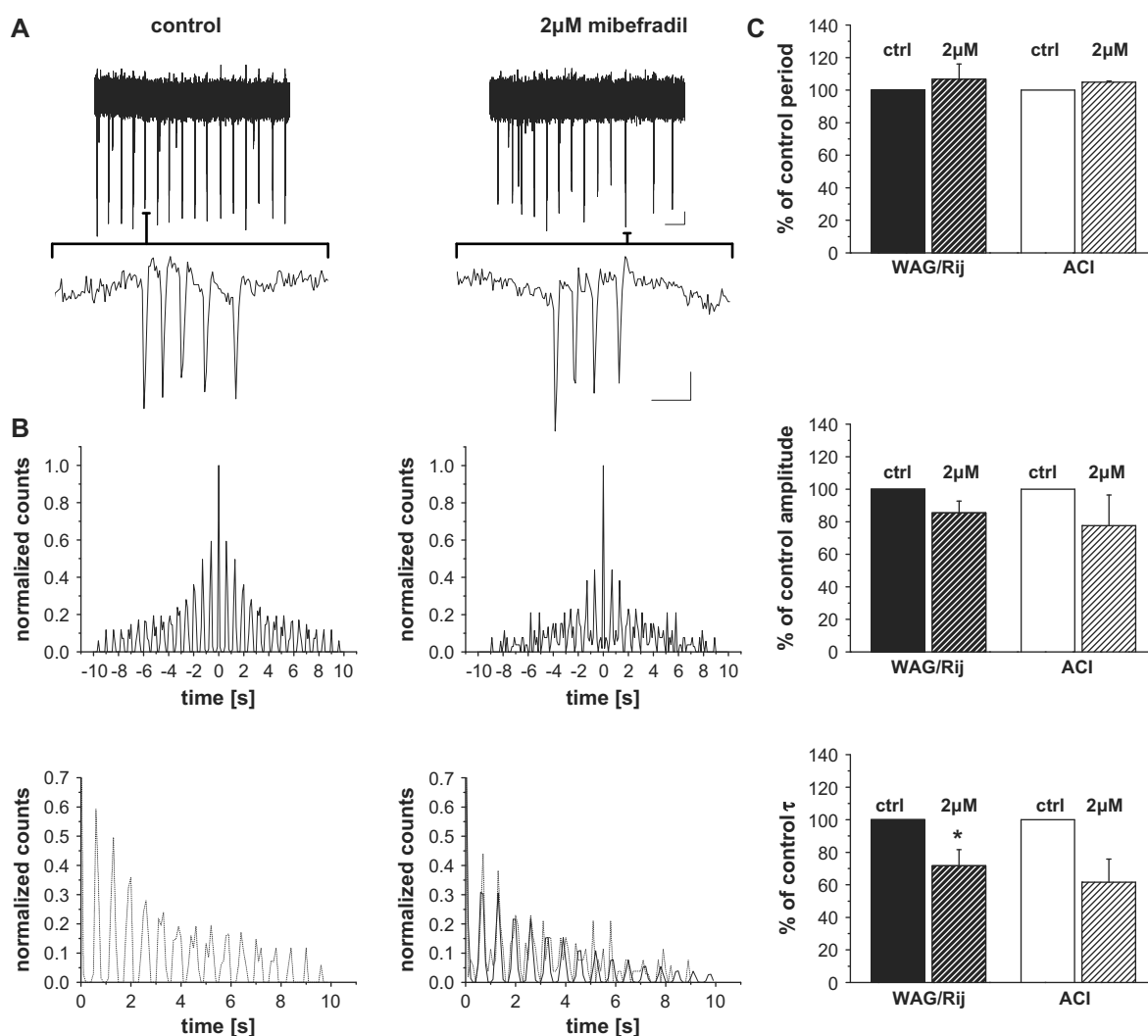


Fig. 10. Attenuation of intrathalamic oscillation through mibefradil. (A) Examples of rhythmic burst activity recorded in the VB under control conditions (upper left panel) and after application of 2 μ M mibefradil (upper right panel). Depicted traces derive from a WAG/Rij rat and were recorded from 1.5 s until 11.5 s after the stimulus. Scale bar represents 1 s and 25 μ V. Enlarged traces (lower two panels) reveal intra burst AP frequencies of \sim 400 Hz in this example. Scale bar represents 5 ms and 50 μ V. (B) Autocorrelograms (upper panels) with the positive half fitted with a modified Gabor function are shown in the lower panels. Autocorrelograms and fits were calculated from the recordings shown in A. The depicted Gabor functions had a period of 0.64 s and 0.65 s under control conditions and in the presence of 2 μ M mibefradil, respectively. The Gabor function's amplitude was 0.57 under control conditions and 0.43 in 2 μ M mibefradil. The decay time constant under control conditions was 4.83 s and 3.75 s in the presence of 2 μ M mibefradil. (C) Summarized effects of 2 μ M mibefradil on Gabor fits of VB burst activity in WAG/Rij (black, $n = 5$) and ACI rats (white, $n = 3$). ($*p < 0.05$).

in WAG/Rij ($n = 5$). Mean Gabor fit decay time constants were 4.37 ± 0.7 s in ACI ($n = 6$) and 3.88 ± 0.3 s in WAG/Rij ($n = 5$). Two μ M mibefradil decreased the decay time constants to $61 \pm 14\%$ of control in ACI ($n = 3$) and to $71 \pm 10\%$ of control in WAG/Rij ($n = 5$, $p = 0.02$).

These experiments show that application of 2 μ M mibefradil reduces evoked, rhythmic burst activity in the VB. An increase of mibefradil concentration to 20 μ M, which completely removed the LTS in neurons recorded in slice preparations, led to a breakdown of rhythmic burst activity.

3.9. Effect of mibefradil on SWDs

To investigate the effect of mibefradil on SWDs, EEG recordings were performed on anesthetized WAG/Rij rats

(Fig. 11). All animals developed bilaterally synchronized SWDs, which started and ended abruptly on a normal background EEG. After development of SWDs, infusion cannulae were inserted into the VB of both hemispheres. The EEG was allowed to recover, and 2 μ l 20 mM or 200 mM mibefradil were injected into the VB at a flow rate of 0.5 μ l/min. Low volumes of high mibefradil concentrations were administered to avoid unspecific volume effects and still affect a large enough area to induce measurable effects on the EEG. Mibefradil application was commenced with a small temporal delay in the two hemispheres (Fig. 11B). In order to avoid the confounding influence of inter-hemispheric interaction, the analysis was restricted to the hemisphere mibefradil was first injected into. The number of SWDs was quantified in 2 min bins using a threshold based algorithm. Application of 2 μ l 20 mM

Table 1
Effect of I_T , I_{NaP} and I_{KCa} reductions on LTS onset time, LTS derivative, and on the number of LTS associated action potentials of a model neuron

	# AP	Delay 1st AP [ms]	Delay increase [%]	Derivative at -57 mV [V/s]	Derivative decrease [%]		
I_T	100%	4	61.3	//	3.33	//	
	90%	4	63.7	4	3.02	8	
	80%	3	66.6	9	2.71	19	
	70%	3	70.2	15	2.4	28	
	60%	2	75.1	23	2.06	38	
	50%	2	82.2	34	1.7	49	
	40%	1	94.8	55	1.25	62	
	30%	0	//	//	//	//	
	20%	0	//	//	//	//	
	10%	0	//	//	//	//	
I_{NaP}	100%	4	61.3	//	3.33	//	
	90%	4	61.7	1	3.27	2	
	80%	4	62.2	2	3.2	4	
	70%	4	62.6	2	3.12	6	
	60%	4	63.1	3	3.05	8	
	50%	4	63.6	4	2.98	10	
	40%	3	64.1	5	2.91	12	
	30%	3	64.6	5	2.84	14	
	20%	3	65.1	6	2.79	16	
	10%	3	65.6	7	2.71	19	
I_{KCa}	100%	4	61.3	//	3.33	//	
	90%	5	61.1	-0.4	3.34	-0.6	
	80%	5	60.9	-0.7	3.36	-0.8	
	70%	5	60.7	-1	3.37	-1.2	
	60%	5	60.4	-1.5	3.38	-1.6	
	50%	5	60.2	-1.8	3.39	-1.8	
	40%	5	60	-2.1	3.4	-2.1	
	30%	6	59.8	-2.5	3.41	-2.5	
	20%	6	59.6	-2.8	3.42	-2.8	
	10%	7	59.4	-3.1	3.43	-2.9	
I_T	80%	4	61.3	//	3.33	//	
	I_{NaP}	40%	3	69.9	14	2.31	31
	I_{KCa}	80%	4	61.3	//	3.33	//
	I_T	70%	4	62.6	2	3.12	6
	I_{NaP}	40%	2	74.5	22	1.98	41
	I_{KCa}	80%	4	61.3	//	3.33	//
	I_T	80%	4	61.3	//	3.33	//
	I_{NaP}	40%	3	69.2	13	2.34	30
	I_{KCa}	60%	5	60.4	-1.5	3.38	-1.6

mibefradil transiently attenuated the number of SWDs (number of SWDs 2 min prior to mibefradil application: 148.3 ± 25.4 SWDs; start to 2 min after application: 238 ± 124.5 SWDs; 3–4 min after application: 119.3 ± 37.8 ; 5–6 min after application: 49.7 ± 13.9 SWDs; 7–8 min after application: 77 ± 14.6 SWDs; 9–10 min after application: 82.3 ± 26.8 SWDs; 11–12 min after application: 55 ± 29.6 SWDs; 13–14 min after application: 72 ± 31.9 SWDs; 15–16 min after application: 115 ± 5.9 SWDs; $n = 3$, Fig. 12A). Injection of 2 μ l 200 mM mibefradil into the VB led to the complete disappearance of SWDs after 12–14 min in all animals tested (number of

SWDs 2 min prior to mibefradil application: 314 ± 73.1 SWDs; start to 2 min after application: 275 ± 24.5 SWDs; 3–4 min after application: 232.3 ± 68.6 SWDs; 5–6 min after application: 175.7 ± 77.2 ; 7–8 min after application: 139 ± 68.9 SWDs; 9–10 min after application: 100.3 ± 43.5 SWDs; 11–12 min after application: 49.3 ± 21.9 SWDs; 13–14 min after application: 10.3 ± 8.9 SWDs; 15–16 min after application: 2.3 ± 2.3 SWDs; $n = 3$; Figs. 11 and 12B number of baseline SWDs prior to mibefradil application were not significantly different between the 20 and 200 mM groups). In two of the 6 in vivo experiments, injection of mibefradil initially increased SWD generation (animals 2 and 6, Fig. 12), before the SWD incidence declined. To control for possible volume effects of substance application 2 μ l physiological saline were injected under identical conditions. No significant alterations of SWD generation were observed ($n = 2$; data not shown).

These experiments demonstrate that application of mibefradil into the ventrobasal thalamus disrupts spike and wave oscillations recorded in the surface EEG of WAG/Rij rats.

4. Discussion

The present study provides a systematic analysis of the effects of a specific T-type Ca^{2+} channel antagonist, as well as absence epilepsy medications on I_T (ETX, valproate, mibefradil), the LTS (ETX, mibefradil), intrathalamic oscillations (mibefradil), and SWDs (mibefradil). All substances blocked I_T in thalamic neurons. While therapeutically relevant concentrations of ETX induced a stronger I_T block in WAG/Rij, higher concentrations were more effective in ACI. An increase in stimulation frequency (from 0.1 to 5 Hz) enhanced the effect of therapeutically relevant ETX concentrations in both strains, indicating a use-dependent component of ETX action. This effect was stronger in ACI than in WAG/Rij. Application of ETX led to a delay in LTS onset, a decrease in LTS depolarization slope, and a reduction of the LTS associated action potentials. No differences in LTS alteration were observed between the strains. Computational modeling demonstrated that the complete effect of ETX can be replicated by a sole reduction of I_T . However, the necessary degree of I_T reduction was not induced by therapeutically relevant ETX concentrations. A combined reduction of I_T , I_{NaP} and I_{KCa} resulted in an LTS alteration resembling the experimental observations. The I_T antagonist mibefradil inhibited intrathalamic oscillations as well as SWDs. In summary this study supports the hypothesis that I_T reduction is part of the mechanism of action of clinically used anti-absence drugs.

4.1. Possible solution to a current controversy

Unlike the ETX effect on isolated I_T , previous studies agree upon an increase in LTS onset latency and a reduction of LTS associated action potentials as results of drug application (Huguenard and Prince, 1994; Leresche et al., 1998), a finding which is confirmed by the results of the present study. Furthermore, an ETX effect on tonic firing, described by Leresche et al. (1998), was replicated in this study. Possible mechanisms

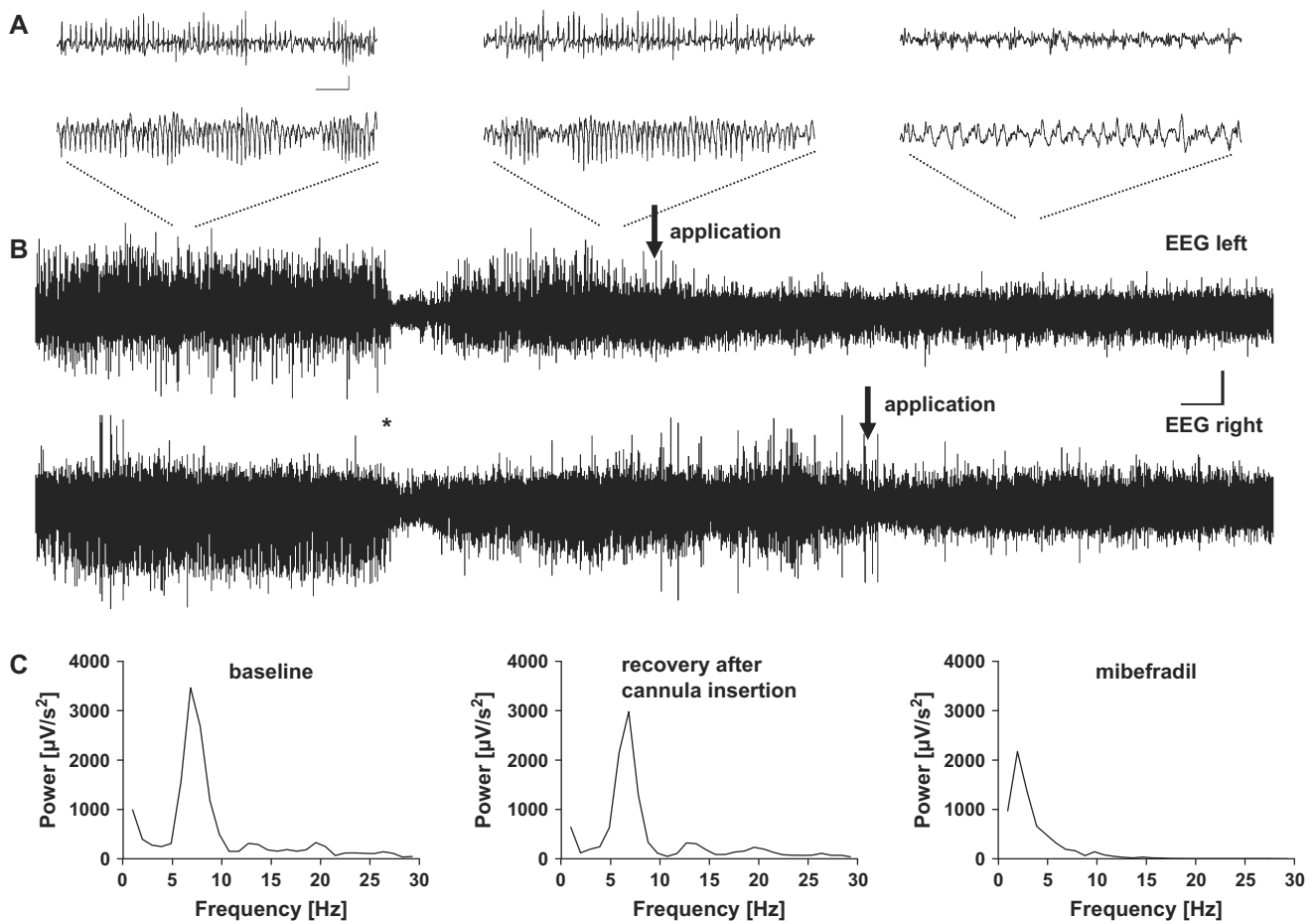


Fig. 11. Effect of mibefradil on SWDs in an anaesthetized WAG/Rij rat. (A) Surface EEG traces prior to cannulae insertion (left panel), after cannulae insertion (middle panel), and after application of 2 µl 200 mM mibefradil into the VB (right panel). Scale bar represents 200 µV and 1 s. Application of 2 µl 200 mM mibefradil led to the complete disappearance of SWDs. (B) An overview of the entire experiment shown in A. Positions of the enlarged traces shown in A are indicated by dotted lines. Insertion of the infusion cannulae, indicated by an asterisk, led to a transient suppression of EEG amplitude. Mibefradil effects were clearly visible ~1 min after application, which is indicated by arrows. Scale bar represents 200 µV and 1 min. (C) Fast Fourier transformations of the EEG traces shown in A. Prior to mibefradil application the EEG was dominated by SWDs with frequencies around 7 Hz (left and middle panels). Application of mibefradil suppressed SWDs and shifted the dominant frequency from 7 to 2 Hz (right panel).

underlying these discrepancies have been discussed extensively elsewhere (Crunelli and Leresche, 2002a; Huguenard, 2002). Although we can not provide an ultimate explanation for the differing results obtained by different groups, the present study points to a possible solution to the current controversy: (i) combined effects of ETX on several membrane currents (I_T , I_{NaP} , I_{KCa}) may account for the full anti-absence action of therapeutically relevant ETX concentrations. (ii) The inhibition of I_T in several cell types, especially those important for network synchronization, have to be considered. (iii) The dependency of ETX action on membrane potential and stimulation frequency may enhance I_T inhibition.

4.2. Effects of ETX

The experiments using acutely isolated thalamic neurons extend the original results of Coulter et al. (1989a,b, 1990) by demonstrating a differential ETX effect on I_T of different rat strains and an increase in drug effect with increased stimulation frequency. The latter finding is corroborated by the

results of Gomora et al. (2001), who demonstrated an increase in ETX effect when the membrane potential is slightly depolarized. This voltage-dependency is of particular interest, as it implies an enhanced effectiveness of ETX during SWDs, which have a frequency of 2–3 Hz in human patients and 5–10 Hz in WAG/Rij rats. Furthermore, ETX was found to reduce the persistent sodium current in acutely isolated TC neurons. The inconsistent effect of therapeutically relevant concentrations on I_{NaP} might be caused by the low signal-to-noise ratio due to the small current amplitudes, a run up of I_{NaP} a contamination by rapidly inactivating sodium current components, or by a mixture thereof (Leresche et al., 1998; Parri and Crunelli, 1998). Like ethosuximide, valproate blocked T-type Ca^{2+} currents and displayed different effects between rat strains. Although further strengthening the notion that anti-absence drugs inhibit the I_T , our results are in contrast to previous reports demonstrating an effect of valproate only on I_T expressed in DRG neurons, but not in TC neurons and expression systems (Coulter et al., 1989a; Todorovic and Linggle, 1998; Todorovic et al., 2000).

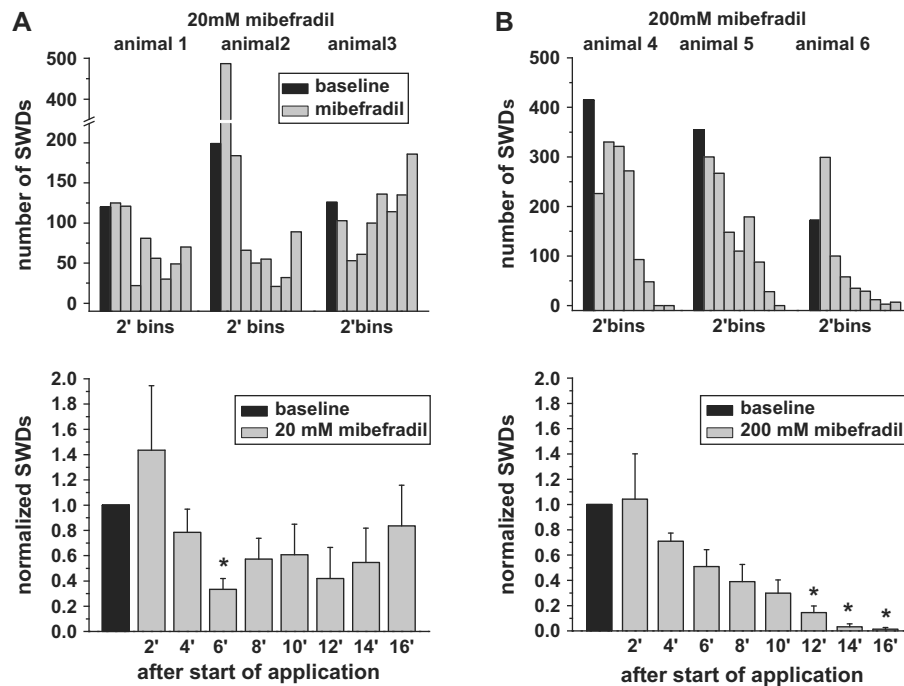


Fig. 12. Summary of the effects of mibefradil application on SWDs recorded in the surface EEG. (A) Effect of injection of 2 μ l 20 mM mibefradil into the VB of anaesthetized WAG/Rij rats. The upper panel displays the data of each of the three animals tested. Bars represent the number of SWDs in 2 min intervals. Black bar represents the number of SWDs recorded in the 2 min bin prior to mibefradil injection. Grey bars represent the number of SWDs after mibefradil injection. Lower panel displays the normalized average of the three animals shown in the upper panel. Application of 2 μ l 20 mM mibefradil resulted in a transient decrease in SWD incidence in all animals. (B) Effect of injection of 2 μ l 200 mM mibefradil into the VB of anaesthetized WAG/Rij rats. Same conventions as in A. Application of 2 μ l 200 mM mibefradil resulted in the complete breakdown of SWD activity in all animals. (* $p < 0.05$).

The modeling results presented here point to a scenario where the complete effect of ETX is ascribed to a combined action on at least three membrane currents, namely I_T (Coulter et al., 1989a,b, 1990; Huguenard and Prince, 1994; this study), I_{NaP} (Leresche et al., 1998; this study), and I_{KCa} (Leresche et al., 1998). Implementing all of these changes into the model neuron resulted in LTS alterations similar to those observed experimentally. While the reduction of I_T and I_{NaP} directly account for the increase in LTS onset latency and the reduction in LTS associated action potentials (Huguenard and Prince, 1994; Parri and Crunelli, 1998; this study), a reduction of the Ca^{2+} -activated potassium current had opposite effects on both parameters. Although a reduction of I_{KCa} in our model prolonged LTS activity, it is likely that a reduction of this current results in an overall attenuation of network oscillation, as it is thought to be responsible for the after-hyperpolarization following the LTS in NRT neurons and has been proposed to underlie the ETX induced increase in tonic firing (Bal and McCormick, 1993; Crunelli and Leresche, 2002a; Leresche et al., 1998). Furthermore, it is important to note that a strong I_T reduction was necessary to replicate all aspects of ETX-induced LTS alterations.

4.3. Block of I_T in interneurons

Similar to TC neurons, I_T of local circuit interneurons was reduced by ETX and mibefradil. It is reasonable to assume that this effect contributes to the systemic action of ETX, as

GABAergic local circuit interneurons are likely to contribute to thalamic network synchronization, as has been shown for GABAergic NRT neurons (Contreras et al., 1993; Rinzel et al., 1998). The ETX effect on I_T of both NRT neurons (Huguenard and Prince, 1994) and local circuit interneurons might be functionally even more important than I_T reduction in TC neurons. This notion is supported by the observation of Song et al. (2004) that a genetically induced 25% reduction of α_1G carried I_T in TC neurons of mutant mice did not affect SWD generation. The effect of this mutation was probably restricted to thalamic and cortical areas strongly expressing α_1G , but presumably left the α_1H and α_1I carried I_T of NRT neurons unchanged (McKay et al., 2006; Talley et al., 1999). As therapeutically relevant concentrations of ETX can be expected to block around 25% of the I_T in TC neurons, this effect alone would not be sufficient to disrupt SWDs according to this genetic model. Possibly, an ETX induced reduction of I_T of GABAergic NRT and local circuit interneurons provides the extra anti-oscillatory effect necessary to cause a systemic SWD breakdown. Furthermore, the role of cortical I_T is less clear. While the work by Song et al. (2004) indicated that a 25% reduction of cortical I_T did not affect SWD generation in the mutant mice, the application of ETX into the epileptic cortical “focus” of GAERS rats was proven to be extremely effective in reducing SWD incidence (Manning et al., 2004; Meeran et al., 2002). Possibly this is due to different mechanisms underlying SWD genesis in the mutant mice and GAERS rats (Budde et al., 2006).

4.4. Antiepileptic potential of mibefradil

If I_T reduction significantly contributes to the anti-absence effect of ethosuximide and valproate, a selective I_T antagonist, like mibefradil, should disrupt slow intrathalamic oscillations as well as SWDs. This was tested and verified experimentally, although several factors should be taken into consideration: (i) in addition to a blockade of I_T , 2 μ M mibefradil blocked $\sim 20\%$ of whole cell HVA Ca^{2+} as well as $\sim 20\%$ of voltage gated Na^+ currents (Bezprozvanny and Tsien, 1995; Strege et al., 2005). Action potential generation in the tonic transmission mode was only slightly affected in the presence of 2 and 20 μ M mibefradil, arguing against a contribution of Na^+ current reduction to the anti-oscillatory effect of application of 2 μ M mibefradil in horizontal slice preparations. Although a reduction of I_{NaP} contributing to the suppression of burst activity cannot be excluded. Further, HVA Ca^{2+} channels are thought to be responsible for presynaptic Ca^{2+} influx necessary for transmitter release (Gundelfinger et al., 2003; Reid et al., 2003). It is thus possible that a reduction of synaptic efficiency also contributes to the attenuation of network activity. While the period of intrathalamic oscillations should initially decrease under these conditions, it should increase with a reduction of I_T (Porcello et al., 2003; Sohal and Huguenard, 1998), as was observed experimentally. A reduction of I_T is thus the most plausible explanation for the effects of mibefradil on thalamic burst activity. (ii) During the *in vivo* experiments rather high substance concentrations were applied locally, which subsequently diffused from the site of delivery, becoming progressively more dilute. In the immediate vicinity of the infusion cannulae the high mibefradil concentration will likely block most of I_T , I_{NaP} , and HVA Ca^{2+} current in addition to perturbing local osmolarity and pH. As distance from the injection site increases, mibefradil concentration declines, and substance effects will narrow down to a sole blockade of I_T . It is thus likely that not the entire effect of mibefradil is due to a blockade of I_T . We did not investigate the reason for the initial increase in SWD incidence following mibefradil injection in two of the six *in vivo* experiments. Volume effects after substance application cannot be ruled out. However, the stable SWD generation in the control experiments corroborate the idea that mibefradil induced effects were responsible for the decline in SWD incidence observed in all experiments. In any case, the complete breakdown of SWDs after administration of 2 μ l 200 mM mibefradil into the VB demonstrates that this nucleus is an essential part of the network generating spike and wave activity.

Acknowledgements

Supported by DFG (BU 1019/7-1; Pa 336/17-1; Leibniz-program to HCP), Novartis Stiftung, Innovative Medizinische Forschung (IMF; BU 120501), and Interdisziplinäres Zentrum für Klinische Forschung (IZKF; Bud/005/07). T. Broicher was a fellow of the Boehringer Ingelheim Foundation. Thanks are

due to E. Boening, A. Jahn, S. Mücke, E. Naß, R. Ziegler and S. Vorwerk for excellent technical assistance.

References

- Anderson, M.P., Mochizuki, T., Xie, J., Fischler, W., Manger, J.P., Talley, E.M., Scammell, T.E., Tonegawa, S., 2005. Thalamic Cav3.1 T-type Ca^{2+} channel plays a crucial role in stabilizing sleep. *Proc. Natl. Acad. Sci. U.S.A.* 102, 1743–1748.
- Avoli, M., Rogawski, M.A., Avanzini, G., 2001. Generalized epileptic disorders: an update. *Epilepsia* 42, 445–457.
- Bal, T., McCormick, D.A., 1993. Mechanisms of oscillatory activity in guinea-pig nucleus reticularis thalami *in vitro*: a mammalian pacemaker. *J. Physiol.* 468, 669–691.
- Bezprozvanny, I., Tsien, R.W., 1995. Voltage-dependent blockade of diverse types of voltage-gated Ca^{2+} channels expressed in *Xenopus* oocytes by the Ca^{2+} channel antagonist mibefradil (Ro 40-5967). *Mol. Pharmacol.* 48, 540–549.
- Budde, T., Pape, H.-C., Kumar, S.S., Huguenard, J.R., 2006. Thalamic, thalamo-cortical, and cortico-cortical models of epilepsy with an emphasis on absence seizures. In: Pitkänen, A., Schwartzkroin, P.A., Moshé, S.L. (Eds.), *Models of Seizures and Epilepsy*. Elsevier, Amsterdam, pp. 73–88.
- Coenen, A.M., Van Luijckelaar, E.L., 2003. Genetic animal models for absence epilepsy: a review of the WAG/Rij strain of rats. *Behav. Genet.* 33, 635–655.
- Contreras, D., Curro Dossi, R., Steriade, M., 1993. Electrophysiological properties of cat reticular thalamic neurones *in vivo*. *J. Physiol.* 470, 273–294.
- Coulter, D.A., Huguenard, J.R., Prince, D.A., 1989a. Characterization of ethosuximide reduction of low-threshold calcium current in thalamic neurons. *Ann. Neurol.* 25, 582–593.
- Coulter, D.A., Huguenard, J.R., Prince, D.A., 1989b. Specific petit mal anti-convulsants reduce calcium currents in thalamic neurons. *Neurosci. Lett.* 98, 74–78.
- Coulter, D.A., Huguenard, J.R., Prince, D.A., 1990. Differential effects of petit mal anticonvulsants and convulsants on thalamic neurones: calcium current reduction. *Br. J. Pharmacol.* 100, 800–806.
- Crill, W.E., 1996. Persistent sodium current in mammalian central neurons. *Annu. Rev. Physiol.* 58, 349–362.
- Crunelli, V., Leresche, N., 2002a. Block of thalamic T-type Ca^{2+} channels by ethosuximide is not the whole story. *Epilepsy Curr.* 2, 53–56.
- Crunelli, V., Leresche, N., 2002b. Childhood absence epilepsy: genes, channels, neurons and networks. *Nat. Rev. Neurosci.* 3, 371–382.
- Gloor, P., 1968. Generalized cortico-reticular epilepsies. Some considerations on the pathophysiology of generalized bilaterally synchronous spike and wave discharge. *Epilepsia* 9, 249–263.
- Gomora, J.C., Daud, A.N., Weiergraber, M., Perez-Reyes, E., 2001. Block of cloned human T-type calcium channels by succinimide antiepileptic drugs. *Mol. Pharmacol.* 60, 1121–1132.
- Gundelfinger, E.D., Kessels, M.M., Qualmann, B., 2003. Temporal and spatial coordination of exocytosis and endocytosis. *Nat. Rev. Mol. Cell Biol.* 4, 127–139.
- Hernandez-Cruz, A., Pape, H.C., 1989. Identification of two calcium currents in acutely dissociated neurons from the rat lateral geniculate nucleus. *J. Neurophysiol.* 61, 1270–1283.
- Hines, M.L., Carnevale, N.T., 2001. NEURON: a tool for neuroscientists. *Neuroscientist* 7, 123–135.
- Huguenard, J.R., 1996. Low-threshold calcium currents in central nervous system neurons. *Annu. Rev. Physiol.* 58, 329–348.
- Huguenard, J.R., 2002. Block of T-type Ca^{2+} channels is an important action of succinimide antiabsence drugs. *Epilepsy Curr.* 2, 49–52.
- Huguenard, J.R., McCormick, D.A., 1992. Simulation of the currents involved in rhythmic oscillations in thalamic relay neurons. *J. Neurophysiol.* 68, 1373–1383.
- Huguenard, J.R., Prince, D.A., 1994. Intrathalamic rhythmicity studied *in vitro*: nominal T-current modulation causes robust antioscillatory effects. *J. Neurosci.* 14, 5485–5502.

- Kim, D., Song, I., Keum, S., Lee, T., Jeong, M.J., Kim, S.S., McEnery, M.W., Shin, H.S., 2001. Lack of the burst firing of thalamocortical relay neurons and resistance to absence seizures in mice lacking alpha1G T-type Ca(2+) channels. *Neuron* 31, 35–45.
- Konig, P., 1994. A method for the quantification of synchrony and oscillatory properties of neuronal activity. *J. Neurosci. Methods* 54, 31–37.
- Lee, J., Kim, D., Shin, H.S., 2004. Lack of delta waves and sleep disturbances during non-rapid eye movement sleep in mice lacking alpha1G-subunit of T-type calcium channels. *Proc. Natl. Acad. Sci. U.S.A.* 101, 18195–18199.
- Leresche, N., Parri, H.R., Erdemli, G., Guyon, A., Turner, J.P., Williams, S.R., Asproдини, E., Crunelli, V., 1998. On the action of the anti-absence drug ethosuximide in the rat and cat thalamus. *J. Neurosci.* 18, 4842–4853.
- Manning, J.P., Richards, D.A., Leresche, N., Crunelli, V., Bowerly, N.G., 2004. Cortical-area specific block of genetically determined absence seizures by ethosuximide. *Neuroscience* 123, 5–9.
- McCormick, D.A., Bal, T., 1997. Sleep and arousal: thalamocortical mechanisms. *Annu. Rev. Neurosci.* 20, 185–215.
- McCormick, D.A., Huguenard, J.R., 1992. A model of the electrophysiological properties of thalamocortical relay neurons. *J. Neurophysiol.* 68, 1384–1400.
- McKay, B.E., McRory, J.E., Molineux, M.L., Hamid, J., Snutch, T.P., Zamponi, G.W., Turner, R.W., 2006. Ca(V)3 T-type calcium channel isoforms differentially distribute to somatic and dendritic compartments in rat central neurons. *Eur. J. Neurosci.* 24, 2581–2594.
- Meeren, H.K., Pijn, J.P., Van Luijckelaar, E.L., Coenen, A.M., Lopes da Silva, F.H., 2002. Cortical focus drives widespread corticothalamic networks during spontaneous absence seizures in rats. *J. Neurosci.* 22, 1480–1495.
- Mehrke, G., Zong, X.G., Flockerzi, V., Hofmann, F., 1994. The Ca(++)-channel blocker Ro 40-5967 blocks differently T-type and L-type Ca(++) channels. *J. Pharmacol. Exp. Ther.* 271, 1483–1488.
- Meuth, S., Pape, H.C., Budde, T., 2002. Modulation of Ca2+ currents in rat thalamocortical relay neurons by activity and phosphorylation. *Eur. J. Neurosci.* 15, 1603–1614.
- Meuth, S.G., Kanyshkova, T., Meuth, P., Landgraf, P., Munsch, T., Ludwig, A., Hofmann, F., Pape, H.C., Budde, T., 2006. Membrane resting potential of thalamocortical relay neurons is shaped by the interaction among TASK3 and HCN2 channels. *J. Neurophysiol.* 96, 1517–1529.
- Mishra, S.K., Hermsmeyer, K., 1994. Selective inhibition of T-type Ca2+ channels by Ro 40-5967. *Circ. Res.* 75, 144–148.
- Pace-Schott, E.F., Hobson, J.A., 2002. The neurobiology of sleep: genetics, cellular physiology and subcortical networks. *Nat. Rev. Neurosci.* 3, 591–605.
- Pape, H.C., Budde, T., Mager, R., Kisvarday, Z.F., 1994. Prevention of Ca(2+)-mediated action potentials in GABAergic local circuit neurones of rat thalamus by a transient K+ current. *J. Physiol.* 478 (Pt 3), 403–422.
- Parri, H.R., Crunelli, V., 1998. Sodium current in rat and cat thalamocortical neurons: role of a non-inactivating component in tonic and burst firing. *J. Neurosci.* 18, 854–867.
- Perez-Reyes, E., 2003. Molecular physiology of low-voltage-activated t-type calcium channels. *Physiol. Rev.* 83, 117–161.
- Pfriefer, F.W., Veselovsky, N.S., Gottmann, K., Lux, H.D., 1992. Pharmacological characterization of calcium currents and synaptic transmission between thalamic neurons in vitro. *J. Neurosci.* 12, 4347–4357.
- Porcello, D.M., Smith, S.D., Huguenard, J.R., 2003. Actions of U-92032, a T-type Ca2+ channel antagonist, support a functional linkage between I(T) and slow intrathalamic rhythms. *J. Neurophysiol.* 89, 177–185.
- Posner, E.B., Mohamed, K., Marson, A.G., 2005. Ethosuximide, sodium valproate or lamotrigine for absence seizures in children and adolescents. *Cochrane Database Syst. Rev.* CD003032.
- Reid, C.A., Bekkers, J.M., Clements, J.D., 2003. Presynaptic Ca2+ channels: a functional patchwork. *Trends Neurosci.* 26, 683–687.
- Rinzel, J., Terman, D., Wang, X., Ermentrout, B., 1998. Propagating activity patterns in large-scale inhibitory neuronal networks. *Science* 279, 1351–1355.
- Rogawski, M.A., Loscher, W., 2004. The neurobiology of antiepileptic drugs. *Nat. Rev. Neurosci.* 5, 553–564.
- Sayer, R.J., Brown, A.M., Schwandt, P.C., Crill, W.E., 1993. Calcium currents in acutely isolated human neocortical neurons. *J. Neurophysiol.* 69, 1596–1606.
- Seidenbecher, T., Pape, H.C., 2001. Contribution of intralaminar thalamic nuclei to spike-and-wave-discharges during spontaneous seizures in a genetic rat model of absence epilepsy. *Eur. J. Neurosci.* 13, 1537–1546.
- Seidenbecher, T., Staak, R., Pape, H.C., 1998. Relations between cortical and thalamic cellular activities during absence seizures in rats. *Eur. J. Neurosci.* 10, 1103–1112.
- Sohal, V.S., Huguenard, J.R., 1998. Long-range connections synchronize rather than spread intrathalamic oscillations: computational modeling and in vitro electrophysiology. *J. Neurophysiol.* 80, 1736–1751.
- Song, I., Kim, D., Choi, S., Sun, M., Kim, Y., Shin, H.S., 2004. Role of the alpha1G T-type calcium channel in spontaneous absence seizures in mutant mice. *J. Neurosci.* 24, 5249–5257.
- Staak, R., Pape, H.C., 2001. Contribution of GABA(A) and GABA(B) receptors to thalamic neuronal activity during spontaneous absence seizures in rats. *J. Neurosci.* 21, 1378–1384.
- Strege, P.R., Bernard, C.E., Ou, Y., Gibbons, S.J., Farrugia, G., 2005. Effect of mibefradil on sodium and calcium currents. *Am. J. Physiol. Gastrointest. Liver Physiol.* 289, G249–G253.
- Talley, E.M., Cribbs, L.L., Lee, J.H., Daud, A., Perez-Reyes, E., Bayliss, D.A., 1999. Differential distribution of three members of a gene family encoding low voltage-activated (T-type) calcium channels. *J. Neurosci.* 19, 1895–1911.
- Thompson, S.M., Wong, R.K., 1991. Development of calcium current subtypes in isolated rat hippocampal pyramidal cells. *J. Physiol.* 439, 671–689.
- Todorovic, S.M., Lingle, C.J., 1998. Pharmacological properties of T-type Ca2+ current in adult rat sensory neurons: effects of anticonvulsant and anesthetic agents. *J. Neurophysiol.* 79, 240–252.
- Todorovic, S.M., Perez-Reyes, E., Lingle, C.J., 2000. Anticonvulsants but not general anesthetics have differential blocking effects on different T-type current variants. *Mol. Pharmacol.* 58, 98–108.
- Ulrich, D., Huguenard, J.R., 1995. Purinergic inhibition of GABA and glutamate release in the thalamus: implications for thalamic network activity. *Neuron* 15, 909–918.
- Williams, D., 1953. A study of thalamic and cortical rhythms in petit mal. *Brain* 76, 50–69.

Specific expression of low-voltage-activated calcium channel isoforms and splice variants in thalamic local circuit interneurons

Tilman Broicher,^a Tatyana Kanyshkova,^a Peter Landgraf,^b Vladan Rankovic,^c Patrick Meuth,^a Sven G. Meuth,^d Hans-Christian Pape,^{a,e} and Thomas Budde^{a,e,*}

^aInstitut für Physiologie I, Westfälische Wilhelms-Universität Münster, Robert-Koch-Str. 27a, D-48149 Münster, Germany

^bLeibniz Institut für Neurobiologie, Brenneckestr. 6, D-39118 Magdeburg, Germany

^cInstitut für Physiologie, Otto-von-Guericke-Universität, Leipziger-Str. 44, 39120 Magdeburg, Germany

^dNeurologische Klinik, Bayerische Julius-Maximilians-Universität, Josef-Schneider-Str. 11, D-97080 Würzburg, Germany

^eInstitut für Experimentelle Epilepsieforschung, Hüfferstr. 68, D-48149 Münster, Germany

Received 7 December 2006; revised 10 May 2007; accepted 22 May 2007

Available online 24 July 2007

It has been suggested that the specific burst firing patterns of thalamic neurons reflect differential expression of low-voltage-activated (LVA) Ca²⁺ channel subtypes and their splice variants. By combining electrophysiological, molecular biological, immunological, and computational modeling techniques we here show that diverging LVA Ca²⁺ currents of thalamocortical relay (TC) and GABAergic interneurons of the dLGN correlate with a differential expression of LVA Ca²⁺ channel splice variations and isoforms (α 1G-a in TC; α 1G-bc and α 1I in interneurons). Implementation of the observed LVA Ca²⁺ current differences into a TC neuron model changed the burst firing from TC-like to interneuron-like. We conclude that alternative splicing of the α 1G isoform in dLGN TC and interneurons, and the exclusive expression of the α 1I isoform in interneurons play a prominent role in setting the different LVA Ca²⁺ current properties of TC and interneurons, which critically contribute to the diverging burst firing behavior of these neurons.

© 2007 Elsevier Inc. All rights reserved.

Keywords: Patch clamp; T-type Ca²⁺ channel; Absence epilepsy; Thalamus; Real time PCR

Introduction

Our present understanding of the function and dysfunction of the thalamocortical system has evolved along several lines of evidence. The first and most fundamental finding was the correlation of different behavioral states with specific neuronal activity patterns (Steriade et al., 1997). The sleeping brain is dominated by synchronized low frequency, high amplitude oscillations and the thalamus is thought to

play a key role in generating and maintaining these slow sleep rhythms (Pace-Schott and Hobson, 2002). In addition to its involvement in physiological activity, the thalamus is believed to be implicated in the generation of abnormal, hyper-synchronous spike and wave discharges (SWD) observed during absence seizures (Crunelli and Leresche, 2002). The systemic observations were followed by the identification of LVA (also termed T-type) Ca²⁺ currents as the electrogenic basis of stereotypic low-threshold Ca²⁺ spikes (LTS), which is the key mechanism of burst firing during slow-wave sleep and absence epilepsy, as well as a pharmacological target of anti-epileptic drugs (Huguenard, 1996). Finally, the recent advances in molecular biology have identified three genes (CACNA1G, CACNA1H, CACNA1I) coding for three different pore-forming α 1 (α 1G, Ca_v3.1; α 1H, Ca_v3.2; α 1I, Ca_v3.3) subunit isoforms as the molecular basis of LVA Ca²⁺ currents (Perez-Reyes, 2003). All of the gene products seem to be subjected to alternative splicing, thus vastly increasing the number of physiologically distinct channel types (Perez-Reyes, 2006). While currents generated by α 1G and α 1H isoforms in heterologous expression systems are fairly similar, currents carried by the α 1I isoform display a depolarized voltage dependency and slower kinetics (Chemin et al., 2002; Perez-Reyes, 2003). The generation of genetic knock-out mouse strains allowed the analysis of the physiological and pathophysiological role of specific Ca_v3 isoforms (Anderson et al., 2005; Kim et al., 2001; Lee et al., 2004; Song et al., 2004).

Based on the advances described above it was found that anti-absence drugs act on LVA Ca²⁺ currents and induce a breakdown of intrathalamic oscillations (Coulter et al., 1989; Huguenard and Prince, 1994). Furthermore, genetic rat models of absence epilepsy reveal increased expression of Ca_v3 genes and LVA Ca²⁺ current density in the thalamus (Talley et al., 2000; Tsakiridou et al., 1995). Genetic knock-out studies demonstrated the strong dependence of slow-wave sleep oscillations and SWDs on the presence of the α 1G isoform (Anderson et al., 2005; Kim et al., 2001; Lee et al., 2004; Song et al., 2004). The latter is in line with the expression profile of LVA Ca²⁺ channels as α 1G is the most prominent thalamic LVA Ca²⁺ channel

* Corresponding author. Institut für Experimentelle Epilepsieforschung, Hüfferstr. 68, D-48149 Münster, Germany. Fax: +49 251 83 55551.

E-mail address: tbudde@uni-muenster.de (T. Budde).

Available online on ScienceDirect (www.sciencedirect.com).

isoform (Talley et al., 1999). In an attempt to correlate the Ca_v3 expression pattern with channel properties in expression systems and native currents, different thalamic nuclei were found to exhibit distinct differences. While $\alpha 1G$ and moderate levels of $\alpha 1H$ were found in thalamic relay nuclei, the thalamic reticular nucleus (NRT) is characterized by expression of $\alpha 1H$ and $\alpha 1I$ (McKay et al., 2006; Talley et al., 1999). This expression pattern is accompanied by more depolarized voltage dependency and slower kinetics of LVA Ca^{2+} currents in NRT neurons compared to TC neurons (Destexhe et al., 1996, 1998).

The intra-thalamic circuitry is composed of three basic cell types: excitatory thalamocortical relay (TC) neurons, GABAergic local circuit interneurons, and GABAergic cells of the NRT (Steriade et al., 1997). Much is known about LVA Ca^{2+} currents, LTS generation and their contribution to slow-wave sleep and pathophysiological absence oscillations in NRT and TC neurons (Crunelli et al., 2006; Crunelli and Leresche, 2002; Llinas and Steriade, 2006; Pape et al., 2004). The role of local circuit interneurons during these oscillations however remains poorly understood. Our knowledge about LVA Ca^{2+} currents in interneurons is currently limited to the fact that they reveal small LVA Ca^{2+} currents of depolarized voltage dependency and slow kinetics in comparison to TC neurons and, despite of the burst firing of putative interneurons *in vivo*, these neurons generate a quite variable LTS, ranging from subthreshold depolarization towards the generation of one to several action potentials in individual cells *in vitro* (Ahlsen et al., 1984; Burke and Jervie Sefton, 1966; Deschenes et al., 1984; McKay et al., 2006; Munsch et al., 2005; Pape et al., 1994; Pape and McCormick, 1995; Talley et al., 1999; Zhu et al., 1999a,b).

Since few data are available on the intrinsic properties of interneurons and literally nothing is known about their possible role in absence epilepsy, the present study focussed on the relationship between Ca_v3 expression, LVA Ca^{2+} current properties and the LVA Ca^{2+} current-dependent burst firing in thalamic interneurons. Therefore we investigated the dorsal part of the lateral geniculate nucleus (dLGN), a nucleus consisting of two well defined neuronal cell types, namely TC neurons and local circuit interneurons (Gabbott et al., 1986; Grossman et al., 1973; Ohara et al., 1983). We further explored whether cellular properties may be of relevance for absence epilepsy by comparing two rat strains, a genetic model of absence epilepsy, the WAG/Rij rats, and a non-epileptic control strain, the ACI rats (Coenen

and Van Luijtelaaar, 2003). WAG/Rij rats develop absence seizures, which are similar to the ones observed in human patients and are effectively antagonized by clinically used anti-epileptic drugs (Budde et al., 2006). To allow straightforward identification of cell types, acute isolation of neurons was combined with electrophysiological, molecular biological and immunological techniques to determine the cell type-specific LVA Ca^{2+} current properties and expression profile of channel isoforms and splice variants. Confirmatory experiments were conducted in brain slices. The observed LVA Ca^{2+} current properties were validated in a mathematical model to address their effect on the LVA Ca^{2+} current-dependent burst firing.

Results

Identification of thalamic cell types in WAG/Rij and ACI rats

In a first step we identified TC and interneurons according to molecular and morphological criteria. Previous work has shown the dLGN to be composed of large multipolar (75–85%) and small bipolar cells (15–25%) representing γ -aminobutyric acid (GABA)-negative TC neurons and GABA-positive local circuit interneurons, respectively (Gabbott et al., 1986; Ohara et al., 1983; Pape et al., 1994). Therefore we investigated the expression pattern of the GABA synthesizing enzymes glutamic acid decarboxylase (GAD) 65, and GAD 67, and the vesicular inhibitory amino acid transporter (ViAAT) in the dLGN. We did not detect any significant differences between WAG/Rij and ACI and therefore data was pooled.

In situ hybridization (ISH)

In dLGN slices, *in situ* hybridization revealed positive staining in $34 \pm 1\%$ and $20 \pm 1\%$ of all cells for the expression of GAD65 and GAD67, respectively (*GAD65*: $n = 10$ slices, 5 from WAG/Rij, 5 from ACI; a total of 3 WAG/Rij and 3 ACI rats were investigated; *GAD67*: $n = 16$ slices, 7 from WAG/Rij, 9 from ACI; a total of 3 WAG/Rij and 4 ACI rats were investigated). Normalization was done with respect to the average cell density obtained by Nissl staining (808 ± 31 cells/mm², $n = 6$ slices from 3 rats; data not shown). Next, *in situ* hybridization of acutely isolated neurons (Fig. 1A) revealed positive staining in $28 \pm 4\%$ and $25 \pm 6\%$ of multipolar neurons as well as $91 \pm 3\%$ and $90 \pm 3\%$ of

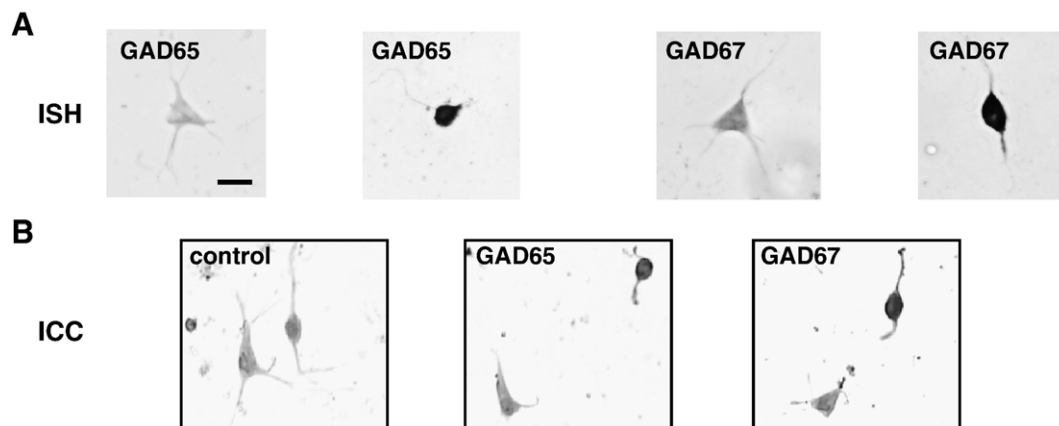


Fig. 1. Molecular classification of dLGN neurons. (A) *In situ* hybridization (ISH) using GAD65- and GAD67-specific probes. Representative examples of negatively and positively labeled acutely isolated cells are shown. Scale bar represent 20 μ m. (B) Immunocytochemical staining (ICC) of acutely isolated dLGN neurons without primary antibody (control), using a GAD65-specific antibody (middle panel), and using a GAD67-specific antibody (right panel).

small bipolar neurons for GAD65 and GAD67, respectively (a total of 370 cells were analyzed from 6 animals; 3 WAG/Rij and 3 ACI).

RT-PCR

For RT-PCR analysis, samples of multipolar and small bipolar cells were harvested (10–15 cells per sample) and probed for expression of genes involved in GABAergic signalling in cell samples isolated from 7 WAG/Rij and 7 ACI rats. All samples of small bipolar neurons revealed strong expression of GAD65, GAD67, and *ViAAT* (*GAD65*: $\Delta C_t = 0.9 \pm 0.2$; 15 samples of bipolar cells, 7 from WAG/Rij and 8 from ACI; *GAD67*: $\Delta C_t = 1.3 \pm 0.3$; 14 samples of bipolar cells, 7 from WAG/Rij and 7 from ACI; *ViAAT*: $\Delta C_t = -0.5 \pm 0.2$; 15 samples of bipolar cells, 7 from WAG/Rij and 8 from ACI, data not shown), while only a subset of multipolar neuron samples was found to express these genes (*GAD65*: 24%; 4 of 17 samples of multipolar cells, 8 from WAG/Rij and 9 from ACI; $\Delta C_t = 3.1 \pm 0.4$ for the 4 positive samples, 2 from WAG/Rij and 2 from ACI; *GAD67*: 21%; 4 of 19 samples of multipolar cells, 10 samples from WAG/Rij and 9 samples from ACI; $\Delta C_t = 2.6 \pm 0.7$, for the 4 positive samples, 2 from WAG/Rij and 2 from ACI; *ViAAT*: 53%; 9 of 17 samples, 8 samples from WAG/Rij and 9 samples from ACI; $\Delta C_t = 2.9 \pm 0.4$; of the 9 positive samples, 3 from WAG/Rij and 6 from ACI, data not shown).

Immunocytochemistry (ICC)

In the following, immunocytochemical staining of acutely isolated cells revealed that $12 \pm 2\%$ and $8 \pm 3\%$ of multipolar cells as well as $82 \pm 2\%$ and $85 \pm 2\%$ of bipolar cells were positively stained for the protein expression of GAD65 and GAD67 (Fig. 1B), respectively (data were derived from 3 WAG/Rij and 3 ACI rats). In a second set of immunological stainings, antibodies directed against GAD65 and parvalbumin, a TC neuron-specific cell marker in the dLGN of several species (Jones and Hendry, 1989; Meuth et al., 2005; Sieg et al., 1998) were co-incubated in thalamic cell cultures. Typical multipolar neurons were positively stained for the presence of parvalbumin but lacked GAD65 resulting in an absence of co-localization (observed in 72 of 90 multipolar neurons; the cells derive from 4 independent preparations; data not shown). Cells with typical interneuron morphology (small cell bodies, thin dendrites arborizing extensively in a bitufted manner) could be rarely identified in cell cultures. However these cells lacked parvalbumine staining and were GAD65-positive (data not shown).

It is concluded that TC (multipolar) neurons and interneurons (bipolar) of the dLGN reveal a complementary protein expression profile concerning GAD65, GAD67, and parvalbumine irrespective of the rat strains under investigation, and that these two types of neurons can be reliably identified after acute isolation. On the mRNA level,

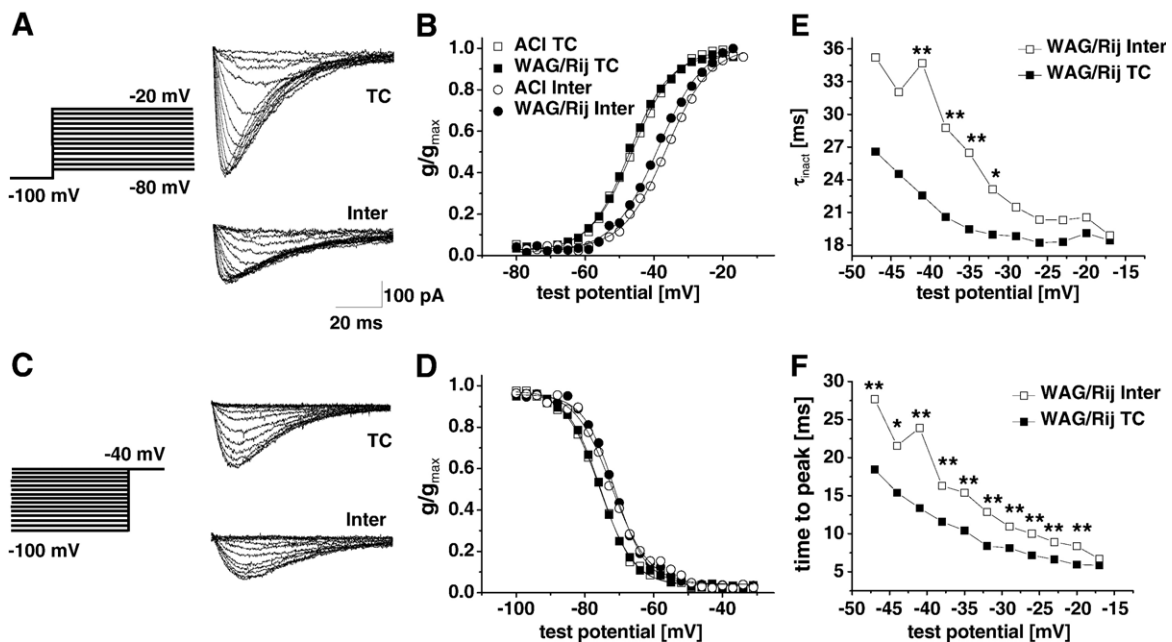


Fig. 2. Steady-state voltage-dependent properties of dLGN TC and interneuron LVA Ca^{2+} currents. Current traces were derived from neurons of a WAG/Rij rat. (A) Voltage dependency of LVA Ca^{2+} current activation. Stimulation protocol is shown on the left. Neurons were clamped to -100 mV (700 ms) and stepped to increasingly positive test potentials starting from -80 mV in 3 mV intervals (200 ms). Representative LVA Ca^{2+} current traces of TC neurons are depicted on the upper right, representative current traces of interneurons are shown on the lower right. (B) Activation curves from TC neurons and interneurons of WAG/Rij and ACI rats (symbols as indicated) were obtained by fitting a Boltzmann equation to plots of mean values of normalized peak conductance vs. the test potential. Standard error bars have been omitted for clarity; see text for statistical data. (C) Voltage dependency of LVA Ca^{2+} current inactivation. Stimulation protocol is shown on the left. Neurons were clamped to increasingly positive conditioning potentials for 700 ms before being stepped to a constant analyzing potential of -40 mV for 200 ms. Initial conditioning potential was -100 mV, which was varied in decrements of 3 mV. Representative LVA Ca^{2+} current traces of TC neurons are depicted on the upper right, representative current traces of interneurons are shown on the lower right. (D) Inactivation curve for TC and interneurons of WAG/Rij and ACI TC and interneurons obtained through fitting a Boltzmann equation to plots of mean values of normalized peak conductance vs. the conditioning potential. Symbols as indicated in (B). (E) Mean values of the inactivation time constant of TC (closed squares) and interneurons (open squares) obtained by fitting a monoexponential function. Data obtained from WAG/Rij rats are shown. Time constants are plotted against test potentials of the activation protocol. Standard error bars have been omitted for clarity. (F) Mean values of the time to peak amplitude of LVA Ca^{2+} currents of TC (closed squares) and interneurons (open squares) in relation to the activation protocol test potential. Depicted data derived from WAG/Rij rats. Standard error bars have been omitted for clarity. * $p < 0.05$, ** $p < 0.01$.

however, a relatively high number of TC neurons also express GAD65 and GAD67.

Electrophysiological properties of LVA Ca²⁺ currents in dLGN TC and interneurons of WAG/Rij and ACI rats

Next, we examined the basic voltage-dependent activation and inactivation properties of LVA Ca²⁺ currents in TC and interneurons of WAG/Rij and ACI rats. Prior to recording, cell types were identified according to morphological criteria established as described above (Gabbott et al., 1986; Ohara et al., 1983; Pape et al., 1994; Meuth et al., 2001). Small bipolar and large multipolar cells were regarded as interneurons and TC neurons, respectively. Whole-cell voltage-clamp techniques were applied on acutely isolated cells from rats older than postnatal day 15. From a conditioning potential of -100 mV inward currents in TC neurons of both strains were detectable at around -60 mV and rapidly increased in amplitude with increasing step potential (Fig. 2A). No differences in the voltage dependency of LVA Ca²⁺ current activation were observed between TC neurons of WAG/Rij and ACI. Appearance of Ca²⁺ inward currents in interneurons was shifted to more depolarized values of the membrane potential (Pape et al., 1994) (Figs. 2A, B). No differences in the voltage dependency of LVA Ca²⁺ current activation were observed between interneurons of WAG/Rij and ACI. Construction of steady-state activation curves revealed half-maximal values (V_h) of activation which were significantly different between TC neurons (WAG/Rij TC: $V_h = -47 \pm 1.5$ mV, $n = 12$; ACI TC: $V_h = -46 \pm 3$, $n = 5$; Fig. 2B) and interneurons (WAG/Rij interneurons: $V_h = -36.4 \pm 1.5$ mV, $n = 17$; ACI interneurons: $V_h = -35.3 \pm 1$ mV, $n = 9$; WAG/Rij TC vs. WAG/Rij interneurons: $p < 0.001$; ACI TC vs. ACI interneurons: $p = 0.01346$; Fig. 2B) of both strains.

Next, steady-state inactivation properties were determined by holding the cells at various conditioning potentials and stepping to a constant analyzing pulse at -40 mV (Fig. 2C). Values of half-maximal inactivation were significantly different between TC neurons (WAG/Rij TC: $V_h = -75.9 \pm 0.8$ mV, $n = 12$; ACI TC: -76.6 ± 2 mV, $n = 5$; Fig. 2D) and interneurons (WAG/Rij interneurons: $V_h = -72.5 \pm 0.2$ mV, $n = 8$; ACI interneurons: 73.1 ± 1 mV, $n = 9$; WAG/Rij TC vs. WAG/Rij interneurons: $p = 0.002$; ACI TC vs. ACI interneurons: $p = 0.07271$; Fig. 2D) in WAG/Rij, while the difference just failed to reach significance in ACI. No differences were observed between the LVA Ca²⁺ current voltage dependency of inactivation between TC neurons of WAG/Rij and ACI. Likewise, the LVA Ca²⁺ current voltage dependency of inactivation was indistinguishable between WAG/Rij and ACI interneurons.

Next, time-dependent activation and inactivation properties of the LVA Ca²⁺ currents were analyzed. In both cell types of both strains activation was fast and inactivation was complete during a 200 ms depolarizing step (Figs. 2A, C). As found for the voltage dependencies of activation and inactivation, there were no differences between neurons of the same type between strains. However, TC neurons revealed significantly faster current kinetics than interneurons in both strains (shown for WAG/Rij in Figs. 2E, F, significances are indicated by asterisks). The time to peak decreased with more positive values of the membrane potential (WAG/Rij TC: ranging from 18.5 ± 2 ms at -47 mV to 5.9 ± 1 ms at -20 mV, $n = 12$; ACI TC: ranging from 21.5 ± 2 ms at -47 mV to 6.5 ± 0.1 ms at -20 mV, $n = 5$; WAG/Rij interneurons: ranging from 27.7 ± 2 ms at -47 mV to 8.4 ± 1 ms at -20 mV, $n = 17$; ACI interneurons: ranging from 31.6 ± 4 ms at -47 mV to 9.1 ± 0.8 ms at -20 mV, $n = 9$; Fig. 2F). Furthermore, the time course of inactivation was approximated by a mono-exponential

function. The inactivation time constants were similar in the same cell types of both strains, but differed between the cell types within each strain. The time constants of inactivation ranged from 24.5 ± 2 ms at -44 mV to 19.1 ± 1 ms at -20 mV (WAG/Rij TC, $n = 12$) and 25.8 ± 6 ms at -44 mV to 21.4 ± 2 ms at -20 mV (ACI TC, $n = 5$) in TC neurons. Inactivation was significantly slower in interneurons. Here, τ -values ranged from 32 ± 2 ms at -44 mV to 20.6 ± 1 ms at -20 mV (WAG/Rij interneurons, $n = 17$; Fig. 2E) and from 39.5 ± 4 ms at -44 mV to 25.4 ± 3 ms at -20 mV (ACI interneurons, $n = 9$).

Furthermore, significant differences in LVA Ca²⁺ current amplitude and density were found between TC and local circuit interneurons in both strains. Neurons were clamped to -100 mV (700 ms) before being stepped to -40 mV (200 ms), close to the maximum of the LVA Ca²⁺ current I/V of both cell types (Pape et al., 1994). Interneurons of WAG/Rij and ACI rats displayed LVA Ca²⁺ current amplitudes which were of about half the size of the LVA Ca²⁺ current amplitudes observed in TC neurons (LVA Ca²⁺ current amplitude in: WAG/Rij TC: -248 ± 15 pA, $n = 78$ neurons; WAG/Rij interneurons: -139 ± 15 pA, $n = 50$ neurons; WAG/Rij TC vs. WAG/Rij interneurons $p = 0.00003$; ACI TC: -181 ± 13 pA, $n = 72$ neurons; ACI interneurons: -86 ± 11 pA, $n = 48$ neurons; ACI TC vs. ACI interneurons $p < 0.00001$; WAG/Rij TC vs. ACI TC $p = 0.00105$; WAG/Rij interneurons vs. ACI interneurons $p = 0.00444$). To obtain a measure of the current density per unit area of cell membrane, the peak LVA Ca²⁺ current amplitudes were divided by the cellular capacitance. In local circuit interneurons of both strains the magnitude of LVA Ca²⁺ current densities were about 75% of the peak LVA Ca²⁺ current densities observed in TC neurons (cellular capacitances in: WAG/Rij TC: 14.5 ± 0.5 pF; WAG/Rij interneurons: 9.0 ± 0.4 pF; ACI TC: 13.7 ± 0.5 pF; ACI interneurons: 7.6 ± 0.3 pF; WAG/Rij TC capacitance vs. WAG/Rij interneuron capacitance $p < 0.00001$; ACI TC capacitance vs. ACI interneuron capacitance $p < 0.00001$; LVA Ca²⁺ current density in: WAG/Rij TC: -18.6 ± 1.4 pA/pF; WAG/Rij interneurons: -14.0 ± 1.3 pA/pF; ACI TC: -14.4 ± 1.2 pA/pF; ACI interneurons: -11 ± 1.3 ; WAG/Rij TC current density vs. WAG/Rij interneuron current density $p = 0.04731$; ACI TC current density vs. ACI interneuron current density $p = 0.06617$; WAG/Rij TC current density vs. ACI TC current density $p = 0.02389$; WAG/Rij interneuron current density vs. ACI interneuron current density $p = 0.09051$).

Expression profile of CACNA1G, -H, -I in the dLGN of WAG/Rij and ACI

Next, the expression of CACNA1G, -H, -I was probed by means of quantitative RT-PCR and *in situ* hybridization. Quantitative RT-PCR of LVA Ca²⁺ channel mRNA in dLGN tissue of WAG/Rij rats revealed the highest expression level for CACNA1G ($\Delta C_t = 1.8 \pm 0.1$, $n = 6$ rats) followed by CACNA1I ($\Delta C_t = 7.0 \pm 0.9$, $n = 6$ rats) and CACNA1H ($\Delta C_t = 7.5 \pm 0.2$, $n = 6$ rats) relative to the constitutively expressed housekeeping gene β_2 -microglobuline (Figs. 3A, B). The same observation was made in the dLGN of ACI rats, although CACNA1G expression was significantly lower compared to WAG/Rij (ACI LGN tissue: CACNA1G, $\Delta C_t = 2.6 \pm 0.3$, $n = 5$ rats, WAG/Rij vs. ACI $p = 0.00079$; CACNA1I, $\Delta C_t = 7.3 \pm 1.3$, $n = 5$ rats; CACNA1H, $\Delta C_t = 7.3 \pm 0.5$, $n = 5$ rats; Fig. 3B).

In the following, *in situ* hybridization techniques employing digoxigenin-labelled antisense RNA probes were used to investigate the spatial pattern of CACNA1G, -H, -I gene expression within the dLGN. In both rat strains, the expression of CACNA1G mRNA was high throughout the dLGN, while CACNA1I transcripts were sparsely distributed with no clear patterning. Positively labelled

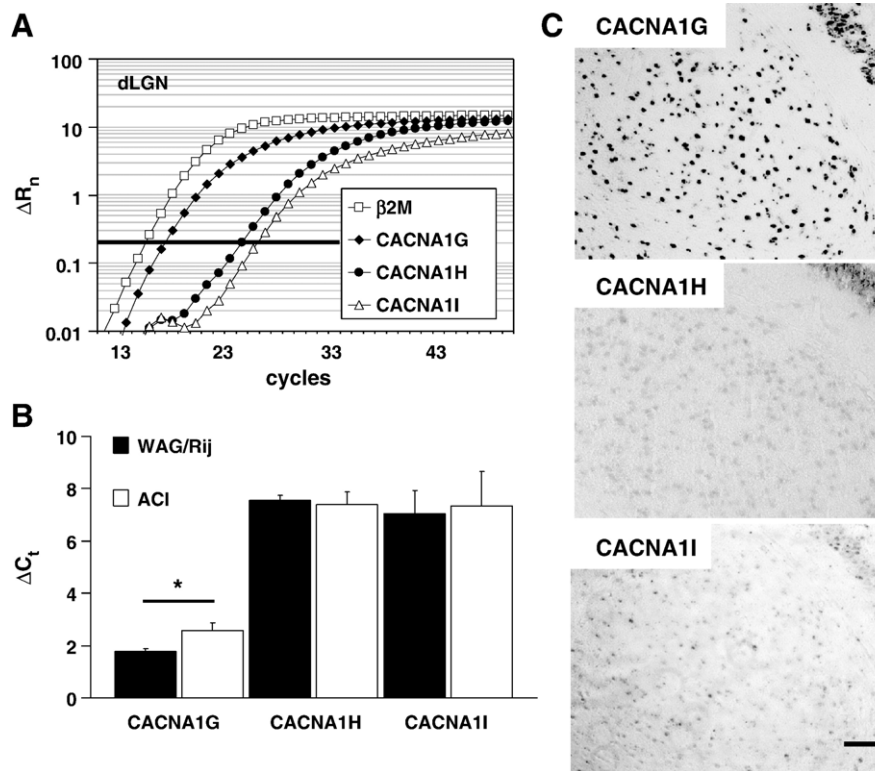


Fig. 3. Expression pattern of CACNA1G, -H and -I mRNA in the dLGN of WAG/Rij and ACI rats. (A) Example of a quantitative RT-PCR experiment, analyzing the CACNA1G, -H and -I mRNA expression in relation to β_2 -microglobulin ($\beta 2M$). The number of PCR cycles is plotted vs. normalized and baseline corrected reporter dye fluorescence. Thick black horizontal line marks the threshold used for quantification. Data derived from a WAG/Rij rat. (B) Mean cycle of threshold differences between CACNA1G, -H, -I and $\beta 2M$ mRNA in the dLGN of WAG/Rij and ACI rats. (C) *In situ* hybridization of dLGN tissue using probes specific for CACNA1G (upper image), CACNA1H (middle image), and CACNA1I (lower image). Images derived from a WAG/Rij rat. Scale bar represents 100 μm . * $p < 0.05$.

cells were found in a density of 823 ± 29 cells/ mm^2 (WAG/Rij, $n = 5$ slices from 3 rats) and 801 ± 85 cells/ mm^2 (ACI, $n = 4$ slices from 3 rats) for CACNA1G mRNA (Fig. 3C, upper panel) and 116 ± 8 cells/ mm^2 (WAG/Rij, $n = 5$ slices from 3 rats) and 115 ± 5 cells/ mm^2 (ACI, $n = 5$ slices from 3 rats) for CACNA1I mRNA (Fig. 3C, lower panel). The expression level of CACNA1H was too low for reliable quantitative analysis (Fig. 3C, middle panel). When compared to the average cell density assessed by Nissl staining (808 ± 31 cells/ mm^2 , $n = 6$ slices from 3 rats), approximately 100% and 15% of the cells in the dLGN of both strains expressed CACNA1G and CACNA1I mRNA, respectively.

The $\alpha 1I$ isoform is selectively expressed in interneurons

In view of the differences between CACNA1I and CACNA1G expression density, the possibility of a cell type specific expression was investigated in cell samples (10–15 cells per sample) derived from 13 ACI and 11 WAG/Rij rats. Quantitative RT-PCR analysis revealed a nearly exclusive expression of CACNA1G in TC neuron samples of both strains (WAG/Rij TC: $\Delta C_t = -0.9 \pm 0.2$, all 14 TC neuron samples were CACNA1G positive; ACI TC: $\Delta C_t = -0.6 \pm 0.3$, all 13 TC neuron samples were CACNA1G positive). In interneuron samples of both strains, expression of the CACNA1G isoform was significantly lower compared to TC neuron samples (WAG/Rij interneurons: $\Delta C_t = 0.8 \pm 0.2$, all 9 samples of interneurons were CACNA1G positive; CACNA1G expression in WAG/Rij TC vs. WAG/Rij interneurons $p = 0.00001$; ACI interneurons: $\Delta C_t = 0.9 \pm 0.3$, all 11 samples of inter-

neurons were CACNA1G positive; CACNA1G expression in ACI TC vs. ACI interneurons $p = 0.007$; Figs. 4A–C). By comparison, CACNA1I coding mRNA was detected in all interneuron samples (WAG/Rij interneurons: $\Delta C_t = 4.8 \pm 0.3$, $n = 9$ samples of interneurons; ACI interneurons: $\Delta C_t = 4.7 \pm 0.5$, $n = 11$ samples of interneurons; Figs. 4B, C), but only in a subset of TC neuron samples (WAG/Rij TC: 3 of 14 samples of TC neurons; ACI TC: 1 of 13 samples of TC neurons). CACNA1H expression was usually below detection limits in both cell types of both strains. To confirm that the CACNA1I mRNA was expressed in interneurons, *in situ* hybridization for the CACNA1I transcript (Fig. 4D, blue labelling) was combined with immunocytochemical detection of parvalbumin (Fig. 4D, brown labelling). The majority of neurons positively stained for the presence of CACNA1I mRNA were negative for parvalbumin (Fig. 4D, arrows), whereas parvalbumin-positive neurons revealed no or low expression (Fig. 4D, arrow head) of CACNA1I (CACNA1I pos. and parvalbumin neg.: $12 \pm 1\%$ of all neurons; CACNA1I neg. and parvalbumin pos.: $77 \pm 1\%$ of all neurons; CACNA1I pos. and parvalbumin pos.: $11 \pm 1\%$ of all neurons; cells were counted in 10 dLGN slices obtained from 3 WAG/Rij rats, percentages are based on a cell total of about 2225 cells in the investigated regions of interest). In addition, dLGN containing brain slices of 3 weeks old WAG/Rij and ACI rats were co-incubated with $\alpha 1I$ and GABA specific antibodies (Figs. 5B–D; WAG/Rij, $n = 3$ animals; ACI, $n = 3$ animals). An overlay of $\alpha 1I$ and GABA associated fluorescence revealed a strong co-localization in the dLGN of both strains. Co-localization of $\alpha 1I$ and GABA was observed in $34 \pm 3\%$ of the cell total in WAG/Rij and in $35 \pm 3\%$ of all cells in ACI (Fig. 5D). Similarly in thalamic primary cell cultures, co-incubations of GAD65

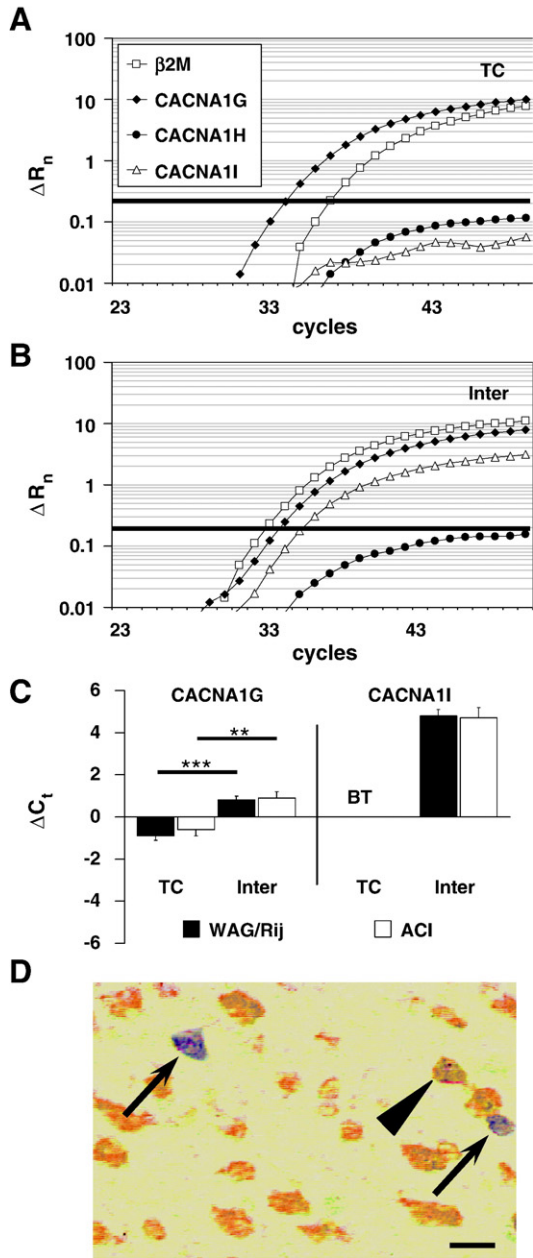


Fig. 4. Expression of CACNA11 mRNA in dLGN local circuit interneurons of WAG/Rij and ACI rats. (A) Example of a quantitative RT-PCR experiment, analyzing the CACNA1G (closed diamonds), -H (closed circles), and -I (open triangles) mRNA expression in relation to β_2 -microglobulin (β_2 M, open squares) in samples of identified TC neurons. The number of PCR cycles is plotted vs. normalized and baseline corrected reporter dye fluorescence. Thick black horizontal line marks the threshold used for quantification. TC neuron samples were usually restricted to the expression of CACNA1G. (B) Example of a quantitative RT-PCR experiment, analyzing the CACNA1G, -H, and -I mRNA expression in relation to β_2 -microglobulin in samples of identified interneurons. Same conventions as in (A). Data shown in (A) and (B) derived from neurons collected from a WAG/Rij rat. (C) Mean cycle of threshold differences between CACNA1G, -H, -I and β_2 M mRNA in WAG/Rij TC and interneurons. BT (below threshold) indicates lack of CACNA11 expression in TC neurons. See text for statistical data. (D) Combined *in situ* hybridization for CACNA11 mRNA (blue labeling) and immunocytochemical staining for parvalbumin (brown labeling) in WAG/Rij dLGN slices. Arrows mark cells exclusively stained for the presence of α II. The arrowhead marks a parvalbumin-positive cell revealing weak labeling for α II. Scale bar represents 20 μ m.

and α II specific antibodies revealed that the majority of bipolar cells were positive for GAD65 and α II (GAD65 pos., α II pos.: 28 of 46 cells, 61%; GAD65 neg., α II pos.: 10 of 46 cells, 22%; GAD65 pos., α II neg.: 8 of 46 cells, 17%; total α II pos. 38 of 46 cells, 83%; in 4 independent preparations; Figs. 5E–G). To verify the α II antibodies specificity, a western blotting analysis of the membrane fraction of rat hippocampus, thalamus and liver was performed. In hippocampus and thalamus a band of the predicted size was detected, while no band was found in the liver samples (Fig. 5A).

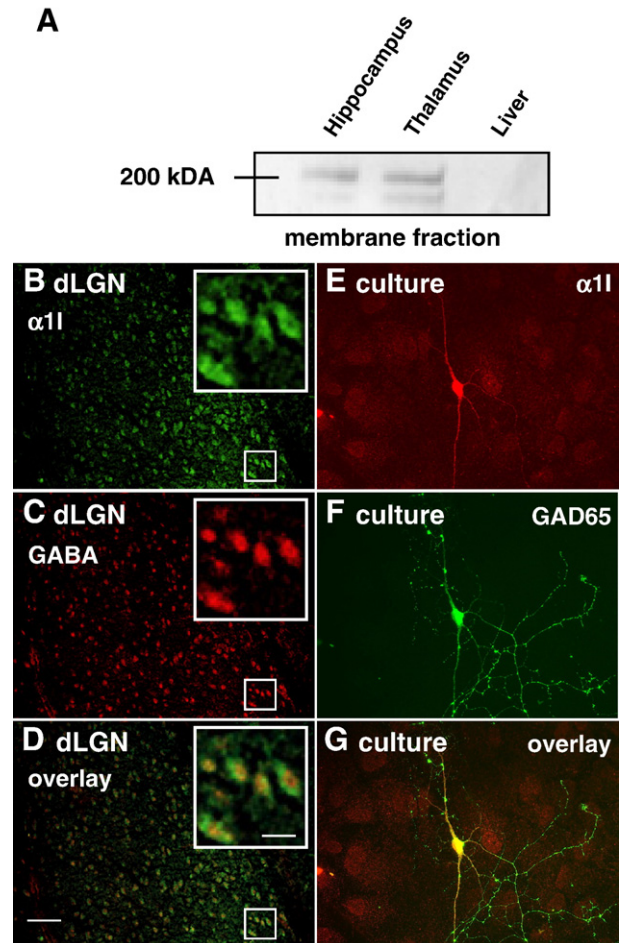


Fig. 5. Co-localization of α II and GABA in the dLGN of WAG/Rij and ACI rats and of α II and GAD65 in primary cultures of the dorsal thalamus. The depicted dLGN slices derived from a WAG/Rij rat. (A) A Western blot of the membrane fraction of hippocampal, thalamic and liver tissues was performed to test the α II antibodies specificity. Bands of the expected size (\sim 210 kDa) were present in membrane fractions of hippocampal and thalamic origin, but were absent in membrane fractions of the liver. A second band in hippocampus and thalamus is likely to represent degraded protein or channels prior to post-translational modification (cf. Alomone Labs; http://www.alomone.com/System/UploadFiles/DGGallery/Docs/ACC-009_AN-02.pdf). (B–D) Immunocytochemical staining of WAG/Rij dLGN slices using α II (B), and GABA (C) specific antibodies. The overlay is shown in (D) and demonstrates colocalization of α II and GABA in the dLGN. Similar observations were made in the dLGN of ACI rats. Enlarged inlays represent magnifications of the area indicated by small rectangles. Scale bars represent 100 μ m and 20 μ m for low and high magnifications, respectively. (E–G) Immunocytochemical staining of primary cultures of the dorsal thalamus using α II (E), and GAD65 (F) specific antibodies. The overlay is shown in (G).

Splice variations of CACNA1G transcripts in TC and interneurons

The expression of splice variants of CACNA1G mRNA was assessed next. The analysis focussed on the structure of the cytosolic linker between the channel homology domains III and IV on the border between exon 25 and 26, as previous studies in heterologous expression systems demonstrated an influence of alternative splicing of these exons on electrophysiological LVA Ca^{2+} channel properties (Chemin et al., 2001; Emerick et al., 2006). Primer locations were chosen to encompass the alternatively spliced 3' border of exon 25 and the complete exon 26. In total, three bands were detected (Fig. 6A). Sequencing revealed that the largest band contained the complete exons 25 and 26. This band was only detected in 2 out of 36 cells (data not shown). The band of intermediate size (upper band in Fig. 6B) lacked the 3' terminus of exon 25, while the smallest band was missing the complete exon 26 (lower band in Fig. 6B). The band of intermediate size will be referred to as Iso2 (analogous to human $\alpha 1G$ -bc) and the smallest band as Iso1 (analogous to human $\alpha 1G$ -a). The largest variant will be referred to as Iso3. TC neurons of both strains primarily expressed the Iso1 splice variant (WAG/Rij TC: Iso1: 5 of 9 cells; Iso2: 2 of 9 cells; Iso1 and Iso2: 2 of 9 cells; ACI TC: Iso1: 11 of 14 cells; Iso2: 0 of 14 cells; Iso1 and Iso2: 2 of 14 cells; Iso3: 1 of 14 cells; Fig. 6C), while the main splice variation in interneurons was Iso2 (WAG/Rij interneurons: Iso1: 1 of 6 cells; Iso2: 3 of 6 cells; Iso1 and Iso2: 1 of 6 cells; Iso3: 1 of 6 cells; ACI interneurons: Iso1: 1 of 6 cells; Iso2: 5 of 6 cells; Iso1 and Iso2: 0 of 6 cells; Iso3: 0 of 6 cells; Fig. 6C).

Modelling of somato-dendritic LVA Ca^{2+} channel distribution

Previous work suggests that LVA Ca^{2+} channels are primarily located in the dendrites and that local circuit interneurons display an increased dendritic channel density compared to TC neurons (Destexhe

et al., 1996, 1998; Munsch et al., 1997). To investigate whether a differential somato-dendritic distribution of LVA Ca^{2+} channels could contribute to the different electrophysiological LVA Ca^{2+} current properties of TC neurons and interneurons, a mathematical model was used. The model consisted of three compartments (soma, proximal dendrite, distal dendrite; Fig. 7A) and contained only the LVA Ca^{2+} current. All simulations were done in voltage clamp and assessed the somatically recorded steady-state activation characteristics of the LVA Ca^{2+} current. The model neuron was hyperpolarized to -100 mV for 720 ms and then stepped to increasingly positive test potentials for 260 ms. A family of LVA Ca^{2+} current traces evoked by this stimulation is shown in Fig. 7C. For the sake of simplicity, a purely somatic LVA Ca^{2+} channel localization was compared to a purely distal dendritic channel localization (Fig. 7B). Steady-state activation curves were constructed as described above and revealed half maximal activation values, which were shifted in the hyperpolarized direction for distal dendritic LVA Ca^{2+} channel localization when compared to the purely somatic distribution (V_h distal dendritic: -60 mV; V_h somatic: -57 mV).

This finding shows that a primarily dendritic localization of LVA Ca^{2+} channels in interneurons cannot account for the depolarized shift in LVA Ca^{2+} current voltage dependency observed in this cell type.

Modelling the effect of the shift in LVA Ca^{2+} current voltage dependency and the decrease in LVA Ca^{2+} current density on the LTS

To assess the functional consequences of a decreased LVA Ca^{2+} current density in combination with a depolarized shift in LVA Ca^{2+} current voltage dependency, a single compartmental model neuron was used. The model cell contained mathematical descriptions of the LVA Ca^{2+} current, the high voltage activated (HVA) Ca^{2+} current, Hodgkin Huxley type transient Na^+ and delayed rectifier K^+ currents, a persistent sodium current, the A-type K^+ current, a Ca^{2+} activated K^+

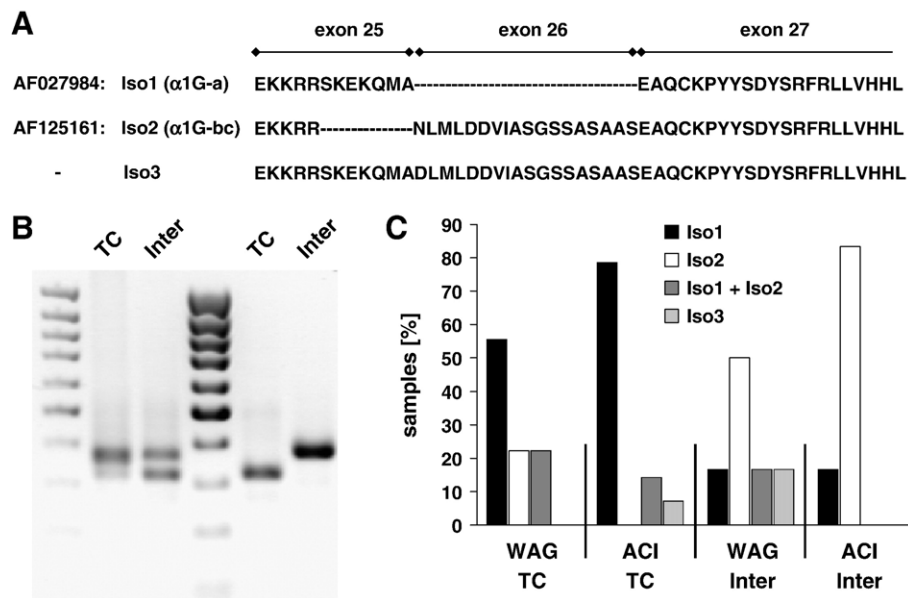


Fig. 6. Analysis of alternative splicing of exons 25 and 26 of the CACNA1G mRNA in WAG/Rij TC and interneurons. (A) Amino acid sequences corresponding to the three different cDNA sequences obtained through RT-PCR. Exon boundaries and accession numbers are indicated. (B) Agarose gel of a TC and an interneuron positive for Iso1 and Iso2 (left) and a TC neuron positive for Iso1 and an interneuron positive for Iso2 (right). All depicted neurons derived from WAG/Rij rats. A 100 bp ladder starting from 1000 bp was used to indicate band size. (C) Quantification of the splice variations detected in TC and interneurons of WAG/Rij and ACI rats.

conductance, as well as Na^+ and K^+ leak currents. The model was able to generate action potentials in the burst and the tonic firing modes characteristic of thalamic neurons. In the modelled interneuron the maximal LVA Ca^{2+} current permeability was set to 75% of that of the TC neuron model. In addition, the LVA Ca^{2+} current voltage dependency of the simulated interneuron was shifted by 10 mV in the depolarized direction in comparison to the TC neuron model (Fig. 8A lower panel). Otherwise all parameters were identical in the TC and interneuron models. Implementation of the changes of the LVA Ca^{2+} current led to a smaller LTS, which elicited fewer action potentials and displayed increased onset latency (Fig. 8A upper panel). The LTS generated by the modelled TC and interneuron resembled LTSs of TC and interneurons recorded in brain slice preparations (brain slice recordings were done in WAG/Rij; WAG/Rij TC neurons $n=5$, WAG/Rij interneurons $n=3$; Fig. 8B).

This finding shows that the implementation of the LVA Ca^{2+} current characteristics of a local circuit interneuron into a TC neuron

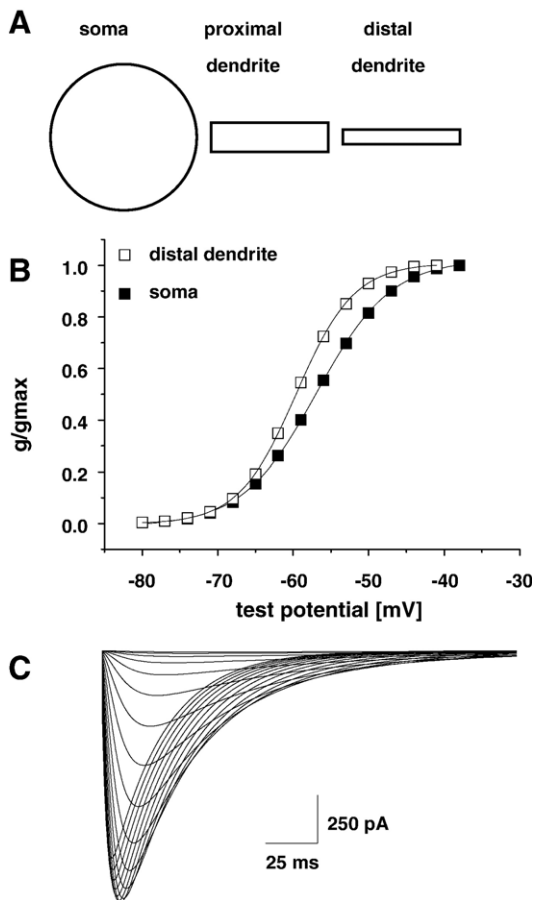


Fig. 7. Effects of different somatodendritic LVA Ca^{2+} channel distributions on the somatically recorded voltage dependency of activation in a model neuron. (A) Schematic illustration of the models morphology. The Model Neuron was composed of three compartments: the soma, the proximal dendrite, and the distal dendrite. (B) Somatically recorded steady state activation of LVA Ca^{2+} currents in a model with the complete LVA Ca^{2+} conductance located in the soma (filled squares), and a model with the complete LVA Ca^{2+} conductance located in the distal dendrite (open squares). The protocol consisted of a hyperpolarization to -100 mV for 720 ms followed by a depolarization to increasingly positive test potentials for 260 ms. Test potentials are plotted against normalized conductance. (C) Example of a family of LVA Ca^{2+} currents evoked by the steady state activation protocol.

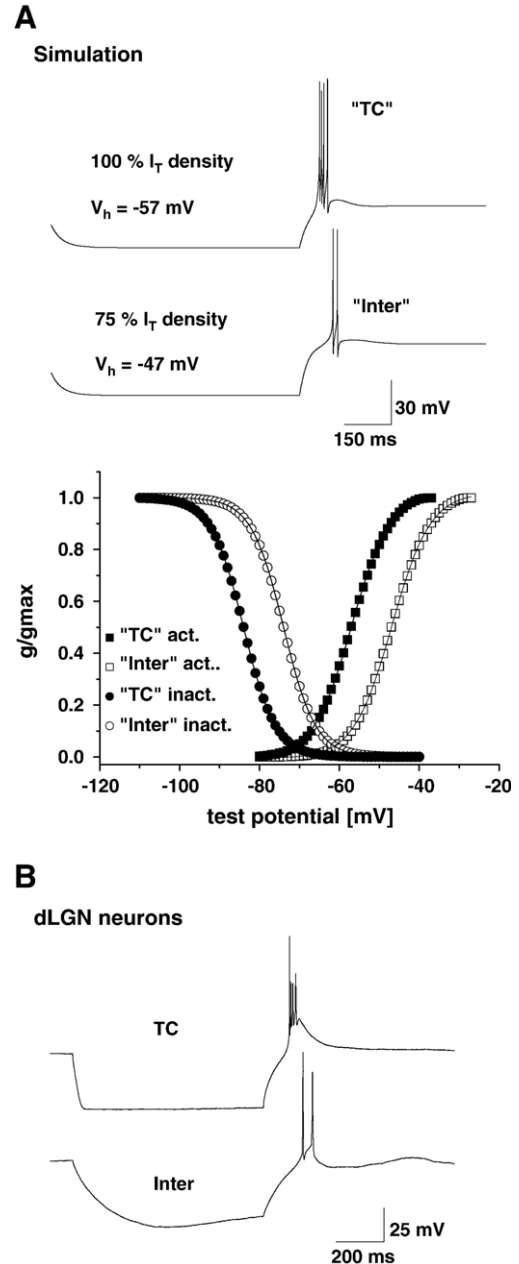


Fig. 8. Effect of the shift in LVA Ca^{2+} current voltage dependency and current density on the LTS of a simulated neuron. (A) The upper panel displays the LTS evoked by a simulated TC neuron. An implementation of a 10 mV depolarized shift of the LVA Ca^{2+} current voltage dependency (lower panel) and a reduction of the LVA Ca^{2+} current density to 75% of the TC neuron model led to a reduction in LTS amplitude, a reduction in LTS associated action potentials, and a delay in LTS onset latency, as shown in the middle panel. (B) For comparison LTSs generated by a dLGN TC neuron (TC, upper panel) and a dLGN local circuit interneuron (Inter, lower panel) recorded in a brain slice preparation are shown.

model changes the models burst firing pattern from TC neuron-like to interneuron-like.

Discussion

The present study is the first extensive comparison of Ca_v3 expression, LVA Ca^{2+} current properties and the LVA Ca^{2+} current-

dependent burst firing in thalamic interneurons and TC neurons in epileptic WAG/Rij and non-epileptic ACI rats. Our findings can be summarized as follows: (1) Interneurons revealed a lower LVA Ca^{2+} current density and more depolarized LVA Ca^{2+} current voltage dependency when compared to TC neurons. (2) These cell type specific differences were present irrespective of the epileptic and non-epileptic genotype. These results are confirmatory to our previous study conducted in Long Evans rats (Pape et al., 1994), a strain that is uncharacterized with respect to its epileptogenic potential. (3) In TC neurons the expression of LVA Ca^{2+} channel genes is restricted to $\alpha 1\text{G}$, while local circuit interneurons express $\alpha 1\text{G}$ and, in addition, the $\alpha 1\text{I}$ isoform. However $\alpha 1\text{I}$ expression levels in interneurons were about 16 times lower compared to $\alpha 1\text{G}$. (4) Alternative splicing of $\alpha 1\text{G}$ mRNA results in expression of the Iso1/ $\alpha 1\text{G}$ -a and Iso2/ $\alpha 1\text{G}$ -bc splice variant in TC neurons and interneurons, respectively. (5) Together with the results of the expression analysis of proteins related to the GABAergic signalling pathway and Ca^{2+} binding proteins, the expression of GAD65, GAD67, Iso2/ $\alpha 1\text{G}$ -bc, and $\alpha 1\text{I}$ as well as Iso1/ $\alpha 1\text{G}$ -a and parvalbumin can be regarded as specific combinations for interneurons and TC neurons, respectively. (6) Mathematical modelling demonstrated a hyperpolarized shift in somatically recorded LVA Ca^{2+} current voltage dependency with distal channel localization. (7) The model also revealed that the characteristic properties of LVA Ca^{2+} currents in interneurons (i.e., more depolarized voltage dependency and decreased current density in comparison to TC neurons) are sufficient to cause their specific burst firing. (8) Taken together it is concluded that the characteristic properties of LVA Ca^{2+} currents in interneurons exist in various rat strains irrespective of the epileptic background. The cell type-specific expression of $\alpha 1\text{G}$ splice variants is very likely the molecular basis of the observed LVA Ca^{2+} current voltage-dependency.

Molecular identification of dLGN neurons

The cellular morphology and synaptic connectivity of neurons in rat dLGN have been extensively studied. The distinction between relatively large (15–20 μm cell diameter), multipolar TC neurons projecting to the primary visual cortex, which are GAD/GABA immunonegative, and small (around 10 μm cell diameter), bipolar local circuit interneurons which react immunopositively for the presence of GAD or GABA, is generally accepted (Gabbott et al., 1986; Grossman et al., 1973; Ohara et al., 1983). Based on these criteria TC neurons and interneurons can be readily distinguished in populations of acutely isolated cells (Pape et al., 1994); Meuth et al., 2001). Thus, the presence of mRNA species coding for GAD65, GAD67, and ViAAT in a minority of TC neurons in the present study should be interpreted in light of the following evidence: (1) It has been suggested that the GAD67 isoform is involved in the synthesis of GABA for general metabolic activity which may take place in TC neurons and interneurons (Martin and Rimvall, 1993). (2) The presence of GAD mRNA in excitatory granule cells and CA1 pyramidal cells of the hippocampus as well as projection neurons of the amygdala has been noted before (Cao et al., 1996; Floyd et al., 2003; Sloviter et al., 1996; Sosulina et al., 2006; Telfeian et al., 2003). It has been suggested that GAD expression is regulated at the translational level in response to environmental influences like epileptic seizures and excitotoxic damage, thereby constituting network inhibition or GABA-mediated neurotrophic effects. The demonstration that TC neurons frequently contain GAD mRNA but lack GAD immunoreactivity supports this suggestion.

Expression of LVA Ca^{2+} channel $\alpha 1$ subunit isoforms in thalamic cell types

Many brain regions, including thalamic relay nuclei, reveal strong expression of $\alpha 1\text{G}$, while the expression of $\alpha 1\text{H}$ and $\alpha 1\text{I}$ is more restricted (for review see: Perez-Reyes, 2003). The present study extends these findings by demonstrating that $\alpha 1\text{H}$ expression was not detectable in isolated TC and interneurons, and may thus not contribute to the LVA Ca^{2+} current. In agreement with previous results (Perez-Reyes, 2003; Talley et al., 1999) we found $\alpha 1\text{G}$ to be the dominant isoform in both cell types. The functional impact of $\alpha 1\text{G}$ channels is indicated by the finding that physiological sleep-related oscillatory activity of the thalamocortical system critically involves this isoform in the thalamus (Anderson et al., 2005; Lee et al., 2004). Furthermore, mutant mice lacking the $\alpha 1\text{G}$ isoform are resistant to generation of SWD in response to pharmacological manipulations (Kim et al., 2001). With respect to the $\alpha 1\text{I}$ isoform, our results from *in situ* hybridization (15% $\alpha 1\text{I}$ -positive cells), RT-PCR and double staining experiments converge onto the conclusion that $\alpha 1\text{I}$ is expressed in dLGN interneurons, but not TC cells.

Since the contribution of LVA Ca^{2+} channels to neuronal excitability is related to the isoform-specific biophysical properties, the expression of $\alpha 1\text{I}$ in interneurons may result in specific functional consequences. Compared to $\alpha 1\text{G}$ and $\alpha 1\text{H}$, currents through $\alpha 1\text{I}$ channels show a positive shift in their steady-state activation and inactivation properties, slower activation and inactivation kinetics, and a larger more depolarized window current component in heterologous expression systems (Chemin et al., 2002; Lee et al., 1999; Monteil et al., 2000b). In agreement with these findings, the expression of $\alpha 1\text{I}$ in dLGN interneurons was correlated with the occurrence of a LVA Ca^{2+} current with slower kinetics and more depolarized steady-state properties compared to TC neurons. It should be noted, however, that other studies on recombinant LVA Ca^{2+} channels found no differences in steady-state voltage dependencies among LVA Ca^{2+} channel subtypes or a negative shift in $\alpha 1\text{I}$ steady-state inactivation (Klockner et al., 1999; McRory et al., 2001). Furthermore, the inactivation kinetics of $\alpha 1\text{I}$ carried currents were found to be about an order of magnitude slower than the inactivation kinetics of $\alpha 1\text{G}$ carried currents in all studies on recombinant LVA Ca^{2+} channels. Consequently, a significant contribution of $\alpha 1\text{I}$ channels to the whole-cell current of interneurons would be expected to result in strong slowing of current kinetics. However, the differences in inactivation kinetics of LVA Ca^{2+} currents observed between TC and interneurons were rather moderate. Together with the lower expression of CACNA1I mRNA in comparison to CACNA1G mRNA, this finding leads us to conclude that the $\alpha 1\text{I}$ isoform is not the primary determinant of the differences in somatically recorded LVA Ca^{2+} current voltage dependency and current kinetics of acutely isolated dLGN cell types.

Expression of $\alpha 1\text{G}$ splice variants in thalamic cell types

The splicing of human LVA Ca^{2+} channels has been extensively studied (Chemin et al., 2001; Emerick et al., 2006; Mittman et al., 1999a,b; Monteil et al., 2000a). In general, variations of LVA Ca^{2+} channel gene splicing are caused by exon skipping, where part or all of an exon is deleted. Alternative splicing of human $\alpha 1\text{G}$ has been found, *inter alia*, in the linker region connecting repeats III and IV, where exon 26 can be skipped in its entirety (human $\alpha 1\text{G}$ -a, Iso1), exon 25 can be spliced partially with exon 26 missing (human $\alpha 1\text{G}$ -b), and exon 26 can be spliced to the $\alpha 1\text{G}$ -b form of exon 25 (human $\alpha 1\text{G}$ -bc, Iso2). Rarely is exon 26 added to the full sequence of exon 25. In humans,

splicing of exons seems to be regulated in a tissue and age specific manner, with adult brain preferentially expressing $\alpha 1G$ -a and peripheral tissues expressing $\alpha 1G$ -bc (Emerick et al., 2006; Monteil et al., 2000a). Furthermore, splice variants differ in their electrophysiological behavior, with $\alpha 1G$ -bc activating and inactivating at about 5–10 mV more depolarized potentials and revealing slower kinetic properties (Chemin et al., 2001; Emerick et al., 2006).

To the best of our knowledge the present results are the first to demonstrate that a very similar splice pattern exists in rat neurons. In particular, $\alpha 1G$ -a/Iso1 and $\alpha 1G$ -bc/Iso2 are predominantly expressed in TC neurons and interneurons, respectively, while the full sequence is found in only about 3% of all investigated cells. For the following reasons it is concluded that the differences in LVA Ca^{2+} current voltage-dependency and current kinetics observed between TC and interneurons are primarily due to the expression of different splice variations of the $\alpha 1G$ isoform: (1) The $\alpha 1G$ isoform was expressed at much higher levels (~ 16 times higher under the assumption of similar primer probe efficiency) than the $\alpha 1I$ isoform in interneurons. (2) The difference in the kinetic properties of activation and inactivation observed in TC neurons and local circuit interneurons resemble the differences between $\alpha 1G$ -a and $\alpha 1G$ -bc found in heterologous expression systems (Chemin et al., 2001; Emerick et al., 2006). (3) The shift in LVA Ca^{2+} current voltage dependency between $\alpha 1G$ -a and $\alpha 1G$ -bc (Chemin et al., 2001; Emerick et al., 2006) as well as the shift between $\alpha 1G$ and $\alpha 1I$ (Chemin et al., 2002) was roughly equal in studies on heterologous expression systems. The shift in LVA Ca^{2+} current voltage-dependency of TC neurons and local circuit interneurons resembled the differences found for both $\alpha 1G$ -a vs. $\alpha 1G$ -bc and $\alpha 1G$ vs. $\alpha 1I$ in expression systems (Chemin et al., 2001, 2002; Emerick et al., 2006). In summary, the low expression level of the $\alpha 1I$ isoform and the rather small differences in current kinetics vote for an effect based primarily on splice variant expression. Nevertheless, both variations may act synergistically in producing the observed differences.

Functional implications of differential LVA Ca^{2+} channel expression

The functional correlate of LVA Ca^{2+} current activation is the generation of a LTS, which in turn triggers a high-frequency burst of typically 2–7 action potentials (Huguenard, 1996). Despite the expression of two $\alpha 1$ isoforms and the presence of LVA Ca^{2+} current, the LTS amplitude in interneurons is quite variable, ranging from subthreshold depolarization towards the generation of one to several action potentials in individual cells (Munsch et al., 2005; Pape et al., 1994; Pape and McCormick, 1995; Zhu et al., 1999b). This variability in LTS form and amplitude reflects the functional interaction between the LVA Ca^{2+} current and a transient K^+ current, I_A , whose voltage-dependent properties widely overlap (Pape et al., 1994; Pape and McCormick, 1995). The alternative splicing of $\alpha 1G$ and the exclusive expression of $\alpha 1I$ in interneurons are likely to critically contribute to the differences in LVA Ca^{2+} current observed in these neurons. The results from mathematical modelling are in favour of this hypothesis, as implementation of an interneuron-like LVA Ca^{2+} current into a TC neuron model changed the burst firing behavior of the modelled neuron to the one observed in local circuit interneurons in brain slices. Furthermore, mathematical modelling data excluded a preferential dendritic distribution of LVA Ca^{2+} channels as the basis for a depolarized voltage-dependency of the LVA Ca^{2+} current in interneurons. However, it can not be excluded that somato-dendritic channel distribution and the overall cellular morphology influence the burst activity of dLGN TC and interneurons (Destexhe et al., 1996,

1998; Munsch et al., 1997; Williams and Stuart, 2000; Zhou et al., 1997).

Although the LTS is the main voltage expression of LVA Ca^{2+} channel activity, these channels generate a physiologically relevant window current at the region of overlap between steady-state activation and inactivation curves (Chevalier et al., 2006; Hughes et al., 1999; Perez-Reyes, 2003; Williams et al., 1997). In TC neurons the functional interaction between the window Ca^{2+} current and the leak K^+ current, I_{Leak} , can generate a bistable system which shows two stable (resting) membrane potentials in the absence of other substantial currents in this voltage region (Crunelli et al., 2005). Similar bistable behavior may be expected for interneurons, though with the stable equilibrium points shifted to more depolarized potentials compared to TC neurons. In this way $\alpha 1G$ -bc- and $\alpha 1I$ -influenced bistability in interneurons could shape the rhythmic activity of the thalamocortical network during natural sleep and absence epilepsy.

In conclusion the present study suggests that alternative splicing of the $\alpha 1G$ isoform in dLGN TC and interneurons, and the exclusive expression of the $\alpha 1I$ isoform in interneurons play a prominent role in setting the different LVA Ca^{2+} current properties of TC and interneurons, which in turn critically contributes to the diverging burst firing behavior of these neurons. In addition, the differences in LVA Ca^{2+} current properties were unaffected by an epileptic genotype, indicating a phenomenon of general physiological relevance.

Experimental methods

Preparation

All animal procedures were approved by local authorities. In the present study the WAG/Rij model (Harlan Winkelmann GmbH, Borcheln, Germany) was compared with rats of the ACI strain (bred in house), the only inbred rat strain free of spike and wave activity (Coenen and Van Luitelaar, 2003; Inoue et al., 1990). Rats (P15–P25) were deeply anaesthetized using halothane and decapitated. Brains were removed and placed in cold, oxygenated artificial cerebrospinal fluid (ACSF) containing (mM): Sucrose, 210; PIPES, 20; KCl, 2.4; $MgCl_2$, 10; $CaCl_2$, 0.5; dextrose, 10; pH 7.25 with NaOH. Thalamic slices (500 μm) were obtained from coronal vibratome sections (Model 1000, Ted Pella, Redding, CA) and dLGN tissue was transferred to a spinner flask and incubated for 25–30 min at 30 °C in an oxygenated solution containing trypsin (0.5–1 mg/ml, Sigma, Taufkirchen, Germany; used for electrophysiology) or papain (0.5–1 mg/ml, Sigma; used for RT-PCR, *in situ* hybridization, and immunocytochemistry) and (mM): NaCl, 120; KCl, 5; $MgCl_2$, 3; $CaCl_2$, 1; PIPES, 20; dextrose, 25; pH adjusted to 7.35 with NaOH.

Preparation of brain slices was performed as described previously (Budde et al., 2005). Briefly, slices (300 μm) were prepared as described for acutely isolated cells and transferred into a holding chamber where they were heated to 30 °C for 20 min and allowed to rest for 60 to 90 min. The holding chamber was filled with a solution of the following composition (mM): $CaCl_2$, 3; KCl, 2.5; NaCl, 125; $MgSO_4$, 4; NaH_2PO_4 , 1.25; $NaHCO_3$, 22; dextrose, 10; pH ~ 7.4 .

Electrophysiology

Single neurons were obtained by trituration and whole-cell recordings were performed at room temperature using borosilicate glass pipettes (GC150TF-10, Clark Electromedical Instruments, Pangbourne, UK) connected to an EPC-7 amplifier (E.S.F. electronics, Friedland, Germany). Cell type identification was performed according to the criteria described in the Results section. Recordings were done on cells from rats older than postnatal day 15. The typical electrode resistance was 3–5 M Ω , while access resistance was in the range of 3–8 M Ω . Voltage clamp experiments were governed by pClamp software, operating via an interface (Digidata

1200, Axon Instruments, Foster City, CA). The following recording solutions were used: i.) Extracellular solution (mM): NaCl, 112; CsCl, 4; KCl, 1; HEPES, 10; dextrose, 10, MgCl₂, 0.5; CaCl₂, 5.5; TTX, 0.001; TEA-Cl, 20; 4-AP, 6; pH 7.35 with NaOH. ii.) Intracellular solution: Cs-gluconate, 85; Cs₃-citrate, 10; NaCl, 10; KCl, 1; EGTA, 5.5; CaCl₂, 0.5; MgCl₂, 0.25; HEPES, 10; TEA-Cl, 15; Mg-ATP, 3; Na₂-GTP, 0.5, phosphocreatin 15; pH 7.25 with NaOH. Data were not corrected for the liquid junction potential (Neher, 1992). Osmolarity of internal and external solution were kept at 295 and 305 mosM, respectively.

Recordings in brain slice preparations were done as described previously (Budde et al., 2005), using the following solutions: i) Extracellular solution (mM): CaCl₂, 1.5; KCl, 2.5; NaCl, 120; MgSO₄, 2; NaH₂PO₄, 1.25; HEPES, 30; dextrose, 10; pH 7.24 with NaOH; ~300 mosM. ii) Intracellular solution (mM): CaCl₂, 0.5; NaCl, 10; MgCl₂, 1; HEPES, 10; K-BAPTA, 5; K-gluconate, 95; K₃-citrate, 20; phosphocreatine, 15; Na₂-GTP, 0.5; Mg-ATP, 3; Biocytin; 3 mg/ml internal solution; pH 7.24 with KOH; ~290 mosM. Interneurons were identified according to input resistance and cellular capacitance (Zhu et al., 1999b). An EPC 10 (HEKA) amplifier and Pulse (HEKA) software was used for brain slice recordings. Typical electrode resistances ranged from 1.8 to 2.5 MΩ.

All results were presented as mean±S.E.M. Statistical significance was tested using Student's *t*-test. Differences were considered statistically significant if *p*<0.05.

Collection of identified cells

For isoform expression experiments single neurons were obtained by trituration and placed on membrane coated object slides (PALM MembraneSlides, P.A.L.M. Microlaser Technologies AG, Bernried, Germany). Cells were allowed to adhere to the membrane for 1 h. Thereafter object slides were placed under an inverted laser capture microscope (P.A. L.M. Microlaser Technologies AG) and 10–15 identified neurons were collected in tubes and frozen in liquid nitrogen for further processing. Batches containing equal numbers of cells were compared for quantitative analysis.

For splice variation analysis single neurons were obtained by trituration and placed on an object slide and allowed to settle for 20 min. After this, identified single TC- and interneurons were collected with borosilicate glass pipettes with a tip diameter of ~10 μm, and subjected to RT-PCR procedures.

Preparation of dissociated cell cultures from the dorsal thalamus

Dorsal thalami were prepared from embryos (E 19), subsequently transferred into ice cold Hanks Balanced Salt Solution (HBSS, without Ca/Mg), and washed 3 times. Thereafter thalami were incubated in HBSS containing 0.5% Trypsin for 20 min at 37 °C, washed, and transferred into tubes filled with 2 ml HBSS, containing 0.01% DNaseI. For dissociation, thalamic tissue was slowly pressed 3 times through a 0.9 mm-gauged needle followed by 3 times pressuring through a 0.45 mm-gauged needle. The cell suspension was poured through a Nylon-tissue (mesh aperture 125 μm) into a 50 ml tube and filled up with 18 ml Dulbecco's modified Eagle Medium (DMEM; Gibco, Eggenstein, Germany). Five hundred microliters suspension (density of 16.000 cells/ml) was placed on each well of a 24-well plate, containing poly-D-lysine coated cover slips. Cell cultures were incubated at 37.0 °C and 5% CO₂ up to the appropriate time points and finally fixed with 4% PFA for 10 min.

Immunocytochemistry of acutely isolated dLGN neurons and cell cultures from the dorsal thalamus

Acutely isolated cells adhered to poly-L-lysine-coated glass slides, were fixed by increasing concentrations of paraformaldehyde (0.4%, 1.2%, and 3% 2 PFA in PBS for 2 min each, 4% PFA in PBS for 4 min), and treated with 0.3% H₂O₂ for 30 min followed by washing in PBS. After washing, cells were blocked in 10% normal goat serum, 2% BSA, 0.3% Triton X-100 in PBS for 1 h and then incubated with primary antibodies (mouse anti-GAD65 or mouse anti-GAD67, Chemicon International; 1:1000 for both)

overnight at 4 °C. Secondary antibodies (biotinylated anti-mouse Abs, Vector Labs; PK 4000, 1:100) were applied for 1 h. Detection was done using an avidin-biotin-peroxidase system (ABC-Kit, Vector Laboratories, USA) with 3,3'-diaminobenzidine as a chromogene (0.05% solution in 0.01% H₂O₂, 0.02% (NH₄)₂Ni(SO₄)₂, and 0.025% CoCl₂) resulting in an enhanced dark grey to black staining of positively labelled neurons.

Cultured cells were washed in PBS, fixed and subsequently pre-incubated at 4 °C in blocking solution (as above). After 1 h, primary antibodies against GAD65 and parvalbumin or αII (rabbit polyclonal antibody to parvalbumin, 1:500, SWANT, Switzerland; rabbit anti-αII, Alomone Labs, product No. ACC-009, 1:500) were added and incubated overnight. After washing with PBS containing 0.3% Triton X-100 cultures were incubated with secondary antibodies (Cy3-conjugated rabbit anti-mouse IgG, 1:1000, Dianova, Hamburg, Germany; Alexa Fluor 488-conjugated goat anti-rabbit IgG, 1:1000, Molecular Probes, Eugene, OR, USA; in blocking solution) for 2 h at RT, washed again and cover slipped with Moviol.

For negative controls, occlusion of the primary antibody from the staining procedure was routinely performed with no positive immunological signal detected.

Immunocytochemistry of brain sections

Rat brain fresh-frozen sections (16 μm) were fixed in 4% paraformaldehyde followed by washing in PBS for 3 × 10 min. After blocking in 10% normal goat serum, 2% BSA in PBS for 2 h at RT sections were incubated with primary antibodies (guinea pig anti-GABA, Abcam; 1:500 and rabbit anti-αII, Alomone Labs; 1:700 in 2% normal goat serum, 2% BSA in PBS) overnight at 4 °C. Next day, sections were washed with PBS and incubated with secondary antibodies (Cy3-conjugated goat anti-guinea pig IgG and Cy2-conjugated goat anti-rabbit IgG, Dianova, Hamburg, Germany; 1:400 for both in 2% normal goat serum, 2% BSA in PBS) for 2 h at RT, washed again and cover slipped with Immumount. For negative controls occlusion of the primary antibody from the staining procedure were routinely performed with no positive immunological signal detected.

Western blotting procedures

For immuno-blot experiments 30 μg of solubilized protein fractions were separated on 5–20% SDS-polyacrylamide gradient gels and subsequently transferred to nitrocellulose membranes (90 min, 200 mA). The transfer buffer contained 25 mM Tris, 192 mM glycine, 0.02% SDS and 20% methanol. After blotting, membranes were blocked with 5% dry milk and 0.1% Tween 20 in 1 × TBS (Tris buffered saline) for 2 h and subsequently incubated at 4 °C overnight with a 1:200 dilution of antibodies raised against αII (rabbit anti-αII, Alomone Labs) in 1 × TBS containing 0.1% Tween 20. After final washing steps, the blots were incubated with HRP-conjugated secondary antibodies (1:4000) for 2 h, washed again and finally developed using ECL films.

In situ hybridization

Rat brains were removed and frozen in –50 °C isopentane. Cryostat coronal sections of 16 μm thickness were cut at the level of the dLGN, thaw-mounted onto silane-coated slide glasses and air-dried. Acutely isolated cells adhered to poly-L-lysine-coated glass slides were prepared as above. Digoxigenin-labeled antisense and sense riboprobes were generated by *in vitro* transcription from vectors containing cDNA of rat α1G (corresponding to bp 6376–6732, AF027984), α1H (bp 3093–3393, AF290213), αII (bp 5294–5617, AF290214) and the entire open reading frames of mouse GAD65 and GAD67 (NM_008078 and NM_00877, respectively). For *in situ* hybridization sections or cells were fixed in 4% paraformaldehyde followed by washing in PBS for 3 × 5 min and then treated with 0.1 μg/ml proteinase K for 30 min at 37 °C. Subsequently slices were washed (3 × 5 min, PBS), acetylated and prehybridized for 2 h at 37 °C. The prehybridization solution consisted of 50% formamide, 5 × SSC, 1 × Denhardt's solution, 0.5 mg/ml yeast tRNA and 1.0 mg/ml total yeast RNA. For hybridization sections were exposed in 50% formamide, 1 ×

Denhardt's solution, 0.1 mg/ml yeast tRNA, 0.1 mg/ml total yeast RNA, 10% Dextran sulphate, 0.125% SDS, 10 mM Tris-HCl (pH 7.5), 1 mM EDTA and 300 mM NaCl. Digoxigenin-labeled RNA probes were added (with a final concentration of 50 pg/ml) and sections were incubated at 45 °C for 16–18 h. For all steps, RNase-free solutions were used. Following hybridization, sections were subjected to washes of increasing stringency including 2× SSC at room temperature (1×2 min), 50% formamide/2× SSC at 48.5 °C for α1G-I or 55 °C for GAD65/67 (2×30 min), 50% formamide/0.2× SSC at 48.5/55 °C (2×60 min) and 50% formamide/0.1× SSC at 48.5/55 °C (1×60 min). Labeled cells were detected with an anti-digoxigenin antibody tagged with alkaline phosphatase (1:500, Roche, Germany). Staining was carried out using 4-nitro blue tetrazolium chloride and 5-bromo-4-chloro-3-indolyl phosphate as substrates (Roche, Germany).

Specificity of the hybridization reaction was verified by substituting labeled sense probes for the antisense probes. No labeling was observed under these conditions.

In situ hybridization combined with immunocytochemistry

For double-labeling, fresh-frozen sections were processed first for *in situ* hybridization for α1I. Thereafter sections were subjected to 0.3% H₂O₂ for 30 min and washed with TBS before being incubated with primary antibodies (rabbit anti-parvalbumin, 1:1000, SWANT, Switzerland) overnight at 4 °C in 2% normal goat serum, 2% BSA, 0.3% Triton X-100 in TBS. Primary antibodies were detected using an avidin-biotin-peroxidase detection system (ABC-Kit, Vector Laboratories, USA) with 3,3'-diaminobenzidine as a chromogene (0.02% solution in 0.005% H₂O₂).

Reverse transcription and RT-PCR assays

Quantitative RT-PCR analysis was performed on dLGN tissue and on samples of identified acutely isolated cells. Total RNA from freshly dissected tissue was prepared by extraction with Trizol reagent according to the manufacturer's instructions (RNeasy Lipid Tissue, Qiagen, Germany). First-strand cDNA was primed with oligo(dT)₁₈ primers (Roche, IN, USA) from 0.5–1 μg of mRNA and synthesized using the SuperScript II enzyme (Invitrogen Life Technologies) at 42 °C for 50 min. The mRNA of collected cells was transcribed into cDNA using oligo(dT)₁₈ primers (Roche, Germany) and the Sensiscript RT Kit (Qiagen, Hilden, Germany). The hybridization primer/probe assays for real-time PCR detection were purchased from Applied Biosystems. Following intron spanning assay-on-demand probes were used: α1G: Rn0058105_m1; α1H: Rn01460351_g1; α1I: Rn00571684_m1; β₂-microglobulin: Rn00560865_m1; GAD65: Rn00561244_m1; GAD67: Rn00566593; ViAAT: Rn00824654_m1. Real time PCR was performed using the TaqMan universal PCR Master Mix (Applied Biosystems) and the ABI Prism 7000 Sequence Detection System (Applied Biosystems); PCR program was: 2 min at 50 °C, 10 min at 95 °C, 50 cycles: 15 s at 95 °C and 1 min at 60 °C. Results were analyzed with the ABI Prism 7000 SDS software. The efficiency of real time primer/probes was nearly identical. Quantification was done using the comparative C_T or ΔΔC_T method as described earlier (Budde et al., 2005).

Non-quantitative RT-PCR for detection of splice variations was performed on single identified dLGN TC- and interneurons. Reverse transcription was done using the Revert Aid First Strand cDNA Synthesis Kit (Fermentas, Germany). All probes as well as bath solutions from which cells were collected were subjected to an amplification of GAPDH. Probes were further analyzed only if the neuron was positive and the bath was negative for GAPDH. The PCR protocol for GAPDH amplification was: 3 min 94 °C; 50 cycles (30 s 94 °C, 1 min 61 °C, 1 min 72 °C); 7 min 72 °C. Primer sequences for GAPDH (nucleotides 789–1028, accession No. NM017008) were: forward, 5'-TGATGACATCAAGAAGGTGGTGA-3'; reverse, 5'-TCCTTGGAGCCATGTAGCCAT-3'. Amplification of the exon 25, 26 region was done using a nested PCR approach. The PCR protocol for the multiplex step was: 3 min 94 °C; 50 cycles (30 s 94 °C, 1 min 62 °C, 1 min 72 °C); 7 min 72 °C. The PCR protocol for the nested step was: 3 min 94 °C; 35 cycles (30 s 94 °C, 1 min 64 °C, 1 min 72 °C); 7 min 72 °C. Primer

sequences for the multiplex step were (nucleotides 4557–5361; accession No. AF290212): forward, 5'-CAGCAGCCATCATGAACCACAC-3'; reverse, 5'-GCCGACCAAGCCCTCACAAG-3'. Primer sequences for the nested step were (nucleotides 4709–5034; accession No. AF290212): forward, 5'-GCGGCGTGAGGAGAAGCGACTAC-3'; reverse, 5'-CCTGGAA-GAAACGGCGGAAGC-3'. For all non-quantitative PCRs the Taq DNA Polymerase (5 U/μl, Quiagen) was used.

Modelling

For computer simulations on the cellular LVA Ca²⁺ channel distribution a TC neuron model (Huguenard and McCormick, 1992; McCormick and Huguenard, 1992) was adapted, as described previously (Hines and Carnevale, 2001; Meuth et al., 2006). Two further compartments were added to allow the simulation of a differential LVA Ca²⁺ current distribution between soma, distal, and proximal dendrite. The soma had a diameter of 30 μm and a length of 30 μm. The dendritic compartments were each 50 μm long and had diameters of 2 μm (proximal dendrite) and 1 μm (distal dendrite). The model was based solely on the mathematical description of the LVA Ca²⁺ current (I_T). All simulations were done in voltage clamp. The LVA Ca²⁺ current was adapted from Huguenard and McCormick (1992). Simulations were carried out at 25 °C.

For computer simulations addressing the effects of an alteration of the LVA Ca²⁺ current on the LTS, a single compartment TC neuron model was adapted, as described previously (Meuth et al., 2006). The model was based on the mathematical description of I_{K leak}, I_{Na leak}, I_L, I_T, I_{Na HH}, I_{NaP}, I_{K HH}, I_A, and I_{KCa}. Neuronal membrane potential was described by the following equation: C_M(dV/dt) = -I_M + I_{inject}. I_M is the sum of all membrane currents, I_{inject} is the injected current, and C_M is the membrane capacitance. The model was capable of generating action potentials in both burst and tonic transmission modes. Simulations were carried out at 35 °C.

Acknowledgments

Supported by DFG (BU 1019/7-1; Pa 336/17-1), Innovative Medizinische Forschung (IMF; BU 120501), and Interdisziplinäres Zentrum für Klinische Forschung (IZKF; Bud/005/07). T. Broicher was a fellow of the Boehringer Ingelheim Foundation. Thanks are due to A. Jahn, A. Markovic, S. Mücke, E. Naß, S. Vorwerk, and R. Ziegler for excellent technical assistance.

References

- Ahlsen, G., Lindstrom, S., Lo, F.S., 1984. Inhibition from the brain stem of inhibitory interneurons of the cat's dorsal lateral geniculate nucleus. *J. Physiol.* 347, 593–609.
- Anderson, M.P., Mochizuki, T., Xie, J., Fischler, W., Manger, J.P., Talley, E.M., Scammell, T.E., Tonegawa, S., 2005. Thalamic Cav3.1 T-type Ca²⁺ channel plays a crucial role in stabilizing sleep. *Proc. Natl. Acad. Sci. U. S. A.* 102, 1743–1748.
- Budde, T., Caputi, L., Kanyshkova, T., Staak, R., Abrahamczik, C., Munsch, T., Pape, H.C., 2005. Impaired regulation of thalamic pacemaker channels through an imbalance of subunit expression in absence epilepsy. *J. Neurosci.* 25, 9871–9882.
- Budde, T., Pape, H.-C., Kumar, S.S., Huguenard, J.R., 2006. Thalamic, thalamo-cortical, and cortico-cortical models of epilepsy with an emphasis on absence seizures. In: Pitkänen, A., Schwartzkroin, P.A., Moshé, S.L. (Eds.), *Models of Seizures and Epilepsy*. Elsevier, Amsterdam, pp. 73–88.
- Burke, W., Jervie Sefton, A., 1966. Discharge patterns of principal cells and interneurons in lateral geniculate nucleus of rat. *J. Physiol.* 187, 201–212.
- Cao, Y., Wilcox, K.S., Martin, C.E., Rachinsky, T.L., Eberwine, J., Dichter, M.A., 1996. Presence of mRNA for glutamic acid decarboxylase in both excitatory and inhibitory neurons. *Proc. Natl. Acad. Sci. U. S. A.* 93, 9844–9849.

- Chemin, J., Monteil, A., Bourinet, E., Nargeot, J., Lory, P., 2001. Alternatively spliced alpha(1G) (Ca(V)3.1) intracellular loops promote specific T-type Ca(2+) channel gating properties. *Biophys. J.* 80, 1238–1250.
- Chemin, J., Monteil, A., Perez-Reyes, E., Bourinet, E., Nargeot, J., Lory, P., 2002. Specific contribution of human T-type calcium channel isoforms (alpha(1G), alpha(1H) and alpha(1I)) to neuronal excitability. *J. Physiol.* 540, 3–14.
- Chevalier, M., Lory, P., Mironneau, C., Macrez, N., Quignard, J.F., 2006. T-type CaV3.3 calcium channels produce spontaneous low-threshold action potentials and intracellular calcium oscillations. *Eur. J. Neurosci.* 23, 2321–2329.
- Coenen, A.M., Van Luijckelaar, E.L., 2003. Genetic animal models for absence epilepsy: a review of the WAG/Rij strain of rats. *Behav. Genet.* 33, 635–655.
- Coulter, D.A., Huguenard, J.R., Prince, D.A., 1989. Specific petit mal anticonvulsants reduce calcium currents in thalamic neurons. *Neurosci. Lett.* 98, 74–78.
- Crunelli, V., Leresche, N., 2002. Childhood absence epilepsy: genes, channels, neurons and networks. *Nat. Rev., Neurosci.* 3, 371–382.
- Crunelli, V., Toth, T.I., Cope, D.W., Blethyn, K., Hughes, S.W., 2005. The 'window' T-type calcium current in brain dynamics of different behavioural states. *J. Physiol.* 562, 121–129.
- Crunelli, V., Cope, D.W., Hughes, S.W., 2006. Thalamic T-type Ca²⁺ channels and NREM sleep. *Cell Calcium* 40, 175–190.
- Deschenes, M., Paradis, M., Roy, J.P., Steriade, M., 1984. Electrophysiology of neurons of lateral thalamic nuclei in cat: resting properties and burst discharges. *J. Neurophysiol.* 51, 1196–1219.
- Destexhe, A., Contreras, D., Steriade, M., Sejnowski, T.J., Huguenard, J.R., 1996. In vivo, in vitro, and computational analysis of dendritic calcium currents in thalamic reticular neurons. *J. Neurosci.* 16, 169–185.
- Destexhe, A., Neubig, M., Ulrich, D., Huguenard, J., 1998. Dendritic low-threshold calcium currents in thalamic relay cells. *J. Neurosci.* 18, 3574–3588.
- Emerick, M.C., Stein, R., Kunze, R., McNulty, M.M., Regan, M.R., Hanck, D.A., Agnew, W.S., 2006. Profiling the array of Ca(v)3.1 variants from the human T-type calcium channel gene CACNA1G: alternative structures, developmental expression, and biophysical variations. *Proteins* 64, 320–342.
- Floyd, D.W., Jung, K.Y., McCool, B.A., 2003. Chronic ethanol ingestion facilitates N-methyl-D-aspartate receptor function and expression in rat lateral/basolateral amygdala neurons. *J. Pharmacol. Exp. Ther.* 307, 1020–1029.
- Gabbott, P.L., Somogyi, J., Stewart, M.G., Hamori, J., 1986. A quantitative investigation of the neuronal composition of the rat dorsal lateral geniculate nucleus using GABA-immunocytochemistry. *Neuroscience* 19, 101–111.
- Grossman, A., Lieberman, A.R., Webster, K.E., 1973. A Golgi study of the rat dorsal lateral geniculate nucleus. *J. Comp. Neurol.* 150, 441–466.
- Hines, M.L., Carnevale, N.T., 2001. NEURON: a tool for neuroscientists. *Neuroscientist* 7, 123–135.
- Hughes, S.W., Cope, D.W., Toth, T.I., Williams, S.R., Crunelli, V., 1999. All thalamocortical neurones possess a T-type Ca²⁺ 'window' current that enables the expression of bistability-mediated activities. *J. Physiol.* 517 (Pt 3), 805–815.
- Huguenard, J.R., 1996. Low-threshold calcium currents in central nervous system neurons. *Annu. Rev. Physiol.* 58, 329–348.
- Huguenard, J.R., McCormick, D.A., 1992. Simulation of the currents involved in rhythmic oscillations in thalamic relay neurons. *J. Neurophysiol.* 68, 1373–1383.
- Huguenard, J.R., Prince, D.A., 1994. Intrathalamic rhythmicity studied in vitro: nominal T-current modulation causes robust antioscillatory effects. *J. Neurosci.* 14, 5485–5502.
- Inoue, M., Peeters, B.W., van Luijckelaar, E.L., Vossen, J.M., Coenen, A.M., 1990. Spontaneous occurrence of spike-wave discharges in five inbred strains of rats. *Physiol. Behav.* 48, 199–201.
- Jones, E.G., Hendry, S.H., 1989. Differential calcium binding protein immunoreactivity distinguishes classes of relay neurons in monkey thalamic nuclei. *Eur. J. Neurosci.* 1, 222–246.
- Kim, D., Song, I., Keum, S., Lee, T., Jeong, M.J., Kim, S.S., McEnery, M.W., Shin, H.S., 2001. Lack of the burst firing of thalamocortical relay neurons and resistance to absence seizures in mice lacking alpha(1G) T-type Ca(2+) channels. *Neuron* 31, 35–45.
- Klockner, U., Lee, J.H., Cribbs, L.L., Daud, A., Hescheler, J., Peverzev, A., Perez-Reyes, E., Schneider, T., 1999. Comparison of the Ca²⁺ currents induced by expression of three cloned alpha1 subunits, alpha1G, alpha1H and alpha1I, of low-voltage-activated T-type Ca²⁺ channels. *Eur. J. Neurosci.* 11, 4171–4178.
- Lee, J.H., Daud, A.N., Cribbs, L.L., Lacerda, A.E., Peverzev, A., Klockner, U., Schneider, T., Perez-Reyes, E., 1999. Cloning and expression of a novel member of the low voltage-activated T-type calcium channel family. *J. Neurosci.* 19, 1912–1921.
- Lee, J., Kim, D., Shin, H.S., 2004. Lack of delta waves and sleep disturbances during non-rapid eye movement sleep in mice lacking alpha1G-subunit of T-type calcium channels. *Proc. Natl. Acad. Sci. U. S. A.* 101, 18195–18199.
- Llinas, R.R., Steriade, M., 2006. Bursting of thalamic neurons and states of vigilance. *J. Neurophysiol.* 95, 3297–3308.
- Martin, D.L., Rinvall, K., 1993. Regulation of gamma-aminobutyric acid synthesis in the brain. *J. Neurochem.* 60, 395–407.
- McCormick, D.A., Huguenard, J.R., 1992. A model of the electrophysiological properties of thalamocortical relay neurons. *J. Neurophysiol.* 68, 1384–1400.
- McKay, B.E., McRory, J.E., Molineux, M.L., Hamid, J., Snutch, T.P., Zamponi, G.W., Turner, R.W., 2006. Ca(V)3 T-type calcium channel isoforms differentially distribute to somatic and dendritic compartments in rat central neurons. *Eur. J. Neurosci.* 24, 2581–2594.
- McRory, J.E., Santi, C.M., Hamming, K.S., Mezeyova, J., Sutton, K.G., Baillie, D.L., Stea, A., Snutch, T.P., 2001. Molecular and functional characterization of a family of rat brain T-type calcium channels. *J. Biol. Chem.* 276, 3999–4011.
- Meuth, S., Budde, T., Pape, H.-C., 2001. Differential control of high voltage activated Ca²⁺ current components by a Ca²⁺-dependent inactivation mechanism in thalamic relay neurons. *Thal. Rel. Sys.* 1, 31–38.
- Meuth, S.G., Kanyshkova, T., Landgraf, P., Pape, H.C., Budde, T., 2005. Influence of Ca²⁺-binding proteins and the cytoskeleton on Ca²⁺-dependent inactivation of high-voltage activated Ca²⁺ currents in thalamocortical relay neurons. *Pflugers Arch.* 450, 111–122.
- Meuth, S.G., Kanyshkova, T., Meuth, P., Landgraf, P., Munsch, T., Ludwig, A., Hofmann, F., Pape, H.C., Budde, T., 2006. Membrane resting potential of thalamocortical relay neurons is shaped by the interaction among TASK3 and HCN2 channels. *J. Neurophysiol.* 96, 1517–1529.
- Mittman, S., Guo, J., Agnew, W.S., 1999a. Structure and alternative splicing of the gene encoding alpha1G, a human brain T calcium channel alpha1 subunit. *Neurosci. Lett.* 274, 143–146.
- Mittman, S., Guo, J., Emerick, M.C., Agnew, W.S., 1999b. Structure and alternative splicing of the gene encoding alpha1I, a human brain T calcium channel alpha1 subunit. *Neurosci. Lett.* 269, 121–124.
- Monteil, A., Chemin, J., Bourinet, E., Mennessier, G., Lory, P., Nargeot, J., 2000a. Molecular and functional properties of the human alpha(1G) subunit that forms T-type calcium channels. *J. Biol. Chem.* 275, 6090–6100.
- Monteil, A., Chemin, J., Leuranguer, V., Altier, C., Mennessier, G., Bourinet, E., Lory, P., Nargeot, J., 2000b. Specific properties of T-type calcium channels generated by the human alpha 1I subunit. *J. Biol. Chem.* 275, 16530–16535.
- Munsch, T., Budde, T., Pape, H.C., 1997. Voltage-activated intracellular calcium transients in thalamic relay cells and interneurons. *NeuroReport* 8, 2411–2418.
- Munsch, T., Yanagawa, Y., Obata, K., Pape, H.C., 2005. Dopaminergic control of local interneuron activity in the thalamus. *Eur. J. Neurosci.* 21, 290–294.
- Neher, E., 1992. Correction for liquid junction potentials in patch clamp experiments. *Methods Enzymol.* 207, 123–131.

- Ohara, P.T., Lieberman, A.R., Hunt, S.P., Wu, J.Y., 1983. Neural elements containing glutamic acid decarboxylase (GAD) in the dorsal lateral geniculate nucleus of the rat; immunohistochemical studies by light and electron microscopy. *Neuroscience* 8, 189–211.
- Pace-Schott, E.F., Hobson, J.A., 2002. The neurobiology of sleep: genetics, cellular physiology and subcortical networks. *Nat. Rev., Neurosci.* 3, 591–605.
- Pape, H.C., McCormick, D.A., 1995. Electrophysiological and pharmacological properties of interneurons in the cat dorsal lateral geniculate nucleus. *Neuroscience* 68, 1105–1125.
- Pape, H.C., Budde, T., Mager, R., Kisvarday, Z.F., 1994. Prevention of Ca(2+)-mediated action potentials in GABAergic local circuit neurones of rat thalamus by a transient K⁺ current. *J. Physiol.* 478 (Pt 3), 403–422.
- Pape, H.C., Munsch, T., Budde, T., 2004. Novel vistas of calcium-mediated signalling in the thalamus. *Pflügers Arch.* 448, 131–138.
- Perez-Reyes, E., 2003. Molecular physiology of low-voltage-activated T-type calcium channels. *Physiol. Rev.* 83, 117–161.
- Perez-Reyes, E., 2006. Molecular characterization of T-type calcium channels. *Cell Calcium* 40, 89–96.
- Sieg, F., Obst, K., Gorba, T., Riederer, B., Pape, H.C., Wahle, P., 1998. Postnatal expression pattern of calcium-binding proteins in organotypic thalamic cultures and in the dorsal thalamus in vivo. *Brain Res. Dev. Brain Res.* 110, 83–95.
- Sloviter, R.S., Dichter, M.A., Rachinsky, T.L., Dean, E., Goodman, J.H., Sollas, A.L., Martin, D.L., 1996. Basal expression and induction of glutamate decarboxylase and GABA in excitatory granule cells of the rat and monkey hippocampal dentate gyrus. *J. Comp. Neurol.* 373, 593–618.
- Song, I., Kim, D., Choi, S., Sun, M., Kim, Y., Shin, H.S., 2004. Role of the alpha1G T-type calcium channel in spontaneous absence seizures in mutant mice. *J. Neurosci.* 24, 5249–5257.
- Sosulina, L., Meis, S., Seifert, G., Steinhauser, C., Pape, H.C., 2006. Classification of projection neurons and interneurons in the rat lateral amygdala based upon cluster analysis. *Mol. Cell. Neurosci.* 33, 57–67.
- Steriade, M., Jones, E.G., McCormick, D.A., 1997. *Thalamus*. Elsevier, Amsterdam.
- Talley, E.M., Cribbs, L.L., Lee, J.H., Daud, A., Perez-Reyes, E., Bayliss, D.A., 1999. Differential distribution of three members of a gene family encoding low voltage-activated (T-type) calcium channels. *J. Neurosci.* 19, 1895–1911.
- Talley, E.M., Solorzano, G., Depaulis, A., Perez-Reyes, E., Bayliss, D.A., 2000. Low-voltage-activated calcium channel subunit expression in a genetic model of absence epilepsy in the rat. *Brain Res. Mol. Brain Res.* 75, 159–165.
- Telfeian, A.E., Tseng, H.C., Baybis, M., Crino, P.B., Dichter, M.A., 2003. Differential expression of GABA and glutamate-receptor subunits and enzymes involved in GABA metabolism between electrophysiologically identified hippocampal CA1 pyramidal cells and interneurons. *Epilepsia* 44, 143–149.
- Tsakiridou, E., Bertollini, L., de Curtis, M., Avanzini, G., Pape, H.C., 1995. Selective increase in T-type calcium conductance of reticular thalamic neurons in a rat model of absence epilepsy. *J. Neurosci.* 15, 3110–3117.
- Williams, S.R., Stuart, G.J., 2000. Action potential backpropagation and somato-dendritic distribution of ion channels in thalamocortical neurons. *J. Neurosci.* 20, 1307–1317.
- Williams, S.R., Toth, T.I., Turner, J.P., Hughes, S.W., Crunelli, V., 1997. The ‘window’ component of the low threshold Ca²⁺ current produces input signal amplification and bistability in cat and rat thalamocortical neurones. *J. Physiol.* 505 (Pt 3), 689–705.
- Zhou, Q., Godwin, D.W., O’Malley, D.M., Adams, P.R., 1997. Visualization of calcium influx through channels that shape the burst and tonic firing modes of thalamic relay cells. *J. Neurophysiol.* 77, 2816–2825.
- Zhu, J.J., Lytton, W.W., Xue, J.T., Uhlrich, D.J., 1999a. An intrinsic oscillation in interneurons of the rat lateral geniculate nucleus. *J. Neurophysiol.* 81, 702–711.
- Zhu, J.J., Uhlrich, D.J., Lytton, W.W., 1999b. Burst firing in identified rat geniculate interneurons. *Neuroscience* 91, 1445–1460.

Reciprocal modulation of I_h and I_{TASK} in thalamocortical relay neurons by halothane

Thomas Budde · Philippe Coulon ·
Matthias Pawlowski · Patrick Meuth ·
Tatyana Kanyshkova · Ansgar Japes · Sven G. Meuth ·
Hans-Christian Pape

Received: 7 November 2007 / Revised: 12 February 2008 / Accepted: 21 February 2008 / Published online: 14 May 2008
© Springer-Verlag 2008

Abstract By combining electrophysiological, immunohistochemical, and computer modeling techniques, we examined the effects of halothane on the standing outward current (I_{SO}) and the hyperpolarization-activated current (I_h) in rat thalamocortical relay (TC) neurons of the dorsal lateral geniculate nucleus (dLGN). Hyperpolarizing voltage steps elicited an instantaneous current component (I_i) followed by a slower time-dependent current that represented I_h . Halothane reduced I_h by shifting the voltage dependency of activation toward more negative potentials and by reducing the maximal conductance. Moreover, halothane augmented I_i and I_{SO} . During the blockade of I_h through Cs^+ , the current–voltage relationship of the halothane-sensitive current closely resembled the properties of a current through members of the TWIK-related acid-sensitive K^+ (TASK) channel family (I_{TASK}). Computer simulations in a

single-compartment TC neuron model demonstrated that the modulation of I_h and I_{TASK} is sufficient to explain the halothane-induced hyperpolarization of the membrane potential observed in current clamp recordings. Immunohistochemical staining revealed protein expression of the hyperpolarization-activated cyclic nucleotide-gated (HCN) channel proteins HCN1, HCN2, and HCN4. Together with the dual effect of halothane on I_h properties, these results suggest that I_h in TC neurons critically depends on HCN1/HCN2 heterodimers. It is concluded that the reciprocal modulation of I_h and I_{TASK} is an important mechanism of halothane action in the thalamus.

Keywords TC neurons · Anesthetic · Halothane · HCN · TASK

Introduction

Our understanding of the reversible action of inhaled anesthetics on central nervous function is far from complete. Today, ion channels are considered to be their most likely molecular and functional targets [5]. Inhaled anesthetics enhance inhibitory postsynaptic channel activity (GABA_A and glycine receptors; [29]) and inhibit excitatory channel activity (acetylcholine, serotonin, and glutamate receptors; [11, 12]). Volatile anesthetics cause neurons to hyperpolarize, which was attributed to the activation of K^+ leak currents (I_{KL}) and suggested to be a possible mechanism of action [11, 38, 42, 43, 52]. This view is corroborated by the finding that several two-pore-domain K^+ (K_{2P}) channels are activated (TASK1, TASK3; TWIK-related K^+ channel 1 [TREK1]) by inhalational anesthetics. In contrast, one type (TWIK-related halothane-inhibited K^+ channel [THIK]) is inhibited [38, 41]. The involvement of

Thomas Budde and Philippe Coulon are equally contributing first authors.

T. Budde (✉) · P. Coulon · M. Pawlowski · P. Meuth ·
T. Kanyshkova · H.-C. Pape
Institut für Physiologie I,
Westfälische Wilhelms-Universität Münster,
Robert-Koch-Str. 27a,
48149 Münster, Germany
e-mail: tbudde@uni-muenster.de

A. Japes
Institut für Anorganische und Analytische Chemie,
Westfälische Wilhelms-Universität Münster,
Corrensstr. 30/36,
48149 Münster, Germany

S. G. Meuth
Klinik für Neurologie, Julius-Maximilians-Universität Würzburg,
Josef-Schneider-Straße 11,
97080 Würzburg, Germany

TREK1 in general anesthesia was demonstrated by showing that TREK1-deficient mice revealed reduced sensitivity to halothane, sevoflurane, desflurane, and isoflurane [13]. In a similar way, TASK1- and TASK3-deficient mice were less sensitive to halothane and isoflurane [18, 19]. Furthermore, hyperpolarization-activated cyclic nucleotide-gated (HCN) channels are modulated by the binding of halothane, making them potentially relevant targets for the clinical action of inhaled anesthetics [6]. HCN channels expressed in HEK 293 cells and in higher motoneurons have been shown to be affected by halothane in two ways: a negative shift of the voltage dependency of activation mediated by HCN1 and a reduction in current amplitude mediated by HCN2.

Anesthesia is often intuitively compared to sleep, although the electroencephalogram (EEG) pattern during anesthesia does not show distinct stages or cycling between stages that is characteristic of naturally occurring sleep. Moreover, in anesthesia, an isoelectric EEG may occur that is never seen during sleep. The neurophysiological basis of anesthesia is, therefore, commonly assumed to be different from sleep, but there are, nevertheless, some parallels [56]. Anesthetic effects at specific molecular targets in specific brain regions alter brain activity in a way that is very similar to the alterations observed during sleep [33]. Together with behavioral similarities, these results raise the question, whether neuronal networks that are normally involved in the generation or maintenance of sleep, are also influenced by anesthetics.

The thalamocortical network is the major cellular substrate of sleep-related activity. During periods of slow-wave sleep or drowsiness, a marked reduction of the response to sensory stimuli is accompanied by rhythmic burst firing of thalamocortical relay (TC) neurons which are hyperpolarized during these states [22]. On the other hand, wakefulness is associated with TC neurons being depolarized and showing tonic single-spike activity [50]. In this state, the neurons faithfully relay the sensory information from the sensory organs through the thalamus to the primary sensory areas of the cortex, which is commonly assumed to be a prerequisite for the conscious perception of our environment. A strong arousing function is exerted by the ascending brainstem system (for review, see [22]) which governs the switch from burst to tonic firing by the release of neurotransmitters that predominantly act on two types of ion channels: TASK channels, which give rise to I_{TASK} [27] and are affected by ACh, and HCN channels, giving rise to I_h [20, 24], which are affected by noradrenalin and serotonin. Modulation by brainstem transmitters shifts the voltage dependency of activation of HCN channels to more depolarized potentials and inhibits I_{TASK} . Consequently, the membrane depolarizes and the input resistance increases, thereby favoring the tonic firing mode. This arousing mechanism is obviously inactive under anesthesia.

In the dorsal part of the lateral geniculate nucleus (dLGN), which is the primary gateway for the processing and relaying of visual information in the thalamus, I_{TASK} and I_h contribute to the standing outward current (I_{SO}) of TC neurons. The interplay between these currents critically determines the resting membrane potential (V_{rest}), and their state of modulation controls the activity mode of these cells. On the molecular level, these functions are based on the mRNA expression of TASK1, TASK3, and all HCN isoforms (HCN1–4) and the protein coexpression of HCN2 and TASK3 in identified TC neurons [28]. In these cells, halothane increases a K^+ conductance [43], and we have shown previously that this is at least in part due to ion channels of the TASK family [27]. However, the reversal potential of the halothane-sensitive component was more positive than expected of a TASK current alone, suggesting the contribution of at least one other ion channel.

In the present study, electrophysiological techniques, immunohistochemical staining, and computer simulations were used to investigate whether the interplay of I_h and I_{TASK} is the basis for the clinical effect of anesthetics that are antagonistic to the arousing brainstem effects in the thalamus.

Materials and methods

Preparation

All animal preparations were done according to the European Communities Council Directive of 24 November 1986 (86/609/EEC). Rats (postnatal days 12–30) were anesthetized with isoflurane and decapitated. In rapid sequence, after surgically removing a skull cap caudal to the bregma, a block of brain tissue containing the thalamus was removed from the cranial vault and submerged in ice-cold aerated (O_2) saline solution containing (in mM): sucrose, 200; PIPES, 20; KCl, 2.5; NaH_2PO_4 , 1.25; $MgSO_4$, 10; $CaCl_2$, 0.5; dextrose, 10; pH 7.35, adjusted with NaOH. Thalamic slices were prepared as coronal sections on a vibratome. Before recording, slices were kept submerged in artificial cerebrospinal fluid (ACSF) containing (in mM): NaCl, 125; KCl, 2.5; NaH_2PO_4 , 1.25; $NaHCO_3$, 24; $MgSO_4$, 2; $CaCl_2$, 2; dextrose, 10; pH adjusted to 7.35 by bubbling with carbogen (95% O_2 and 5% CO_2).

Whole-cell patch clamp

Recordings were performed on thalamocortical relay neurons of the dLGN at room temperature in a solution containing (in mM): NaCl, 120; KCl, 2.5; NaH_2PO_4 , 1.25; HEPES, 30; $MgSO_4$, 2; $CaCl_2$, 2; dextrose, 10; pH 7.35

was adjusted with HCl. Individual cells were visually identified by infrared differential interference contrast videomicroscopy. Membrane currents were measured with glass microelectrodes pulled from borosilicate glass capillaries (GC150T-10; Clark Electromedical Instruments, Pangbourne, UK) and filled with (in mM): K-gluconate, 95; K₃-citrate, 20; NaCl, 10; HEPES, 10; MgCl₂, 1; CaCl₂, 0.5; BAPTA, 3; Mg-ATP, 3; and Na-GTP, 0.5. The internal solution was set to a pH of 7.25 with KOH and an osmolality of 295 mOsm/kg. The electrodes were connected to an EPC-10 amplifier (HEKA Elektronik, Lamprecht, Germany) with a chlorinated silver wire. Electrode resistances were in the range of 2–3 MΩ with access resistances in the range of 5–20 MΩ. Series resistance compensation of 30% was routinely applied. Voltage clamp experiments were controlled by the software Pulse or PatchMaster (HEKA Elektronik) operating on an IBM-compatible personal computer. Measurements were corrected for liquid junction potential. All results are presented as the mean±SEM. Substance effects were tested for statistical significance using the nonparametric Mann–Whitney test (Graph Pad Prism software; Graph Pad, San Diego, CA, USA). Where applicable, the parametric *t* test was used (Origin software). Differences were considered statistically significant if *p*<0.05.

To increase the stability of whole-cell recordings and account for increasingly fast activation kinetics of *I*_h, the pulse length was shortened by 500 ms with increasing hyperpolarization (1.5 s pulse length at –133 mV). This protocol was used for experiments in which cells had to tolerate long recording times with extracellular halothane application. In experiments where halothane was applied directly with the pipette solution, protocols eliciting long pulses ranging from 15.5 s at –53 mV to 3.5 s at –133 mV (1.5 s decrement) were used. Slight differences in the values of half-maximal activation could be observed between protocols (see also [44]). We found, while shorter steps are better tolerated by the cells, halothane effects were slightly underestimated. Steady-state activation of *I*_h, *p*(*V*), was estimated by normalizing the tail current amplitudes (*I*) 50 ms after stepping to a constant potential (indicated by the circles in Fig. 1a) from a variable amplitude step using the following equation:

$$p(V) = (I - I_{\min}) / (I_{\max} - I_{\min})$$

with *I*_{max} being the tail current amplitude for the voltage step from –133 to –103 mV and *I*_{min} for the voltage step from –43 to –103 mV. *I*_h activation was well accounted for by a Boltzmann distribution of the following form:

$$p(V) = 1 / (1 + \exp((V - V_h) / k))$$

where *V*_h is the voltage of half-maximal activation and *k* is the slope factor. The fully activated current vs. voltage

relationship was obtained from instantaneous tail currents. *I*_h was evoked by a hyperpolarizing step to –123 mV from a holding potential of –43 mV. The post step test potential was varied between –123 and –33 mV in 10 mV increments. The tail current amplitude was plotted against the test pulse potential, fitted using a linear regression, and fully activated conductance and reversal potential were calculated from slope and zero-point, respectively.

The amplitude of *I*_h (indicated by the bracket in Fig. 1a, left current traces) was calculated by subtracting the instantaneous current amplitude (*I*_i) from the steady-state current (*I*_{SS}). The density of *I*_h was calculated by dividing the *I*_h current amplitude at –133 mV by the membrane capacitance obtained during whole-cell recordings. The density of *I*_i was calculated accordingly.

During current clamp recordings, the instantaneous frequency (*f*_i) of action potential generation was determined by analyzing the first two action potentials elicited by a depolarizing current pulse.

Drugs

Halothane, isoflurane, sevoflurane, BaCl₂, and CsCl were obtained from Sigma (Deisenhofen, Germany). CsCl and BaCl₂ were prepared as stock solution in distilled water and added to the perfusion medium. In one set of experiments, volatile anesthetics were added in liquid form to the extracellular solution and administered by perfusion (3–5 min) of the thalamic slices. In another set of experiments, halothane was delivered to an individual cell via the patch electrode solution. In both cases, after adding the anesthetic to the respective aqueous solution at room temperature, solutions were sonicated for 5 min. If not stated otherwise, halothane was used at a concentration of 0.1% (v/v). At 25°C, saturation with halothane in aqueous solution occurs at 0.345% and is slightly increased at room temperature. Therefore, solutions to which 1% halothane were added can be considered saturated.

Concentration of halothane in the recording chamber

Several factors influence the final halothane concentration in the recording chamber: outgassing during the preparation of the solution, absorption by tubing, evaporation along the line of application and the recording chamber, and delayed uptake into the slice preparation during the application. Even the decline in the concentration of a volatile anesthetic along the length of a typical bath chamber has been shown to be as high as 33% [39]. Based on the dose–response characteristic of cloned TASK channels expressed in cell cultures [38], we concluded that only about 10% of the nominal halothane concentration reaches the target cells.

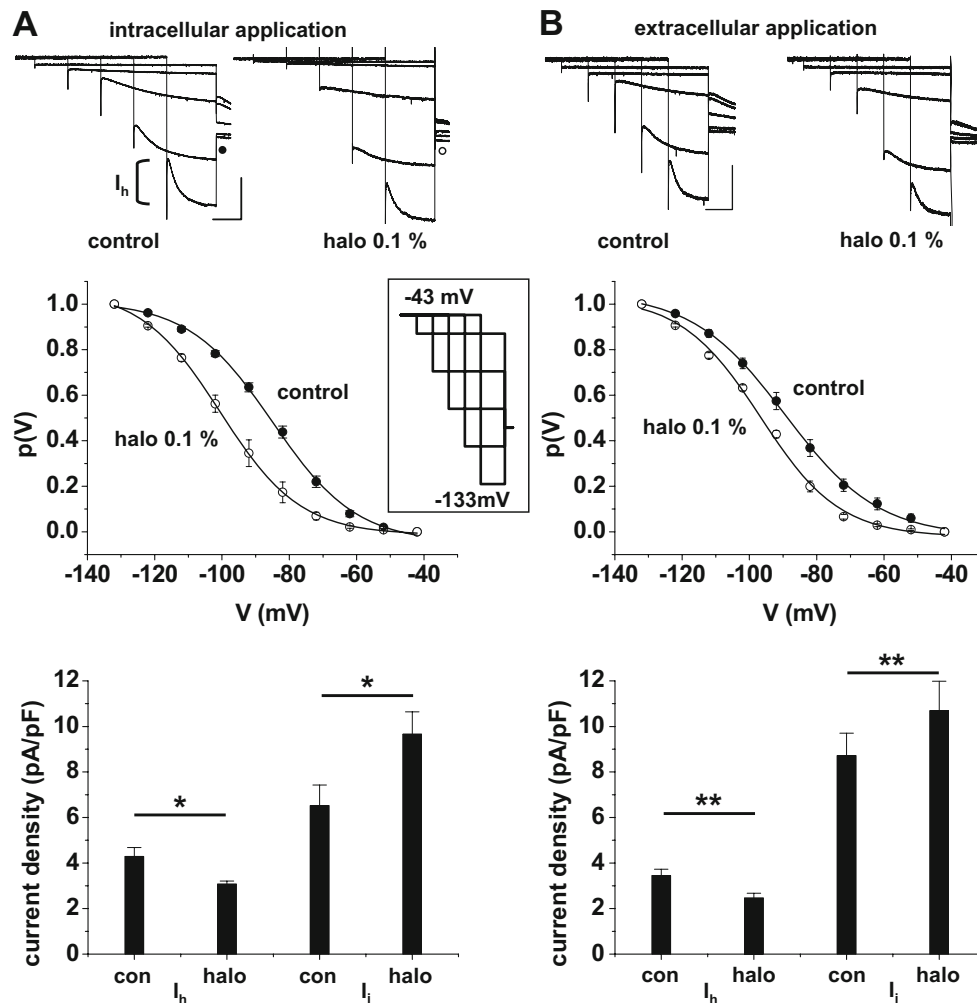


Fig. 1 Halothane effect on hyperpolarization-activated inward currents in TC neurons. Representative current traces and analyses obtained from experiments with intracellular (**a**) and extracellular (**b**) application of halothane are shown. *Upper panels* current traces obtained by stepping from a holding potential of -43 to -53 , -73 , -93 , -113 , and -133 mV (*inset, middle panel*) are shown (*left superimposed traces* control conditions, *right superimposed traces* presence of 0.1% halothane). The tail current voltage was -103 mV. The duration of each hyperpolarizing step was shortened as command potentials became more negative. This accounts for increasingly fast activation kinetics of I_h and improves cell viability. The total trace

length is 18 and 7 s in **a** and **b**, respectively. *Scale bars* represent 3 s/400 pA (**a**) and 1 s/300 pA (**b**, see text for details). The *bracket* indicates the amplitude of I_h . The *circle* indicates the tail current amplitude measured to calculate the steady-state activation curve. *Middle panels* mean steady-state activation curves were obtained by plotting normalized tail current amplitudes against the step potential and fitting with a Boltzmann function. *Lower panels* mean bar graph representations of current density. I_h amplitude was calculated as $I_{ss} - I_i$. Current densities were calculated by dividing amplitudes at -133 mV by the membrane capacitance obtained during whole-cell recordings. * $p < 0.05$, ** $p < 0.01$

After adding 0.1% of halothane, the recording solution was expected to contain 9.4 mM of the anesthetic. To assess the actual concentration of halothane in the recording chamber, we measured it using gas chromatography (GC). GC analyses were carried out on an Agilent HP5890 Series II (Agilent Technologies, Waldbronn, Germany) equipped with a flame ionization detector and a Gerstel MPS2 autosampler (Gerstel, Mühlheim/Ruhr, Germany). GC conditions were as follows: 30 m \times 0.25 mm i.d. Agilent DB-17ms fused silica capillary column with 0.25 μ m film thickness; carrier gas hydrogen at 1.4 ml/min; isothermal

temperature program at 40°C; splitless injection, injector temperature 250°C; detector temperature 250°C.

Probes were taken from both the original solution, i.e., before passing the tubing leading to the bath chamber, and from the recording chamber, and conveyed into gas-tight containers. For calibration, a stock solution of halothane was prepared in cold dimethyl sulfoxide. The solution was mixed and kept cold and sealed to avoid evaporation of the analyte. A calibration curve was recorded using final concentrations from 0 to 12 mM in the same solution used for the electrophysiological recordings. The necessity of

an internal standard was tested. No additional volatile compound was found. Calibration solutions or sample solutions (200 μ l) were prepared in a glass vial (1.5 ml) with septum, vigorously shaken, and equilibrated at room temperature. Thirty microliters of the headspace was injected using a gas-tight 100- μ l syringe. Five measurements of independent solutions were done, showing a high reproducibility.

From the 9.4 mM (0.1% *v/v*) halothane added to the recording solution, only 2.96 ± 0.02 mM remained in solution after mixing. After passing the tubing and the bath chamber, only 1.24 ± 0.04 mM ($n=5$) remained in solution. In addition, we tested a 0.2% halothane solution and found that, of the 18.8 mM halothane added, only 3.94 ± 0.08 mM were dissolved in the recording solution and only 2.18 ± 0.06 mM remained in solution after passing the tubing and recording chamber (all $n=5$).

The minimum alveolar concentration (MAC) of halothane, the concentration that prevents movement in response to a noxious stimulus in 50% of the animals, is around 1% for rats, corresponding to a concentration of around 0.3 mM in an artificial cerebrospinal fluid (ACSF), while it is 2.2% for isoflurane, corresponding to 0.71 mM in ACSF [39]. For young rats, the MAC value is slightly increased, and around 1.9% in juvenile rats [42]. This corresponds to a halothane concentration of about 0.7 mM in ACSF at 22°C [30]. Therefore, the halothane concentration used in most of our experiments (nominal 0.1%, which relates to 1.2 mM in the recording chamber) is about 1.8 times higher and, thus, not necessarily in the clinical range. However, measurable effects on I_{SO} were already found with a nominal concentration of 0.02% (see Fig. 3b, d). It is noted that short application times (<5 min) were necessary to achieve reversible effects. For a detailed discussion of halothane concentrations used *in situ* compared with those used for anesthesia *in vivo*, see [42].

Computer simulations with NEURON

A previously described single-compartment TC neuron model [16, 23] was adapted and used within the NEURON Simulation Environment [14, 25, 26]. The model is based on the mathematical description of $I_{passive}$, I_{HH2} , I_{TASK} , I_{Aslow} , I_T , and I_h and displays the two typical modes of action potential generation in thalamic cells: burst firing with two to six action potentials riding on a low-threshold Ca^{2+} spike and single-spike activity with tonic trains of action potentials. All simulations were calculated at 25°C. The magnitude of halothane-dependent effects on I_{TASK} (30% increase) and I_h (–10 mV hyperpolarizing shift in the activation curve) used for computer modeling were estimated from the experiments achieved with 0.1% halothane.

Immunohistochemistry

Long-Evans rats (postnatal days 25–27) were deeply anesthetized using pentobarbital (50 mg/kg body weight) and transcardially perfused with PBS, followed by an ice-cold 4% PFA/PBS for 35–40 min. Brains were removed, postfixed for 4 h in 4% PFA/PBS, and cryoprotected with 30% sucrose. Coronal sections (20 μ m) were cut at the level of the dLGN, mounted onto Polysine slide glass (Menzel, Germany), and air dried. For detection of HCN2, fresh-frozen sections were used. In this case, brains from isoflurane-anesthetized rats were removed and frozen in –50°C isopentane. Cryostat coronal sections of 20 μ m thickness were cut at the level of the dLGN, thaw-mounted onto Polysine slide glass, air dried, and fixed in 4% PFA/PBS for 10 min.

After permeabilization with 0.1% Triton X-100 in PBS for 10 min and several washings with PBS, sections were blocked with 10% normal horse serum (NHS), 2% BSA in PBS for 3 h to minimize nonspecific binding before incubation of slices with primary antibodies: rabbit anti-HCN1 (1:500, Alomone Labs, Israel), goat anti-HCN2 (1:250, Santa Cruz Biotechnology, USA) and rabbit anti-HCN4 (1:100, Alomone Labs, Israel) in 2% NHS, 2% BSA in PBS at 4°C for 16–18 h. After washing (3 \pm 10 min with PBS), sections were exposed to Cy3-conjugated donkey antirabbit IgG or Cy2 donkey antigoat IgG (1:400 in 2% NHS, 2% BSA in PBS, Dianova, Germany) for 1.5 h, washed again, and coverslipped with Immumount. For the negative controls, occlusion of the primary antibody from the staining procedure was routinely performed with no positive immunological signal detected (see Fig. 6, insets).

Results

Intracellular and extracellular modulation of I_h

We examined effects of halothane on the hyperpolarization-activated current (I_h) in rat TC neurons in dLGN. In Fig. 1, we compare the controls (upper left panels) to the results obtained in the presence of halothane (upper right panels). First, halothane was added to the pipette solution, thus allowing diffusion into the cytosol (Fig. 1a). I_h was activated from a holding potential of –43 mV by using hyperpolarizing voltage steps of increasing ($\Delta V = -10$ mV) amplitude and decreasing ($\Delta t = -1500$ ms) duration (3.5 s at –133 mV, see the “Materials and methods” section) followed by a constant step to –93 mV (Fig. 1a, upper panel; the inset shows a scheme of the voltage protocol). An analysis of the deactivating currents revealed a half-maximal value of I_h activation (V_h) at a membrane potential of -86 ± 1 mV ($n=16$) under control conditions (Fig. 1a

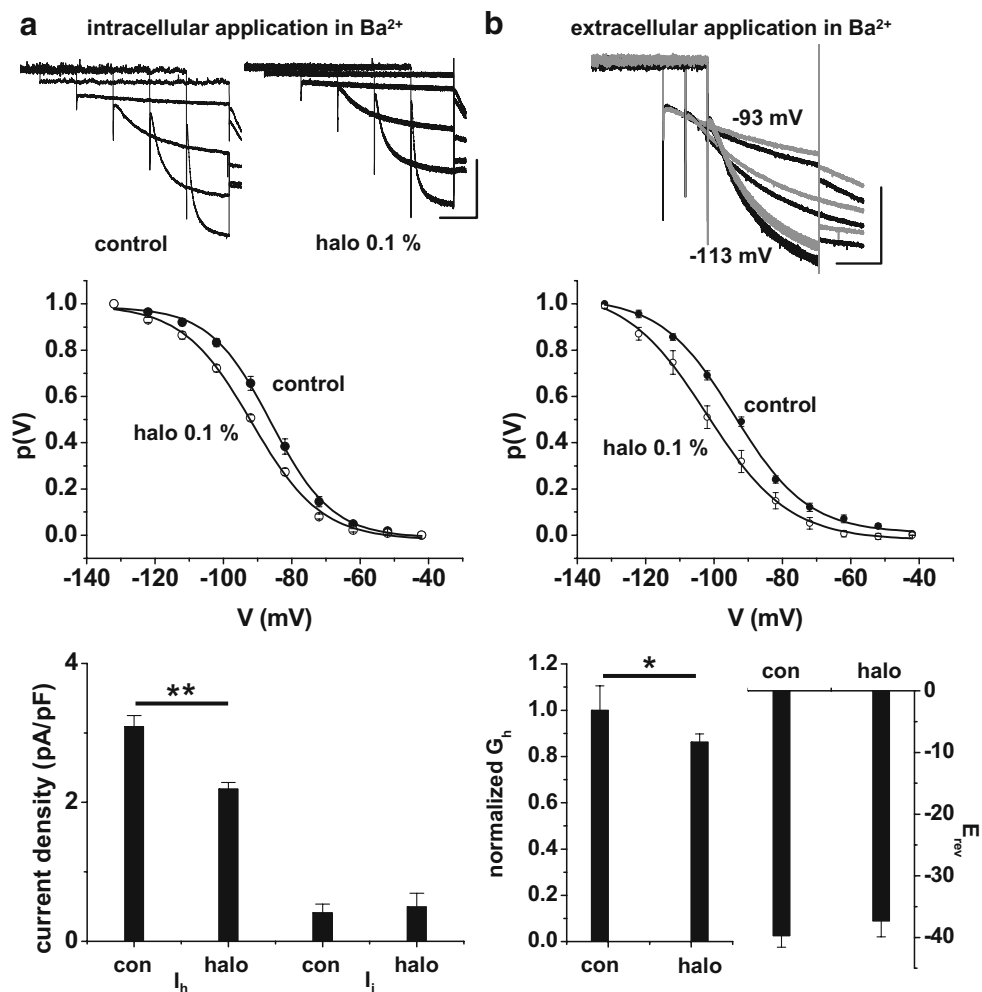


Fig. 2 Halothane effect on isolated I_h in TC neurons. **a** Representative current traces and analyses obtained from experiments with intracellular application of halothane in the presence of Ba^{2+} (in the bathing solution) are shown. Current traces (upper panel; long protocol; scale bars represent 3 s and 100 pA), mean steady-state activation curves (middle panel), and mean bar graph representations of current density (lower panel) were obtained as described in Fig. 1. **b** Superimposed current traces (upper panel; short protocol) recorded in Ba^{2+} -containing extracellular solution in the presence (gray traces)

and absence (black traces) of halothane (currents in response to voltage commands from -43 to -93 , -103 , and -113 mV are shown; scale bars represent 1 s and 200 pA). Mean steady-state activation curves (middle panel) were obtained by plotting the absolute tail current amplitudes against the step potential and fitting with a Boltzmann function. The lower panel shows the mean bar graph representations of the normalized fully activated conductance (left) and the reversal potential (right) obtained from the fully activated current-voltage relationship of I_h (not shown). * $p < 0.05$, ** $p < 0.01$

middle panel, filled circles) and a significantly ($p < 0.001$) more hyperpolarized value (-99 ± 2 mV, $n = 7$) for cells recorded with halothane added to the pipette solution (Fig. 1a, middle panel, open circles). A comparison of the current densities of I_i and I_h at -133 mV revealed a halothane-induced increase ($p < 0.05$) in I_i (control = 6.5 ± 0.9 pA/pF, $n = 6$; halothane = 9.7 ± 1.0 pA/pF, $n = 7$) and a decrease ($p < 0.02$) in I_h (control = 4.3 ± 0.4 pA/pF, $n = 6$; halothane = 3.1 ± 0.1 pA/pF, $n = 7$; Fig. 1a, lower panel).

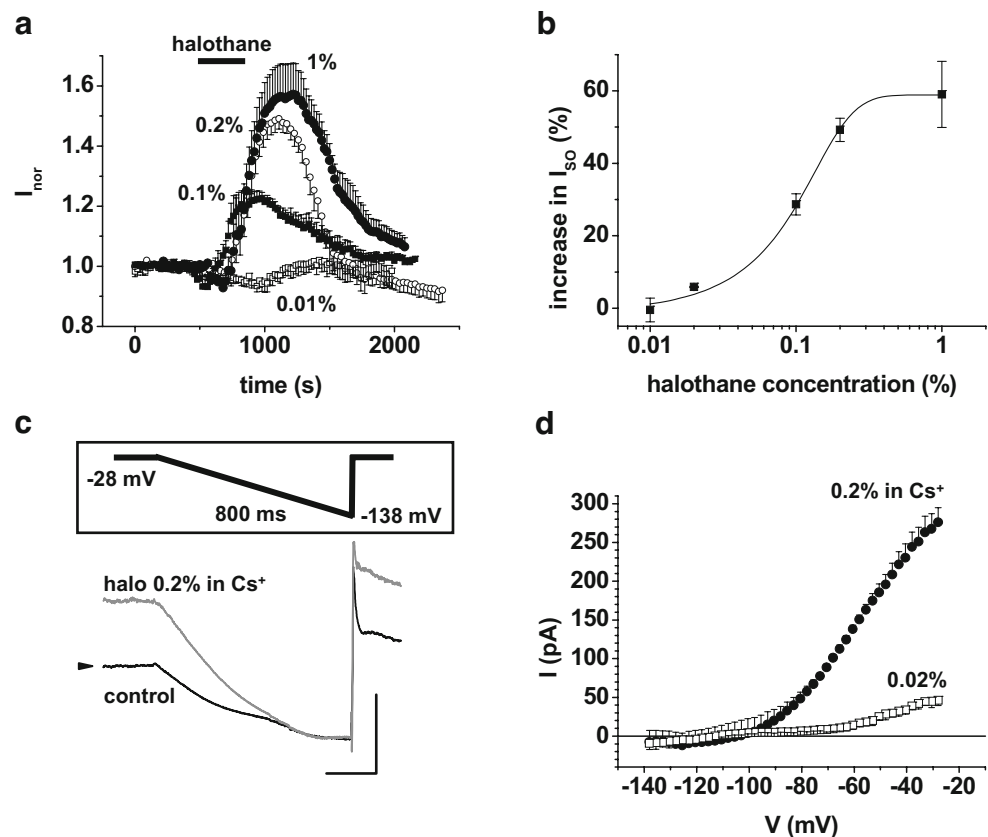
To more directly demonstrate the effect of halothane on I_h in TC neurons, control currents and currents in the presence of halothane (3–5 min after wash in) were recorded from the

same cells (Fig. 1b, upper panel). In this set of experiments, shorter activation protocols were used (see the “Materials and methods” section, holding potential = -43 mV, $\Delta V = -10$ mV, $\Delta t = -500$ ms, 1.5 s duration at -133 mV). Extracellular application resulted in a shift of the activation curve of I_h toward more negative holding potentials (control: $V_h = -90 \pm 1$ mV; halothane: $V_h = -97 \pm 1$ mV; $n = 7$; $p < 0.002$; Fig. 1b, middle panel) and the simultaneous increase ($p < 0.003$) in I_i (control = 8.7 ± 1.0 pA/pF, $n = 6$; halothane = 10.7 ± 1.3 pA/pF, $n = 7$) and decrease ($p < 0.008$) in I_h (control = 3.5 ± 0.3 pA/pF; halothane = 2.5 ± 0.2 pA/pF; $n = 7$; Fig. 1b, lower panel).

Effect on I_h during blockade of I_{KL}

To assess the effect of halothane on I_h alone, experiments were performed in the presence of 1 mM Ba^{2+} , which, at this concentration, is known to block TASK and inward rectifier channels in TC neurons [27]. Under these recording conditions, I_i density in the presence (0.5 ± 0.2 pA/pF, $n=7$) and absence (0.4 ± 0.1 pA/pF, $n=6$) of intracellular halothane was indistinguishable ($p > 0.7$). In contrast, I_h density (control = 3.1 ± 0.2 pA/pF, $n=6$; halothane = 2.2 ± 0.1 pA/pF, $n=7$; $p < 0.004$; Fig. 2a, lower panel) and voltage dependency (control: $V_h = -86 \pm 1$ mV, $n=7$; halothane: $V_h = -92 \pm 1$ mV; $n=7$; $p < 0.002$; Fig. 2a, middle panel) were significantly different between the two recording conditions. To more directly demonstrate the effect of halothane on I_h in a given cell, extracellular application was used while stimulating the cell with short activation protocols. While I_i was unchanged, I_h was clearly reduced (Fig. 2b, upper panel). This effect was accompanied by a hyperpolarizing shift in the activation curve (control: $V_h = -93 \pm 1$ mV; halothane: $V_h = -99 \pm 2$ mV; $n=6$; $p < 0.003$; Fig. 2b, middle panel) and a decrease of the fully activated I_h conductance (G_h ; control: $G_h = 4.5 \pm 0.7$ nS; halothane: $G_h = 4.0 \pm 0.7$ nS; $n=9$; $p < 0.02$), but no significant changes of the reversal potential were found (E_{rev} ; control: $E_{rev} = -40 \pm 2$ mV; halothane: $E_{rev} = -37 \pm 3$ mV; $n=9$; Fig. 2b, lower panel).

Fig. 3 Halothane effect on the standing outward current (I_{SO}) of TC neurons. **a** Normalized mean I_{SO} amplitude vs. time plots for the indicated halothane concentrations. Horizontal bar marks the duration of halothane application. **b** Dose–response curve of the halothane effect on I_{SO} . The increase in I_{SO} amplitude is plotted against the nominal halothane concentration. **c** Experiments were performed in the continuous presence of Cs^+ to block I_h . Current response to ramp stimulation (see inset) in the presence (gray trace) and absence (black trace) of halothane are shown. Arrowhead indicates I_{SO} amplitude. Scale bars represent 200 ms and 50 pA, respectively. **d** Current–voltage relationship of the halothane-sensitive current with 0.02% (open squares) and 0.2% (in the presence of Cs^+ , closed circles) halothane added to the external solution



To test whether modulation of I_h is a more general feature of inhalational anesthetics, the widely used substances isoflurane and sevoflurane were tested (short activation protocol; 1–2 mM Ba^{2+} ; data not shown). At a concentration of 0.1% (control: $V_h = -93 \pm 1$ mV; isoflurane: $V_h = -104 \pm 1$ mV; $n=3$ /control: $V_h = -94 \pm 1$ mV; sevoflurane: $V_h = -101 \pm 1$ mV; $n=3$) and 0.2% (control: $V_h = -94 \pm 1$ mV; isoflurane: $V_h = -102 \pm 2$ mV; $n=3$), both substances induced a significant shift of the voltage dependency of I_h ($p < 0.04$). This hyperpolarizing shift was associated with a significant ($p < 0.04$) decrease in I_h density (0.1% isoflurane = 4.3 ± 0.4 pA/pF under control conditions, 2.6 ± 0.3 pA/pF in the presence of isoflurane, $n=3$; 0.2% isoflurane = 4.7 ± 0.5 pA/pF under control conditions, 2.2 ± 0.3 pA/pF in the presence of isoflurane, $n=3$; 0.1% sevoflurane = 3.7 ± 0.6 pA/pF under control conditions, 2.7 ± 0.5 pA/pF in the presence of sevoflurane, $n=3$). Because both substances induced an increase in leak currents even in the presence of 2 mM Ba^{2+} , an analysis of I_h conductance and reversal potential was not possible by using the tail current protocol as above.

Effect of halothane on I_{SO}

Next, the effect of halothane on the I_{SO} (arrowhead in Fig. 3c) of the TC neurons was analyzed. We have shown

earlier that current through TASK channels significantly contributes to this steady-state current component [26, 27]. Application of halothane (3–5 min) at different concentrations resulted in a fully reversible (Fig. 3a) and dose-dependent (Fig. 3b) increase in I_{SO} amplitude at -28 mV (0.01% halothane = $0.5 \pm 3.3\%$ normalized current increase, $n=4$; 0.02% halothane = $5.9 \pm 0.2\%$, $n=3$; 0.1% halothane = $28.7 \pm 2.9\%$, $n=3$; 0.2% halothane = $49.2 \pm 3.2\%$, $n=5$; 1% halothane = $59.0 \pm 9.2\%$, $n=7$). At pH 6.0, the increasing effect of 1% halothane on I_{SO} was reduced to $48.0 \pm 6.7\%$ ($n=3$; data not shown). Furthermore, 0.1% halothane decreased I_{SO} amplitudes by $-12.8 \pm 2.1\%$ ($n=4$) under acidic recording conditions (data not shown). To further characterize the current component sensitive to halothane, the membrane potential was ramped from -28 mV in 800 ms to -138 mV once every 20 s (Fig. 3c, inset). The rate of hyperpolarization (0.14 mV/ms) is sufficiently slow to allow the membrane current to reach steady-state at each potential and it is expected that only constitutively open channels can follow the ramp. The current–voltage relationship of the halothane-sensitive current was obtained by subtracting the control currents from those recorded in the presence of halothane (i.e., halothane–control) and was characterized by an outward rectification (mean current at -28 mV = 104.9 ± 4.9 pA) and a reversal potential (E_{rev}) of -96.9 ± 7.0 mV ($n=3$; data not shown), i.e., approximately 7 mV positive to the expected K^+ equilibrium potential ($E_K = -104$ mV). As this slight deviation from E_K could be attributed to the contribution of I_h , experiments were performed in the presence of the I_h blocker Cs^+ [35]. As before, the application of halothane (0.2%) resulted in a strong increase in I_{SO} amplitude (Fig. 3c). The current–voltage relationship of the halothane-sensitive current revealed strong outward rectification and a reversal ($E_{rev} = -105.5 \pm 2.2$ mV; $n=4$) very close to E_K (Fig. 3d, closed circles).

Effect of halothane on thalamic activity modes

The functional consequences of halothane application on TC neuron activity were probed under current clamp conditions. To ensure tonic responses, recordings were obtained at depolarized membrane potentials using DC injection ($V_M = -59.7 \pm 0.2$ mV, $n=6$). Under these conditions, depolarizing current steps elicited tonic firing ($f_i = 20.0 \pm 2.6$ Hz, $n=6$; Fig. 4b, left panel). The application of halothane resulted in a significant ($p < 0.004$) hyperpolarization of the membrane potential to $V_M = -65.5 \pm 1.2$ mV (Fig. 4a) and a change from tonic to burst firing ($f_i = 152.6 \pm 17.8$ Hz; $n=5$; Fig. 4b, right panel). It is noted that most low-threshold Ca^{2+} spikes under these recording conditions were crowned by only a single action potential. In one out of six cells, no burst was observed. This was possibly due to halothane reducing the input resistance and T-type Ca^{2+} current [42].

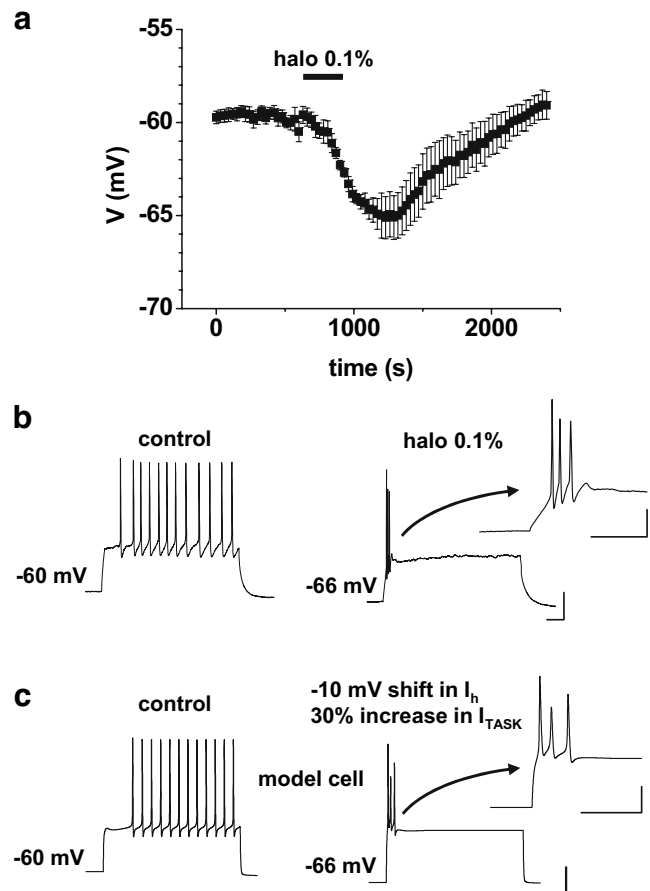


Fig. 4 Halothane effect on the membrane potential of TC neurons. **a** Normalized mean voltage vs. time plot. Horizontal bar indicates the duration of halothane application. **b** Voltage response to a depolarizing current step under control conditions (left trace) and in the presence of halothane (right trace). The slightly depolarized holding potential of -60 mV was obtained by DC current injection ($V_{rest} \sim -71$ mV). This current was not changed during the experiment. **c** Voltage response of a single-compartment TC neuron computer model to a depolarizing current step under control conditions (left trace) and after shifting I_h and increasing I_{TASK} (right trace). The resting membrane potential of the computer model was -70 mV. The control value of -60 mV was achieved by DC current injection which was not changed in the course of the simulation. The low-threshold Ca^{2+} spike with the crowning burst of action potentials is displayed at an expanded time scale. Scale bars represent 100 ms and 20 mV in the main panel and 50 ms and 20 mV in the inset

To further characterize the effect of halothane on TC neurons, continuous current clamp recordings including manual voltage clamp were performed (Fig. 5). Again, recordings were obtained at depolarized membrane potentials using DC injection ($V_M = -57.0 \pm 0.9$ mV; DC = 79.3 ± 10.8 pA, $n=7$). Bath application of halothane (0.2%) resulted in a significant ($p < 0.001$) membrane hyperpolarization of -6.5 ± 1.0 mV ($n=7$). The injection of hyperpolarizing (-150 pA) and depolarizing current pulses ($+200$ pA, 800 ms, 0.4 Hz) resulted in deflections of the membrane potential which indicated an apparent input

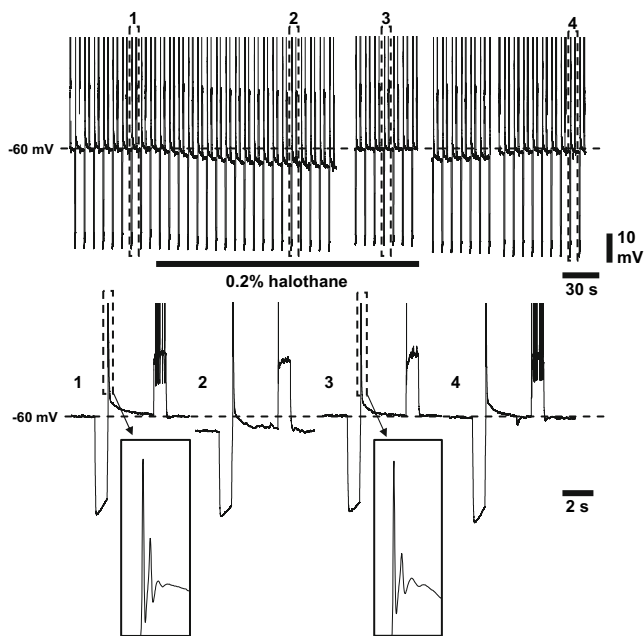


Fig. 5 Typical response of a TC neuron to halothane. Application of halothane (0.2%) resulted in a membrane hyperpolarization and decrease in apparent input resistance. Responses of the cell to the constant current pulses before (1), during (2 and 3; the latter with manual voltage clamp), and after 10 min recovery (4; note that the timeline is noncontinuous) from halothane are expanded for comparison. The low-threshold Ca^{2+} spike is displayed at an expanded time scale. The *black bar* represents halothane application as indicated. *Dashed lines* indicate membrane potential before the application of halothane. Fast Na^+/K^+ -mediated action potentials are truncated

resistance of $284 \pm 30 \text{ M}\Omega$ ($n=7$). Compensation of the halothane-induced hyperpolarization with intracellular injection of DC current (manual voltage clamp) revealed a significant ($p < 0.02$) decrease in input resistance associated with the response ($218 \pm 22 \text{ M}\Omega$, $n=7$). Moreover, while under control conditions, every depolarizing current step elicited tonic firing (Fig. 5, insets 1 and 4); this was abolished in the presence of halothane (Fig. 5, inset 2) even after compensating for the halothane-induced hyperpolarization (Fig. 5, inset 3).

To determine whether the modulation of I_h and I_{TASK} are sufficient to account for the halothane effects seen under current clamp conditions, we used computer modeling techniques [28]. The model cell was held at a potential of -60 mV using DC injection. From this potential, a sufficiently strong step depolarization evoked tonic firing ($f_i = 18 \text{ Hz}$; Fig. 4c, left panel). Incorporating the effect of 0.1% halothane on I_h (-10 mV shift in V_h) and I_{TASK} (30% increase in I_{SO}) into the computer model resulted in a hyperpolarization of the membrane potential to -66 mV which was accompanied by an induction of typical burst firing ($f_i = 98 \text{ Hz}$; Fig. 4c, right panel) upon step depolarization.

Expression of HCN channel proteins in dLGN

The HCN family of ion channels represents the molecular substrate for I_h in native cells. Halothane seems to exert a dual effect on the electrophysiological properties of I_h : a negative shift of the activation potential and a reduction of the current amplitude. The negative shift of the activation potential can be attributed to HCN1, and the reduction of the current amplitude can be attributed to HCN2 [6]. To verify the presence of the channel isoform proteins in TC neurons and thus, that the electrophysiological effects can indeed be caused by an action of halothane on these two isoforms, we applied immunohistochemical staining. The results indicate that HCN1, HCN2, and HCN4 are expressed in dLGN (Fig. 6). HCN1 (Fig. 6, left panel), HCN2 (Fig. 6, middle panel), and HCN4 (Fig. 6, right panel) show a clear somatic localization with some dendritic staining for HCN1.

Discussion

Effect of halothane on HCN channels in TC neurons

We have shown previously that the halothane-sensitive current in TC neurons had a reversal potential positive to the K^+ equilibrium potential and was—in addition to the TASK channels—carried by as yet uncharacterized Na^+ and/or Ca^{2+} channels [27]. This conclusion is corroborated by the finding that Na^+ -permeable HCN channels are modulated by halothane. Inhibition of I_h by halothane in native TC neurons is characterized by two effects: a hyperpolarizing shift in the activation curve and a decrease in the maximal available current. Recent studies on cloned channels in expression systems indicate sub-unit-specific effects of clinically relevant concentrations of halothane with the shift in I_h voltage dependency and the reduction in the maximal available current being mediated by HCN1 and HCN2, respectively [6], and both effects can be observed concurrently in HCN1–HCN2 heteromeric channels. Therefore, our results suggest that I_h in TC neurons is critically based on functional HCN1–HCN2 heterodimers, which is corroborated by the findings that HCN1 and HCN2 mRNA expression was found in TC neurons [4, 28] and the respective proteins are present in the plasma membrane (this study). Although HCN2 was found to be the dominant isoform in TC neurons [20, 28], only a small reduction in the maximal available current was observed (Fig. 2b, lower panel). This discrepancy may be explained by the finding that the predominant action of halothane on HCN1–HCN2 heterodimers depends on the relief of the C-terminal-dependent basal inhibition by cAMP [6].

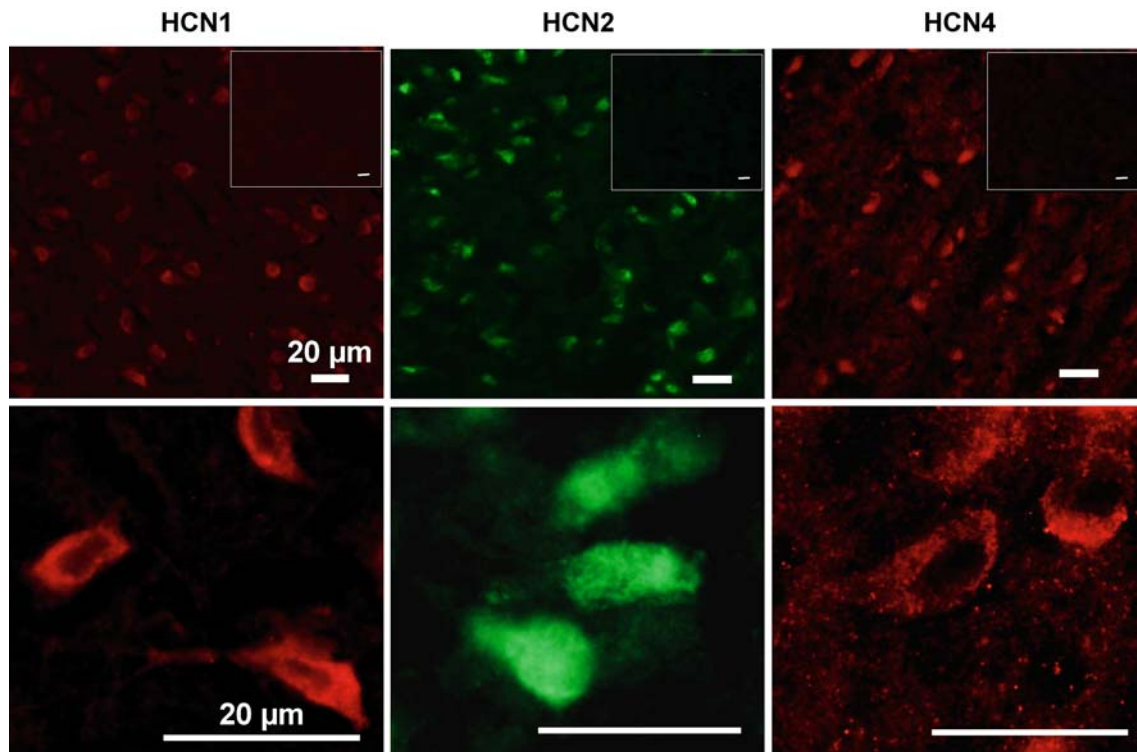


Fig. 6 Immunohistochemical labeling of HCN channels in dLGN. Specific antibodies directed against HCN1 (left images), HCN2 (middle images), and HCN4 (right images) were detected by fluorescent microscopy and detection of fluorochrome-coupled appropriate secondary antibodies (Cy2, HCN2; Cy3, HCN1, and HCN4;

upper row low resolution; lower row high resolution). The insets (upper row) show negative controls (occlusion of the primary antibody). Images were deconvoluted using the Zeiss AxioVision (4.6.3) software package

However, the conclusion that I_h in TC neurons is based on HCN1–HCN2 heterodimers is complicated by several circumstances: (1) TC neurons express HCN4 [36]; this study). HCN channel subunits assemble to a variety of different heteromers, including HCN1/HCN4 and HCN2/HCN4 [1, 32]. The modulation of HCN4 and heteromeric channels containing HCN4 has not yet been determined. (2) The manifestation of the two halothane effects on I_h depends on the degree of HCN channel relief from basal inhibition by cAMP [6]. Therefore, the more prominent effect of halothane on I_h voltage dependency in TC neurons may be attributed to significant basal adenylate cyclase activity, resulting in basal cAMP levels of around 10 nM and influencing I_h voltage dependency [4]. (3) Halothane has been shown to directly affect adenylate cyclase in rat cerebellum and cerebral cortex [54], thereby increasing the rate of cAMP production. This would lead to a depolarizing shift of the voltage dependence of I_h with G_h remaining unaltered [21, 37].

Correlation of K_{2P} channel expression and halothane effects in TC neurons

TC neurons carry a prominent pH-sensitive outwardly rectifying K^+ current that is mediated by TASK1 and TASK3 channels. The TASK3 channel represents the

dominant isoform [26–28]. Although the results presented in this study demonstrate that TASK channels are a major target of halothane in TC cells, the interpretation of the halothane effect is complicated by the finding that *TREK1* and *THIK2* genes are expressed in dLGN [28]. Because numerous current components underlie I_{SO} in TC neurons [28], the specific contribution of ion channel subtypes is difficult to assess and has not been performed for K_{2P} channels other than TASK. Nevertheless, the presence of an I_{SO} component that is inhibited by cAMP [3] and activated by arachidonic acid [28] is in agreement with the functional expression of TREK1 [15]. Therefore, TREK1 cannot be excluded to contribute to the halothane-sensitive outward current in TC neurons. Furthermore, it is likely that the reduction of I_{SO} by halothane seen during extracellular acidification is caused by the inhibition of THIK2 [41], which points to a complex activation and inhibition of K_{2P} channels in TC neurons by halothane.

Halothane suspends sensory system relay

The thalamocortical neuronal network exerts two distinct states of activity: (1) low-frequency oscillatory activity (delta activity and spindling) during natural sleep and deep anesthesia and (2) high-frequency oscillatory activity in the

gamma range and tonic activity during waking and REM sleep [45, 49]. TC neurons accordingly possess two modes of activity: (1) hyperpolarized and rhythmically bursting during states of slow-wave sleep and anesthesia, (2) depolarized and tonic firing of single action potentials that relay incoming sensory signals through the dorsal thalamus toward the cortex [46]. The thalamus is, therefore, regarded as being one of the central structures in the control of the sleep–wake cycle and in the induction and maintenance of anesthesia.

Adenosine is directly linked to the energy metabolism of cells and is regarded as a sleep-inducing factor [2, 40]. In the central nervous system, an increase in neuronal activity enhances energy consumption and extracellular adenosine concentrations. In most brain areas, high extracellular adenosine concentrations via A_1 adenosine receptors decrease neuronal activity and, thus, energy consumption. In the thalamus, adenosine hyperpolarizes TC neurons due to an increase in membrane potassium conductance and a decrease in I_h , which possibly results in an inhibition of tonic firing and promotes burst discharges [34]. Similarly, halothane will strongly disfacilitate conditions of faithful signal transfer in the thalamocortical system in that the hyperpolarization in relay neurons shifts the membrane potential out of the range of tonic action potential firing. These findings indicate that the intuitive analogy between natural sleep and anesthesia is not only a matter of common sense but indeed has a cellular basis because halothane and adenosine modulate very similar ionic mechanisms to counteract the ascending brainstem system.

Both TASK and HCN channels have been identified as major molecular determinants of the resting membrane potential, and the reciprocal modulation of the corresponding currents has been shown to be the most effective way to toggle between the two activity modes of TC neurons [28]. Thus, in addition to NA, serotonin [22], and adenosine [34], halothane represents another example for this type of modulatory mechanism. Moreover, reciprocal modulation of a TASK-like current and I_h has been observed before in brainstem motoneurons and has been attributed to the decreased motoneuronal excitability that accompanies anesthetic-induced immobilization [48]. The present study adds to this scenario by showing that very similar mechanisms lead to sleep-like activity of TC neurons, thereby pointing to a more general principle.

It could be argued that the action of halothane on TC neurons is a specific blockade of ion channels rather than the basis for its anesthetic effect. Indeed, halothane seems to specifically bind to a number of ion channels (for review, see [55]). However, halothane acts on target brain regions that are in perfect strategic positions to affect essential parameters of anesthesia, including consciousness (thalamus), pain perception (thalamus), and voluntary movement

(brainstem motoneurons): (1) Halothane action on TC neurons may lead to the breakdown of sensory transmission and the loss of conscious awareness via the induction of a membrane hyperpolarization and, hence, the switch from tonic to burst firing (this study). (2) The membrane hyperpolarization and decrease in excitability of hypoglossal motoneurons may lead to the dampening of muscle activity [48]. (3) The bradycardic action of halothane may have its cause in its effect on cardiac HCN channels. (4) The counteracting balance of HCN and TASK is essential for maintaining the resting membrane potential in central neurons [7, 28, 48]. Given the widespread distribution of TASK and HCN channels in the brain, it may be concluded that the modulation of these channels is an essential part of the clinical action of halothane [31, 53]. This view is further corroborated by the finding that isoflurane and sevoflurane also act on I_h (this study) and I_{TASK} [38, 47].

Is the reciprocal modulation of TASK and HCN channels sufficient to explain the halothane effect?

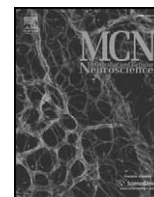
Although the reciprocal modulation of TASK and HCN channels seems to be a more general mechanism of halothane action in central areas for motor control and awareness, and computer modeling indicates that this effect is sufficient to explain the halothane-induced hyperpolarization seen in TC neurons, additional effects can be expected. The shunting effect of the increased K^+ conductance on postsynaptic potentials, Na^+/K^+ action potentials, and low-threshold Ca^{2+} spikes [42, 51] will block the transfer of all sensory and motor activity coded as tonic or burst firing [10, 58], contributing in analgesia, loss of awareness, and the suppression of motor activity and leading to the observed isoelectric EEG during anesthesia. Furthermore, anesthetic sites on GABA receptors cause lower GABA concentrations to work but also increase the amplitude of GABAergic signals [17], while the amplitudes of excitatory postsynaptic cholinergic and/or glutamatergic currents are decreased [9] (for review, see [5]), although the ratio between these effects may vary between cell types. For example, in somatosensory TC neurons in Wistar rats in vivo, the volatile anesthetic isoflurane exerts a concentration-dependent effect on GABAergic inhibition leading to a block of thalamocortical information transfer and, to a lesser extent, a suppression of glutamatergic signals and synapses [8, 57].

Acknowledgements The authors wish to thank E. Naß and A. Jahn for the excellent technical assistance. We also wish to thank Prof. J. Andersson for his kind help with the gas chromatography and Prof. E. Pogatzki-Zahn for kindly providing the sevoflurane. This study was supported by DFG (BU 1019/7-1; Pa 336/17-1), Innovative Medizinische Forschung (IMF; BU 120501), and Interdisziplinäres Zentrum für Klinische Forschung (IZKF; Bud/005/07 to TB; A-54 to SGM).

References

- Altomare C, Terragni B, Brioschi C, Milanesi R, Pagliuca C, Viscomi C, Moroni A, Baruscotti M, DiFrancesco D (2003) Heteromeric HCN1–HCN4 channels: a comparison with native pacemaker channels from the rabbit sinoatrial node. *J Physiol (Lond)* 549:347–359
- Basheer R, Strecker RE, Thakkar MM, McCarley RW (2004) Adenosine and sleep–wake regulation. *Prog Neurobiol* 73:379–396
- Budde T, Biella G, Munsch T, Pape H-C (1997) Lack of regulation by intracellular Ca^{2+} of the hyperpolarization-activated cation current in rat thalamic neurons. *J Physiol (Lond)* 503.1:79–85
- Budde T, Caputi L, Kanyshkova T, Staak R, Abrahamczik C, Munsch T, Pape HC (2005) Impaired regulation of thalamic pacemaker channels through an imbalance of subunit expression in absence epilepsy. *J Neurosci* 25:9871–9882
- Campagna JA, Miller KW, Forman SA (2003) Mechanisms of actions of inhaled anesthetics. *N Engl J Med* 348:2110–2124
- Chen X, Sirois JE, Lei Q, Talley EM, Lynch C III, Bayliss DA (2005) HCN subunit-specific and cAMP-modulated effects of anesthetics on neuronal pacemaker currents. *J Neurosci* 25:5803–5814
- Day M, Carr DB, Ulrich S, Ilijic E, Tkatch T, Surmeier DJ (2005) Dendritic excitability of mouse frontal cortex pyramidal neurons is shaped by the interaction among HCN, Kir2, and K leak channels. *J Neurosci* 25:8776–8787
- Detsch O, Kochs E, Siemers M, Bromm B, Vahle-Hinz C (2002) Differential effects of isoflurane on excitatory and inhibitory synaptic inputs to thalamic neurones in vivo. *Br J Anaesth* 89:294–300
- Dilger JP, Vidal AM, Mody AI, Liu Y (1994) Evidence for direct actions of general anesthetics on an ion channel protein. A new look at a unified mechanism of action. *Anesthesiology* 81:431–442
- Fanselow EE, Sameshima K, Baccala LA, Nicolelis MA (2001) Thalamic bursting in rats during different awake behavioral states. *Proc Natl Acad Sci U S A* 98:15330–15335
- Franks NP, Lieb WR (1994) Molecular and cellular mechanisms of general anaesthesia. *Nature* 367:607–614
- Franks NP, Lieb WR (1998) Which molecular targets are most relevant to general anaesthesia? *Toxicol Lett* 100–101:1–8
- Heurteaux C, Guy N, Laigle C, Blondeau N, Duprat F, Mazzuca M, Lang-Lazdunski L, Widmann C, Zanzouri M, Romey G, Lazdunski M (2004) TREK-1, a K^{+} channel involved in neuroprotection and general anesthesia. *EMBO J* 23:2684–2695
- Hines ML, Carnevale NT (2001) NEURON: a tool for neuroscientists. *Neuroscientist* 7:123–135
- Honore E (2007) The neuronal background $\text{K}^{2\text{P}}$ channels: focus on TREK1. *Nat Rev Neurosci* 8:251–261
- Huguenard JR, McCormick DA (1992) Simulation of the currents involved in rhythmic oscillations in thalamic relay neurons. *J Neurophysiol* 68:1373–1383
- Jones MV, Harrison NL (1993) Effects of volatile anesthetics on the kinetics of inhibitory postsynaptic currents in cultured rat hippocampal neurons. *J Neurophysiol* 70:1339–1349
- Linden A-M, Aller MI, Leppä E, Vekovischeva O, Aitta-aho T, Veale EL, Mathie A, Rosenberg P, Wisden W, Korpi ER (2006) The in vivo contributions of TASK-1-containing channels to the actions of inhalation anesthetics, the α_2 adrenergic sedative dexmedetomidine, and cannabinoid agonists. *J Pharmacol Exp Ther* 317:615–626
- Linden A-M, Sandu C, Aller MI, Vekovischeva OY, Rosenberg PH, Wisden W, Korpi ER (2007) TASK-3 knockout mice exhibit exaggerated nocturnal activity, impairments in cognitive functions, and reduced sensitivity to inhalation anesthetics. *J Pharmacol Exp Ther* 323:924–934
- Ludwig A, Budde T, Stieber J, Moosmang S, Wahl C, Holthoff K, Langebartels A, Wotjak C, Munsch T, Zong X, Feil S, Feil R, Lancel M, Chien KR, Konnerth A, Pape HC, Biel M, Hofmann F (2003) Absence epilepsy and sinus dysrhythmia in mice lacking the pacemaker channel HCN2. *EMBO J* 22:216–224
- Maingret F, Patel AJ, Lesage F, Lazdunski M, Honore E (1999) Mechano- or acid stimulation, two interactive modes of activation of the TREK-1 potassium channel. *J Biol Chem* 274:26691–26696
- McCormick DA (1992) Neurotransmitter actions in the thalamus and cerebral cortex and their role in neuromodulation of thalamocortical activity. *Prog Neurobiol* 39:337–388
- McCormick DA, Huguenard JR (1992) A model of the electrophysiological properties of thalamocortical relay neurons. *J Neurophysiol* 68:1384–1400
- McCormick DA, Pape H-C (1990) Properties of a hyperpolarization-activated cation current and its role in rhythmic oscillation in thalamic relay neurones. *J Physiol (Lond)* 431:291–318
- Meuth P, Meuth SG, Jacobi D, Broicher T, Pape HC, Budde T (2005) Get the rhythm: modeling of neuronal activity. *Journal of Undergraduate Neuroscience Education* 4(1):A1–A11
- Meuth SG, Aller MI, Munsch T, Schuhmacher T, Seidenbecher T, Kleinschmitt C, Pape HC, Wiendl H, Wisden W, Budde T (2006a) The contribution of TASK-1-containing channels to the function of dorsal lateral geniculate thalamocortical relay neurons. *Mol Pharmacol* 69:1468–1476
- Meuth SG, Budde T, Kanyshkova T, Broicher T, Munsch T, Pape H-C (2003) Contribution of TWIK-related acid-sensitive K^{+} channel 1 (TASK1) and TASK3 channels to the control of activity modes in thalamocortical neurons. *J Neurosci* 23:6460–6469
- Meuth SG, Kanyshkova T, Meuth P, Landgraf P, Munsch T, Ludwig A, Hofmann F, Pape HC, Budde T (2006b) The membrane resting potential of thalamocortical relay neurons is shaped by the interaction among TASK3 and HCN2 channels. *J Neurophysiol* 96:1517–1529
- Mihic SJ, Ye Q, Wick MJ, Koltchine VV, Krasowski MD, Finn SE, Mascia MP, Valenzuela CF, Hanson KK, Greenblatt EP, Harris RA, Harrison NL (1997) Sites of alcohol and volatile anaesthetic action on GABAA and glycine receptors. *Nature* 389:385–389
- Mikulec AA, Pittson S, Amagasa SM, Monroe FA, MacIver MB (1998) Halothane depresses action potential conduction in hippocampal axons. *Brain Res* 796:231–238
- Monteggia LM, Eisch AJ, Tang MD, Kaczmarek LK, Nestler EJ (2000) Cloning and localization of the hyperpolarization-activated cyclic nucleotide-gated channel family in rat brain. *Brain Res Mol Brain Res* 81:129–139
- Much B, Wahl-Schott C, Zong X, Schneider A, Baumann L, Moosmang S, Ludwig A, Biel M (2003) Role of subunit heteromerization and N-linked glycosylation in the formation of functional hyperpolarization-activated cyclic nucleotide-gated channels. *J Biol Chem* 278:43781–43786
- Nelson LE, Guo TZ, Lu J, Saper CB, Franks NP, Maze M (2002) The sedative component of anesthesia is mediated by GABAA receptors in an endogenous sleep pathway. *Nat Neurosci* 5:979–984
- Pape H-C (1992) Adenosine promotes burst activity in guinea-pig geniculocortical neurones through two different ionic mechanisms. *J Physiol (Lond)* 447:729–753
- Pape H-C (1996) Queer current and pacemaker: the hyperpolarization-activated cation current in neurons. *Annu Rev Physiol* 58:299–327
- Pape HC, Kanyshkova T, Broicher T, Budde T (2007) Developmental and functional profile of the thalamic hyperpolarization-activated cation current, I_h , in absence epilepsy. *Thalamus & Related Systems* DOI 10.1017/S1472928807000180

37. Patel A, Lazdunski M (2004) The 2P-domain K⁺ channels: role in apoptosis and tumorigenesis. *Pflügers Arch* 448:261–273
38. Patel AJ, Honore E, Lesage F, Fink M, Romey G, Lazdunski M (1999) Inhalational anesthetics activate two-pore-domain background K⁺ channels. *Nat Neurosci* 2:422–426
39. Pearce RA (1996) Volatile anaesthetic enhancement of paired-pulse depression investigated in the rat hippocampus in vitro. *J Physiol (Lond)* 492:823–840
40. Porkka-Heiskanen T, Alanko L, Kalinchuk A, Stenberg D (2002) Adenosine and sleep. *Sleep Med Rev* 6:321–332
41. Rajan S, Wischmeyer E, Karschin C, Preisig-Muller R, Grzeschik K-H, Daut J, Karschin A, Derst C (2001) THIK-1 and THIK-2, a novel subfamily of tandem pore domain K⁺ channels. *J Biol Chem* 276:7302–7311
42. Ries CR, Puil E (1999a) Mechanism of anesthesia revealed by shunting actions of isoflurane on thalamocortical neurons. *J Neurophysiol* 81:1795–1801
43. Ries CR, Puil E (1999b) Ionic mechanism of isoflurane's actions on thalamocortical neurons. *J Neurophysiol* 81:1802–1809
44. Seifert R, Scholten A, Gauss R, Mincheva A, Lichter P, Kaupp UB (1999) Molecular characterization of a slowly gating human hyperpolarization-activated channel predominantly expressed in thalamus, heart, and testis. *Proc Natl Acad Sci U S A* 96:9391–9396
45. Sherman SM, Guillery RW (1996) Functional organization of thalamocortical relays. *J Neurophysiol* 76:1367–1395
46. Sherman SM, Guillery RW (2001) *Exploring the thalamus*. Academic Press, San Diego
47. Sirois JE, Lei Q, Talley EM, Lynch C 3rd, Bayliss DA (2000) The TASK-1 two-pore domain K⁺ channel is a molecular substrate for neuronal effects of inhalation anesthetics. *J Neurosci* 20:6347–6354
48. Sirois JE, Lynch C 3rd, Bayliss DA (2002) Convergent and reciprocal modulation of a leak K⁺ current and I_h by an inhalational anaesthetic and neurotransmitters in rat brainstem motoneurons. *J Physiol (Lond)* 541:717–729
49. Steriade M (1997) Synchronized activities of coupled oscillators in the cerebral cortex and thalamus at different levels of vigilance. *Cereb Cortex* 7:583–604
50. Steriade M, Jones EG, McCormick DA (1997) *Thalamus*. Elsevier, Amsterdam
51. Sugiyama K, Muteki T, Shimoji K (1992) Halothane-induced hyperpolarization and depression of postsynaptic potentials of guinea pig thalamic neurons in vitro. *Brain Res* 576:97–103
52. Talley EM, Bayliss DA (2002) Modulation of TASK-1 (Kcnk3) and TASK-3 (Kcnk9) potassium channels. Volatile anesthetics and neurotransmitters share a molecular site of action. *J Biol Chem* 277:17733–17742
53. Talley EM, Solorzano G, Lei Q, Kim D, Bayliss DA (2001) CNS distribution of members of the two-pore-domain (KCNK) potassium channel family. *J Neurosci* 21:7491–7505
54. Triner L, Vulliamoz Y, Woo S-Y, Verosky M (1980) Halothane effect on cAMP generation and hydrolysis in rat brain. *Eur J Pharmacol* 66:73–80
55. Trudell JR, Bertaccini E (2002) Molecular modelling of specific and non-specific anaesthetic interactions. *Br J Anaesth* 89:32–40
56. Tung A, Mendelson WB (2004) Anesthesia and sleep. *Sleep Med Rev* 8:213–225
57. Vahle-Hinz C, Detsch O, Siemers M, Kochs E (2007) Contributions of GABAergic and glutamatergic mechanisms to isoflurane-induced suppression of thalamic somatosensory information transfer. *Exp Brain Res* 176:159–172
58. Weyand TG, Boudreaux M, Guido W (2001) Burst and tonic response modes in thalamic neurons during sleep and wakefulness. *J Neurophysiol* 85:1107–1118



Correlation of T-channel coding gene expression, I_T , and the low threshold Ca^{2+} spike in the thalamus of a rat model of absence epilepsy

Tilman Broicher, Tatyana Kanyshkova, Patrick Meuth, Hans-Christian Pape, Thomas Budde*

Institut für Physiologie I, Westfälische Wilhelms-Universität Münster, Robert-Koch-Str. 27a, D-48149 Münster, Germany

ARTICLE INFO

Article history:

Received 22 April 2008

Revised 27 June 2008

Accepted 16 July 2008

Available online 29 July 2008

Keywords:

Patch clamp

T-type Ca^{2+} channel

Absence epilepsy

Thalamus

Burst firing

Real-time PCR

ABSTRACT

T-type Ca^{2+} current-dependent burst firing of thalamic neurons is thought to be involved in the hyper-synchronous activity observed during absence seizures. Here we investigate the correlation between the expression of T-channel coding genes ($\alpha 1G$, $-H$, $-I$), T-type Ca^{2+} current, and the T-current-dependent low threshold Ca^{2+} spike in three functionally distinct thalamic nuclei (lateral geniculate nucleus; centrolateral nucleus; reticular nucleus) in a rat model of absence epilepsy, the WAG/Rij rats, and a non-epileptic control strain, the ACI rats. The lateral geniculate nucleus and centrolateral nucleus were found to primarily express $\alpha 1G$ and $\alpha 1I$, while the reticular thalamic nucleus expressed $\alpha 1H$ and $\alpha 1I$. Expression was higher in WAG/Rij when compared to ACI. The T-type Ca^{2+} current properties matched the predictions derived from the expression pattern analysis. Current density was larger in all nuclei of WAG/Rij rats when compared to ACI and correlated with LTS size and the minimum LTS generating slope, while T-type Ca^{2+} current voltage dependency correlated with the LTS onset potential.

© 2008 Elsevier Inc. All rights reserved.

Introduction

The thalamocortical system displays low frequency oscillatory activity during slow wave sleep as well as spike and wave discharges (SWD) observed during episodes of absence epilepsy (Avoli et al., 2001; Crunelli and Leresche, 2002; Steriade, 1997). The neural substrates of these slow oscillations are the thalamus and the cortex. Based on efferent projections, the thalamus can be divided into three groups of nuclei: (1) the specific nuclei, which project to well circumscribed cortical regions (e.g. lateral geniculate nucleus, LGN); (2) the non-specific nuclei, which project to broader, primarily frontal cortical regions and the striatum (e.g. centrolateral nucleus of the intralaminar nuclei, CL); (3) the reticular thalamic nucleus (NRT), which projects onto thalamocortical relay nuclei in an inhibitory manner, serving as a pacemaker.

Within the thalamus, the slow oscillations are accompanied by burst firing in thalamocortical relay (TC) as well as reticular neurons (Paz et al., 2007; Pinault et al., 1998; Seidenbecher and Pape, 2001; Seidenbecher et al., 1998; Slaght et al., 2002; Williams, 1953). Burst firing in thalamic neurons depends on the action of T-type Ca^{2+} channels. These channels generate a low threshold Ca^{2+} spike (LTS), which triggers a high frequency burst of action potentials (Huguenard, 1996). Until now, three genes (CACNA1G, $-H$, $-I$) coding for three T-type Ca^{2+} channel isoforms, termed $\alpha 1G$, $\alpha 1H$, and $\alpha 1I$, have been

identified (Perez-Reyes, 2003). All isoforms seem to be subjected to alternative splicing, thus vastly increasing the number of physiologically distinct channel types (Perez-Reyes, 2006). Currents generated by the $\alpha 1G$ and $\alpha 1H$ isoforms appear rather similar in heterologous expression systems, while currents generated by the $\alpha 1I$ isoform differ in voltage dependency and kinetics (Chemin et al., 2002).

Previous studies have shown that neurons of different thalamic nuclei (specific relay nuclei vs. reticular nucleus) display different T-type Ca^{2+} currents (I_T) and different LTS properties (Huguenard, 1996). In line with these findings, expression of T-channel isoforms has been found to vary between thalamic nuclei: relay nuclei primarily express the $\alpha 1G$ isoform, while $\alpha 1H$ and $\alpha 1I$ expression has been observed in the NRT (Talley et al., 1999).

Several lines of evidence link thalamic I_T to slow oscillations of the thalamocortical system. Genetic rat models of absence epilepsy reveal an increased I_T and an increased expression of T-channel coding genes in the NRT (Talley et al., 2000; Tsakiridou et al., 1995). Knock-out mouse models have demonstrated the dependence of slow sleep oscillations as well as spike and wave discharges on the presence of the $\alpha 1G$ isoform in the thalamus (Anderson et al., 2005; Kim et al., 2001; Song et al., 2004). Furthermore, anti-epileptic medications effective in human patients have been shown to suppress thalamic T-type Ca^{2+} currents (Broicher et al., 2007b; Coulter et al., 1989a,b; Leresche et al., 1998).

This study was designed to investigate the correlation between the expression of T-type Ca^{2+} channel coding genes, I_T , and the LTS in thalamic neurons. To include neuronal populations known to display differences in these parameters, neurons from LGN and NRT were

* Corresponding author. Fax: +49 251 83 55551.

E-mail address: tbudde@uni-muenster.de (T. Budde).

investigated. To extend the experiments to a neuronal population of largely unknown function and cellular properties, but a potential role in spreading epileptic activity throughout the thalamocortical system, CL neurons of the non-specific intralaminar nuclei have been included in the study. To scrutinize the effects of differences in the expression of T-type Ca^{2+} channel coding genes, I_T , and the LTS with respect to absence epilepsy all experiments have been performed in a genetic rat model of absence epilepsy, the WAG/Rij rats, and a non-epileptic control strain, the ACI rats (Coenen and Van Luijckelaer, 2003) by combining quantitative RT-PCR, whole-cell patch clamping in brain slices, and computer modeling.

Results

Expression pattern of CACNA1G, -H, -I transcripts in the LGN, CL, and NRT of WAG/Rij and ACI rats

First, the expression profile of the three T-type Ca^{2+} channel coding genes was examined in the LGN, CL, and NRT of WAG/Rij and ACI rats. Samples of tissue yielded through laser capturing were subjected to quantitative RT-PCR procedures (Fig. 1A, note that lower

ΔCt values indicate higher mRNA expression). Distinct differences in gene expression were found between nuclei and strains. In the LGN and CL of both strains the CACNA1G isoform was strongly expressed, while only a weak signal could be detected in the NRT. In both LGN and CL, expression levels of the CACNA1G transcript were significantly higher in WAG/Rij than in ACI rats (Fig. 1B, Table 1).

The CACNA1H isoform was usually below detection limits in the CL and LGN, but was strongly expressed in the NRT of both strains and expression levels tended to be higher in WAG/Rij, although this trend failed to reach significance (Fig. 1C, Table 1).

The CACNA1I transcript was found to be expressed in all three nuclei of both strains. The expression levels were significantly different between strains and nuclei. The CL and NRT of WAG/Rij rats expressed significantly higher levels of CACNA1I mRNA than the same nuclei of ACI rats. Within each strain, CACNA1I expression was significantly higher in the NRT than in the CL and LGN, while expression in the CL was significantly higher than in the LGN (Fig. 1D, Table 1). A previous study by our group has demonstrated that the expression of CACNA1I can be attributed to the local circuit interneurons in the LGN. Thalamocortical projection neurons of the LGN (LGN TC), which were subjected to electrophysiological

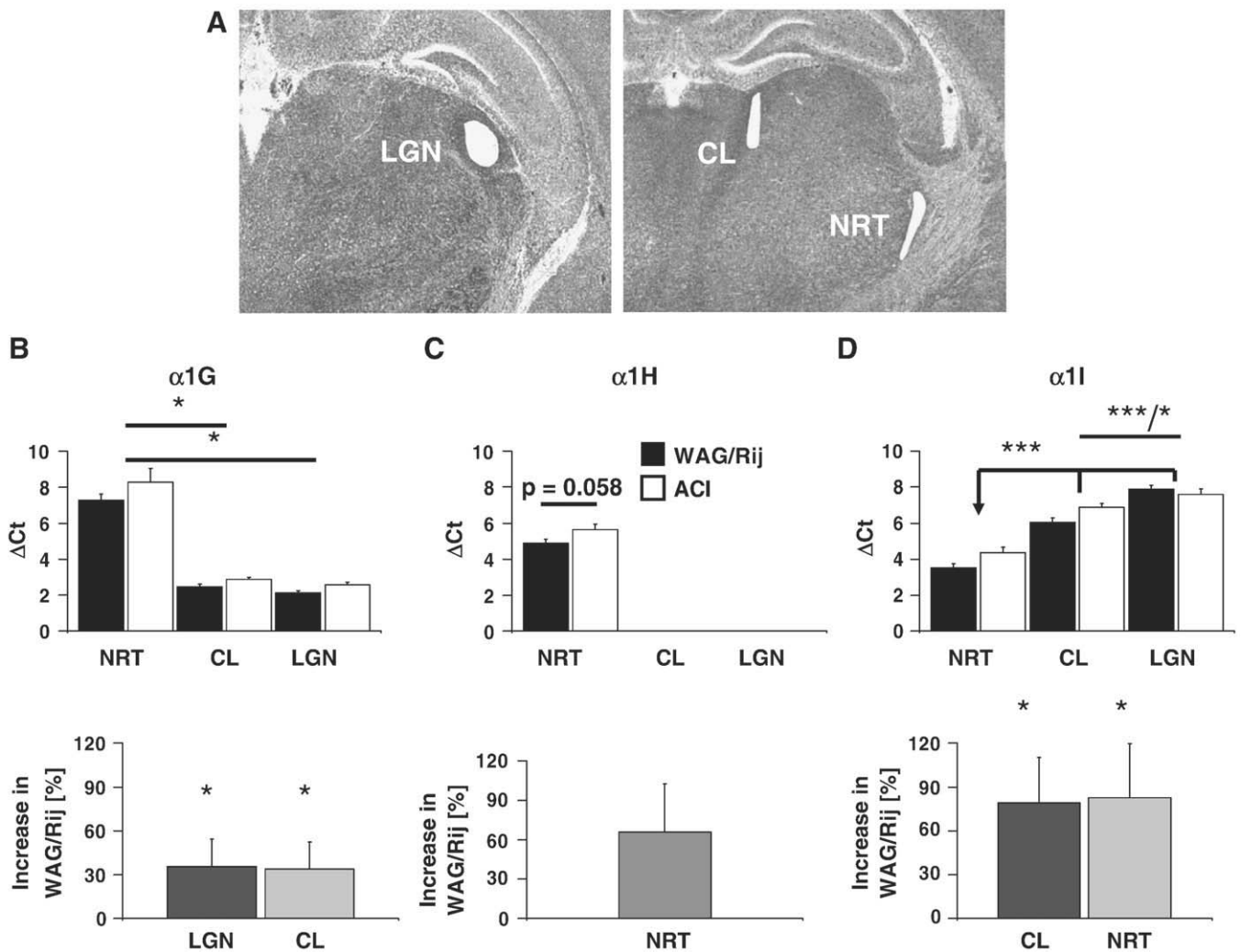


Fig. 1. Tissue level RT-PCR of CACNA1G, -H, and -I expression in the LGN, CL, and NRT of WAG/Rij and ACI rats. All 3 T-channel coding genes revealed an increased expression in WAG/Rij. Note that lower ΔCt values indicate higher mRNA expression. (A) Examples of brain slices after laser microdissection of LGN (left panel), CL (right panel) and NRT (right panel) tissue. (B) Mean cycle of threshold differences between CACNA1G and $\beta 2M$ mRNA in the LGN, CL, and NRT of WAG/Rij and ACI rats (upper panel). The increased CACNA1G expression in WAG/Rij as compared to ACI is depicted in the lower panel. (C) Mean cycle of threshold differences between CACNA1H and $\beta 2M$ -microglobuline ($\beta 2M$) mRNA in the NRT of WAG/Rij and ACI rats (upper panel). CACNA1H expression was usually below the detection limit in the CL and LGN of both strains. In the lower panel the increased CACNA1H expression in WAG/Rij as compared to ACI is shown. (D) Mean differences of threshold circles from CACNA1I and $\beta 2M$ mRNA in the LGN, CL, and NRT of WAG/Rij and ACI rats (upper panel). The lower panel depicts the increased CACNA1I expression in WAG/Rij as compared to ACI. * $p < 0.05$; ** $p < 0.01$; *** $p < 0.001$.

Table 1
Summary of RT-PCR data and statistical analysis

	CACNA1G [Δ Ct]	CACNA1H [Δ Ct]	CACNA1I [Δ Ct]
WAG/Rij LGN	2.1 \pm 0.1; n=12	//	7.9 \pm 0.2; n=12
CL	2.5 \pm 0.1; n=12	//	6.1 \pm 0.2; n=12
NRT	7.3 \pm 0.3; n=12	4.9 \pm 0.2; n=12	3.5 \pm 0.2; n=12
ACI LGN	2.6 \pm 0.1; n=13	//	7.6 \pm 0.3; n=13
CL	2.9 \pm 0.1; n=12	//	6.9 \pm 0.2; n=12
NRT	8.3 \pm 0.8; n=12	5.6 \pm 0.3; n=12	4.4 \pm 0.3; n=12
Statistical significances CACNA1G			
	LGN vs. CL	LGN vs. NRT	CL vs. NRT
WAG/Rij	N.S.	*	*
ACI	N.S.	*	*
	LGN vs. LGN	CL vs. CL	NRT vs. NRT
WAG/Rij vs. ACI	*	*	N.S.
* p <0.05; ** p <0.01; *** p <0.001.			
Statistical significances CACNA1H			
	LGN vs. CL	LGN vs. NRT	CL vs. NRT
WAG/Rij	//	//	//
ACI	//	//	//
	LGN vs. LGN	CL vs. CL	NRT vs. NRT
WAG/Rij vs. ACI	//	//	N.S. (p =0.058)
* p <0.05; ** p <0.01; *** p <0.001.			
Statistical significances CACNA1I			
	LGN vs. CL	LGN vs. NRT	CL vs. NRT
WAG/Rij	***	***	***
ACI	*	***	***
	LGN vs. LGN	CL vs. CL	NRT vs. NRT
WAG/Rij vs. ACI	N.S.	*	*
* p <0.05; ** p <0.01; *** p <0.001.			

N.S.: not significant.

investigation in this study, solely express the CACNA1G gene (Broicher et al., 2007a).

Next, the possibility of alternative splicing of the CACNA1G transcript (exons 25/26) was investigated in the CL of both strains. Alternatively spliced CACNA1G transcripts have been shown to give rise to physiologically distinct channels (Chemin et al., 2001; Emerick et al., 2006) and have been implicated in the generation of the diverging T-type Ca^{2+} currents of LGN projection and local circuit interneurons (Broicher et al., 2007a). Non-quantitative RT-PCR experiments on CL tissue samples gathered through laser dissection microscopy revealed the presence of two alternatively spliced isoforms in the CL, data not shown. The smaller isoform will be referred to as Iso1 (analogous to human α 1G-a, AF027984), the larger isoform will be referred to as Iso2 (analogous to human α 1G-bc, AF125161). In the majority of CL tissue samples from both strains bands corresponding to both isoforms could be detected (WAG/Rij CL: Iso1 only: 1 of 7 samples, Iso2 only: 0 of 7 samples; Iso1 and Iso2: 6 of 7 samples; ACI CL: Iso1 only: 2 of 8 samples, Iso2 only: 1 of 8 samples, Iso1 and Iso2: 5 of 8 samples; data not shown).

Assuming that the differences on the mRNA level translate into differences in channel protein, these results allow some predictions concerning the properties of the T-type Ca^{2+} currents. The increased expression of T-channel coding mRNA could lead to an increase in I_T density in WAG/Rij. According to data from heterologous expression systems (Chemin et al., 2001, 2002; Emerick et al., 2006), NRT neurons of both strains should display a T-type Ca^{2+} current voltage dependency of comparatively positive values and slow kinetics, while the I_T of LGN TC neurons should display a rather negative I_T voltage dependency and fast kinetics. The I_T of CL neurons should be of intermediate voltage dependency and kinetics, when compared to the I_T recorded in LGN TC and NRT neurons.

Electrophysiological properties of T-type Ca^{2+} currents in LGN, CL, and NRT neurons of WAG/Rij and ACI rats

To correlate I_T of LGN TC, CL, and NRT neurons of WAG/Rij and ACI rats with the expression of the T-channel coding genes and the LTS, the T-type Ca^{2+} current properties were investigated. Whole-cell voltage clamp techniques were employed on neurons in brain slice preparations. Between the stimulation protocols neurons were held at -60 mV.

Voltage dependency of activation

The steady-state voltage dependency of activation was investigated by stepping neurons to increasingly positive test potentials (200 ms, CL and LGN; 500 ms, NRT) from a conditioning potential of -110 mV (700 ms, all nuclei; Fig. 2A). Construction of steady-state activation curves revealed half maximal activation voltages (V_h), which were significantly different between nuclei and strains (Fig. 2B). In both strains, the T-type Ca^{2+} current of LGN TC neurons activated at the most negative potentials, followed by neurons of the CL, where I_T activated at intermediate potentials, and neurons of the NRT, whose T-type Ca^{2+} currents activated at the most positive voltages (Fig. 2B, Table 2). The steady-state activation curves of the T-type Ca^{2+} currents recorded in LGN and CL relay neurons of WAG/Rij rats revealed significantly more negative V_h values when compared to the corresponding V_h values obtained from recordings in neurons of ACI rats. In the NRT the opposite situation was observed. Here, the V_h values of steady-state activation revealed a small but significant shift towards more positive potentials in WAG/Rij when compared to ACI (Table 2).

Voltage dependency of inactivation

In the following, the steady-state inactivation was investigated by holding neurons at increasingly positive potentials, starting from -110 mV (700 ms, all nuclei), and stepping to a constant analyzing potential of -55 mV (200 ms, CL and LGN; 500 ms, NRT; Fig. 2C). As found for the steady-state activation, the half maximal voltages of steady-state inactivation revealed significant differences between strains and nuclei (Fig. 2D). In WAG/Rij, the T-type Ca^{2+} currents recorded in LGN TC neurons inactivated at the most negative potentials, followed by T-type Ca^{2+} currents recorded in CL neurons, and by T-type Ca^{2+} currents of NRT neurons, which inactivated at the most positive potentials. In ACI, the inactivation voltage dependencies of LGN TC and NRT neurons were similar, while CL neurons displayed more positive voltage dependencies of inactivation (Table 2). A comparison between strains proved the differences between the steady-state inactivation V_h of WAG/Rij and ACI CL and NRT to be significant. Within the WAG/Rij strain the differences between the inactivation V_h of all three nuclei were significant, while in ACI rats only the difference between CL and NRT was found to be significant ACI (Table 2).

Current density

As differences in T-type Ca^{2+} current density have been observed in other models of absence epilepsy, the maximal amplitudes and T-type Ca^{2+} current densities evoked by the activation type protocol have been compared between nuclei and strains. Within both strains, CL neurons displayed the highest T-type Ca^{2+} current amplitude, followed by the LGN, and the NRT. All differences in T-type Ca^{2+} current amplitudes between nuclei were significant within strains. Between strains, differences were significant for I_T amplitudes of LGN TC and CL neurons (Fig. 3A; Table 2). To obtain a measure of channel density per unit area of cell membrane, the T-type Ca^{2+} current amplitudes were divided by the capacitance of the neurons. Within and between both strains, capacitances of relay neurons of the LGN and CL were indistinguishable, while neurons of the NRT displayed significantly smaller capacitances than relay neurons of the LGN and

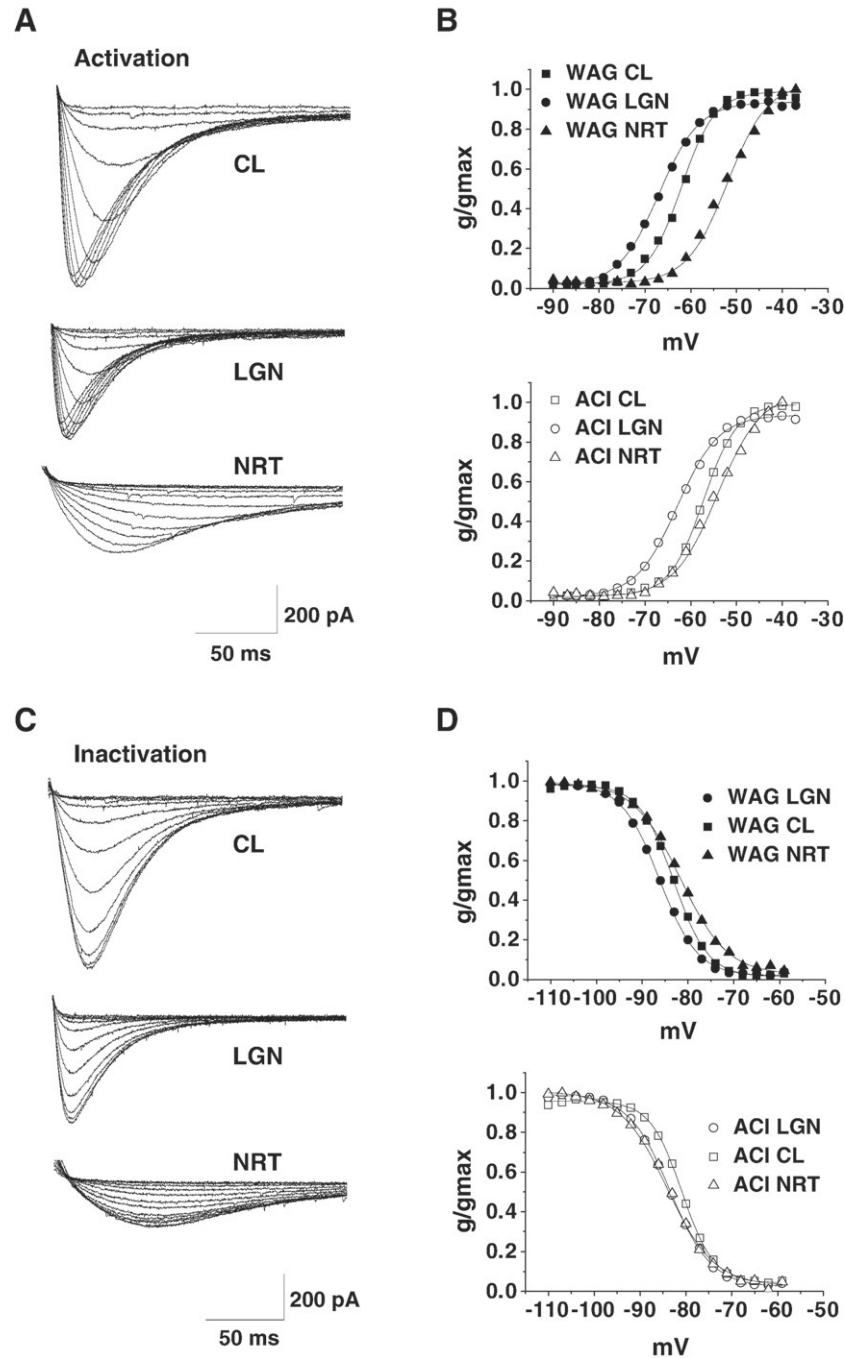


Fig. 2. Voltage dependency of activation and inactivation of T-type Ca^{2+} currents in LGN TC, CL, and NRT neurons of WAG/Rij and ACI rats. (A) Representative families of I_T of a LGN TC, a CL, and a NRT neuron. Displayed recordings derive from neurons taken from ACI rats. Neurons were clamped to increasingly positive test potentials from a holding potential of -110 mV. The initial test potential was -90 mV, which was increased in steps of 3 mV. (B) Activation curves from LGN TC, CL, and NRT neurons of WAG/Rij (upper panel) and ACI rats (lower panel; symbols as indicated) were obtained by fitting a Boltzmann equation to plots of mean values of normalized peak conductance vs. the test potential. Standard error bars have been omitted for clarity; see Table 2 for statistical data. (C) Representative families of I_T in LGN TC, CL, and NRT neurons. Recordings derived from neurons of ACI rats are shown. Neurons were stepped to a constant analyzing potential of -55 mV from increasingly positive conditioning potentials. Initial conditioning potential was -110 mV, which was altered in increments of 3 mV. (D) Inactivation curves from LGN, CL, and NRT neurons of WAG/Rij (upper panel) and ACI rats (lower panel; symbols as indicated) were obtained by fitting a Boltzmann equation to plots of mean values of normalized peak conductance vs. the test potential. Standard error bars have been omitted for clarity; see Table 2 for statistical data.

CL (Table 2). Within both strains NRT neurons displayed the largest T-type Ca^{2+} current densities, followed by neurons of the CL and the LGN (Fig. 3B, Table 2). Within both strains, the T-type Ca^{2+} current densities of LGN TC neurons were significantly smaller than the T-type Ca^{2+} current densities recorded in CL and NRT neurons, while the differences between CL and NRT neurons were not significant. All T-type Ca^{2+} current densities were significantly increased in WAG/Rij compared to ACI (Fig. 3B, Table 2).

Activation and inactivation kinetics

Next, time-dependent activation and inactivation properties of the T-type Ca^{2+} currents recorded in LGN TC, CL, and NRT neurons were analyzed. The inactivation of T-type Ca^{2+} currents was complete in all nuclei of both strains. In WAG/Rij and ACI rats, the T-type Ca^{2+} current recorded in LGN TC neurons was fastest to activate and inactivate, followed by I_T recorded in the CL, which displayed intermediate kinetics, and the I_T of NRT neurons, which was slowest to activate and inactivate.

Table 2
Summary of electrophysiological data and statistical analysis

	WAG/Rij LGN TC	WAG/Rij CL	WAG/Rij NRT	ACI LGN TC	ACI CL	ACI NRT
$I_T V_h$ act [mV]	-66 ± 1.5 ; $n=19$	-62.3 ± 1 ; $n=24$	-52 ± 0.5 ; $n=31$	-61.7 ± 1.4 ; $n=24$	-57.4 ± 1 ; $n=26$	-54.4 ± 0.5 ; $n=40$
$I_T V_h$ inact [mV]	-86.1 ± 1 ; $n=18$	-83.4 ± 0.8 ; $n=25$	-81.6 ± 0.3 ; $n=30$	-83.1 ± 1.1 ; $n=21$	-80.8 ± 0.7 ; $n=24$	-83.5 ± 0.3 ; $n=39$
TTP at -61 mV [ms]	22.8 ± 2 ; $n=19$	35.7 ± 2 ; $n=2$	97 ± 6 ; $n=31$	22.1 ± 1 ; $n=24$	37.8 ± 3 ; $n=27$	99.6 ± 5 ; $n=40$
TTP at -37 mV [ms]	13 ± 1 ; $n=19$	18 ± 2 ; $n=24$	35.8 ± 1 ; $n=31$	15 ± 3 ; $n=24$	16.1 ± 1 ; $n=27$	34.7 ± 1 ; $n=40$
Inact τ at -61 mV [ms]	28.9 ± 2 ; $n=19$	38.6 ± 2 ; $n=24$	137.7 ± 16 ; $n=31$	29.9 ± 2 ; $n=24$	44.6 ± 4 ; $n=27$	116.7 ± 7 ; $n=40$
Inact τ at -37 mV [ms]	23.5 ± 1 ; $n=19$	34.9 ± 2 ; $n=24$	55 ± 2 ; $n=31$	26.8 ± 2 ; $n=24$	30.4 ± 2 ; $n=27$	54.2 ± 2 ; $n=40$
I_T peak amp [pA]	-647 ± 37 ; $n=29$	-941 ± 60 ; $n=25$	-421 ± 28 ; $n=28$	-509 ± 26 ; $n=34$	-703 ± 53 ; $n=25$	-372 ± 24 ; $n=40$
Capacitance [pF]	119 ± 4 ; $n=29$	133 ± 7 ; $n=25$	59 ± 4 ; $n=31$	110 ± 4 ; $n=34$	118 ± 7 ; $n=25$	60 ± 3 ; $n=40$
CD [pA/pF]	5.4 ± 0.2 ; $n=34$	7.2 ± 0.3 ; $n=25$	7.4 ± 0.4 ; $n=31$	4.7 ± 0.2 ; $n=34$	6.1 ± 0.3 ; $n=25$	6.4 ± 0.3 ; $n=40$
V_{Rest} [mV]	-72.6 ± 1 ; $n=29$	-69.5 ± 1 ; $n=43$	-75.6 ± 1 ; $n=21$	-74.4 ± 1 ; $n=29$	-70.7 ± 1 ; $n=35$	-74.3 ± 1 ; $n=40$
# LTS APs	2.4 ± 0.2 ; $n=25$	2.3 ± 0.2 ; $n=39$	9.9 ± 1.7 ; $n=21$	2.4 ± 0.2 ; $n=25$	1.8 ± 0.2 ; $n=26$	10.4 ± 1.2 ; $n=39$
LTS onset [mV]	-62.3 ± 1 ; $n=14$	-63.8 ± 1 ; $n=19$	-51.3 ± 2 ; $n=9$	-65.8 ± 1 ; $n=13$	-62.8 ± 1 ; $n=16$	-53.6 ± 2 ; $n=12$
LTS generating slope [mV/s]	8.3 ± 0.5 ; $n=14$	4.8 ± 0.6 ; $n=18$	5.3 ± 0.5 ; $n=9$	11.5 ± 0.8 ; $n=13$	5 ± 0.6 ; $n=16$	4.6 ± 0.4 ; $n=12$
Δ depolarization slopes	5.8 ± 0.5 ; $n=14$	2.5 ± 0.5 ; $n=18$	0.5 ± 0.3 ; $n=9$	9.7 ± 0.9 ; $n=13$	2.6 ± 0.6 ; $n=16$	0.3 ± 0.2 ; $n=12$
LTS generating slope TTX [mV/s]	17.2 ± 4 ; $n=3$	6.4 ± 1 ; $n=3$	13.6 ± 2 ; $n=3$	20.9 ± 2 ; $n=3$	10.7 ± 3 ; $n=3$	20.1 ± 4 ; $n=3$
Δ depolarization slopes TTX	14.1 ± 4 ; $n=3$	2.9 ± 1 ; $n=3$	8.3 ± 1 ; $n=3$	17.4 ± 2 ; $n=3$	7.1 ± 3 ; $n=3$	13.9 ± 4 ; $n=3$
LTS generating slope TTX/4-AP [mV/s]	3.9 ± 0.4 ; $n=11$	4.0 ± 0.5 ; $n=9$	5.2 ± 0.2 ; $n=12$	5.6 ± 0.6 ; $n=9$	4.9 ± 0.9 ; $n=11$	4.9 ± 0.5 ; $n=9$
Δ depolarization slopes TTX/4-AP	1.2 ± 0.3 ; $n=11$	1.8 ± 0.5 ; $n=9$	0.6 ± 0.2 ; $n=12$	3.8 ± 0.6 ; $n=9$	2.4 ± 0.8 ; $n=11$	0.8 ± 0.4 ; $n=9$
Statistical significances within strains						
	WAG/Rij LGN vs. CL	WAG/Rij LGN vs. NRT	WAG/Rij NRT vs. CL	ACI LGN vs. CL	ACI LGN vs. NRT	ACI NRT vs. CL
$I_T V_h$ act	*	***	***	*	***	**
$I_T V_h$ inact	*	***	*	N.S.	N.S.	***
TTP	** to ***	***	***	* to ***	***	***
Inact τ	** to ***	***	***	** to ***	***	***
I_T peak amp	***	***	***	***	***	***
Capacitance	N.S.	***	***	N.S.	***	***
CD	***	***	N.S.	***	***	N.S.
V_{Rest}	*	N.S.	***	*	N.S.	*
# LTS APs	N.S.	***	***	N.S.	***	***
LTS onset	N.S.	***	***	*	***	***
LTS generating slope	***	**	N.S.	***	***	N.S.
Δ depolarization slopes	***	***	**	***	***	**
* $p < 0.05$; ** $p < 0.01$; *** $p < 0.001$.						
Statistical significances between strains						
		LGN		CL		NRT
$I_T V_h$ act		*		**		**
$I_T V_h$ inact		N.S.		*		***
TTP		N.S.		N.S.		N.S.
Inact τ		N.S.		N.S.		N.S.
I_T peak amp		**		**		N.S.
Capacitance		N.S.		N.S.		N.S.
CD		*		*		*
V_{Rest}		N.S.		N.S.		N.S.
# LTS APs		N.S.		N.S.		N.S.
LTS onset		*		N.S.		N.S.
LTS generating slope		**		N.S.		N.S.
Δ depolarization slopes		***		N.S.		N.S.
* $p < 0.05$; ** $p < 0.01$; *** $p < 0.001$.						

Differences in current kinetics were minor between strains, but were found to be significant between nuclei. The time to maximum current amplitude was used as a measure of activation kinetics (Figs. 3C, D), while the time constants of inactivation were obtained by fitting the current traces with a mono-exponential function (Figs. 3E, F; Table 2).

In summary the predictions of the T-type Ca^{2+} current properties derived from the expression analysis have been validated for the differences in I_T voltage dependency of activation and the I_T kinetics between nuclei. While the internucleus variations were expected, the differences in voltage dependency between WAG/Rij and ACI were unexpected and cannot be explained by the T-channel isoform expression pattern or differential splicing of exons 25/26 investigated in this study. Furthermore, the increased expression of T-channel coding mRNA in WAG/Rij translated into increased I_T densities.

Predicting the influence of different I_T characteristics on the LTS

After having established the expression pattern of the pore forming T-type Ca^{2+} channel $\alpha 1$ subunits and the electrophysiological

properties of T-type Ca^{2+} currents in LGN TC, CL, and NRT neurons of WAG/Rij and ACI rats, we focused our attention on the functional correlate of I_T , the LTS. There are a number of LTS parameters which could be directly determined by certain T-type Ca^{2+} current properties. Intuition predicts the LTS onset potential to correlate with the voltage dependency of I_T activation, while the number of LTS associated action potentials and the stimulation intensity required to generate a LTS should depend on the T-type Ca^{2+} current density.

To test the validity of these assumptions, a single compartment model based on the mathematical descriptions of I_T , I_{NaHH} , I_{KHH} , I_{NaP} , I_L , I_A , I_{KCa} , as well as a sodium and a potassium leak current was used (Broicher et al., 2007a). Two types of protocols were used to stimulate the model neuron in the current-clamp regime. To assess the influence of different I_T parameters on the number of LTS associated action potentials, a step depolarization protocol was used. The model cell was hyperpolarized to -100 mV for 800 ms, before being stepped to -70 mV, whereupon a LTS was generated. The influence of changes of I_T on the LTS onset potential and the stimulation intensity required to elicit a LTS was investigated using a current ramp protocol. Here, the

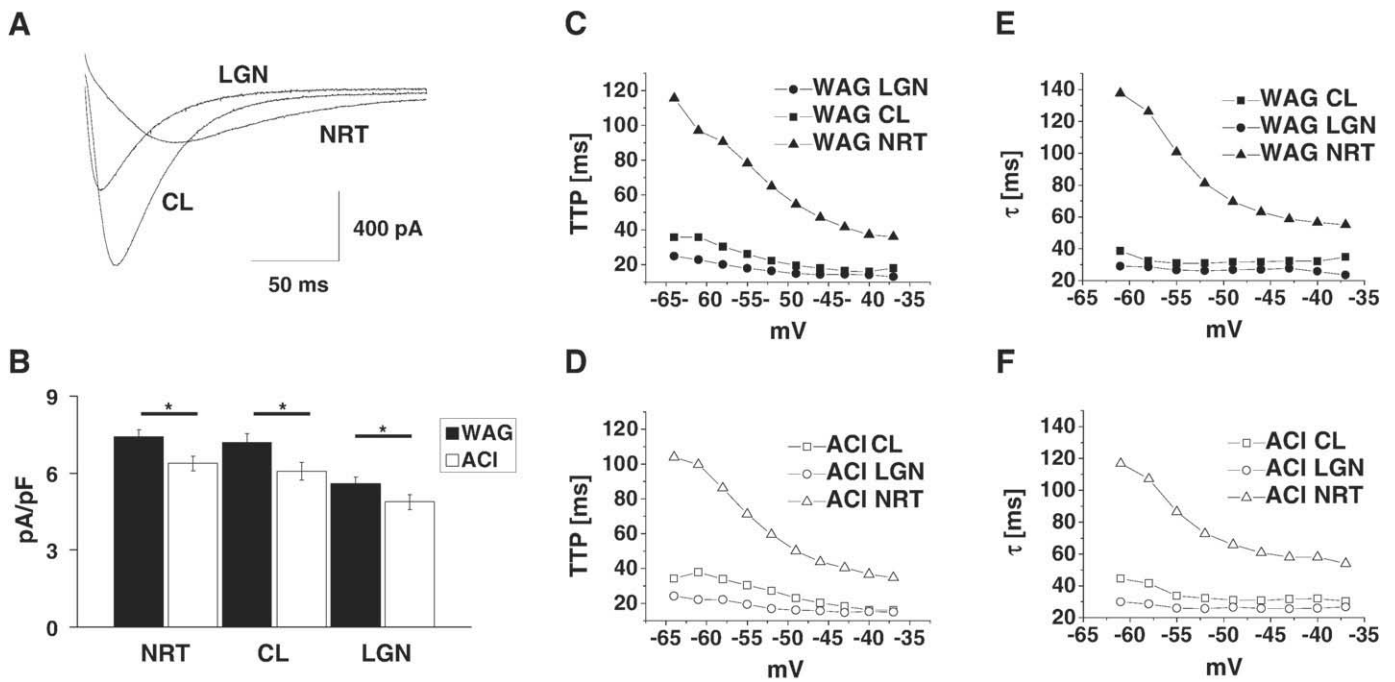


Fig. 3. T-type Ca^{2+} current density and current kinetics of LGN TC, CL, and NRT neurons of WAG/Rij and ACI rats. (A) Representative peak T-type Ca^{2+} currents of a LGN TC, a CL, and a NRT neuron. Displayed recordings derive from neurons taken from ACI rats. (B) I_T density of WAG/Rij and ACI LGN, CL, and NRT neurons. See text for statistical data. $*p < 0.05$. (C) Mean values of the time to peak amplitude of T-type Ca^{2+} currents of WAG/Rij LGN TC, CL, and NRT neurons in relation to the activation protocol test potential (symbols as indicated). Standard error bars have been omitted for clarity. (D) Mean values of the time to peak amplitude of T-type Ca^{2+} currents of ACI LGN TC, CL, and NRT neurons in relation to the activation protocol test potential (symbols as indicated). (E) Mean values of the time constant of inactivation of WAG/Rij LGN TC, CL, and NRT neurons obtained by fitting of current traces with a mono-exponential function (symbols as indicated). (F) Mean values of the time constant of inactivation of ACI LGN TC, CL, and NRT neurons obtained by fitting of current traces with a mono-exponential function (symbols as indicated). Standard error bars have been omitted for clarity.

model neuron was held at -100 mV before being depolarized by current ramps of varying slopes. I_T parameters including the T-type Ca^{2+} current voltage dependency and current density were shifted by ± 5 mV and $\pm 30\%$, respectively.

Under control conditions (initial I_T configuration), the model neuron generated 4 LTS associated action potentials in response to current step stimulation (Fig. 4B). Increasing the T-type Ca^{2+} current density by 30% led to an increase in the number of action potentials to 5 (Fig. 4C, upper panel), while decreasing the T-type Ca^{2+} current density by 30% reduced the number of LTS associated action potentials to 3 (Fig. 4C, lower panel). The number of LTS associated action potentials was unaffected by hyperpolarizing the I_T voltage dependency by 5 mV, while a 5 mV depolarizing shift reduced the number of action potentials to 3 (Fig. 4A).

The LTS onset potential during current ramp stimulations was estimated by a threshold based algorithm using the first derivative of the voltage trace (see Experimental methods). We began the simulations using supra threshold stimuli and progressively decreased the stimulus intensity. This initially leads to the disappearance of the LTS associated action potentials followed by a gradual decline in LTS amplitude with weaker stimuli (data not shown). The first LTS without any associated action potentials was used for quantification. Under control conditions the model cell's LTS onset potential was -75.4 mV. Shifting the I_T voltage dependency by 5 mV in the negative direction resulted in a hyperpolarization of the LTS onset potential to -79.9 mV, while shifting the I_T voltage dependency by 5 mV in the positive direction depolarized the LTS onset potential to -68.1 mV (Fig. 4D). The effects of changes in I_T density on the LTS onset potential were comparatively minor (data not shown).

To investigate the effects of changes in I_T parameters on the stimulus intensity required for LTS generation, the depolarization slopes were investigated. The depolarization slopes were obtained by linearly fitting the simulated voltage trace between the start of the

stimulation and the LTS onset point (as defined above). Again, the stimulation intensity was continuously decreased. The first LTS without any associated action potentials was used for quantification. Under control conditions, a depolarization slope of 42.6 mV/s generated the first LTS without associated action potentials. Shifting the I_T voltage dependency by 5 mV in the negative direction shifted the depolarization slope to 38.9 mV/s. Depolarizing the I_T voltage dependency by 5 mV increased the depolarization slope to 52.5 mV/s (data not shown). The effects of changes in I_T density on depolarization slopes were more pronounced than the effects of changes in I_T voltage dependency. Increasing the T-type Ca^{2+} current density by 30% reduced the depolarization slope to 28.1 mV/s. Decreasing I_T density by 30% increased the depolarization slope to 68.5 mV/s (Fig. 4E).

In summary, the LTS onset potential of the model neuron was dependent on the I_T voltage dependency, while the number of LTS associated action potentials and the stimulation intensity were dependent on the T-type Ca^{2+} current density. If the differences in T-type Ca^{2+} current properties directly translate into differences of the LTS onset potential in neurons of WAG/Rij and ACI rats recorded in the LGN, CL, and NRT, the model predicts that: (1) LTS onset potentials of LGN TC neurons should be negative to the LTS onset potentials of CL neurons in both strains. (2) LTS onset potentials of NRT neurons should be depolarized to the LTS onset potentials of LGN TC and CL neurons in both strains. (3) LGN and CL neurons of WAG/Rij should display LTS onset potentials negative to the LTS onset potentials of ACI LGN and CL neurons. (4) The LTS onset potential of NRT neurons of WAG/Rij and ACI rats should be approximately similar. Furthermore, the model predicts that neurons of the NRT should generate the most LTS associated action potentials, followed by neurons of the CL. LGN neurons should generate the least amount of LTS associated action potentials, due to the comparatively small I_T density. Analogous, neurons of WAG/Rij rats are predicted to generate more LTS associated action potentials than ACI neurons. A similar pattern should be

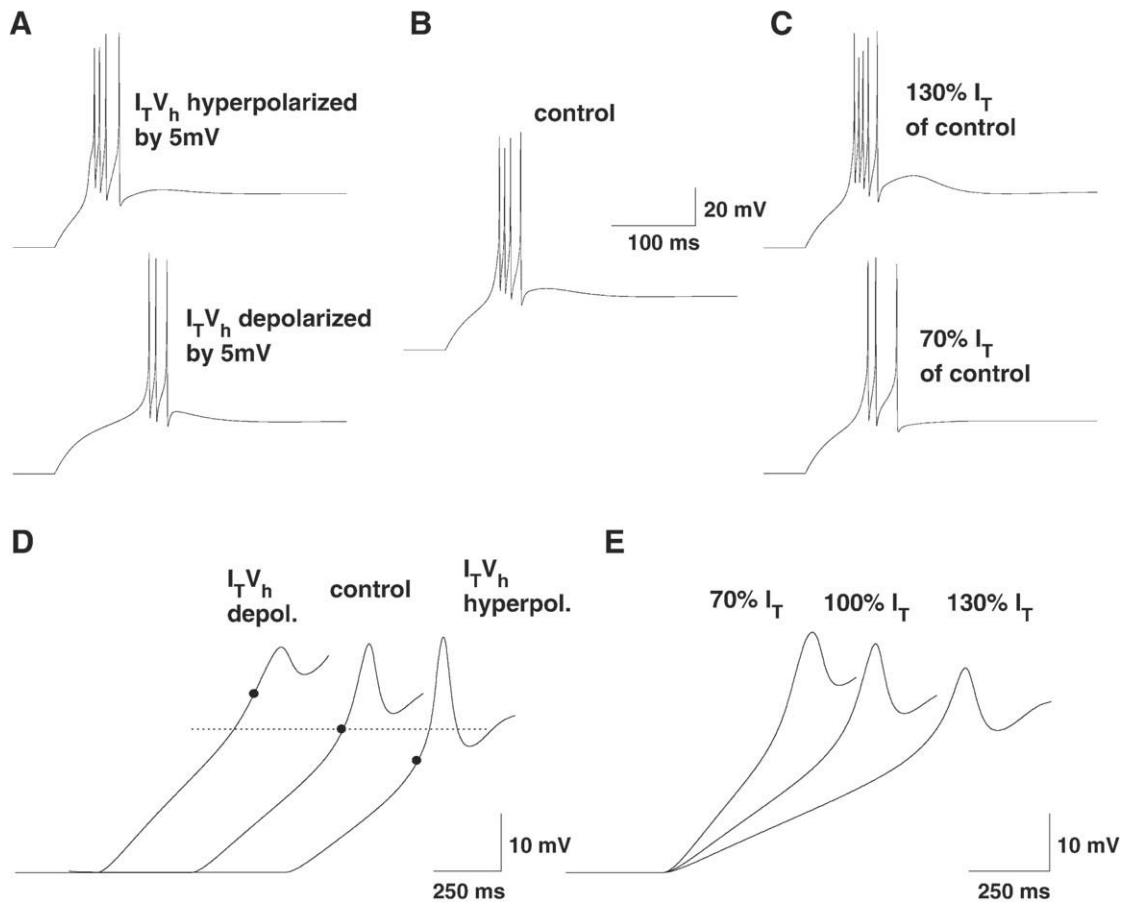


Fig. 4. The influence of the V_h of I_T activation as well as the T-type Ca^{2+} current density on the number of LTS associated action potentials of a model neuron is shown in A, B, and C. A current step protocol was used to elicit the LTS. The modeled LTS under control conditions is shown in (B). The influences of changes in V_h are depicted in (A). The upper panel displays the effect of a negative 5 mV shift of the $I_T V_h$ on the LTS. The influence of a shift of 5 mV in the positive direction is shown in the lower panel. In (C) the effects of alterations of I_T density on the LTS are depicted. The upper panel shows a LTS generated by a modeled neuron with 130% of the control T-current density. In the lower panel a LTS generated in the presence of 70% of the control T-current density is displayed. In D and E the effects of alterations in I_T voltage dependency and current density on the LTS onset potential and the minimal LTS generating slope are displayed. Current ramp stimulations were used to elicit the LTS. The LTS onset potential was defined using the derivatives of the voltage traces (dV/dt) by a threshold based algorithm (see text). The simulations were started using above threshold depolarization slopes. Subsequently, the depolarization slopes were decreased by a fixed amount, until all LTS associated action potentials were lost. The first trace without any LTS associated action potentials was used for quantification (see text). (D) Effect of changes of the I_T voltage dependency on the LTS onset potential. LTS onset potentials are marked by black circles. A model with the initial I_T configuration is shown in the middle (control). On the left side the effect of a 5 mV depolarization of the I_T voltage dependency is shown, while the right side displays the effect of a 5 mV hyperpolarization. (E) Effect of changes in I_T density on the minimal LTS generating slope. A simulation using the initial I_T configuration is shown in the middle (100% I_T). On the left side, the effect of a reduction of the I_T density by 30% is shown. On the right the influence of an increase of the I_T density by 30% on the minimal LTS generating slope is depicted.

observed for the minimal stimulation intensity leading to LTS generation. NRT neurons should require the smallest depolarization slopes leading to LTS generation, while CL and LGN neurons should require stronger stimulation intensities.

Electrophysiological properties of LGN, CL, and NRT neurons of WAG/Rij and ACI rats

To test the predictions made by the mathematical model we went on to do whole-cell current-clamp recordings on neurons in brain slice preparations. The resting membrane potentials of neurons recorded in the same nucleus of WAG/Rij and ACI rats were similar. However, significant differences were found for the resting membrane potentials of neurons recorded in the different nuclei within both strains. Neurons of the CL displayed significantly more positive resting membrane potentials when compared to neurons of the LGN and the NRT, while resting membrane potentials of LGN TC and NRT neurons were indistinguishable (Table 2). In addition to the stable resting membrane potential at around -75 mV, some NRT neurons of both strains displayed a prominent membrane potential bistability, as described previously (Blethyn et al., 2006; Fuentealba et al., 2005).

This bistable behavior consisted of an oscillation between an “up state” and a “down state” (data not shown). The “up state” was usually initiated by a LTS crowned by a high frequency burst of action potentials, which gave way to tonic action potential generation (data not shown). The “up state” usually displayed membrane potentials in the range of -40 to -55 mV, while membrane potentials in the “down state” ranged from -50 to -65 mV. In some cases, rhythmic LTS generation was observed during the “down state” (not shown). In both strains, no intrinsic membrane potential rhythmicity was observed in LGN neurons. Some CL neurons of both strains displayed spontaneous LTS generation at sub-delta frequencies (data not shown).

Basic properties of the LTS of LGN, CL, and NRT neurons of WAG/Rij and ACI rats

Next, the basic features of the LTS in LGN TC, CL, and NRT neurons of WAG/Rij and ACI rats were examined. Via DC current injection, neurons were held at potentials around -60 mV, hyperpolarized to -100 mV for 800 ms to deinactivate I_T and repolarized to -60 mV (LGN TC and CL neurons) or to -55 mV (NRT neurons). A stronger DC current injection in NRT neurons was necessary to consistently evoke a LTS.

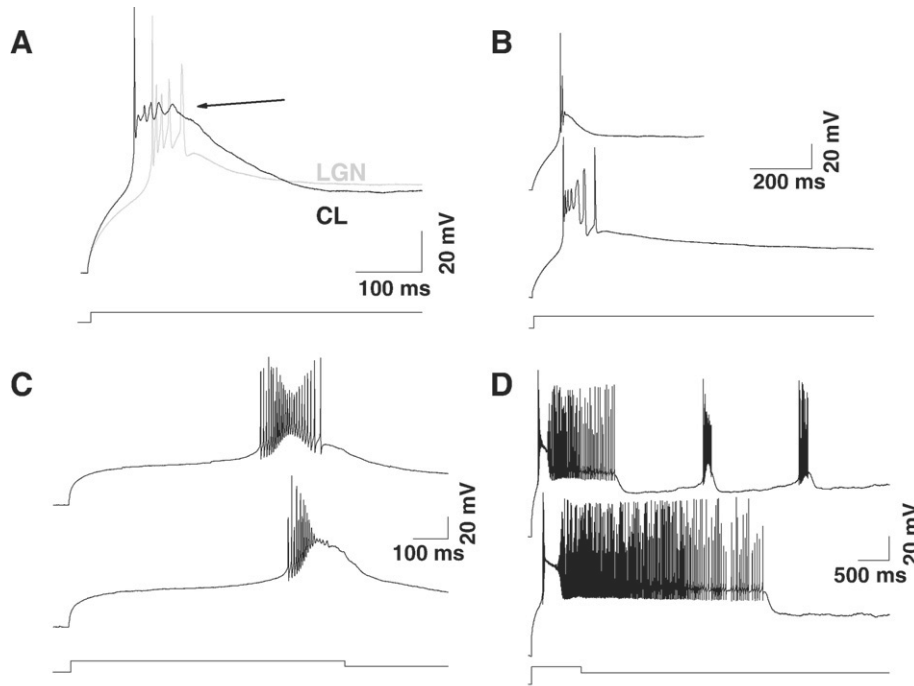


Fig. 5. The LTS of LGN TC, CL and NRT neurons. (A) Overlay of the LTS generated by a LGN TC neuron (grey trace) and a CL neuron (black trace). The LTS of CL neurons was of larger amplitude than the LTS of LGN TC neurons, but oftentimes generated only a single action potential. In case only a single action potential was generated, CL neurons often displayed a small amplitude membrane potential oscillation after the AP (indicated by the arrow). Both cells were taken from ACI rats. (B) Comparison of the LTS of two further LGN TC (upper panel) and CL (lower panel) neurons. The LTS of the CL neuron is of larger overall size and longer duration than the LTS of the LGN TC neuron. Note the increased width of the 5th and 6th action potentials of the CL neuron. The LTS of NRT neurons are displayed in C and D. (C) The LTS generated by NRT neurons oftentimes fell into one of two categories. Lower amplitude LTS evoked a large train of action potentials, displaying an accelerando/decelerando pattern (upper panel). The amplitudes of the action potentials generated in this manner were inversely correlated to the amplitude of the LTS. LTS of higher amplitude generated action potentials only during the initial rising phase (lower panel). Both recordings derive from the same ACI neuron. (D) In some NRT neurons, the LTS initiated upstate tonic action potential generation. Black lines below the recordings indicate DC current injection duration and magnitude. Both recordings derive from another ACI NRT neuron.

The shape of the LTS was similar in neurons recorded in the same nucleus of WAG/Rij and ACI rats. In comparison to CL neurons, the LTS of LGN TC neurons revealed smaller amplitudes and shorter durations, peaking at around 10–20 mV more negative values of the membrane potential (LGN TC: ~ -40 mV; CL: ~ -30 to -20 mV; Fig. 5A).

In the following, the number of LTS associated action potentials was investigated. On average, the LTS of a LGN TC neuron evoked 2.4 ± 0.2 action potentials ($n=25$) in WAG/Rij and 2.4 ± 0.2 action potentials ($n=25$) in ACI rats. The LTS of CL neurons oftentimes generated only a single action potential (15 of 26 ACI CL, 19 of 39 WAG/Rij CL) (Fig. 5A). In some of these cells, the initial action potential was followed by a transient depolarization of small amplitude reminiscent of an action potential, suggesting a depolarization block of I_{Na} , or a low amplitude membrane potential oscillation (arrow in Fig. 5A). On average, the LTS of a CL neuron evoked 2.3 ± 0.2 action potentials ($n=39$) in WAG/Rij and 1.8 ± 0.2 action potentials ($n=26$) in ACI rats. Furthermore, the LTS of CL neurons was usually slow to decline (Fig. 5B). The LTS of NRT neurons had a higher activation threshold and generated significantly higher numbers of action potentials than those of LGN TC and CL neurons. On average, the LTS of a NRT neuron elicited 9.9 ± 1.7 action potentials ($n=21$) in WAG/Rij and 10.4 ± 1.2 action potentials ($n=39$) in ACI rats (Table 2). Two main patterns of action potential generation were observed. Lower amplitude LTS evoked a large train of action potentials, displaying an accelerando/decelerando pattern (Fig. 5C, upper panel). The amplitudes of action potentials evoked in this manner were inversely correlated to the amplitude of the LTS, declining in amplitude from the beginning to the peak of the LTS and increasing in amplitude while the LTS declined. A LTS of higher amplitude generated action potentials only during the initial rising phase (Fig. 5C, lower panel). These action potentials also declined in amplitude as the LTS increased in amplitude. It is important to note,

that both patterns of LTS associated action potential generation could be observed in the same neuron (Fig. 5C). In a subset of NRT neurons of both strains the LTS initialized “up state” tonic action potential generation (Fig. 5D).

In order to more clearly deduce whether variations in T-type Ca^{2+} currents cause alterations in LTS properties, we performed current-clamp experiments when Na^+-K^+ action potentials were blocked by 1 μ M Tetrodotoxin (TTX, Figs. 6A–C). In the presence of TTX, the qualitative differences between nuclei were preserved in both strains. LGN TC neurons generated the smallest LTS (Fig. 6A), while CL (Fig. 6B) and NRT (Fig. 6C) neurons displayed LTS of higher amplitude and longer duration. The LTS of CL and LGN TC neurons were, except for the larger size in CL neurons, of quite similar shape. The LTS of NRT neurons differed by displaying slower rise and decay kinetics. No differences in the overall shape of the LTS were observed between WAG/Rij and ACI rats. The bistable behavior of a subset of NRT neurons was preserved in the presence of TTX (data not shown).

Since a close functional antagonism between I_T and the fast transient A-type K^+ current (I_A) has been described in LGN TC and NRT neurons (Meis et al., 1996; Pape et al., 1994) we further tried to isolate I_T generated LTS properties by blocking I_A with 4-Aminopyridine (4-AP, 5 mM) in combination with 1 μ M TTX. Wash in of TTX and 4-AP enlarged the LTS and removed all action potentials (Figs. 6D–F). No qualitative differences were observed between strains. In LGN TC neurons, application of TTX and 4-AP increased the amplitude and prolonged the duration of the LTS (Fig. 6D, middle trace). In some neurons the initial LTS onset was followed by a second depolarizing rise of roughly equal slope (arrow in Fig. 6D, lower panel) probably representing a high threshold Ca^{2+} spike (HTS) (Hernandez-Cruz and Pape, 1989; Lo et al., 2002; Tegnigkeit et al., 1998). It is important to note, that both forms could be observed in the same neuron, as shown

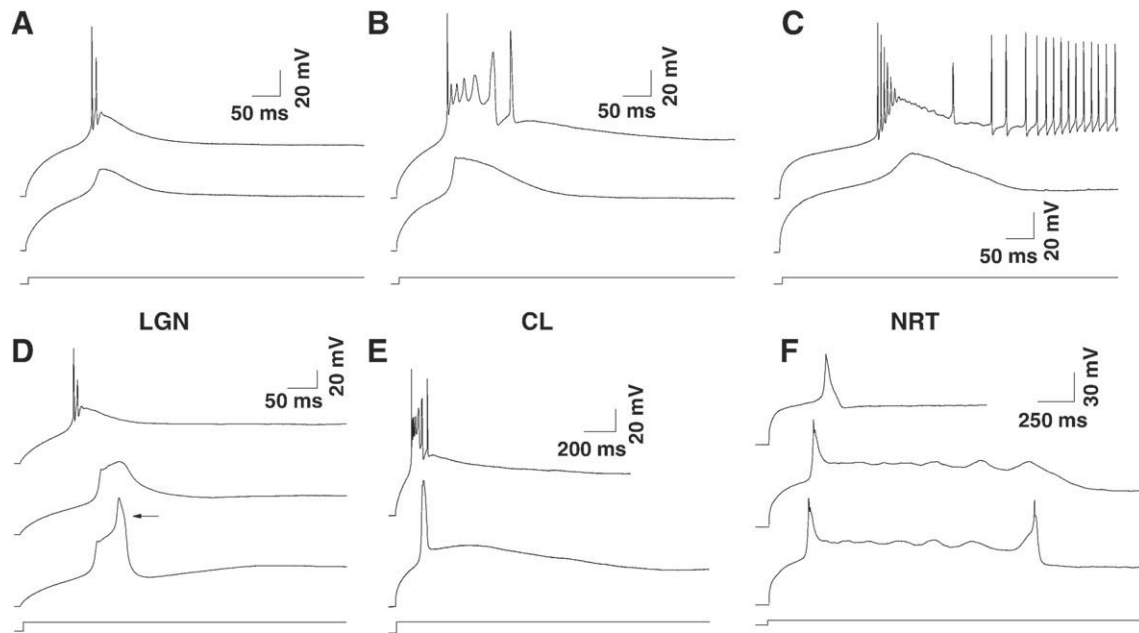


Fig. 6. LTS of LGN TC, CL, and NRT neurons under control conditions, in the presence of 1 μM TTX and under the influence of 1 μM TTX in combination with 5 mM 4-AP. Recordings in the presence of TTX are shown in A, B, and C. The effects of co-application of TTX and 4-AP are shown in D, E, and F. Neurons were held at -60 mV hyperpolarized to -100 mV for 800 ms before being stepped to ~ -60 mV (LGN TC and CL) or ~ -55 mV (NRT). The LTS of an LGN TC neuron is shown in A, the LTS of a CL neuron is shown in B, while C depicts the LTS of a NRT neuron. The upper panels show recordings under control conditions, the lower panels display recordings in the presence of TTX. (D) LTS of a LGN TC neuron under control conditions (upper panel) and in the presence of 1 μM TTX and 5 mM 4-AP (middle and lower panels). TTX and 4-AP transformed the LTS into a biphasic depolarization. The second depolarization could be of lower slope than the first (middle panel) or could be equally steep (arrow in the lower panel). The steep second depolarization shown in the lower panel was termed a “high threshold spike” (HTS), see text. (E) LTS of a CL neuron under control conditions (upper panel) and in the presence of 1 μM TTX and 5 mM 4-AP (lower panel). In CL neurons, drug application transformed the LTS into an initial depolarization, similar to the LTS of LGN TC neurons, and a slow depolarization. The slow depolarization could be of varying amplitude and duration. A prominent example of the slow depolarization is shown here. (F) After application of 1 μM TTX and 5 mM 4-AP the LTS of NRT neurons usually displayed one of three patterns: either the LTS was transformed into a single spike like depolarization (upper panel), which could be generated repetitively in some cells, or the LTS was transformed into a spike which was followed by a plateau depolarization (middle and lower panel panels). This plateau could or could not be terminated by a second spike depolarization in the same neuron. Black lines below the recordings indicate DC current injection duration and magnitude.

in Fig. 6D, and that the transition between the two phases could be more subtle than displayed. Similar to the LTS, the HTS behaved in a “nearly all or none manner” (Zhan et al., 1999), meaning either its complete presence or absence. Furthermore, the HTS was more readily observed when stronger/steeper depolarization was applied. In CL neurons, application of TTX and 4-AP transformed the LTS into a biphasic depolarization with an initial steep and transient component, similar to the LTS of LGN TC neurons, followed by a slow depolarization of varying duration and amplitude (Fig. 6E). In NRT neurons three patterns of LTS generation were observed after drug administration (Fig. 6F). In a subset of NRT neurons, the LTS was transformed into a single spike depolarization (Fig. 6F, upper panel), which could be generated repetitively in some cells. In other neurons, the LTS changed into a single spike followed by a plateau depolarization of varying duration, displaying low amplitude membrane potential oscillations (Fig. 6F, middle panel), reminiscent of the “up state” (see above). This plateau potential could sometimes be terminated by a second spike depolarization (Fig. 6F, lower panel).

Quantification of the LTS onset potential and the minimum LTS generating slope using current ramp stimulation

To correlate the I_T properties recorded under voltage clamp conditions with the LTS and to test the predictions of the mathematical model, we used current ramp stimulations. The experiments were designed to obtain a measure of the LTS onset potential and to investigate the stimulus intensity necessary for LTS generation.

Depolarizing current ramps were applied from a holding potential of -75 mV (Fig. 7). The slope of the current ramp induced depolarization was decreased until LTS generation ceased (Fig. 7). As has been observed previously, the LTS behaved in a “nearly all or none”

manner (Zhan et al., 1999), meaning that it was present or absent with only very rarely displaying an intermediate size. The depolarization slope was decreased using two protocols: (1) Stimulation intensity was decreased, while the duration of the current ramps was kept constant (5 s). (2) Duration of the current ramps was increased, while the stimulation intensity was kept constant. Similar results were obtained with both paradigms. In the following only the results from the first paradigm using decreasing stimulation intensity will be presented. For quantification of LTS parameters, the LTS onset point was computed using the first derivative of the voltage trace. As described previously by Gutierrez et al. (2001), the LTS onset point was defined as the point where the slopes of 4 consecutive binned data points exceeded the baseline slope (see Experimental methods). Baseline slopes were obtained by a Gaussian fit of the differentiated membrane voltage prior to ramp stimulation (see Experimental methods). In a series of ramp stimulations with decreasing slopes the following parameters were obtained: (1) where applicable the voltage of the LTS onset point of the first LTS, (2) the minimum slope eliciting a LTS, and (3) the maximum slope eliciting no LTS, thereby setting the limits of a slope interval which includes the true minimal LTS generating slope. Application of depolarizing current ramps from -75 mV led to the generation of one or more LTS, followed by tonic action potential generation, if stimulation intensity was strong enough (Fig. 7). Decreasing the stimulation intensity first led to the disappearance of tonic action potentials, and subsequently to the disappearance of the LTS. In some cases ramps with shallow slope did not lead to LTS generation even though the threshold potential was reached. To account for this phenomenon the theoretical minimum slope necessary to reach the LTS onset potential was calculated for each neuron and the difference between this value and the minimal slope actually eliciting a LTS in the experiment was analyzed.

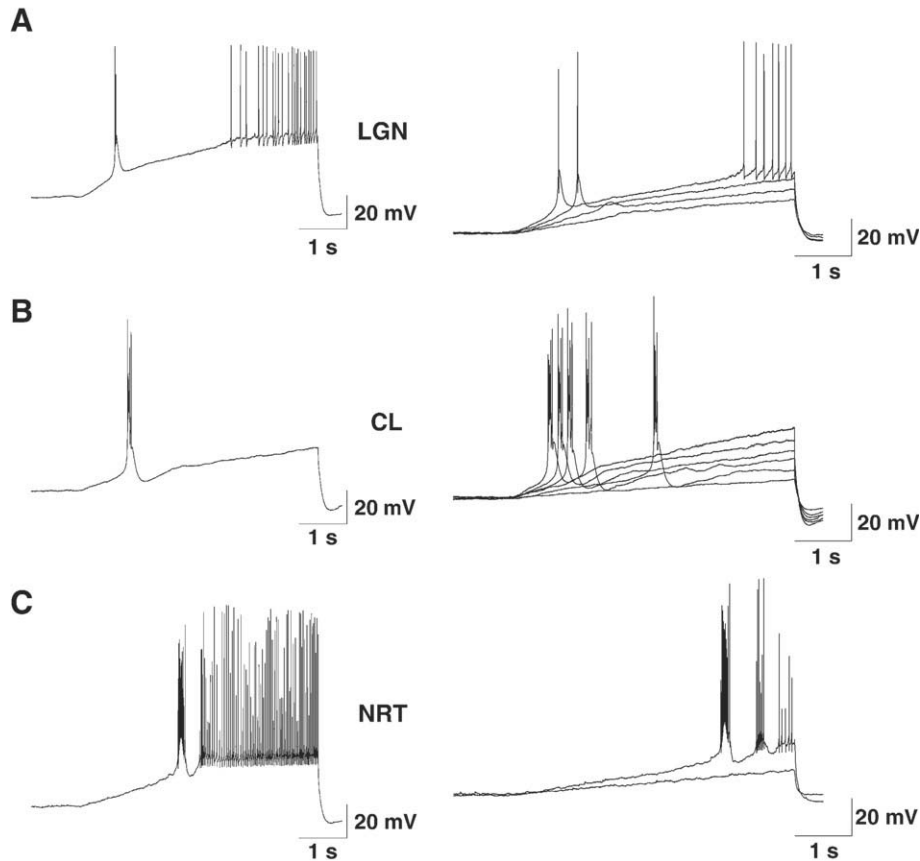


Fig. 7. LTS elicited via current ramp stimulation in LGN TC, CL, and NRT neurons. Single representative voltage traces are shown on the left side. The right side displays examples of the effects of stimulations of decreasing slope. Tonic action potentials disappeared first, followed by the disappearance of the LTS. Recordings from LGN TC neurons are shown in A, recordings from CL neurons are displayed in B, and recordings from NRT neurons are shown in C.

The LTS onset potentials varied little when elicited through current ramps of decreasing stimulus intensity in individual neurons. In both strains, NRT neurons displayed significantly more positive LTS onset potentials when compared to LGN TC and CL neurons (~ -50 to -55 mV in NRT vs. ~ -60 to -65 mV in LGN TC and CL; Fig. 8A, Table 2). LGN TC neurons displayed a slightly more depolarized LTS onset potential than CL neurons in WAG/Rij, while the opposite was found in ACI. The difference between LGN TC and CL neurons was significant in ACI. A comparison between WAG/Rij and ACI revealed ACI LGN TC neurons to generate the LTS at significantly more negative potentials when compared to WAG/Rij LGN TC neurons (Table 2).

In the following, the minimum depolarization slope leading to the generation of a LTS was analyzed. The minimal LTS generating slope varied between nuclei (Fig. 8B). In both strains, LGN TC neurons displayed the largest minimal LTS generating slope, while minimal LTS generating slopes in CL and NRT neurons were roughly similar (~ 8 to 11 mV/s in LGN TC vs. ~ 5 mV/s in CL and NRT, Table 2). In both strains, minimal LTS generating slopes were significantly higher in LGN TC neurons when compared to CL and NRT neurons, while differences between CL and NRT neurons were not significant. Furthermore, the minimal LTS generating slopes recorded in WAG/Rij LGN TC neurons were significantly smaller in comparison to the minimal LTS generating slopes recorded in ACI LGN TC neurons (Table 2). The relation between nuclei and strains observed for the maximum slope without LTS generation was similar to the results for the minimum slope generating a LTS (Fig. 8B).

Next, the difference between the calculated slope required for reaching the LTS onset potential and the measured minimal LTS generating slope was investigated. In both strains this difference was greatest in LGN TC neurons, with CL neurons displaying intermediate

differences and minimal differences being observed in NRT neurons (Fig. 8C, Table 2). Within both strains, all differences between nuclei were significant. A comparison between strains revealed significant differences for LGN TC neurons (Table 2). Furthermore, these differences inversely correlated with the T-type Ca^{2+} current density within both strains, with cells displaying lower T-current density revealing a greater difference (Fig. 8D). This correlation was found to be nearly linear. It should be noted, however, that for neurons in the CL and NRT the higher T-current density in WAG/Rij compared to ACI did not translate into smaller differences between the minimal measured LTS generating slope and the minimal slope reaching the LTS onset potential.

In the following, LTS parameters were quantified in the presence of TTX ($1 \mu\text{M}$). An analysis of the LTS onset potentials and the minimal depolarization slopes leading to LTS generation during current ramp stimulation revealed no effect of TTX on the LTS onset potential in LGN TC and CL neurons of both strains (Figs. 9A, B). In contrast, the LTS onset potential of NRT neurons was depolarized by about 8 mV in both strains (from -52 ± 3 to -44 ± 1 mV in ACI, from -56 ± 2 to -49 ± 2 mV in WAG/Rij, in both strains $n=3$, Fig. 9C). Furthermore the minimal LTS generating slope was increased in all neurons (Figs. 9A–C; Table 2), indicating the contribution of persistent sodium currents (I_{NaP}) to the depolarization preceding an LTS. This effect was strongest in NRT neurons in both strains. Within both strains, LGN TC neurons, NRT neurons, and CL neurons revealed the greatest, intermediate, and smallest difference between the minimal LTS generating slope and the slope needed to cross the LTS onset potential, respectively. When strains were compared, neurons of WAG/Rij rats displayed smaller differences between the minimal LTS generating slope and the slope required to reach the LTS onset potential in all nuclei (Table 2).

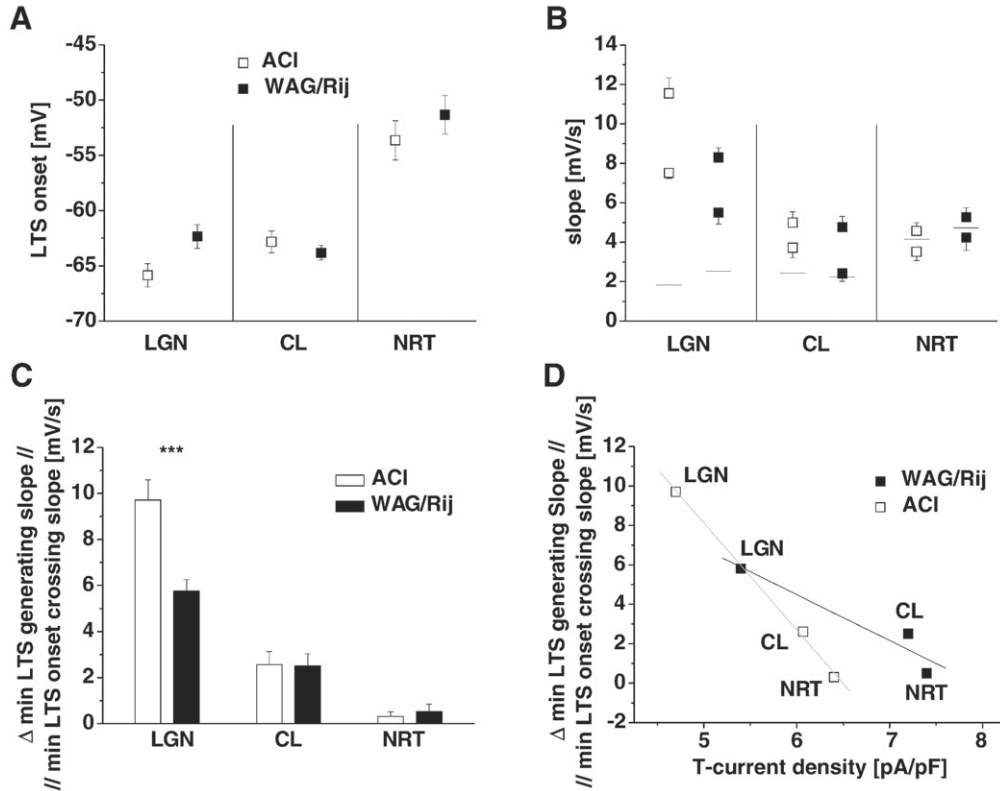


Fig. 8. Quantification of current ramp experiments. (A) The LTS onset potential of WAG/Rij (black) and ACI (white) LGN TC (left), CL (middle), and NRT (right) neurons. (B) Approximated minimal LTS generating slopes in WAG/Rij (black) and ACI (white) LGN TC (left), CL (middle), and NRT (right) neurons. For each population of neurons (e.g. WAG/Rij LGN TC, ACI LGN TC, WAG/Rij CL etc.) the upper square represents the mean minimal slope, which triggered a LTS in the experiment. The lower square represents the mean maximal slope, which did not trigger a LTS. The horizontal lines represent the mean minimum slope required to cross the LTS onset potential. (C) Difference between the minimal LTS generating slope and the minimal slope required to cross the LTS onset potential. (D) Correlation of the difference between the minimal LTS generating slope and the minimal slope required to cross the LTS onset potential and the T-type Ca^{2+} current density. The linear fit of the correlation for ACI is shown in grey ($r=0.999$). The linear fit for WAG/Rij is depicted in black ($r=0.958$).

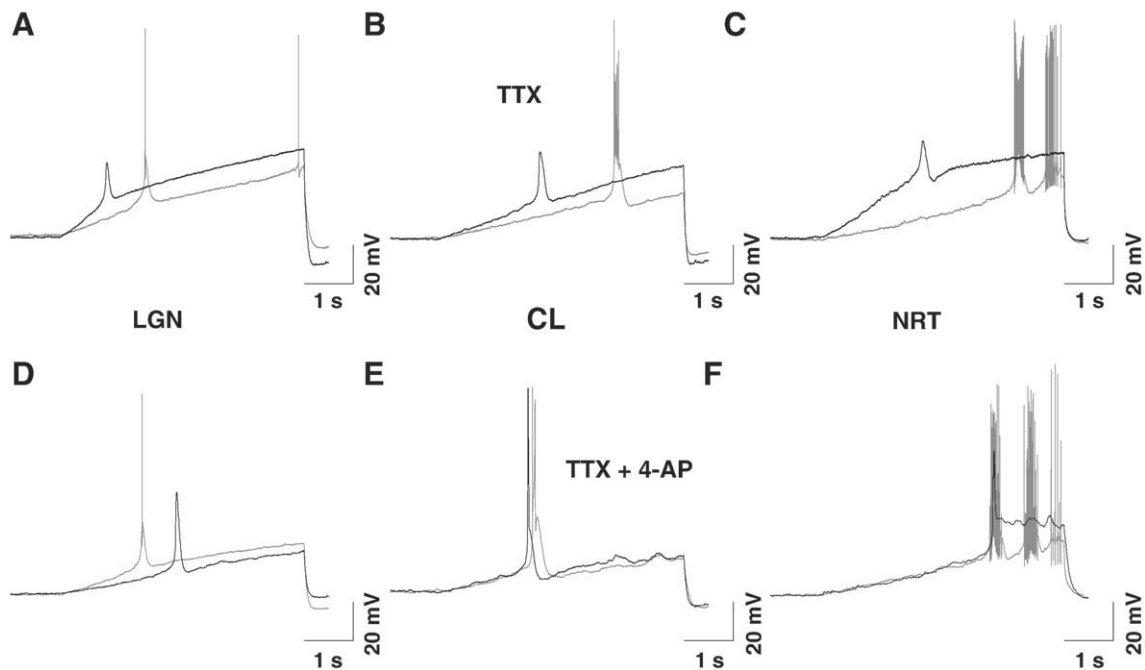


Fig. 9. Minimal LTS generating slopes during current ramp stimulation (from -75 mV, 5 s duration) under control conditions (grey traces) with the minimal LTS generating slopes in the presence of $1 \mu\text{M}$ TTX (A, B, C, black traces), or $1 \mu\text{M}$ TTX and 5mM 4-AP (D, E, F, black traces). The LTS of LGN TC neurons are shown in (A) and (D), CL neurons are shown in (B) and (E), and NRT neurons are depicted in (C) and (F). Note the increased minimal LTS generating slope in all nuclei under the influence of $1 \mu\text{M}$ TTX (A, B, C). The combined effect of $1 \mu\text{M}$ TTX and 5mM 4-AP reduced the minimal LTS generating slope in LGN TC neurons (D), while leaving the minimal LTS generating slopes of CL and NRT neurons basically unchanged (E, F).

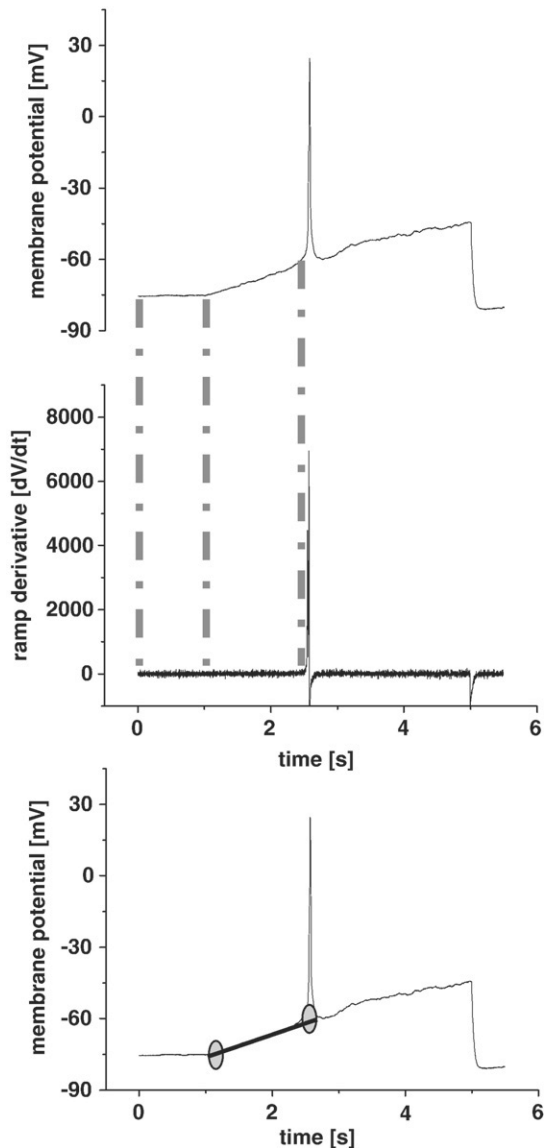


Fig. 10. The LTS onset point during current ramp stimulation. Prior to the beginning of the current ramp, a constant DC current was injected. This period is indicated by the left and middle lines connecting the upper 2 panels. The upper panel displays a voltage trace obtained using current ramp stimulation (in the presence of TTX and 4-AP) and the middle trace displays the differentiated voltage trace shown in the upper panel. The derivatives of the period of constant DC current injection were fitted with a Gaussian function. The LTS onset point was defined as the point where 4 consecutive derivatives exceeded the upper 95% confidence limit of the Gaussian fit of the baseline period and is indicated by the right line connecting the upper 2 panels. Subsequently, the voltage trace between the beginning of current ramp stimulation (middle line connecting the upper two panels, left ellipse in the lower panel) and the LTS onset point (right line connecting upper two panels and right ellipse in the lower panel) was fit with a linear equation (line in the lower panel), yielding the depolarization slope. See also Gutierrez et al., 2001.

In a next step TTX and 4-AP (1 μ M and 5 mM, respectively) were co-applied to thalamic slices. The LTS onset potential was hyperpolarized to -66 ± 1 mV ($n=11$) in ACI CL, with no changes observed in the other two nuclei or in WAG/Rij. The minimal slope leading to LTS generation did not change much in NRT neurons of both strains (Fig. 9F), but was decreased in LGN TC and CL neurons, although this effect was small in the CL (Figs. 9D, E; Table 2). When strains were compared, neurons of WAG/Rij rats displayed smaller differences between the minimal LTS generating slope and the slope required to reach the LTS onset potential in all nuclei (Table 2).

Discussion

The present study investigated the expression of T-channel coding mRNA, as well as the I_T and the LTS in three functionally distinct thalamic nuclei of WAG/Rij and ACI rats. Results show that distinct T-channel expression patterns translate into different T-currents, which give rise to different LTS. While a good correlation between T-channel coding mRNA and I_T was observed, the correlation between I_T and the LTS was more complex, suggesting the contribution of additional factors. When WAG/Rij and ACI rats are compared, this study indicates that the LTS is similar in both strains, despite quantitative differences in I_T . For LGN TC neurons, a population of prototypical specific thalamo-cortical relay neurons, an increased robustness of LTS generation was observed in WAG/Rij. If this finding extends to other populations of TC neurons, the increased robustness of burst firing could be implicated in the generation and/or maintenance of SWD, which is thought to be accompanied by thalamic burst mode transmission.

Relation of tissue mRNA expression and neuronal subpopulations in the LGN, CL, and NRT

In agreement with previous studies (Talley et al., 1999) and the results of RT-PCR experiments on isolated neurons (Broicher et al., 2007a), the thalamic relay nuclei of WAG/Rij and ACI rats primarily expressed the $\alpha 1G$ isoform, while the NRT was found to primarily express the $\alpha 1H$ and $\alpha 1I$ isoforms. In addition to $\alpha 1G$, expression of the $\alpha 1I$ isoform was detected in the LGN and CL. While $\alpha 1I$ expression can be attributed to local circuit interneurons in the LGN (Broicher et al., 2007a), the cell type specific attribution of expression signals in the CL is less clear. Electrophysiological evidence as well as anatomical tracing studies indicate a uniform population of neurons displaying similar electrophysiological characteristics as well as homogeneous axonal projections (Deschenes et al., 1996; Lacey et al., 2007; Van der Werf et al., 2002; Yasukawa et al., 2004). It is thus reasonable to assume that both splice variations of the $\alpha 1G$ isoform as well as the $\alpha 1I$ isoform are present in typical CL neurons.

In case of the reticular nucleus, a functional distinction between bursting and non-bursting neurons, which either do or do not possess a T-type Ca^{2+} conductance is proposed by some authors (Lee et al., 2007). Furthermore, a subpopulation of NRT neurons has been described to display a membrane potential bistability (Blethyn et al., 2006; Fuentealba et al., 2005). All NRT neurons recorded during the course of this study possessed a T-type Ca^{2+} conductance or a LTS, while a subpopulation of NRT neurons displayed membrane potential bistability. There was no obvious correlation between the presence and absence of bistable behavior and LTS properties or other cellular parameters investigated in this study. The expression $\alpha 1H$ and $\alpha 1I$ observed in NRT tissue samples is thus interpreted to correspond to an expression of both isoforms in typical NRT neurons.

Correlation of T-channel coding mRNA and I_T in neurons of the LGN, CL, and NRT

The relation of the T-type Ca^{2+} current voltage dependencies of activation and inactivation, as well as the relation of the activation and inactivation kinetics between LGN TC, CL, and NRT neurons within both strains matched the predictions from studies on cloned channels (Chemin et al., 2001, 2002; Emerick et al., 2006): (i) As has been shown before (Broicher et al., 2007a), LGN TC neurons solely express the $\alpha 1G$ -a isoform. This correlates well with an I_T of comparatively negative voltage dependency and fast kinetics. (ii) Neurons of the CL displayed T-type Ca^{2+} currents of intermediate voltage dependency and kinetics. These neurons expressed both the $\alpha 1G$ -a, and the $\alpha 1G$ -bc splice variants, as well as the $\alpha 1I$ isoform. The I_T voltage dependency of activation of CL neurons can be

explained by the presence of the $\alpha 1G$ -bc splice variation and the $\alpha 1I$ isoform or by a combination of both (Chemin et al., 2001, 2002; Emerick et al., 2006). Furthermore, currents carried by $\alpha 1G$ (irrespective of splice variation) display considerably faster current kinetics than currents carried by $\alpha 1I$, while the differences in I_T kinetics between $\alpha 1G$ -a and $\alpha 1G$ -bc splice variations are rather moderate by comparison (Chemin et al., 2001, 2002; Emerick et al., 2006). Together with the current properties of LGN TC (primarily $\alpha 1G$ -a) and NRT (primarily $\alpha 1I$) neurons and the higher expression of $\alpha 1G$ than $\alpha 1I$ (~16 times, under the assumption of similar primer/probe efficiency), these data argue for a stronger contribution of $\alpha 1G$ -bc than $\alpha 1I$ in CL neurons. (iii) In NRT neurons, the slow kinetics of activation and inactivation argue for a stronger influence of the $\alpha 1I$ isoform than the $\alpha 1H$ isoform on the whole-cell T-type Ca^{2+} current. Further support of this notion comes from experiments investigating the deactivation kinetics of I_T . Here, the I_T of NRT neurons displayed faster kinetics than the I_T of LGN TC and CL neurons (T.B. and T.B., unpublished observations), which correlates well with the fast deactivation kinetics of $\alpha 1I$ carried currents in heterologous expression systems. This interpretation is further supported by the ~2.5-times higher expression of $\alpha 1I$ coding mRNA in comparison to $\alpha 1H$ coding mRNA (under the assumption of similar primer/probe efficiency) in the NRT.

Correlation of T-channel coding mRNA and I_T in neurons of WAG/Rij and ACI

Neurons recorded in all three nuclei of WAG/Rij rats displayed increased I_T densities when compared to ACI. This finding is in good agreement with the increased expression of T-channel coding mRNA in WAG/Rij. Surprisingly, and in contrast to previous recordings performed on isolated neurons of the LGN (Broicher et al., 2007a), I_T voltage dependencies were different between neurons of the same nucleus recorded in WAG/Rij and ACI in brain slice preparations. LGN TC neurons and CL neurons of WAG/Rij displayed more negative I_T voltage dependencies in comparison to ACI, while NRT neurons of WAG/Rij were found to display slightly more positive I_T voltage dependencies. The molecular data suggests that this difference is neither due to differences in isoform expression or alternative splicing of exons 25/26, nor caused by a different ratio of isoform quantities. It should be kept in mind however, that alternative splicing in other regions of the pre-mRNA may underlie the observed differences. A previously described mathematical model, investigating the effects of different somatodendritic T-type Ca^{2+} channel distributions on the somatically recorded I_T voltage dependency, offers a possible explanation for this unexpected finding (Broicher et al., 2007a). The model has shown that an increased distal dendritic T-channel localization results in a negative shift of the somatically recorded T-type Ca^{2+} current voltage dependency. Possibly, there is a difference in the localization of T-type Ca^{2+} channels between thalamocortical neurons of WAG/Rij and ACI. This differential channel distribution could cause a difference in the somatically recorded T-type Ca^{2+} current voltage dependency in brain slice preparations, but would be undetectable in acutely isolated neurons, which lack most of their distal dendrites (Destexhe et al., 1998; Zhang et al., 2002). It has been shown that the synaptic terminals of inhibitory NRT and excitatory cortical afferents are located on the distal dendrites of TC neurons (Sherman and Guillery, 2006). An increased T-channel density in this region may thus augment TC neuron burst firing and contribute to SWD in WAG/Rij rats (Budde et al., 2006).

General correlation of I_T with the LTS in LGN TC, CL, and NRT neurons of WAG/Rij and ACI rats

The most straight forward correlation of I_T and the LTS could be established for the relationship between current density and the size

of the LTS. NRT and CL neurons displayed LTS of higher amplitude and longer duration than LGN TC neurons. Another central finding of the present study is that the LTS recorded in LGN TC, CL, and NRT neurons are qualitatively different, while the LTS recorded in the same nucleus of WAG/Rij and ACI rats are qualitatively similar. Although differences in T-type Ca^{2+} currents can be expected to be the primary cause for differences in the LTS, a number of other factors influence shape and amplitude of the LTS. These factors include channel distribution, cell geometry, K^+ currents activating below threshold (I_A), Ca^{2+} -dependent K^+ currents (I_{KCa}), the persistent sodium current (I_{NaP}), and the hyperpolarization-activated cation current (I_h) (Broicher et al., 2007a; Destexhe et al., 1998; Mainen and Sejnowski, 1996; van Ooyen et al., 2002; Williams and Stuart, 2000; Zhang et al., 2002).

In an attempt to exclude some of these complicating factors we used the Na^+ current blocker TTX. Indeed this maneuver more clearly dissected the shape of the LTS. While the mainly $\alpha 1G$ -based Ca^{2+} currents in LGN TC and CL neurons generated spikes of similar shape (with LTS amplitudes being higher in CL neurons), the $\alpha 1I/\alpha 1H$ -based I_T of NRT neurons generated an LTS of slower rise and decay kinetics and thus longer duration. Although TTX was helpful for the interpretation of step responses, it created additional complicating factors for the analysis of ramp responses since blocking of I_{NaP} altered the steepness of the ramp. The additional block of I_A by 4-AP allowed the occurrence of HTS possibly due to the activation of high voltage-activated (HVA) Ca^{2+} channels, distal dendritic T-type Ca^{2+} channels, or a combination of both (Crunelli et al., 2006; Hernandez-Cruz and Pape, 1989; Lo et al., 2002; Tennyigkeit et al., 1998) thereby masking the exact LTS shape. The HTS was only observed in LGN TC and CL neurons, but never in NRT neurons. The rising phase of the LTS in TTX/4-AP was rapid in all cell types, thereby demonstrating the influence of 4-AP sensitive currents. These findings demonstrate that a clear correlation between T-type Ca^{2+} current properties and LTS is difficult to achieve.

Correlation of I_T voltage dependency and the LTS in neurons of the LGN, CL, and NRT of WAG/Rij and ACI rats

With keeping the above mentioned problems in mind the LTS onset potential was used in an attempt to find a correlation with the voltage dependency of I_T activation. The LTS onset potential was approximated by an algorithm using the increasing voltage slopes (dV/dt) during LTS generation. Computational modeling predicted the LTS onset potential to correlate with the voltage dependency of I_T activation. Overall this suggestion was corroborated by the experimental data retrieved from both strains. Only the LTS onset potential of WAG/Rij LGN TC neurons seems too depolarized with respect to the V_h value of I_T activation. A possible explanation for this finding comes from the fact that the LTS is shaped by I_h (Pape, 1996; Ying et al., 2006). Since it has been shown that the voltage dependency of I_h is shifted to more hyperpolarized potentials in WAG/Rij compared to ACI LGN TC neurons, the weaker I_h -induced overshoot may contribute to the more depolarized LTS onset in WAG/Rij (Budde et al., 2005). While there seems to be no influence of Na^+ currents on the LTS onset potential in LGN TC and CL neurons, a strong depolarization was observed in NRT neurons. Interestingly, the depolarization of the LTS onset potential was not observed after wash in of TTX/4-AP, pointing to a scenario where TTX and 4-AP sensitive components exert equal, functionally antagonistic influences on the LTS onset potential in NRT neurons.

Correlation of T-current density and the LTS in neurons of the LGN, CL, and NRT of WAG/Rij and ACI rats

The number of LTS associated action potentials was predicted to be influenced by the T-type Ca^{2+} current density by the mathematical model. In the model, an increased I_T density resulted in an increased number of action potentials. Despite the increased I_T density in WAG/Rij no differences in the number of LTS associated action potentials

were found between WAG/Rij and ACI neurons of the same type, indicating that single bursts of individual thalamic neurons are unchanged in WAG/Rij rats.

Furthermore, a clear correlation of the T-type Ca^{2+} current density and the depolarizing slopes required to elicit a LTS was observed in ramp stimulation experiments. The comparison between the difference of the minimal slope required to reach the LTS onset potential and the minimal slope eliciting a LTS revealed a nearly linear correlation with the T-current density within both strains. Applied to an *in vivo* situation, this finding suggests that weaker depolarizations from hyperpolarized membrane potentials are sufficient to elicit a LTS in CL and NRT neurons in comparison to LGN TC neurons, provided that the potential for the regenerative activation process is reached.

Wash in of TTX increased the minimal LTS generating slopes as well as the differences between the minimal LTS generating slopes and the minimal slope required to cross the LTS onset potential in all neurons tested, indicating a contribution of the persistent sodium current. When TTX was co-applied with 4-AP, LTS generating slopes decreased in LGN TC and CL neurons (although this effect was very small in ACI CL neurons), but not in NRT neurons. Together with the effect of TTX on the LTS onset potential in NRT these data point to a different contribution of TTX and 4-AP sensitive conductances in relay (LGN TC and CL) and NRT neurons.

When strains were compared, the correlation between the T-current density and the LTS generating slopes was less clear. Here, significant differences were found between LGN TC, but not between CL or NRT neurons of WAG/Rij and ACI rats. Still, this finding indicates a more robust LTS generation in a specific thalamic relay nucleus of epileptic WAG/Rij rats. An increased likelihood of burst generation in WAG/Rij rats is in good agreement with an absence epilepsy phenotype, as thalamic burst mode transmission is thought to coincide with SWDs. Possibly, the lack of difference between CL and NRT neurons of WAG/Rij and ACI rats is due to the very small differences between the LTS onset potential crossing slope and the minimal LTS generating slope observed in these neurons. It cannot be excluded that our detection method was insufficient to resolve subtle differences between these two neuronal populations. Under the influence of TTX and TTX/4-AP, LTS generating slopes were smaller in WAG/Rij when compared to ACI. This finding fits well with the increased I_T density observed in the WAG/Rij strain.

Comparison to other models of absence epilepsy

Abnormalities in T-type Ca^{2+} channels have been implicated in the rodent and human absence phenotype for a long time and an augmentation of thalamic I_T seems to be a general motive in rodent models of absence epilepsy (Budde et al., 2006; Crunelli and Leresche, 2002; Pinault and O'Brien, 2007). An increased I_T has been observed in TC neurons of several mutant mouse strains (tottering, lethargic, stargazer, coloboma) and $\alpha 1A$ knock-out mice displaying an absence phenotype with ataxia (Song et al., 2004; Zhang et al., 2002, 2004). Crossbreeding $\alpha 1G$ knock-out mice with these mutant mice abolishes SWD in the progeny (Song et al., 2004). Studies in Genetic Absence Epilepsy Rats from Strasbourg (GAERS) revealed an increased I_T and expression of $\alpha 1H$ mRNA in the NRT of pre-seizure and adult rats (Kuisle et al., 2006; Talley et al., 2000; Tsakiridou et al., 1995), thereby indicating the importance of burst activity in the NRT in the absence phenotype. This view is further supported by the finding that SWDs in mice are unaltered with a genetically induced 25% reduction of $\alpha 1G$ carried I_T , which is presumably restricted to thalamic relay and cortical neurons, but probably leaves the $\alpha 1H$ and $\alpha 1I$ carried I_T of NRT neurons unchanged (Song et al., 2004). Therefore, an enhanced I_T in distinct thalamic regions might be tightly linked to SWD expression.

Experimental methods

The experimental procedures were applied on rats of both strains (WAG/Rij and ACI) in an identical manner. All experiments were performed on rats of both sexes. Unless stated otherwise, all chemicals were obtained from Sigma (Sigma-Aldrich, Germany). All animal procedures were approved by the local authorities.

Preparation of brain slices for electrophysiology

For patch-clamp experiments on brain slices, rats (postnatal day 15 to 25, P15 to P25) were deeply anesthetized with isoflurane (Forene, Abbott) and decapitated. Brains were removed and placed in cold, oxygenated sodium free artificial cerebrospinal fluid (ACSF) containing (mM): sucrose, 210; PIPES, 20; KCl, 2.4; MgCl_2 , 10; CaCl_2 , 0.5; dextrose, 10; pH 7.25 with NaOH. The cerebellum and the anterior third of the brain were removed before the brain was glued on the rostral side onto a vibratome (Model 1000, Ted Pella, Redding, CA), doused with cold sodium free, high sucrose ACSF and cut into coronal slices (300 μm). Brain slices containing the LGN and the CL were transferred into a holding chamber. For recordings in the NRT, horizontal brain slices were used. These were obtained by removing the brain as described above, and gluing the ventral side onto a vibratome. Three hundred μm thick horizontal slices were obtained and transferred into a holding chamber. The holding chamber was filled with identical solutions for coronal and horizontal slices, which were composed of (mM): CaCl_2 , 3; KCl, 2.5; NaCl, 125; MgSO_4 , 4; NaH_2PO_4 , 1.25; NaHCO_3 , 22; dextrose, 10; pH ~ 7.4 , gassed with carbogen. Slices were heated for 20 min to 30 °C before being cooled to room temperature, and allowed to rest for 60 to 90 min.

Electrophysiology

Whole-cell recordings in brain slice preparations were done using glass pipettes (GC150T-10, Clark Electromedical Instruments, Pangbourne, UK) connected to an EPC-10 amplifier (HEKA Elektronik, Friedland, Germany). Pulse software (HEKA) was used for stimulus application and the recording of data. Electrode resistances ranged from 1.8 to 2.5 M Ω . Input resistances ranged from 200 to 800 M Ω , while series resistances ranged from 5 to 15 M Ω . All recordings were performed at room temperature. The following recording solutions were used to isolate Ca^{2+} currents in voltage clamp experiments: i) Extracellular solution (mM): CaCl_2 , 1.5; KCl, 2.5; NaCl, 120; MgSO_4 , 2; NaH_2PO_4 , 1.25; HEPES, 30; dextrose, 10; 4-AP, 2; TEA, 5; TTX, 0.0005; pH 7.24 with NaOH. ii) Intracellular solution (mM): Cs-gluconate, 80; Cs₃-citrate, 10; NaCl, 10; HEPES, 10; EGTA, 11; CaCl_2 , 1; MgCl_2 , 1; KCl, 1; TEA-Cl, 15; QX-314, 1 mg/ml internal solution; Biocytin, 3 mg/ml internal solution; Mg-ATP, 3; Na₂-GTP, 0.5; phosphocreatine, 15; pH 7.25 with CsOH; ~ 290 mOsm. For current-clamp experiments in brain slice preparations the following recording solutions were used: i) Extracellular solution (mM): CaCl_2 , 1.5; KCl, 2.5; NaCl, 120; MgSO_4 , 2; NaH_2PO_4 , 1.25; HEPES, 30; dextrose, 10; pH 7.24 with NaOH; ~ 300 mOsm. ii) Intracellular solution (mM): CaCl_2 , 0.5; NaCl, 10; MgCl_2 , 1; HEPES, 10; K-BAPTA, 5; K-gluconate, 95; K₃-citrate, 20; phosphocreatine, 15; Na₂-GTP, 0.5; Mg-ATP, 3; Biocytin, 3 mg/ml internal solution; pH 7.24 with KOH; ~ 290 mOsm.

Analysis of electrophysiological data

All current traces of voltage clamp experiments were subjected to off-line subtraction of the linear leak according to Ohm's law, using custom made software (Patch by Bernd Letz, HEKA).

The maximum T-type Ca^{2+} current amplitude observed during the steady-state activation protocol was taken as the maximum T-current

amplitude for each individual neuron. This amplitude was used for the calculation of T-current density.

The inactivation time constant of the T-type Ca^{2+} current was obtained by fitting a mono-exponential decay function to the inactivating part of the T-current trace using PulseFit software. The function had the following form:

$$Y = A + I_{\max}e^{-x/t} \quad (1)$$

Numerical analysis of current-clamp data was done using MATLAB® software (MathWorks). For analysis of current ramps, data were binned (9.8 ms intervals) and differentiated. To approximate the beginning of the LTS we adapted a method described by Gutierrez et al. (2001). Briefly, the recorded voltage prior to ramp stimulation (baseline) was differentiated and fitted with a Gaussian function (Fig. 10). The LTS onset point was defined as the first point after which 4 consecutive slopes of binned data exceeded the upper 95% confidence limit of the Gaussian fit of the baseline (Fig. 10) (Gutierrez et al., 2001). Subsequently, the data between the onset point of ramp stimulation and the onset of the LTS were fitted with a linear equation. The voltage of the LTS onset point, and the slope between the beginning of the stimulation and the LTS onset point were used for analysis. In case of ramp stimulations without LTS generation, the entire ramp was fitted with a linear function.

Laser capturing of thalamic tissue

All solutions used during the preparation of slices for laser capturing were prepared with DEPC treated water and RNase free components. Rat brains (P18–28) were removed, embedded in tissue freezing medium (Tissue-Tek, Science Services, Munich, Germany) and stored at -80°C for further processing. Later, brains were placed into a cryo-microtome (-12 to -16°C) and allowed to equilibrate for ~ 1 h. Then, brains were cut into $16\ \mu\text{m}$ thick slices and placed onto Poly-L-lysine (0.05%) treated membrane coated object slides (PALM MembraneSlides, P.A.L.M. Microlaser Technologies AG, Bernried, Germany). Afterwards, the brain slices were stained with Hematoxylin and Eosin (Hematoxylin 1 min; $3\times$ wash in DEPC- H_2O for 1, 2, and 3 min; Eosin 30 s; increasing ethanol series, 50%, 70%, 100% for 3 min each; air dried at room temperature) and placed under an inverted laser capture microscope (P. A.L.M. Microlaser Technologies AG). The LGN, CL, and NRT were shot into mineral oil filled caps of laboratory tubes and frozen in liquid nitrogen to be subjected to RT-PCR procedures.

RT-PCR procedures

Quantitative RT-PCR analysis was performed on LGN, CL, and NRT tissue yielded through laser capturing. The mRNA of laser captured tissue was transcribed into cDNA using oligo(dT)₁₈ primers (Roche, Germany) and the Sensiscript RT Kit (Quiagen, Hilden, Germany). The hybridization primer/probe assays for real-time PCR detection were purchased from Applied Biosystems. The following intron spanning assay-on-demand probes were used: $\alpha 1\text{G}$: Rn0058105_m1; $\alpha 1\text{H}$: Rn01460351_g1; $\alpha 1\text{I}$: Rn00571684_m1; β_2 -microglobulin: Rn00560865_m1. Real-time PCR was performed using the TaqMan universal PCR Master Mix (Applied Biosystems) and the ABI Prism 7000 Sequence Detection System (Applied Biosystems); PCR program was: 2 min at 50°C , 10 min at 95°C , 50 cycles: 15 s at 95°C and 1 min at 60°C . Results were analyzed with the ABI Prism 7000 SDS software. The efficiency of real-time primer/probes was nearly identical. Quantification was done using the comparative C_T or $\Delta\Delta C_T$ method as described earlier (Budde et al., 2005). Non-quantitative RT-PCR for detection of splice variations of the CACNA1G transcript was performed on CL tissue samples obtained through laser capturing (Broicher et al., 2007a). GAPDH expression was checked as a positive control. The PCR protocol for GAPDH amplification was: 3 min 94°C ; 50 cycles (30 s 94°C , 1 min

61°C , 1 min 72°C); 7 min 72°C ; $\infty 4^{\circ}\text{C}$. Primer sequences for GAPDH (nucleotides 789–1028, accession no. NM017008) were: forward, 5'-TGATGACATCAAGAAGGTGGTGA-3'; reverse, 5'-TCCTTGGAGCCATGTAGGCCAT-3'. Amplification of the exon 25, 26 region was done using a nested PCR approach. The PCR protocol for the multiplex step was: 3 min 94°C ; 50 cycles (30 s 94°C , 1 min 62°C , 1 min 72°C); 7 min 72°C ; $\infty 4^{\circ}\text{C}$. The PCR protocol for the nested step was: 3 min 94°C ; 35 cycles (30 s 94°C , 1 min 64°C , 1 min 72°C); 7 min 72°C ; $\infty 4^{\circ}\text{C}$. Primer sequences for the multiplex step were (nucleotides 4557–5361; accession no. AF290212): forward, 5'-CAGCAGCCCATCATGAACCAC-AAC-3'; reverse, 5'-GCCGACCCAAGCCCTCACAAG-3'. Primer sequences for the nested step were (nucleotides 4709–5034; accession no. AF290212): forward, 5'-GCGGCGTGAGGAGAAGCGACTAC-3'; reverse, 5'-CCTGGAAGAAACGCGGAAGC-3'. For all non-quantitative PCRs the Taq DNA Polymerase (5 U/ μl , Quiagen) was used.

Computational modeling

For simulations on the effects of different T-current characteristics on the LTS, a single compartment TC neuron model was used, as described previously (Hines and Carnevale, 2001; Meuth et al., 2006). The model was based on the mathematical description of $I_{K\text{ leak}}$, $I_{Na\text{ leak}}$, I_L , I_T , $I_{Na\text{ HH}}$, I_{NaP} , $I_{K\text{ HH}}$, I_A , and I_{KCa} . Neuronal membrane potential was described by the following equation: $C_M(dV/dt) = -I_M + I_{\text{inject}}$. I_M is the sum of all membrane currents, I_{inject} is the injected current, and C_M is the membrane capacitance. The model was capable of generating action potentials in both burst and tonic transmission modes. Simulations were carried out at 35°C using the NEURON simulation environment (Hines and Carnevale, 2001).

Acknowledgments

The authors would like to thank A. Jahn, A. Ritter, and R. Ziegler for their excellent technical assistance. This work was supported by grants from DFG (Pa 336/17-1 to H.-C.P. and Bu 1019/8-1 to T. Budde), MPG (Research Award to H.-C.P.), IZKF (Bud 3/005/07 to T. Budde), and IMF (Bu 120 501 to T. Budde). T. Broicher was a fellow of the Boehringer Ingelheim Foundation.

References

- Anderson, M.P., Mochizuki, T., Xie, J., Fischler, W., Manger, J.P., Talley, E.M., Scammell, T.E., Tonegawa, S., 2005. Thalamic Cav3.1 T-type Ca^{2+} channel plays a crucial role in stabilizing sleep. *Proc. Natl. Acad. Sci. U. S. A.* 102, 1743–1748.
- Avoli, M., Rogawski, M.A., Avanzini, G., 2001. Generalized epileptic disorders: an update. *Epilepsia* 42, 445–457.
- Blethyn, K.L., Hughes, S.W., Toth, T.I., Cope, D.W., Crunelli, V., 2006. Neuronal basis of the slow (<1 Hz) oscillation in neurons of the nucleus reticularis thalami in vitro. *J. Neurosci.* 26, 2474–2486.
- Broicher, T., Kanyshkova, T., Landgraf, P., Rankovic, V., Meuth, P., Meuth, S.G., Pape, H.C., Budde, T., 2007a. Specific expression of low-voltage-activated calcium channel isoforms and splice variants in thalamic local circuit interneurons. *Mol. Cell. Neurosci.* 36, 132–145.
- Broicher, T., Seidenbecher, T., Meuth, P., Munsch, T., Meuth, S.G., Kanyshkova, T., Pape, H.C., Budde, T., 2007b. T-current related effects of antiepileptic drugs and a Ca^{2+} channel antagonist on thalamic relay and local circuit interneurons in a rat model of absence epilepsy. *Neuropharmacology* 53, 431–446.
- Budde, T., Caputi, L., Kanyshkova, T., Staak, R., Abrahamczik, C., Munsch, T., Pape, H.C., 2005. Impaired regulation of thalamic pacemaker channels through an imbalance of subunit expression in absence epilepsy. *J. Neurosci.* 25, 9871–9882.
- Budde, T., Pape, H.-C., Kumar, S.S., Huguenard, J.R., 2006. Thalamic, thalamo-cortical, and cortico-cortical models of epilepsy with an emphasis on absence seizures. In: Pitkänen, A., Schwartzkroin, P.A., Moshé, S.L. (Eds.), *Models of Seizures and Epilepsy*. Elsevier, Amsterdam, pp. 73–88.
- Chemin, J., Monteil, A., Bourinet, E., Nargeot, J., Lory, P., 2001. Alternatively spliced alpha (1G) ($\text{Ca}_v3.1$) intracellular loops promote specific T-type Ca^{2+} channel gating properties. *Biophys. J.* 80, 1238–1250.
- Chemin, J., Monteil, A., Perez-Reyes, E., Bourinet, E., Nargeot, J., Lory, P., 2002. Specific contribution of human T-type calcium channel isoforms (alpha(1G), alpha(1H) and alpha(1I)) to neuronal excitability. *J. Physiol.* 540, 3–14.
- Coenen, A.M., Van Luitelaar, E.L., 2003. Genetic animal models for absence epilepsy: a review of the WAG/Rij strain of rats. *Behav. Genet.* 33, 635–655.
- Coulter, D.A., Huguenard, J.R., Prince, D.A., 1989a. Characterization of ethosuximide reduction of low-threshold calcium current in thalamic neurons. *Ann. Neurol.* 25, 582–593.

- Coulter, D.A., Huguenard, J.R., Prince, D.A., 1989b. Specific petit mal anticonvulsants reduce calcium currents in thalamic neurons. *Neurosci. Lett.* 98, 74–78.
- Crunelli, V., Leresche, N., 2002. Childhood absence epilepsy: genes, channels, neurons and networks. *Nat. Rev. Neurosci.* 3, 371–382.
- Crunelli, V., Cope, D.W., Hughes, S.W., 2006. Thalamic T-type Ca²⁺ channels and NREM sleep. *Cell. Calcium* 40, 175–190.
- Deschenes, M., Bourassa, J., Parent, A., 1996. Striatal and cortical projections of single neurons from the central lateral thalamic nucleus in the rat. *Neuroscience* 72, 679–687.
- Destexhe, A., Neubig, M., Ulrich, D., Huguenard, J., 1998. Dendritic low-threshold calcium currents in thalamic relay cells. *J. Neurosci.* 18, 3574–3588.
- Emerick, M.C., Stein, R., Kunze, R., McNulty, M.M., Regan, M.R., Hanck, D.A., Agnew, W.S., 2006. Profiling the array of Ca(v)3.1 variants from the human T-type calcium channel gene CACNA1G: alternative structures, developmental expression, and biophysical variations. *Proteins* 64, 320–342.
- Fuentealba, P., Timofeev, I., Bazhenov, M., Sejnowski, T.J., Steriade, M., 2005. Membrane bistability in thalamic reticular neurons during spindle oscillations. *J. Neurophysiol.* 93, 294–304.
- Gutierrez, C., Cox, C.L., Rinzel, J., Sherman, S.M., 2001. Dynamics of low-threshold spike activation in relay neurons of the cat lateral geniculate nucleus. *J. Neurosci.* 21, 1022–1032.
- Hernandez-Cruz, A., Pape, H.C., 1989. Identification of two calcium currents in acutely dissociated neurons from the rat lateral geniculate nucleus. *J. Neurophysiol.* 61, 1270–1283.
- Hines, M.L., Carnevale, N.T., 2001. NEURON: a tool for neuroscientists. *Neuroscientist* 7, 123–135.
- Huguenard, J.R., 1996. Low-threshold calcium currents in central nervous system neurons. *Annu. Rev. Physiol.* 58, 329–348.
- Kim, D., Song, I., Keum, S., Lee, T., Jeong, M.J., Kim, S.S., McEnery, M.W., Shin, H.S., 2001. Lack of the burst firing of thalamocortical relay neurons and resistance to absence seizures in mice lacking alpha(1G) T-type Ca(2+) channels. *Neuron* 31, 35–45.
- Kuisle, M., Wanaverbecq, N., Brewster, A.L., Frere, S.G., Pinault, D., Baram, T.Z., Luthi, A., 2006. Functional stabilization of weakened thalamic pacemaker channel regulation in rat absence epilepsy. *J. Physiol.* 575, 83–100.
- Lacey, C.J., Bolam, J.P., Magill, P.J., 2007. Novel and distinct operational principles of intralaminar thalamic neurons and their striatal projections. *J. Neurosci.* 27, 4374–4384.
- Lee, S.H., Govindaiah, G., Cox, C.L., 2007. Heterogeneity of firing properties among rat thalamic reticular nucleus neurons. *J. Physiol.* 582, 195–208.
- Leresche, N., Parri, H.R., Erdemli, G., Guyon, A., Turner, J.P., Williams, S.R., Crunelli, V., 1998. On the action of the anti-absence drug ethosuximide in the rat and cat thalamus. *J. Neurosci.* 18, 4842–4853.
- Lo, F.S., Ziburkus, J., Guido, W., 2002. Synaptic mechanisms regulating the activation of a Ca(2+)-mediated plateau potential in developing relay cells of the LGN. *J. Neurophysiol.* 87, 1175–1185.
- Mainen, Z.F., Sejnowski, T.J., 1996. Influence of dendritic structure on firing pattern in model neocortical neurons. *Nature* 382, 363–366.
- Meis, S., Biella, G., Pape, H.C., 1996. Interaction between low voltage-activated currents in reticular thalamic neurons in a rat model of absence epilepsy. *Eur. J. Neurosci.* 8, 2090–2097.
- Meuth, S.G., Kanyshkova, T., Meuth, P., Landgraf, P., Munsch, T., Ludwig, A., Hofmann, F., Pape, H.C., Budde, T., 2006. Membrane resting potential of thalamocortical relay neurons is shaped by the interaction among TASK3 and HCN2 channels. *J. Neurophysiol.* 96, 1517–1529.
- Pape, H.C., 1996. Queer current and pacemaker: the hyperpolarization-activated cation current in neurons. *Annu. Rev. Physiol.* 58, 299–327.
- Pape, H.C., Budde, T., Mager, R., Kisvarday, Z.F., 1994. Prevention of Ca(2+)-mediated action potentials in GABAergic local circuit neurones of rat thalamus by a transient K⁺ current. *J. Physiol.* 478 (Pt 3), 403–422.
- Paz, J.T., Chavez, M., SAILLET, S., Deniau, J.M., Charpier, S., 2007. Activity of ventral medial thalamic neurons during absence seizures and modulation of cortical paroxysms by the nigrothalamic pathway. *J. Neurosci.* 27, 929–941.
- Perez-Reyes, E., 2003. Molecular physiology of low-voltage-activated t-type calcium channels. *Physiol. Rev.* 83, 117–161.
- Perez-Reyes, E., 2006. Molecular characterization of T-type calcium channels. *Cell Calcium* 40, 89–96.
- Pinault, D., O'Brien, T.J., 2007. Cellular and network mechanisms of genetically-determined absence seizures. *Thalamus & Related Systems*, doi:10.1017/S1472928807000209, 1–23.
- Pinault, D., Leresche, N., Charpier, S., Deniau, J.M., Marescaux, C., Vergnes, M., Crunelli, V., 1998. Intracellular recordings in thalamic neurones during spontaneous spike and wave discharges in rats with absence epilepsy. *J. Physiol.* 509 (Pt 2), 449–456.
- Seidenbecher, T., Pape, H.C., 2001. Contribution of intralaminar thalamic nuclei to spike-and-wave-discharges during spontaneous seizures in a genetic rat model of absence epilepsy. *Eur. J. Neurosci.* 13, 1537–1546.
- Seidenbecher, T., Staak, R., Pape, H.C., 1998. Relations between cortical and thalamic cellular activities during absence seizures in rats. *Eur. J. Neurosci.* 10, 1103–1112.
- Sherman, S.M., Guillery, R.W., 2006. Exploring the Thalamus and its Role in Cortical Function. MIT Press, Cambridge, Massachusetts.
- Slaght, S.J., Leresche, N., Deniau, J.M., Crunelli, V., Charpier, S., 2002. Activity of thalamic reticular neurons during spontaneous genetically determined spike and wave discharges. *J. Neurosci.* 22, 2323–2334.
- Song, I., Kim, D., Choi, S., Sun, M., Kim, Y., Shin, H.S., 2004. Role of the alpha1G T-type calcium channel in spontaneous absence seizures in mutant mice. *J. Neurosci.* 24, 5249–5257.
- Steriade, M., 1997. Synchronized activities of coupled oscillators in the cerebral cortex and thalamus at different levels of vigilance. *Cereb. Cortex* 7, 583–604.
- Talley, E.M., Cribbs, L.L., Lee, J.H., Daud, A., Perez-Reyes, E., Bayliss, D.A., 1999. Differential distribution of three members of a gene family encoding low voltage-activated (T-type) calcium channels. *J. Neurosci.* 19, 1895–1911.
- Talley, E.M., Solorzano, G., Depaulis, A., Perez-Reyes, E., Bayliss, D.A., 2000. Low-voltage-activated calcium channel subunit expression in a genetic model of absence epilepsy in the rat. *Brain Res. Mol. Brain Res.* 75, 159–165.
- Tennigkeit, F., Schwarz, D.W., Puil, E., 1998. Modulation of bursts and high-threshold calcium spikes in neurons of rat auditory thalamus. *Neuroscience* 83, 1063–1073.
- Tsakiridou, E., Bertolini, L., de Curtis, M., Avanzini, G., Pape, H.C., 1995. Selective increase in T-type calcium conductance of reticular thalamic neurons in a rat model of absence epilepsy. *J. Neurosci.* 15, 3110–3117.
- Van der Werf, Y.D., Witter, M.P., Groenewegen, H.J., 2002. The intralaminar and midline nuclei of the thalamus. Anatomical and functional evidence for participation in processes of arousal and awareness. *Brain Res. Brain Res. Rev.* 39, 107–140.
- van Ooyen, A., Duijnhouwer, J., Remme, M.W., van Pelt, J., 2002. The effect of dendritic topology on firing patterns in model neurons. *Network* 13, 311–325.
- Williams, D., 1953. A study of thalamic and cortical rhythms in petit mal. *Brain* 76, 50–69.
- Williams, S.R., Stuart, G.J., 2000. Action potential backpropagation and somato-dendritic distribution of ion channels in thalamocortical neurons. *J. Neurosci.* 20, 1307–1317.
- Yasukawa, T., Kita, T., Xue, Y., Kita, H., 2004. Rat intralaminar thalamic nuclei projections to the globus pallidus: a biotinylated dextran anterograde tracing study. *J. Comp. Neurol.* 471, 153–167.
- Ying, S.W., Abbas, S.Y., Harrison, N.L., Goldstein, P.A., 2006. Propofol block of I(h) contributes to the suppression of neuronal excitability and rhythmic burst firing in thalamocortical neurons. *Eur. J. Neurosci.* 23, 465–480.
- Zhan, X.J., Cox, C.L., Rinzel, J., Sherman, S.M., 1999. Current clamp and modeling studies of low-threshold calcium spikes in cells of the cat's lateral geniculate nucleus. *J. Neurophysiol.* 81, 2360–2373.
- Zhang, Y., Mori, M., Burgess, D.L., Noebels, J.L., 2002. Mutations in high-voltage-activated calcium channel genes stimulate low-voltage-activated currents in mouse thalamic relay neurons. *J. Neurosci.* 22, 6362–6371.
- Zhang, Y., Vilaythong, A.P., Yoshor, D., Noebels, J.L., 2004. Elevated thalamic low-voltage-activated currents precede the onset of absence epilepsy in the SNAP25-deficient mouse mutant coloboma. *J. Neurosci.* 24, 5239–5248.

Postnatal Expression Pattern of HCN Channel Isoforms in Thalamic Neurons: Relationship to Maturation of Thalamocortical Oscillations

Tatyana Kanyshkova,^{1*} Matthias Pawlowski,^{1*} Patrick Meuth,^{1*} Celine Dubé,² Roland A. Bender,^{2,3} Amy L. Brewster,^{2,4} Arnd Baumann,⁵ Tallie Z. Baram,² Hans-Christian Pape,¹ and Thomas Budde¹

¹Institut für Physiologie I, Westfälische Wilhelms-Universität Münster, D-48149 Münster, Germany, ²Anatomy/Neurobiology and Pediatrics, University of California, Irvine, California 92697-4475, ³Institut für Anatomie I, Universitätsklinikum Hamburg-Eppendorf, D-20246 Hamburg, Germany, ⁴Department of Pediatrics, Baylor College of Medicine, Houston, Texas 77030, and ⁵Institut für Strukturbiologie und Biophysik 1, Forschungszentrum Jülich, D-52425 Jülich, Germany

Hyperpolarization-activated cyclic nucleotide-gated cation (HCN) channels are the molecular substrate of the hyperpolarization-activated inward current (I_h). Because the developmental profile of HCN channels in the thalamus is not well understood, we combined electrophysiological, molecular, immunohistochemical, EEG recordings *in vivo*, and computer modeling techniques to examine HCN gene expression and I_h properties in rat thalamocortical relay (TC) neurons in the dorsal part of the lateral geniculate nucleus and the functional consequence of this maturation. Recordings of TC neurons revealed an approximate sixfold increase in I_h density between postnatal day 3 (P3) and P106, which was accompanied by significantly altered current kinetics, cAMP sensitivity, and steady-state activation properties. Quantification on tissue levels revealed a significant developmental decrease in cAMP. Consequently the block of basal adenylyl cyclase activity was accompanied by a hyperpolarizing shift of the I_h activation curve in young but not adult rats. Quantitative analyses of HCN channel isoforms revealed a steady increase of mRNA and protein expression levels of HCN1, HCN2, and HCN4 with reduced relative abundance of HCN4. Computer modeling in a simplified thalamic network indicated that the occurrence of rhythmic delta activity, which was present in the EEG at P12, differentially depended on I_h conductance and modulation by cAMP at different developmental states. These data indicate that the developmental increase in I_h density results from increased expression of three HCN channel isoforms and that isoform composition and intracellular cAMP levels interact in determining I_h properties to enable progressive maturation of rhythmic slow-wave sleep activity patterns.

Introduction

As sleep approaches in adult mammals, the low-voltage, fast-frequency EEG pattern of alert wakefulness begins to slow down until slow-wave sleep, characterized by the increasing presence of spindle waves and high-amplitude, slow delta waves, occurs (Sinton and McCarley, 2004; Staunton, 2005). The thalamocortical system is the neuronal substrate of rhythmic synchronized activity during slow-wave sleep. During this state, thalamocortical relay (TC) neurons display intrinsic pacemaker activity, leading to the rhythmic generation of bursts of action potentials, which are synchronized throughout the thalamocortical network (Steriade et al., 1997). This pace-making property is based on I_h , which is gated by membrane voltage as well as cAMP (Pape,

1996). The regulation of the voltage dependence of I_h through cAMP is considered an important mechanism for the control of rhythmic burst firing during the sleep-wake cycle.

Four members of a gene family encoding mammalian HCN channels (HCN1–HCN4) give rise to I_h (Kaupp and Seifert, 2001; Robinson and Siegelbaum, 2003; Santoro and Baram, 2003). Four subunits are thought to assemble to form functional channels, and cAMP acts directly on the C-terminal intracellular domain to rapidly regulate channel opening (Wainger et al., 2001; Robinson and Siegelbaum, 2003). The expression pattern of HCN isoforms in the mammalian brain varies with age, region, and species (Moosmang et al., 1999; Monteggia et al., 2000; Bender and Baram, 2008), and the electrophysiological properties of functional HCN channels seem to critically depend on homomeric or heteromeric formation of channel subunits (Much et al., 2003; Brewster et al., 2005; Chen et al., 2005).

Recent evidence suggests that altered I_h properties and HCN channel expression plays a critical role during epileptic seizures in different brain regions (Bender et al., 2003). In the thalamocortical system, two genetic rat models of absence epilepsy revealed that abnormal regulation of I_h accompanies the pathogenesis in that there is a reduction in responsiveness to cAMP associated

Received Feb. 10, 2009; revised April 23, 2009; accepted May 20, 2009.

This work was supported by Deutsche Forschungsgemeinschaft Grants BU 1019/8-1 and BE 4107/2-1, Interdisziplinäres Zentrum für Klinische Forschung Grant Bud/005/07, and National Institutes of Health Grants NS 35439 and NS 45540. This work was done in partial fulfillment of the MD thesis of M.P. and the PhD thesis of P.M. We thank A. Markovic, E. Naß, and S. Ruppel for excellent technical assistance.

*T.K., M.P., and P.M. contributed equally to this work.

Correspondence should be addressed to Thomas Budde, Institut für Physiologie I, Westfälische Wilhelms-Universität Münster, Robert-Koch-Strasse 27a, D-48149 Münster, Germany. E-mail: tbudde@uni-muenster.de.

DOI:10.1523/JNEUROSCI.0689-09.2009

Copyright © 2009 Society for Neuroscience 0270-6474/09/298847-11\$15.00/0

with a selective increase in the expression of the relatively cAMP-insensitive HCN1 isoform in TC neurons (Budde et al., 2005; Kuisle et al., 2006).

The developmental maturation of HCN channels in the thalamus is not well understood. In general, these developmental changes influence I_h conductance, either by governing the levels of expression of different HCN isoforms or via regulation of cAMP levels (Surges et al., 2006). In rat thalamus, HCN expression patterns are established at early postnatal stages in a nucleus-specific manner, with HCN2 and HCN4 being most robustly expressed in relay nuclei (Bender et al., 2001; Ludwig et al., 2003). However, a comprehensive quantitative study of mRNA and protein expression of the HCN channels in the thalamus, and, importantly, of the consequences of this developmental profile on the properties and magnitude of I_h and the resulting modulation of thalamocortical sleep patterns has not been reported. Therefore, we combined *in vitro* and *in vivo* electrophysiological, immunological, molecular biological, and computational modeling techniques to correlate I_h current density, voltage dependence, and kinetics with the HCN expression pattern and the generation of rhythmic activity in single TC neurons as well as thalamic networks.

Materials and Methods

Preparation. All animal preparations were done according to the European Communities Council Directive of November 24, 1986 (86/609/EEC). Rats [the Sprague Dawley strain was used for all experiments presented here; postnatal day 3 (P3) to P106] were anesthetized with isoflurane and decapitated. In rapid sequence, after surgically removing a skull cap caudal to the bregma, a block of brain tissue containing the thalamus was removed from the cranial vault and submerged in ice-cold aerated (O_2) saline containing the following (in mM): 200 sucrose, 20 PIPES, 2.5 KCl, 1.25 NaH_2PO_4 , 10 $MgSO_4$, 0.5 $CaCl_2$, and 10 dextrose, pH 7.35, with NaOH. Thalamic slices were prepared as coronal sections on a vibratome. Before recording, slices were kept submerged in artificial CSF containing the following (in mM): 125 NaCl, 2.5 KCl, 1.25 NaH_2PO_4 , 24 $NaHCO_3$, 2 $MgSO_4$, 2 $CaCl_2$, and 10 dextrose, pH adjusted to 7.35 by bubbling with carbogen (95% O_2 and 5% CO_2).

Whole-cell patch clamp. Recordings were performed on TC neurons of the dorsal part of the lateral geniculate nucleus (dLGN) at room temperature in a solution containing the following (in mM): 120 NaCl, 2.5 KCl, 1.25 NaH_2PO_4 , 30 HEPES, 2 $MgSO_4$, 2 $CaCl_2$, and 10 dextrose, pH 7.25 adjusted with HCl. Individual cells were visually identified by infrared differential interference contrast video microscopy. Membrane currents were measured with glass microelectrodes pulled from borosilicate glass capillaries (GC150T-10; Clark Electromedical Instruments) and filled with the following (in mM): 95 K-gluconate, 20 K_3 -citrate, 10 NaCl, 10 HEPES, 1 $MgCl_2$, 0.5 $CaCl_2$, 3 BAPTA, 3 Mg-ATP, and 0.5 Na-GTP. The internal solution was set to a pH of 7.25 with KOH and an osmolality of 295 mOsm/kg. The electrodes were connected to an EPC-10 amplifier (HEKA) with a chlorided silver wire. Electrode resistances were in the range of 2–3 M Ω , with access resistances in the range of 5–20 M Ω . Series resistance compensation of >30% was routinely applied. Voltage-clamp experiments were controlled by the software Pulse or PatchMaster (HEKA) operating on an IBM-compatible personal computer. Measurements were corrected for liquid junction potential. All results are presented as mean \pm SEM. Substance effects were tested for statistical significance using the nonparametric Mann–Whitney test (Prism software; GraphPad Software). When applicable, the parametric *t* test was used (Origin software). Differences were considered statistically significant if $p < 0.05$.

The protocol used to assess I_h was designed to increase the stability of whole-cell recordings and account for increasingly fast activation kinetics of I_h . Therefore, the pulse length was shortened by 1500 ms with increasing hyperpolarization (3.5 s pulse length at -130 mV). Steady-state activation of I_h , $p(V)$, was estimated by normalizing the tail current amplitudes (I) 50 ms after stepping to a constant potential of -100 mV

(see Fig. 1A, arrow) from a variable amplitude step using the following equation:

$$p(V) = (I - I_{\min}) / (I_{\max} - I_{\min}),$$

with I_{\max} being the tail current amplitude for the voltage step from -130 to -100 mV and I_{\min} for the voltage step from -40 to -100 mV, respectively. I_h activation was well accounted for by a Boltzmann equation of the following form:

$$p(V) = 1 / (1 + \exp((V - V_h) / k)),$$

where V_h is the voltage of half-maximal activation, and k is the slope factor.

The amplitude of I_h (see Fig. 1A, bracket) was calculated by subtracting the instantaneous current amplitude I_i from the steady-state current (I_{ss}). The density of I_h was calculated by dividing the I_h current amplitude at -130 mV by the membrane capacitance obtained during whole-cell recordings.

The time course of I_h activation in TC neurons was best approximated by the following single-exponential equation:

$$I_h(t) = A_0 + A_1 \times e^{-t/\tau},$$

where $I_h(t)$ is the current amplitude at time t , and A_0 , A_1 , and τ are axis intercept, amplitude coefficient, and time constant, respectively. In $\sim 10\%$ of the cells recorded under different conditions, the time course of activation was best fitted by a biexponential function. These cells were not included for analysis of activation kinetics.

In vivo electrophysiology. Rats aged P6, P11, P13, P17, and P89 were bilaterally implanted with two cortical electrodes (Plastics One) positioned over the frontoparietal cortex. A ground electrode was placed in the cerebellum, and the assembly was anchored with dental cement and four stainless steel screws. Digital video EEG recordings were performed on the following day in freely moving, non-anesthetized rats, with concurrent video monitoring (Camcorder, ZR40; Canon). Electrophysiological data were recorded at a frequency band of 0.1–200 Hz, sampled at 400 Hz/channel using Powerlab 8SP (AD Instruments) equipped with Chart 4 for Windows. The data were filtered (0.1–30 Hz) for analysis and synchronized with the video monitoring.

Computer simulations. All simulations were processed within the NEURON Simulation Environment at a temperature of 36°C (Hines and Carnevale, 2001; Meuth et al., 2005). Given the four-cell neuronal network model (see Fig. 7B) (supplemental Table S1, available at www.jneurosci.org as supplemental material) published by Destexhe et al. (1996), the corresponding TC cell template was used to investigate the impact of I_h on the two typical firing modes of a single TC neuron (burst and tonic activity) (see Fig. 5A). The I_h current kinetic and voltage dependency (supplemental Fig. S1, available at www.jneurosci.org as supplemental material) of this template originates from a previously McCormick and Huguenard implementation (McCormick and Huguenard, 1992) and has been expanded with Ca^{2+} dependence by Destexhe et al. (1996). To reach a stable membrane resting potential of -60 mV, the default parameter setting was adapted as follows:

<i>e_pas</i>	-44 (mV)	reversal potential of $I_{passive}$
<i>kl.gmax</i>	0.003 (μ mho)	maximum I_{leak} conductance,
<i>ghbar_iar</i>	$1e-5$ (mho/cm 2)	maximum I_h conductance, and
<i>ginc_iar</i>	1	augmentation of I_h conductance with Ca^{2+} .

Evaluation of the I_h driven voltage sag (see Fig. 5B) was accomplished by successively decreasing the maximum I_h conductance in 10% steps from 100 to 0%. Thereby the strength of the applied hyperpolarizing pulse was continuously lowered to compensate the increased membrane resistance and to ensure a constant step potential of -130 mV. All other model parameters remained unchanged during the simulations. In each step, the voltage sag was calculated by subtracting the initial (global minimum) (see Fig. 5B, inset) from the final (right at the end of the hyperpolarizing stimulus) (see Fig. 5B, inset) membrane voltage.

A second set of simulations is based on the simplified neuronal net-

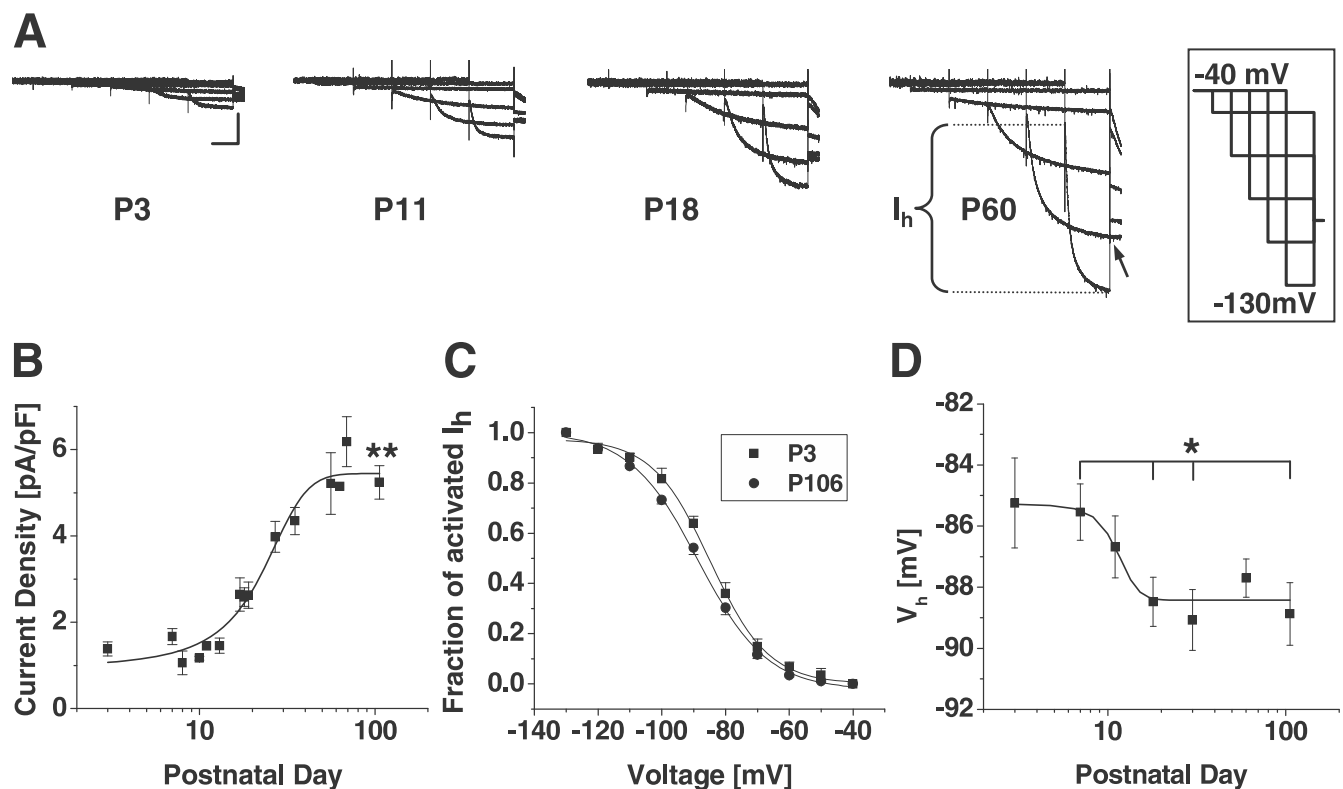


Figure 1. Postnatal development of I_h properties in TC neurons. **A**, Representative current traces obtained from cells of different postnatal age. Currents were elicited by applying the shown voltage-clamp protocol from -40 mV (inset). The tail current voltage was -100 mV (see arrow). The duration of each hyperpolarizing step was shortened as command potentials became more negative. Calibration: 3 s, 100 pA. The bracket indicates the amplitude of I_h . **B**, Mean current density versus postnatal age reveals increasing I_h currents ($n = 63$; 1–8 per data point). Current densities were calculated by dividing amplitudes at -130 mV by the membrane capacitance obtained during whole-cell recordings. Data from P3 and P106 were highly significantly different (** $p < 0.01$). **C**, Mean steady-state activation curves for P3 and P106 were obtained by plotting normalized tail current amplitudes against the step potential and fitting them with a Boltzmann function. **D**, Mean half-maximal activation voltages (V_h) versus postnatal age reveals a hyperpolarizing shift in V_h with age ($n = 6$ –17 per data point). Significantly different results were obtained for some combinations of postnatal ages (see Results) (* $p < 0.05$).

work (Destexhe et al., 1996) given in Figure 7B. To have two autonomous oscillators, parameters in both TC cells (in variation from the original model by Destexhe) were set to the following:

$ghbar_iar$	$1e-5$ (mho/cm ²)	maximum I_h conductance,
kl_gmax	0.005 (μ mho)	maximum I_{leak} conductance, and
$ginc_iar$	1	augmentation of I_h conductance with Ca^{2+} .

Additionally, the duration of all simulations was extended to 20 s so that the networks could reach a steady state. Part 1 of the simulations (see Fig. 7A, top and middle) comprises altogether 11 separate runs, in which the maximum I_h conductance of both TC cells was successively decremented by 10%. Based on the traces of the first TC cell (TC1), the interburst intervals of the last seven bursts were considered and finally averaged per run (see Fig. 7C, gray bars). Calculating the interburst interval of two consecutive bursts was done with regard to the tip of the first action potential in each case. In part 2 (see Fig. 7A, bottom), the I_h activation curve was shifted by 15 mV to more depolarized values. This shift applied to both TC cells. The mean interburst interval was evaluated as mentioned previously (see Fig. 7C, white bar).

Drugs. During experiments with 8-bromo-cAMP (water soluble; Sigma) added to the recording pipette, properties of I_h were determined 8–15 min after obtaining the whole-cell configuration. The adenylyl cyclase inhibitor 9-(tetrahydro-2-furanyl)-9H-purin-6-amine (SQ22,536) was obtained from Sigma and prepared as stock solution in water. Before recording, slices were incubated for 2 h in extracellular solution containing 300μ M SQ22,536 and were transferred to the recording chamber thereafter. The blocker was not present in the recording solution. Prop-

erties of I_h were determined 8 min after obtaining the whole-cell configuration.

Determination of cAMP level in tissue samples. Samples of the dLGN were prepared from freshly dissected coronal sections and put immediately into 300μ l of ice-cold buffer containing 50 mM HEPES, pH 7.6, 1 mM EDTA, 25 mM sucrose, complete protease inhibitor cocktail (Roche), and 50μ M IBMX (3-isobutyl-1-methylxanthine). Protein samples were centrifuged at $2500 \times g$ for 10 min at 4° C, and pellets were discarded. From these homogenates, 50μ l aliquots were used to determine the cAMP content. Values of cAMP per milligram total protein were determined in triplicate using the TRK432 cAMP assay kit (GE Healthcare).

Immunohistochemistry. Rats of different ages (P10 and P70) were deeply anesthetized with sodium pentobarbital (100 mg/kg, i.p.) and transcardially perfused with 4% phosphate-buffered paraformaldehyde (PFA). Brains were removed, postfixed for 4 h in 4% PFA, cryoprotected in 25% sucrose for 48–72 h, and frozen in isopentane. Coronal sections (40μ m) through the thalamus were cut on a cryostat and collected in PBS. Sections were treated for 30 min with 0.3% H_2O_2 /PBS, then washed three times for 10 min in PBS, preincubated for 1 h in 10% normal goat serum/PBS, and finally incubated with primary antisera in PBS plus 0.3% Triton X-100 for 48 h at 4° C. Polyclonal guinea pig anti-HCN1 (1:500), HCN2 (1:1500), or HCN4 (1:800) antisera were used for these studies (kind gifts from Dr. Ryuichi Shigemoto, Okazaki, Japan). After primary antibody incubation and several washes, sections were transferred to secondary antibody solution (biotinylated goat anti-guinea pig IgGs, 1:250; Vector Laboratories) for 3 h, followed by additional washes and avidin–biotin–peroxidase complex solution (Vector Laboratories) for 2 h at room temperature. Antibody binding was visualized by incubating

sections in a solution containing 0.04% 3,3'-diaminobenzidine, 0.001% H_2O_2 , 0.01% $NiCl_2$, and 0.01% $CoCl_2$. For negative controls, occlusion of the primary antibody from the staining procedure was routinely performed with no positive immunological signal detected.

Western blotting. Rats of different ages (P7, P30, and P90) were rapidly decapitated, and dLGNs were quickly dissected and frozen immediately in liquid nitrogen. Tissue was then homogenized in ice-cold buffer containing 50 mM HEPES, pH 7.6, 1 mM EDTA, and 25 mM sucrose. Protease inhibitor cocktail (Roche) was added according to the guidelines of the manufacturer. Protein samples were centrifuged at $2500 \times g$ for 10 min at $4^\circ C$, and pellets were discarded. The resulting supernatants were separated by 12% SDS-PAGE. Proteins were transferred in 25 mM Tris, 192 mM glycine, 0.1% SDS, and 20% methanol onto Hybond ECL nitrocellulose membranes at 20 V overnight at $4^\circ C$. Thereafter, membranes were blocked with 5% nonfat milk in TBS–0.1% Tween 20 for 1 h and incubated with primary antibodies for 2 h at room temperature. The following antibodies were used: rabbit anti-HCN1, rabbit anti-HCN2, rabbit anti-HCN4 (1:300 for each antibody; Alomone Labs) and monoclonal mouse anti- β -actin (1:4000; Abcam). After washing (three times for 10 min in TBS–0.1% Tween 20), blots were subsequently incubated with horseradish peroxidase-conjugated goat anti-rabbit or anti-mouse antibodies (1:2000 for each antibody; Dako) for 1 h at room temperature. Washing was performed as before, and blots were developed using an ECL Plus detection kit (GE Healthcare) according to the guidelines of the manufacturer.

Quantitation of HCN expression was achieved by densitometric analysis of corresponding protein bands (Quantity One 4.2.2 software, ChemiDoc; Bio-Rad). Protein content was normalized using β -actin as an internal and loading standard.

In situ hybridization. For *in situ* hybridization (ISH), rats were quickly decapitated on P2, P11, or P60 (three to six rats per group), and brains were dissected and placed on powdered dry ice. Coronal sections (20 μm) through the thalamus were cut, mounted on gel-coated slides, and fixed in 4% PFA. After a graded ethanol treatment, sections were exposed to acetic anhydride-triethanolamine and then dehydrated through 70–100% ethanol. Sections were preincubated in hybridization solution [50% formamide, 5 \times sodium–EDTA–Tris (5 \times SET: 750 mM NaCl, 12.5 mM EDTA, and 150 mM Tris, pH 8), 0.2% SDS, 5 \times Denhardt's solution, 0.5 mg/ml salmon sperm-sheared DNA, 250 mg/ml yeast tRNA, 100 mM dithiothreitol, and 10% dextran sulfate] and probed overnight at $55^\circ C$ with antisense [^{35}S]cytidine triphosphate-radiolabeled HCN cRNA probes (0.5–1 $\times 10^6$ cpm/30 μl /section). These probes were synthesized by *in vitro* transcription from cDNAs containing specific gene regions of mouse HCN1, HCN2, and HCN4 channels as described previously (Bender et al., 2001; Brewster et al., 2002). The specific activity of the probes was 1.67–5.2 $\times 10^9$ cpm/ μg . On the following day, sections were washed in decreasing concentrations of SSC solutions, with the most stringent wash at 0.03 \times SSC for 60 min at $62^\circ C$. After dehydration in increasing alcohol concentrations, sections were apposed against Kodak Biomax films. Specificity of signal was verified by hybridizing sections with sense probe or with excess unlabeled (100-fold) antisense probe in addition to labeled

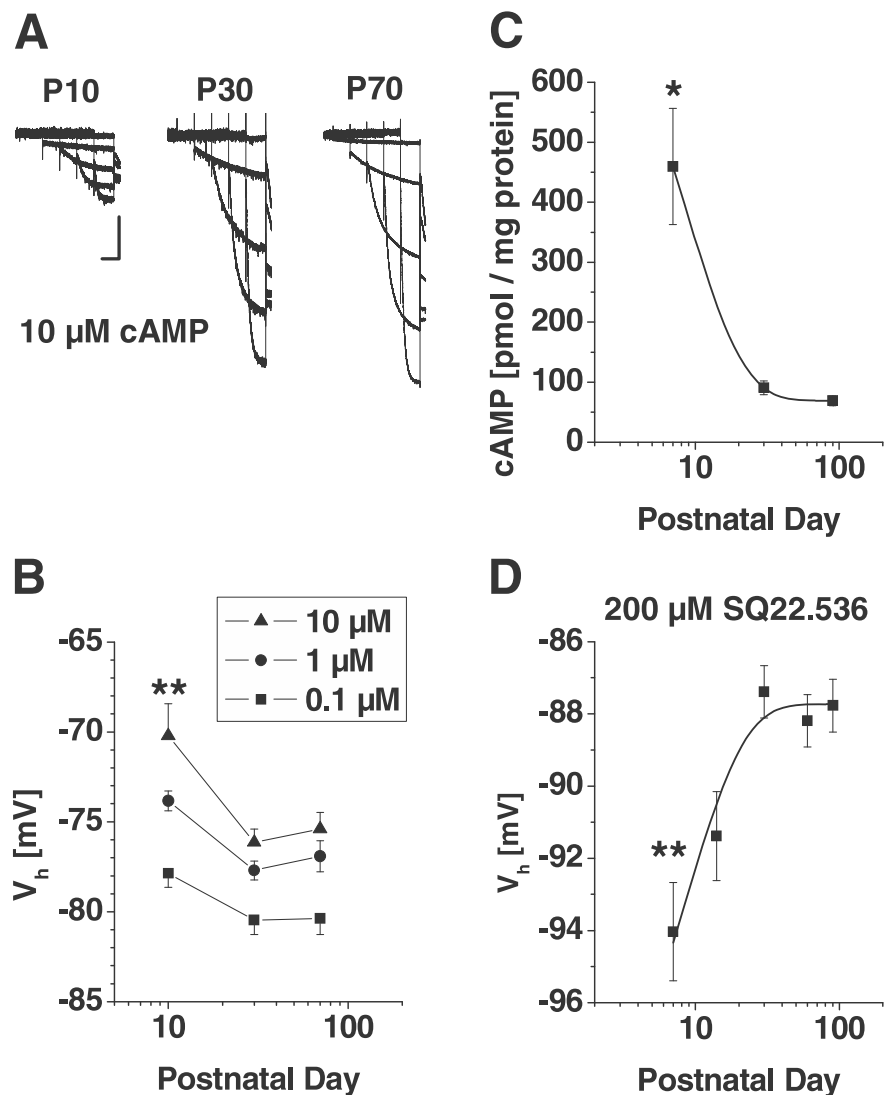


Figure 2. Modulation of I_h by cAMP. **A**, Representative current traces obtained from cells in the presence of 10 μM intracellular cAMP at P10, P30, and P70. Voltage protocols as in Figure 1. Calibration: 3 s, 200 pA. **B**, Mean V_h values of steady-state activation curves at different postnatal ages (P10, P30, and P70) in the presence of 0.1 μM (filled squares), 1 μM (filled circles), and 10 μM (filled triangles) of intracellular cAMP were obtained from independent populations of cells. Data from P7 and P70 cells were highly significantly different (** $p < 0.01$). **C**, Results obtained from a radioactive competition assay revealed a significant decrease in cAMP content with age (* $p < 0.05$). **D**, Mean V_h values of steady-state activation curves at different postnatal ages (P7, P14, P30, P60, and P90) after preincubation of brain slices in SQ22.536 (200 μM , 2 h). Results indicated a highly significant hyperpolarization at P7 compared with age-matched controls (** $p < 0.01$).

probe. Quantification and statistical analyses of the HCN mRNA signals were accomplished by measuring optical density of incorporated radioactivity in dLGN using the image analysis program ImageTool (version 1.27; University of Texas Health Science Center, San Antonio, TX). Optical density measured over the corpus callosum was used as a background signal and subtracted from the signal measured in dLGN. Linearity of the hybridization signal was ascertained using ^{14}C standards (American Radiolabeled Chemicals).

Results

Basic properties of I_h in developing TC neurons

Data from 219 visually and electrophysiologically identified TC neurons of the dLGN were included for analysis. I_h was activated in the presence of Ba^{2+} (1 mM) from a holding potential of -40 mV by using hyperpolarizing voltage steps of increasing ($\Delta V = -10$ mV) amplitude and decreasing ($\Delta t = -1500$ ms) duration, followed by a constant step to -100 mV (Fig. 1A; the inset shows

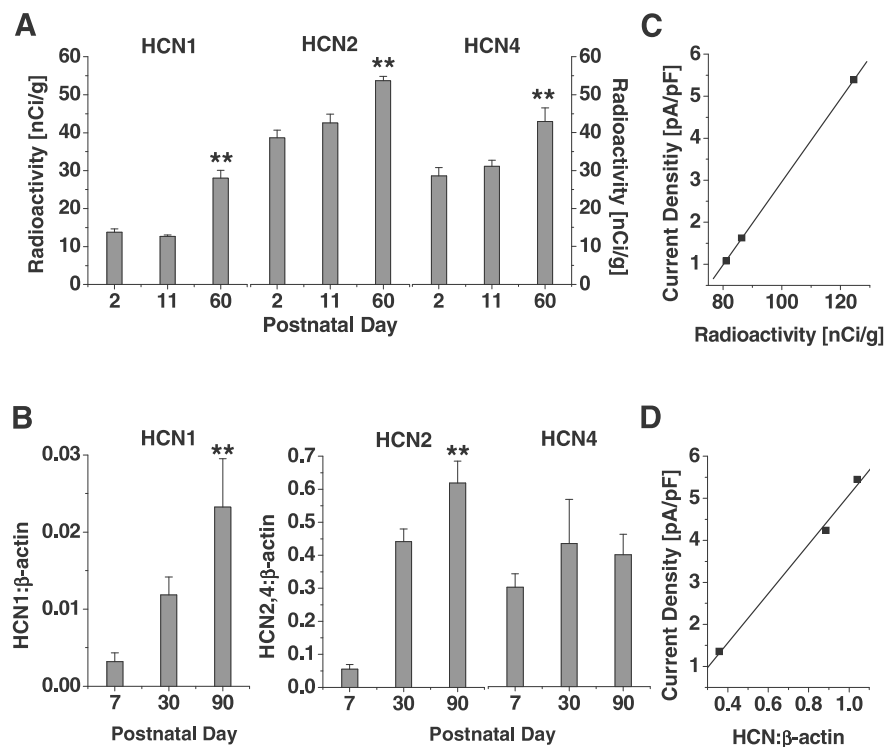


Figure 3. Quantitative analyses of postnatal mRNA and protein expression of HCN channels. **A**, HCN1, HCN2, and HCN4 mRNA levels in dLGN were obtained using radioactively labeled *in situ* hybridization probes ($n = 3-6$ per group). Significance is indicated for the comparison of P2 and P60 (** $p < 0.01$). **B**, HCN1, HCN2, and HCN4 protein levels in dLGN were evaluated using Western blot procedures with β -actin as reference ($n = 9$ per group). Significance is indicated for the comparison of P7 and P90 (** $p < 0.01$). **C**, Relationship between I_h current density and radioactive ISH signals. Values of radioactivity were summed for P2, P11, and P60 and plotted versus age-matched current density values from the fit in Figure 1*B*. **D**, Relationship between I_h current density and normalized Western blot signals. Values of HCN/ β -actin ratios were summed for P7, P30, and P90 and plotted versus age-matched current density values from the fit in Figure 1*B*.

a scheme of the voltage protocol). The density of I_h at -130 mV strongly increased as a function of postnatal age from 1.1 ± 0.1 pA/pF ($n = 6$) at P3 to 5.2 ± 0.4 pA/pF ($n = 7$) at P106 ($p < 0.001$) (Fig. 1*B*), thereby representing a 5.5-fold increase over the observed period of development. An analysis of the deactivating currents revealed a half-maximal value of I_h activation (V_h) at a membrane potential of -85.2 ± 1.5 mV ($n = 6$) at P3, which was not significantly ($p > 0.063$) different from V_h at the other developmental stages (P7, -85.5 ± 0.9 mV, $n = 9$; P11, -86.7 ± 1.0 mV, $n = 10$; P18, -88.5 ± 0.8 mV, $n = 14$; P30, -89.1 ± 1.0 , $n = 17$; P60, -87.7 ± 0.6 mV, $n = 16$; P106, -88.8 ± 1.0 mV, $n = 7$) (Fig. 1*C,D*). Nevertheless, there was a tendency to more hyperpolarized activation curves in older animals (Fig. 1*D*) because comparisons between some datasets revealed significant differences (P7/P18, P7/P30, and P7/P106; $p < 0.04$).

Because the relative contribution of different HCN isoforms to the properties of I_h is also evident in the time course of I_h activation, we analyzed activation time constants as a function of age. Time constants of activation at a potential of -130 mV increased during development (P3, $\tau = 435 \pm 32$, $n = 6$; P7, 432 ± 43 ms, $n = 9$; P11, 483 ± 25 ms, $n = 10$; P18, 530 ± 35 ms, $n = 12$; P30, 692 ± 35 ms, $n = 12$; P60, 576 ± 44 ms, $n = 9$; P106, 598 ± 52 ms, $n = 7$) with the earliest ages (P3 and P7) being significantly ($p < 0.03$) different from P30 and P106 (data not shown).

Strong modulation by intracellular cAMP is a hallmark of I_h in TC neurons and also reflects the relative contribution of the different HCN isoform expression (Pape, 1996; Budde et al., 2005).

To examine the cAMP gating of this conductance throughout the age range studied here, we recorded I_h while the pipette solution contained different concentrations (0.1, 1, and 10 μ M) of 8-bromo-cAMP (Fig. 2*A*). Inclusion of 8-bromo-cAMP induced a significant ($p < 0.001$) concentration-dependent shift of I_h activation curves at all developmental stages. Compared with cells from P10 (0.1 μ M, $V_h = -77.9 \pm 0.8$, $n = 10$; 1 μ M, $V_h = -73.8 \pm 0.5$, $n = 23$; 10 μ M, $V_h = -70.2 \pm 1.8$, $n = 7$), V_h values in P30 (0.1 μ M, $V_h = -80.5 \pm 0.8$, $n = 8$; 1 μ M, $V_h = -77.7 \pm 0.5$, $n = 8$; 10 μ M, $V_h = -76.1 \pm 0.7$, $n = 7$) and P70 (0.1 μ M, $V_h = -80.4 \pm 0.9$, $n = 5$; 1 μ M, $V_h = -76.9 \pm 0.9$, $n = 14$; 10 μ M, $V_h = -75.4 \pm 0.9$, $n = 5$) rats were significantly ($p < 0.004$) more hyperpolarized (Fig. 2*B*). In addition to altering V_h , cAMP significantly ($p < 0.02$) accelerated I_h activation kinetics at -130 mV at all concentrations for P10 and P30 rats (data not shown). For P70 rats only, 1 and 10 μ M induced a significant ($p < 0.05$) acceleration. When different age groups were compared, activation time constants at -130 mV in P10 cells (0.1 μ M, $\tau = 402 \pm 14$ ms, $n = 10$; 1 μ M, $\tau = 300 \pm 20$ ms, $n = 10$; 10 μ M, $\tau = 299 \pm 20$ ms, $n = 7$) were significantly faster than in cells from P30 (0.1 μ M, $\tau = 531 \pm 17$ ms, $n = 8$; 1 μ M, $\tau = 475 \pm 11$ ms, $n = 8$; 10 μ M, $\tau = 470 \pm 13$ ms, $n = 8$) and P70 (0.1 μ M, $\tau = 491 \pm 36$ ms, $n = 5$; 1 μ M, $\tau = 471 \pm 18$ ms, $n = 12$; 10 μ M, $\tau = 435 \pm 19$ ms, $n = 5$) animals.

Next we assessed the possible influence of basal cAMP production on I_h properties. Quantification of cAMP concentration in dLGN tissue revealed a significant ($p < 0.02$) decline with age ranging from 459 ± 97 pmol/mg at P7 to 91 ± 11 pmol/mg at P30 and remained at the lower level thereafter (P90, 69 ± 8 pmol/mg, $n = 3$) (Fig. 2*C*). To test whether this change has an impact on I_h properties, thalamic slices were incubated with the adenylyl cyclase inhibitor SQ22.536 (300 μ M, 2 h) before current recordings (Fig. 2*D*). Inhibition of adenylyl cyclase activity resulted in significant ($p < 0.0002$) hyperpolarization of I_h activation curves at P7 ($V_h = -94.0 \pm 1.4$ mV, $n = 10$) but had very little effect in older animals (P30, $V_h = -87.4 \pm 0.7$ mV, $n = 9$; P60, $V_h = -88.2 \pm 0.7$ mV, $n = 12$; P90, $V_h = -87.8 \pm 0.7$ mV, $n = 13$). This effect was accompanied by a significant ($p < 0.002$) slowing of activation time constants at -130 mV in young (P7, $\tau = 714 \pm 59$ ms, $n = 10$) but not in old (P30, $\tau = 614 \pm 36$ ms, $n = 9$; P60, $\tau = 609 \pm 21$ ms, $n = 11$; P90, $\tau = 554 \pm 14$ ms, $n = 13$) animals (data not shown).

Expression of HCN channel mRNA and proteins in dLGN

By analyzing the molecular basis of I_h throughout the developmental range, we found that three of the four known members of the HCN channel gene family were significantly expressed in the dLGN throughout postnatal development (Fig. 3). Quantitative radioactive analyses of mRNAs indicated a progressive and significant increase of all isoforms as a function of age (increase

from P2 to P60; HCN1, 2.0-fold, $p = 0.0002$; HCN2, 1.4-fold, $p = 0.002$; HCN4, 1.5-fold, $p = 0.0032$) (Fig. 3A).

Protein expression of HCN channel isoforms was approximately concordant with the mRNA results in that the protein expression of HCN1 and HCN2 significantly ($p < 0.004$) increased from P7 to P90. Protein levels of HCN4 were not significantly changed over the analyzed time period, and the discrepancy between the mRNA and protein levels might be a result of the variability among available antisera against this subunit (Brewster et al., 2007; Shin and Chetkovich, 2007). The increase revealed by semiquantitative Western blotting was 7.6-fold ($p > 0.004$), 12.4-fold ($p < 0.0001$), and 1.3-fold ($p > 0.08$) (Fig. 3B) for HCN1, HCN2, and HCN4, respectively. Whereas the ratio of HCN2/HCN1 protein expression remained approximately constant during postnatal development (30 ± 3 , $n = 3$), the ratios of HCN2/HCN4 and HCN1/HCN4 increased approximately eightfold and sixfold between P7 and P90, respectively. To localize the protein expression of HCN channel isoforms in dLGN, immunohistochemical staining was performed. The results indicated that HCN1 (Fig. 4A), HCN2 (Fig. 4B), and HCN4 (Fig. 4C) were present in this, as well as other thalamic nuclei, with an apparent increase of signal intensity between P10 and P70.

How does HCN isoform expression during development govern I_h properties?

To correlate HCN expression levels and membrane current for matching postnatal ages, I_h current density (extrapolated from the fit in Fig. 1B) was plotted against the sum of the detected radioactivity (determined by ISH for P2, P11, and P60) (Fig. 3A) and the HCN/ β -actin ratio (determined by Western blotting for P7, P30, and P90) (Fig. 3B) of all three isoforms. This yielded a linear relationship for both current density and summed mRNA levels ($r^2 = 0.999$) (Fig. 3C) as well as for current density and summed protein levels ($r^2 = 0.994$) (Fig. 3D).

Functional consequences of increased HCN isoform expression

One hallmark of I_h current activation during current-clamp recordings is the depolarizing voltage sag generated during the course of hyperpolarizing current steps (Pape, 1996). Furthermore, TC neurons can act as intrinsic oscillators in the delta frequency range (0.5–4 Hz) during slow-wave sleep (when oscillations are in the same delta frequency) based on the cyclic interaction between I_h and the transient low-threshold Ca^{2+} current (I_T) (Pape, 1996; Lüthi and McCormick, 1998; Cueni et al., 2009). Whereas I_h acts as a pacemaker, I_T is responsible for the generation of low-threshold Ca^{2+} spikes (LTS) underlying bursts of action potentials (supplemental Fig. S2, available at www.jneurosci.org as supplemental material). Because multiple ion channels mature during early postnatal development, it is difficult to isolate the influence of changed compound HCN channel expression on TC neuron firing patterns using experimental approaches. Therefore, we used *in vivo* EEG recordings (see Fig. 6) and computer modeling to assess the effect of changed I_h density on burst and tonic firing in a single-cell model (see Fig. 5) as well as on rhythmic slow-wave sleep activity in a reduced thalamic network model (see Fig. 7).

The single TC neuron model was set to rest at a potential of -60 mV, and time-dependent, anomalous rectification was analyzed by applying hyperpolarizing pulses in current-clamp mode. A maximum I_h conductance of $10 \mu\text{S}/\text{cm}^2$ was considered the adult situation. When applied to the model cell (surface area $\approx 29,000 \mu\text{m}^2$), a hyperpolarization to -130 mV led to a voltage

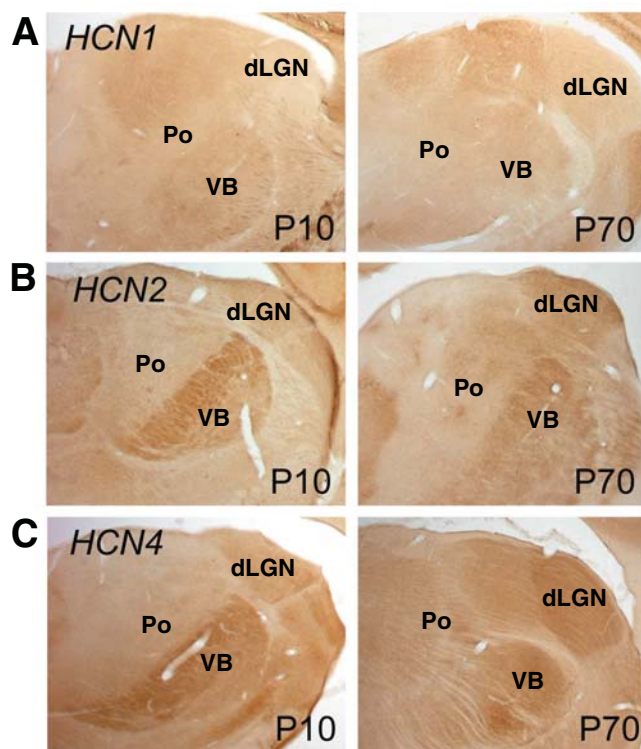


Figure 4. Immunohistochemical characterization of HCN channel localization. Specific antibodies directed against HCN1 (A), HCN2 (B), and HCN4 (C) were applied. All isoforms were detected in the dLGN and immunoreactivity was stronger in adult (P70) compared with P10 animals, which is consistent with the results of the mRNA and protein analysis (see Fig. 3). In both P10 and P70 dLGN, HCN1 immunoreactivity was considerably weaker than the corresponding immunosignal of the HCN2 and HCN4 isoforms. This may reflect the generally lower expression levels of HCN1 compared with these isoforms (see Fig. 3). Po, Posterior thalamic nuclear group; VB, ventrobasal thalamic complex.

sag of 11.5 mV. In this case, the “adult” TC neuron (Fig. 5A, left) showed a prominent slow time-dependent rectification during hyperpolarization and a burst of action potentials superimposed on an LTS after release from hyperpolarization. This rectification was almost gone when reducing the I_h conductance to 20%, levels found during the very early postnatal period (Fig. 5A, right). Although the deactivating component of I_h generates a depolarizing afterpotential after release from hyperpolarization, amplitude and duration of the LTS are dominated by I_T (supplemental Fig. S2, available at www.jneurosci.org as supplemental material). Therefore, a full LTS was generated even in the absence of I_h (Fig. 5A, right). In contrast, tonic firing evoked by depolarizing current steps was not significantly affected by the reduction of I_h . A systematic decrease (10% steps) of the maximum I_h conductance from 100 to 0% was answered by the computer model with linearly decreasing voltage sags (Fig. 5B). Together, anomalous rectification was highly dependent on the maximum I_h conductance.

Next, we examined the role of the developmentally determined, isoform-specific HCN channel expression patterns and the resulting alteration in cAMP modulation in the maturation of sleep patterns. We recorded *in vivo* cortical EEGs from rats at five developmental ages, P7, P12, P14, P18, and P90. As shown in Figure 6A, there was little distinction between the frequency distribution of EEG rhythms in the wake and the sleep state at P7. In contrast, slow-wave oscillations, in the delta frequency range, were sporadically detectable at P12 (Fig. 6B) and P14 (Fig. 6C) and were readily apparent in non-

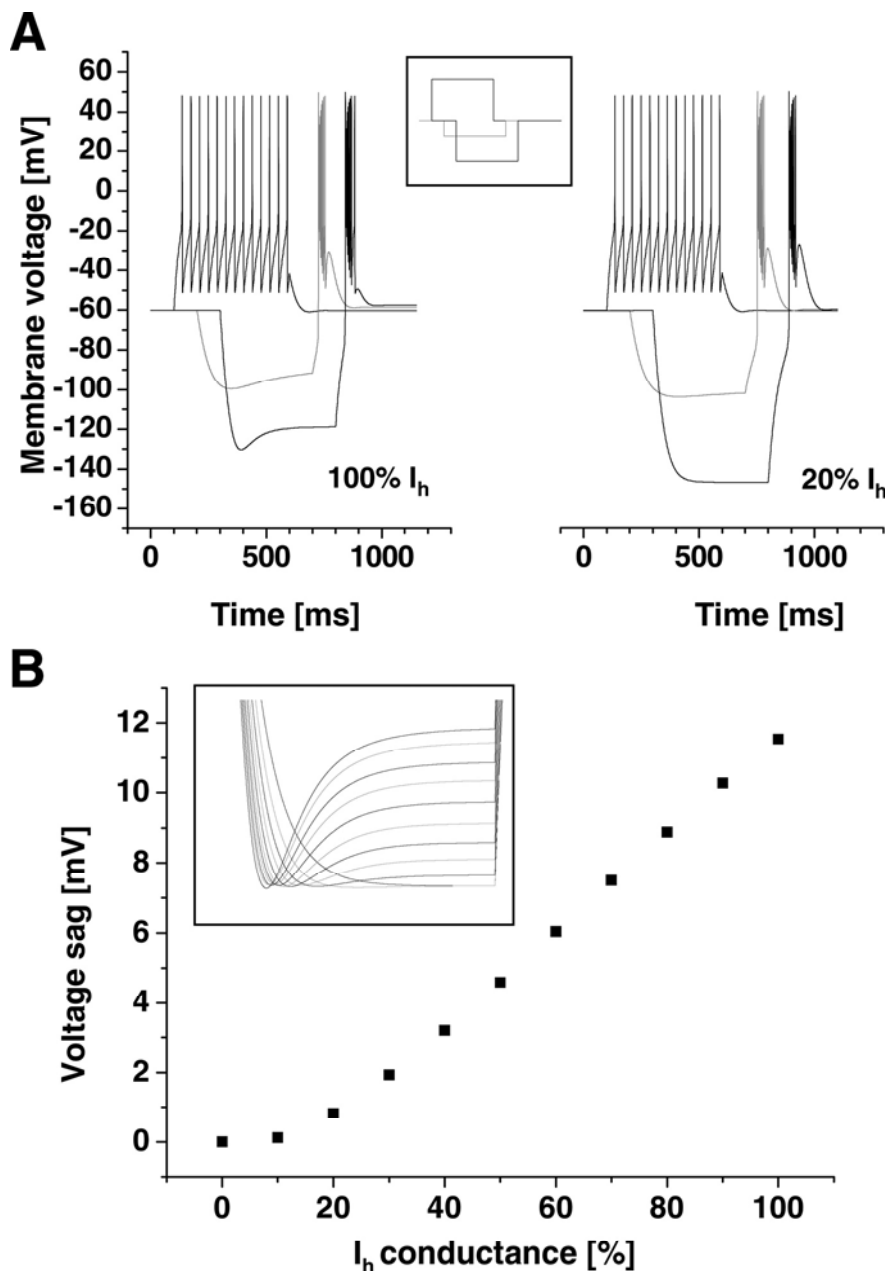


Figure 5. Single-cell modeling. **A**, Reducing I_h affects burst behavior. Although there is no significant difference in the tonic action potential generation, reducing the maximum I_h conductance from 100% (left) to 20% (right) affects the response of the model to hyperpolarization. The applied stimulus protocol is given in the inset. **B**, Incrementing the maximum I_h conductance of the single-cell TC neuron model in 10% steps from 0 to 100% led to a linearly growing voltage sag. The voltage sag was determined by subtracting the initial (global minimum) from the final (right at the end of the stimulus) membrane voltage (see inset).

rapid eye movement (NREM) sleep recordings from rats at P18 (Fig. 6D, right). These were clearly distinguishable from the wake record (Fig. 6B–D, left). A similar, mature sleep pattern was found in adult (P90) cortical EEG recordings, in which well developed delta frequency (1–2 Hz) sleep waves distinguished the NREM sleep state (Fig. 6E).

The contribution of HCN channel maturation to these patterns was evaluated using computer modeling. Spontaneous rhythmic slow-wave sleep activity was analyzed in a model network of four reciprocally connected TC and reticular thalamic (RE) neurons (Destexhe et al., 1996) as depicted in Figure 7B. At a hyperpolarized membrane potential of approxi-

mately -80 mV, both TC neurons generated spontaneous burst activity within a frequency range of 4–6 Hz (close to the delta frequency range of 0.5–4 Hz). Regarding the entire network, synchronized activity could be observed in all four neurons with an underlying frequency of 5.6 Hz under control conditions (Fig. 7A; only traces from TC1 and RE1 are shown in the top and middle, respectively). Because of the decreasing depolarizing and thus pace-making influence, a gradual reduction of the maximum I_h conductance applied to both TC neurons in parallel resulted in a decreasing burst frequency down to 4.1 Hz (Fig. 7C). When the maximum I_h conductance was lowered to 50% of the control condition, spontaneous bursting in the pace-making TC neurons and, consequently, the entire network oscillation stopped (Fig. 7A). To investigate the effect of cAMP-dependent modulation of HCN channels on rhythmic activity, the I_h activation curve was shifted by 15 mV in the depolarizing direction. With the I_h conductance lowered to 40% of the control value (situation at approximately P12–P14) spontaneous burst activity resumed when the voltage dependency of I_h was shifted 15 mV in the depolarizing direction (Fig. 7A, bottom). Under these conditions, the underlying frequency was 3.1 Hz (Fig. 7C).

Discussion

The results of the present study can be summarized as follows. (1) I_h current density strongly increases during the first 9 postnatal weeks until it reaches constant adult values. This change in current properties is associated with an overall increased expression of the three major neuronal HCN channel isoforms (HCN1, HCN2, and HCN4). (2) A linear relationship exists between the summed mRNA/protein expression levels of these channels and I_h current density, consistent with the dependence of current density on HCN gene expression. (3) Current kinetics and sensitivity to modulation by cAMP change significantly with age and the voltage dependence of I_h activation has the tendency to more hyperpolarized potentials in older rats. These findings are in agreement with the increase in HCN1/HCN4 and HCN2/HCN4 expression ratios as well as the decrease in cAMP levels in dLGN with age. (4) The dramatic decrease in cAMP content of dLGN tissue with age is accompanied by a significant decrease in the effect of the adenylyl cyclase blocker SQ22,536 on activation properties. Together with the changes in I_h cAMP sensitivity, these finding suggest that the expression of the I_h building blocks, namely the HCN channels and the intracellular cAMP concentration, act in concert to achieve specific current properties in a changing neu-

ronal environment. In this respect, young cells seem to require an extremely high cAMP sensitivity. (5) Computer modeling indicates that the increase in I_h conductance is necessary to sustain the spontaneous delta activity in TC neurons and, consequently, the synchronized slow-wave sleep rhythms in the thalamic network. Moreover, strong modulation of I_h with low (early developmental situation) conductance induces initiation of rhythmic delta activity. (6) In conclusion, a tight regulation of HCN channel expression and the resulting I_h current density takes place in TC neurons of developing dLGN. This, in turn, is likely to partially contribute to the maturation of slow-wave sleep activity in the thalamic network.

Correlation of HCN expression and I_h properties

In the present study, a clear linear correlation was demonstrated between total HCN mRNA levels as well as total HCN protein levels and I_h current density, thereby also pointing to a linear correlation between total mRNA and protein levels. This tight coupling between mRNA, protein and membrane current has also been found previously for HCN channels in the developing rat hippocampus. In that region, a progressive increase in I_h current amplitude correlated with a strong increase in HCN1, a moderate increase in HCN2, and a decrease in HCN4 expression (Vasilyev and Barish, 2002; Surges et al., 2006; Brewster et al., 2007).

To establish a clear correlation between kinetics, voltage dependence, and cAMP sensitivity of I_h and the HCN channel expression profile is more difficult. In general, this relationship is determined primarily by the HCN subunit composition. The three main isoforms that contribute to I_h in TC neurons reveal different voltage-dependent and kinetic properties in heterologous expression systems (Seifert et al., 1999; Robinson and Siegelbaum, 2003; Santoro and Baram, 2003). For example, compared with HCN2 and HCN4 (the latter reveals the highest cAMP sensitivity), the HCN1 isoform has faster activation kinetics, a more depolarized membrane voltage of activation, and less response to direct cAMP-dependent modulation. The combination of HCN2 and HCN4 is thought to result in a slow activation time course and a high cAMP sensitivity of I_h in TC neurons, with the later being fine tuned by the degree of HCN1 contribution (Ludwig et al., 2003; Budde et al., 2005, 2008). However, the relationship of the HCN isoform expression profile and I_h properties in native cells can be assumed to be more complex because channels might behave differently in expression systems and native cells, considerable differences exist between reported activation curves of cloned isoforms in different studies, and heteromerization of HCN channels may occur. HCN channel heteromers possess novel properties resembling those of neither heterologously expressed homomeric channels nor their arithmetic intermediates (Much et al., 2003; Richichi et al., 2008; Zha et al., 2008). In the

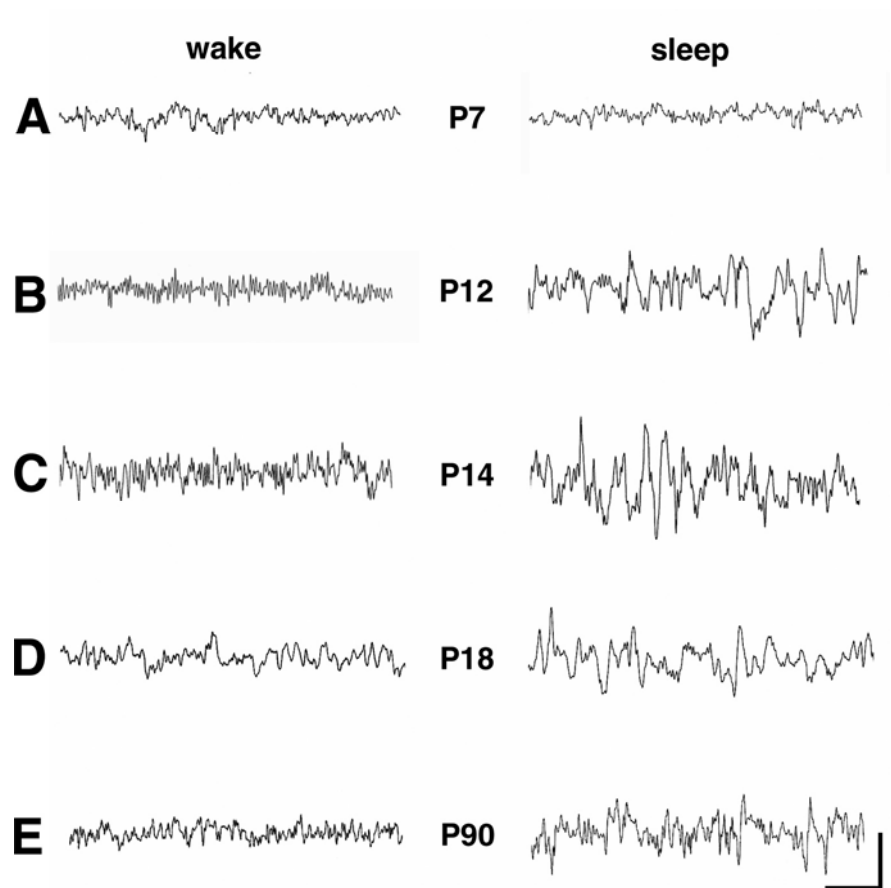


Figure 6. *In vivo* cortical EEGs demonstrating the development of slow-wave sleep patterns with age. At each age, traces from the wake state (assessed via concurrent video monitoring) are on the left, whereas sleep traces are on the right. Traces obtained on P7 (**A**), P12 (**B**), P14 (**C**), P18 (**D**), and P90 (**E**) are shown. **A**, There was little distinction between the frequency distribution of EEG rhythms in the wake and the sleep state at P7. **B**, By P12, initial irregular slow-wave oscillations (2–4 Hz) were apparent in NREM sleep recordings, readily distinguishable from the wake record. **C–E**, Similar, maturing sleep patterns were found in EEG at older ages (**C**, **D**), leading to the well developed delta frequency (1–2 Hz) NREM sleep waves in the adult (**E**). Calibration: 1 s, 50 μ V (P7), 0.1 mV (P12 and P14), 0.5 mV (P18), and 1 mV (P90).

thalamus, the analysis of I_h modulation by cAMP and halothane indeed indicated an important contribution of HCN1/HCN2 heterodimeric channels (Budde et al., 2005, 2008; Kuisle et al., 2006). Nevertheless, it is interesting to note that, in a computer model, using the activation curves established for cloned HCN channel isoforms in expression systems and weighting the influence of each isoform on I_h according to its protein expression level found in the present study resulted in mean activation I_h curves that were surprisingly consistent with those measured in cells in this study (supplemental Fig. S3, available at www.jneurosci.org as supplemental material).

Given the high intracellular cAMP levels and taking the dominance of HCN4 at P7 into account, one might expect more depolarized V_h values as found in this study. Therefore, our findings point to an as yet unidentified hyperpolarizing influence. Among others, two possible mechanisms may account for this. (1) Intracellular acidification leads to a hyperpolarizing shift in the I_h activation curve in TC neurons (Meuth et al., 2006). Because several components of cellular pH homeostasis, like carbonic anhydrases, mature steeply during the second postnatal week (Ruusuvoori et al., 2004), immature pH regulation may negatively modulate I_h activation curves. (2) An even more intriguing scenario may involve

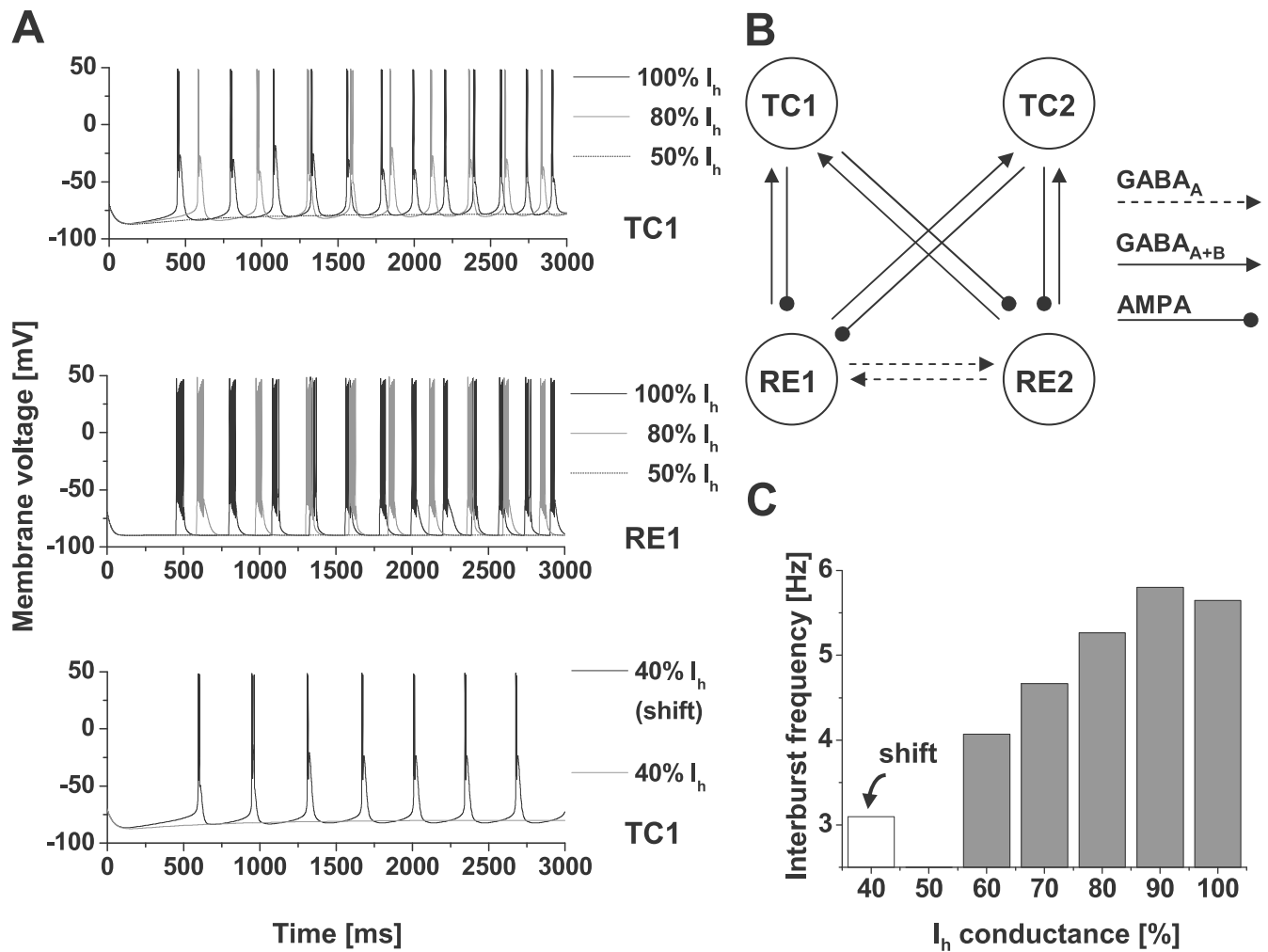


Figure 7. Network modeling. **A**, Results in both TC and RE neurons were identical. Therefore, only TC1 (top) and RE1 (middle) are shown. Oscillations disappear while reducing I_h . Given 100% I_h (black traces), the network shows oscillations at 5.6 Hz. By simultaneously reducing the maximum I_h conductance of both TC cells to 80% (gray traces), the oscillations are decelerated to 5.3 Hz and finally disappear if the I_h level is set to 50% (dashed traces). With I_h levels set to 40% (bottom), a 15 mV depolarizing shift in the activation curve resulted in resuming of oscillatory activity. **B**, The network topology as well as the connection parameters corresponds to Destexhe et al. (1996). RE neurons reciprocally communicate via $GABA_A$ -mediated connections and project to both TC neurons via $GABA_A$ and $GABA_B$. The feedback from TC cells is carried by AMPA receptors in both RE cells. **C**, Interburst frequency. Stepwise reducing the maximum I_h conductance in both TC cells of the network continuously slowed down the oscillations and finally erased all suprathreshold activity in case the I_h level falls to 50%. The interburst frequency was calculated with regard to the tip of the first action potentials of two consecutive bursts. All calculations were based on the traces of TC1 and considered the last seven bursts in each simulation for determining the plotted mean frequency. The arrow indicates the interburst frequency with 40% I_h and a 15 mV shift in the activation curve.

the puzzling HCN3 isoform. Immunohistochemical staining revealed HCN3 expression early postnatally in TC neurons of three rat strains (ACI, Sprague Dawley, and WAG/Rij) but not in adult animals (data not shown). Although the current generated by the HCN3 isoform is very similar to HCN2, cAMP induces a shift of HCN3 voltage dependency to more hyperpolarized potentials (Mistrik et al., 2005). Therefore, the early postnatal expression of this isoform may account for the rather negative activation curve at P7.

Altogether, these findings point to a scenario in which TC neurons regulate the expression of all four distinct I_h building blocks in combination with changing intracellular cAMP levels to achieve a current with maximal modulation by cAMP during early postnatal stages (HCN4 \gg HCN2 > HCN1, presence of HCN3, high cAMP levels) compared with adult stages (HCN2 > HCN4 \gg HCN1, low cAMP levels). Thus, transcriptional control of HCN channel genes in TC neurons represents a potent molecular mechanism that balances current density and modulatory range of I_h .

Functional relevance of I_h properties during development

During states of wakefulness and rapid eye movement (REM) sleep, the thalamocortical system is characterized by tonic action potential generation and high-frequency oscillations (\sim 40 Hz) (Steriade et al., 1997). During states of NREM and slow-wave sleep, the thalamocortical system shows highly synchronized oscillatory burst activity ($<$ 15 Hz). HCN channels play two essential roles in this scenario. (1) Cyclic interaction with T-type Ca^{2+} channels enables the generation of rhythmic activity in TC neurons (McCormick and Bal, 1997). (2) The arousal-inducing function exerted by the ascending brainstem system depends on the release of neurotransmitters that govern the switch from burst to tonic firing. Noradrenaline and 5-HT are of special interest because their effects significantly depend on their modulation of HCN channels (McCormick and Pape, 1990). Modulation by brainstem transmitters shifts the voltage dependence of activation of HCN channels to more depolarized potentials. This consequently depolarizes the membrane, increases the input resistance, and thereby favors the tonic firing mode. Therefore, the

density and the properties of I_h during development are crucial factors in the generation and termination of sleep-related TC activity, and it is not surprising that these are tightly regulated by coordinated expression of all HCN channel isoforms.

Developmental regulation of HCN channels, I_h , and sleep

Two models have been suggested for the appearance of REM and NREM sleep during mammalian ontogeny (Frank and Heller, 2003; Blumberg et al., 2005). REM and NREM sleep is thought to develop from either two different immature, homologous sleep states or a common form of early sleep termed “presleep.” The transformation of presleep into REM and NREM begins if the neocortical EEG exhibits state-dependent differentiated activity. In young rats, the EEG does not exhibit slow-wave activity (Fig. 6A) and rhythmic thalamocortical phenomena do not appear until P12 (Jouvet-Mounier et al., 1970; Mares et al., 1982; Seelke and Blumberg, 2008). Although the maturation of multiple ion channels and receptors as well as neuronal networks contributes to the development of adult sleep patterns, the present study points to a scenario in which an essential molecular prerequisite of intrinsic oscillatory activity in TC neurons, I_h , gradually matures and, as soon as a certain current density is reached, enables the appearance of delta activity in single TC neurons (and in the thalamocortical network). Given the high modulatory reserve of I_h in young animals, computer modeling suggests that this takes place at P12–P14. These findings are in good agreement with dynamic clamp studies in cat TC neurons in which the occurrence of spontaneous delta activity depends on the presence of an artificial I_h of sufficient amplitude (Hughes et al., 1998). Therefore, the maturation of I_h partially contributes to the development of slow-wave sleep rhythms and the establishment of adult sleep/wake patterns in rats.

References

- Bender RA, Baram TZ (2008) HCN channels in developing neuronal networks. *Prog Neurobiol* 86:129–140.
- Bender RA, Brewster A, Santoro B, Ludwig A, Hofmann F, Biel M, Baram TZ (2001) Differential and age-dependent expression of hyperpolarization-activated, cyclic nucleotide-gated cation channel isoforms 1–4 suggests evolving roles in the developing rat hippocampus. *Neuroscience* 106:689–698.
- Bender RA, Soleymani SV, Brewster AL, Nguyen ST, Beck H, Mathern GW, Baram TZ (2003) Enhanced expression of a specific hyperpolarization-activated cyclic nucleotide-gated cation channel (HCN) in surviving dentate gyrus granule cells of human and experimental epileptic hippocampus. *J Neurosci* 23:6826–6836.
- Blumberg MS, Karlsson KA, Seelke AM, Mohns EJ (2005) The ontogeny of mammalian sleep: a response to Frank and Heller (2003). *J Sleep Res* 14:91–98.
- Brewster A, Bender RA, Chen Y, Dube C, Eghbal-Ahmadi M, Baram TZ (2002) Developmental febrile seizures modulate hippocampal gene expression of hyperpolarization-activated channels in an isoform- and cell-specific manner. *J Neurosci* 22:4591–4599.
- Brewster AL, Bernard JA, Gall CM, Baram TZ (2005) Formation of heteromeric hyperpolarization-activated cyclic nucleotide-gated (HCN) channels in the hippocampus is regulated by developmental seizures. *Neurobiol Dis* 19:200–207.
- Brewster AL, Chen Y, Bender RA, Yeh A, Shigemoto R, Baram TZ (2007) Quantitative analysis and subcellular distribution of mRNA and protein expression of the hyperpolarization-activated cyclic nucleotide-gated channels throughout development in rat hippocampus. *Cereb Cortex* 17:702–712.
- Budde T, Caputi L, Kanyshkova T, Staak R, Abrahamczik C, Munsch T, Pape HC (2005) Impaired regulation of thalamic pacemaker channels through an imbalance of subunit expression in absence epilepsy. *J Neurosci* 25:9871–9882.
- Budde T, Coulon P, Pawlowski M, Meuth P, Kanyshkova T, Japes A, Meuth SG, Pape HC (2008) Reciprocal modulation of I_h and I_{TASK} in thalamocortical relay neurons by halothane. *Pflugers Arch* 456:1061–1073.
- Chen X, Sirois JE, Lei Q, Talley EM, Lynch C 3rd, Bayliss DA (2005) HCN subunit-specific and cAMP-modulated effects of anesthetics on neuronal pacemaker currents. *J Neurosci* 25:5803–5814.
- Cueni L, Canepari M, Adelman JP, Lüthi A (2009) Ca(2+) signaling by T-type Ca(2+) channels in neurons. *Pflugers Arch* 457:1161–1172.
- Destexhe A, Bal T, McCormick DA, Sejnowski TJ (1996) Ionic mechanisms underlying synchronized oscillations and propagating waves in a model of ferret thalamic slices. *J Neurophysiol* 76:2049–2070.
- Frank MG, Heller HC (2003) The ontogeny of mammalian sleep: a reappraisal of alternative hypotheses. *J Sleep Res* 12:25–34.
- Hines ML, Carnevale NT (2001) NEURON: a tool for neuroscientists. *Neuroscientist* 7:123–135.
- Hughes SW, Cope DW, Crunelli V (1998) Dynamic clamp study of I_h modulation of burst firing and delta oscillations in thalamocortical neurons in vitro. *Neuroscience* 87:541–550.
- Jouvet-Mounier D, Astic L, Lacote D (1970) Ontogenesis of the states of sleep in rat, cat, and guinea pig during the first postnatal month. *Dev Psychobiol* 2:216–239.
- Kaupp UB, Seifert R (2001) Molecular diversity of pacemaker ion channels. *Annu Rev Physiol* 63:235–257.
- Kuile M, Wanaverbecq N, Brewster AL, Frère SG, Pinault D, Baram TZ, Lüthi A (2006) Functional stabilization of weakened thalamic pacemaker channel regulation in rat absence epilepsy. *J Physiol* 575:83–100.
- Ludwig A, Budde T, Stieber J, Moosmang S, Wahl C, Holthoff K, Langebartels A, Wotjak C, Munsch T, Zong X, Feil S, Feil R, Lancel M, Chien KR, Konnerth A, Pape HC, Biel M, Hofmann F (2003) Absence epilepsy and sinus dysrhythmia in mice lacking the pacemaker channel HCN2. *EMBO J* 22:216–224.
- Lüthi A, McCormick DA (1998) H-current: properties of a neuronal and network pacemaker. *Neuron* 21:9–12.
- Mares P, Maresová D, Trojan S, Fischer J (1982) Ontogenetic development of rhythmic thalamo-cortical phenomena in the rat. *Brain Res Bull* 8:765–769.
- McCormick DA, Bal T (1997) Sleep and arousal: thalamocortical mechanisms. *Annu Rev Neurosci* 20:185–215.
- McCormick DA, Huguenard JR (1992) A model of the electrophysiological properties of thalamocortical relay neurons. *J Neurophysiol* 68:1384–1400.
- McCormick DA, Pape HC (1990) Properties of a hyperpolarization-activated cation current and its role in rhythmic oscillation in thalamic relay neurons. *J Physiol* 431:291–318.
- Meuth P, Meuth SG, Jacobi D, Broicher T, Pape HC, Budde T (2005) Get the rhythm: modeling of neuronal activity. *J Undergrad Neurosci Educ* 4:A1–A11.
- Meuth SG, Kanyshkova T, Meuth P, Landgraf P, Munsch T, Ludwig A, Hofmann F, Pape HC, Budde T (2006) The membrane resting potential of thalamocortical relay neurons is shaped by the interaction among TASK3 and HCN2 channels. *J Neurophysiol* 96:1517–1529.
- Mistrič P, Mader R, Michalakakis S, Weidinger M, Pfeifer A, Biel M (2005) The murine HCN3 gene encodes a hyperpolarization-activated cation channel with slow kinetics and unique response to cyclic nucleotides. *J Biol Chem* 280:27056–27061.
- Monteggia LM, Eisch AJ, Tang MD, Kaczmarek LK, Nestler EJ (2000) Cloning and localization of the hyperpolarization-activated cyclic nucleotide-gated channel family in rat brain. *Brain Res Mol Brain Res* 81:129–139.
- Moosmang S, Biel M, Hofmann F, Ludwig A (1999) Differential distribution of four hyperpolarization-activated cation channels in mouse brain. *Biol Chem* 380:975–980.
- Much B, Wahl-Schott C, Zong X, Schneider A, Baumann L, Moosmang S, Ludwig A, Biel M (2003) Role of subunit heteromerization and N-linked glycosylation in the formation of functional hyperpolarization-activated cyclic nucleotide-gated channels. *J Biol Chem* 278:43781–43786.
- Pape HC (1996) Queer current and pacemaker: the hyperpolarization-activated cation current in neurons. *Annu Rev Physiol* 58:299–327.
- Richichi C, Brewster AL, Bender RA, Simeone TA, Zha Q, Yin HZ, Weiss JH, Baram TZ (2008) Mechanisms of seizure-induced “transcriptional channelopathy” of hyperpolarization-activated cyclic nucleotide gated (HCN) channels. *Neurobiol Dis* 29:297–305.
- Robinson RB, Siegelbaum SA (2003) Hyperpolarization-activated cation currents: from molecules to physiological function. *Annu Rev Physiol* 65:453–480.

- Ruusuvuori E, Li H, Huttu K, Palva JM, Smirnov S, Rivera C, Kaila K, Voipio J (2004) Carbonic anhydrase isoform VII acts as a molecular switch in the development of synchronous gamma-frequency firing of hippocampal CA1 pyramidal cells. *J Neurosci* 24:2699–2707.
- Santoro B, Baram TZ (2003) The multiple personalities of h-channels. *Trends Neurosci* 26:550–554.
- Seelke AM, Blumberg MS (2008) The microstructure of active and quiet sleep as cortical delta activity emerges in infant rats. *Sleep* 31:691–699.
- Seifert R, Scholten A, Gauss R, Mincheva A, Lichter P, Kaupp UB (1999) Molecular characterization of a slowly gating human hyperpolarization-activated channel predominantly expressed in thalamus, heart, and testis. *Proc Natl Acad Sci U S A* 96:9391–9396.
- Shin M, Chetkovich DM (2007) Activity-dependent regulation of h channel distribution in hippocampal CA1 pyramidal neurons. *J Biol Chem* 282:33168–33180.
- Sinton CM, McCarley RW (2004) Neurophysiological mechanisms of sleep and wakefulness: a question of balance. *Semin Neurol* 24:211–223.
- Staunton H (2005) Mammalian sleep. *Naturwissenschaften* 92:203–220.
- Steriade M, Jones EG, McCormick DA (1997) *Thalamus*, Ed 1. Amsterdam: Elsevier.
- Surges R, Brewster AL, Bender RA, Beck H, Feuerstein TJ, Baram TZ (2006) Regulated expression of HCN channels and cAMP levels shape the properties of the h current in developing rat hippocampus. *Eur J Neurosci* 24:94–104.
- Vasilyev DV, Barish ME (2002) Postnatal development of the hyperpolarization-activated excitatory current I_h in mouse hippocampal pyramidal neurons. *J Neurosci* 22:8992–9004.
- Wainger BJ, DeGennaro M, Santoro B, Siegelbaum SA, Tibbs GR (2001) Molecular mechanism of cAMP modulation of HCN pacemaker channels. *Nature* 411:805–810.
- Zha Q, Brewster AL, Richichi C, Bender RA, Baram TZ (2008) Activity-dependent heteromerization of the hyperpolarization-activated, cyclic-nucleotide gated (HCN) channels: role of N-linked glycosylation. *J Neurochem* 105:68–77.

Supplemental Material

Supplemental figure legends

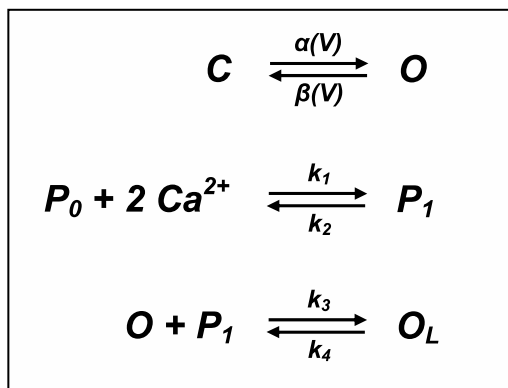
Fig. S1: Voltage-dependent properties of the simulated I_h .

Originally the mathematical description of I_h was derived from data obtained by voltage-clamp recordings with sharp microelectrodes of guinea pig dorsal lateral geniculate relay neurons at 36°C (Huguenard and McCormick, 1992, J. Neurophysiol., 68: 1373-1383).

(A) The activation curve of the modeled I_h had a V_h of -75.0 mV and a slope factor of 5.5 mV⁻¹. I_h does not inactivate, even with prolonged hyperpolarization. (B) The time constants of activation and deactivation of I_h followed single exponential functions and had a bell-shaped dependency on the membrane potential according to

$$\tau_m = 1 / [\exp(-14.59 - 0.086 * V_M) + \exp(-1.87 + 0.0701 * V_M)].$$

The I_h model assumed that the voltage dependency and conductance is influenced by Ca^{2+} indirectly through the binding of Ca^{2+} to a regulating factor (P), which itself binds to the open form of the channel and blocks its transition to the closed form. The full kinetic scheme (Destexhe et al., 1996, J. Neurophysiol., 76: 2049-2070) was



where the first reaction represents the voltage-dependent transitions of HCN channels between closed (C) and open (O) forms, with α and β as transition rates. The second reaction represents the binding of intracellular Ca^{2+} to a regulating factor (P_0 for unbound

and P_1 for bound) with four binding sites for Ca^{2+} and rates of $k_1 = 2.5 * 10^7 \text{ mM}^{-4} \text{ ms}^{-1}$ and $k_2 = 4 * 10^{-4} \text{ ms}^{-1}$. The Ca^{2+} -bound form P_1 associates with the open form of the channel, leading to a *locked* open form O_L , with rates of $k_3 = 0.1 \text{ ms}^{-1}$ and $k_4 = 0.001 \text{ ms}^{-1}$. The current is then proportional to the relative concentration of open channels.

It is reasonable to assume, that the increased availability and faster kinetics of I_h in the computer model in comparison to the measured data presented here leads to higher frequencies of the model network oscillations.

Fig. S2: Contribution of I_h to the low-threshold Ca^{2+} spike (LTS).

All traces were set to an initial potential of -60 mV by DC current injection. Membrane hyperpolarization under current clamp conditions (see current pulse above the traces) induces I_h -dependent anomalous rectification (marked by the asterisk) when I_h is fully present (black voltage trace). After termination of the hyperpolarizing current injection, the membrane potential repolarizes and a LTS is generated (marked by the arrow). With I_h reduced to 20% of the control current anomalous rectification is absent, however a LTS is still generated (red voltage trace). Removal of the T-type Ca^{2+} current (I_T) and the action potential generating Hodgkin-Huxley mechanism (HH) from the model with I_h reduced to 20%, results in a nearly passive behavior of the cell membrane (green voltage trace). Increasing I_h under these conditions back to control levels reinstates anomalous rectification (about 14 mV) and the depolarizing afterpotential (about 6 mV; blue voltage trace). These findings indicate that I_h has only little influence on amplitude and duration of the LTS.

Fig. S3: Dependency of I_h activation curves on HCN isoform composition.

To probe whether the developmentally-regulated HCN expression profile was congruent to the only slightly changed activation curves, we analyzed the steady-state voltage-

dependent I_h properties using a mathematical model. Based on literature given activation curves for the major I_h subcomponents in TC neurons, namely HCN1 (Chen et al., 2001, J. Gen. Physiol., 117: 491-504), HCN2 (Ulens & Tytgat, 2001, J. Biol. Chem., 276: 6069-6072) and HCN4 (Seifert et al., 1999, PNAS, 96: 9391-9396) on the one hand and the corresponding protein levels determined in the present study at three different developmental stages (P7, P30 and P90) on the other hand, a weighted and normalized sum of the activation curves was calculated according to the following equation:

$$result_j = \frac{\sum_i hcn_act_i * hcn_lvl_{ij}}{\sum_i hcn_lvl_{ij}} \quad \begin{array}{l} i = \{\text{HCN1, HCN2, HCN4}\}, \\ j = \{\text{P7, P30, P90}\}, \end{array}$$

hcn_act: activation characteristic,
hcn_lvl: protein level.

(A) The model included the activation curves of cloned HCN channels recorded in expression systems taken from literature (HCN1, open squares; HCN2, open circles; HCN4, closed triangles). **(B-D)** Assuming that each HCN isoform contributes to the compound I_h according to its protein expression level, activation curves were constructed by using different fractions of HCN1, HCN2, and HCN4 for different stages of postnatal development. Pie charts depict the applied weighting. Calculated (closed circles) vs. a global control (mean over all control activation curves of the present study) under control conditions (open circles) for P7 **(B)**, P30 **(C)**, and P90 **(D)** demonstrated good agreement at P7 ($\Delta V_h = 4.7$ mV; Fig. 5B), P30 ($\Delta V_h = 0.5$ mV; Fig. 5C), and P90 ($\Delta V_h = 0.3$ mV; Fig. 5D). It should be noted that this approach involves a number of uncertainties (comparison of results from expression system and native cells; considerable differences between activation curves of one and the same cloned isoform in different studies; formation of heteromers with new properties). Still the experimental data suggest that the relative stability of I_h activation curves throughout development at

least partially results from a coordinated developmental expression of the three HCN channel isoforms.

Supplemental table legend

Tab. S1: Passive and active parameters of the TC neuron and RE neuron model cells.

In order to have an autonomous oscillator and a cell with stable membrane resting potential, respectively, TC cell parameters were adjusted (highlighted in bold) in variation to the non-pacemaking TC neuron template (Desthene et al., 1996, J. Neurophysiol., 76: 2049-2070). TC = thalamocortical relay neuron; RE = reticular thalamic neuron.

Fig. S1

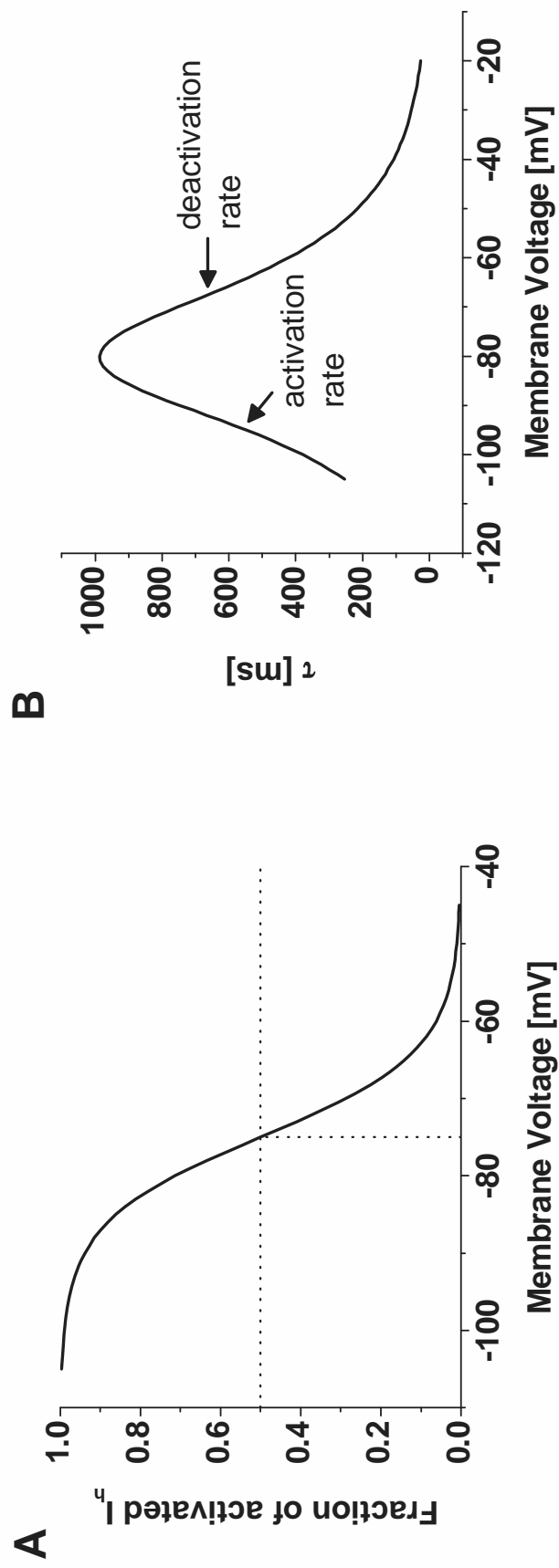


Fig. S2

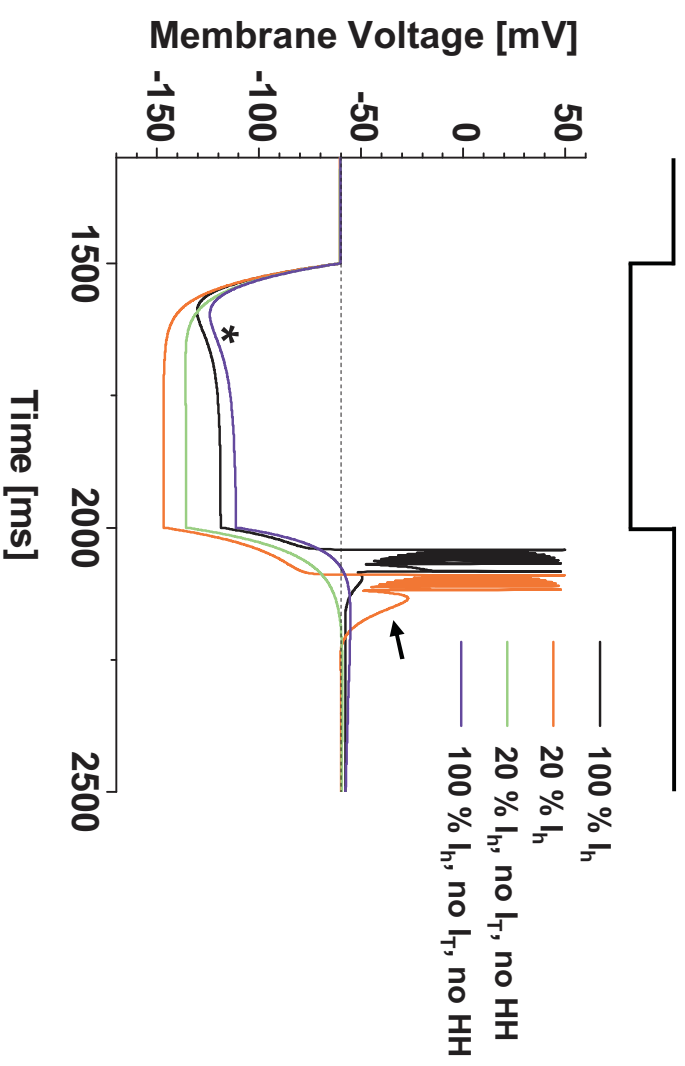
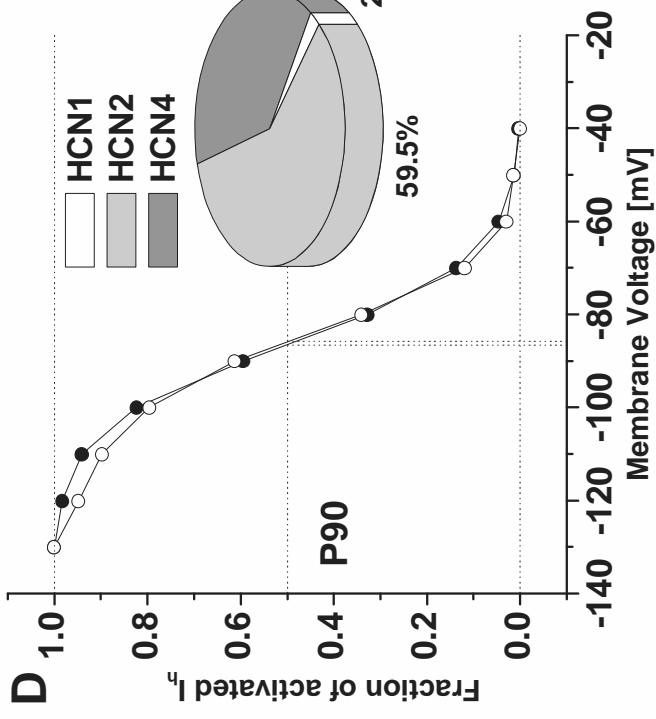
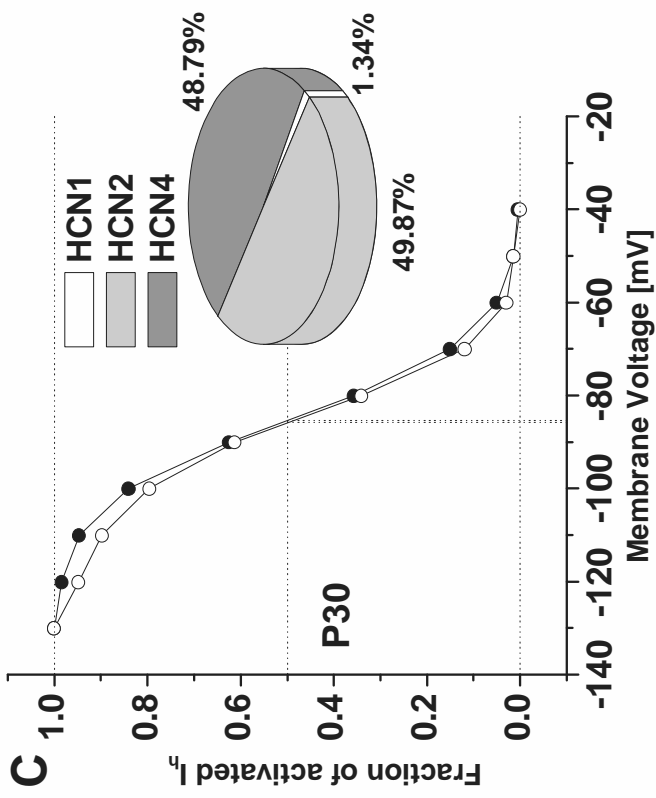
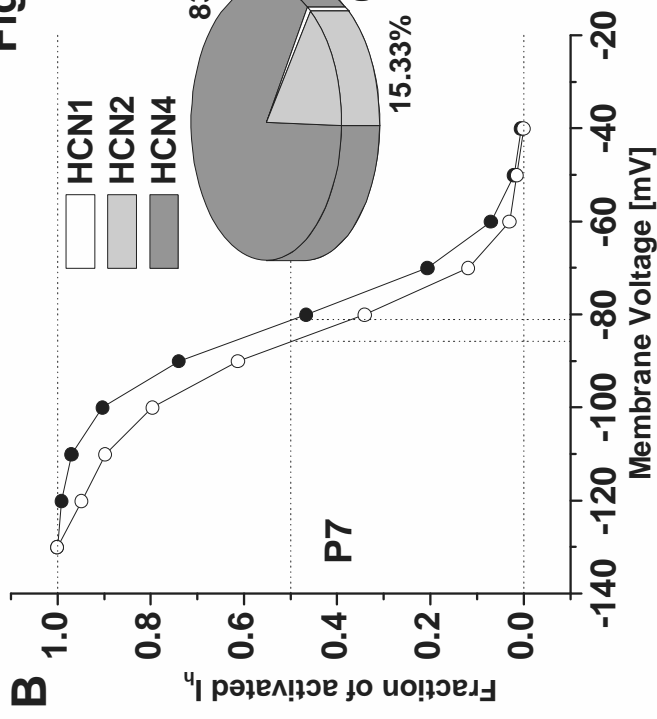
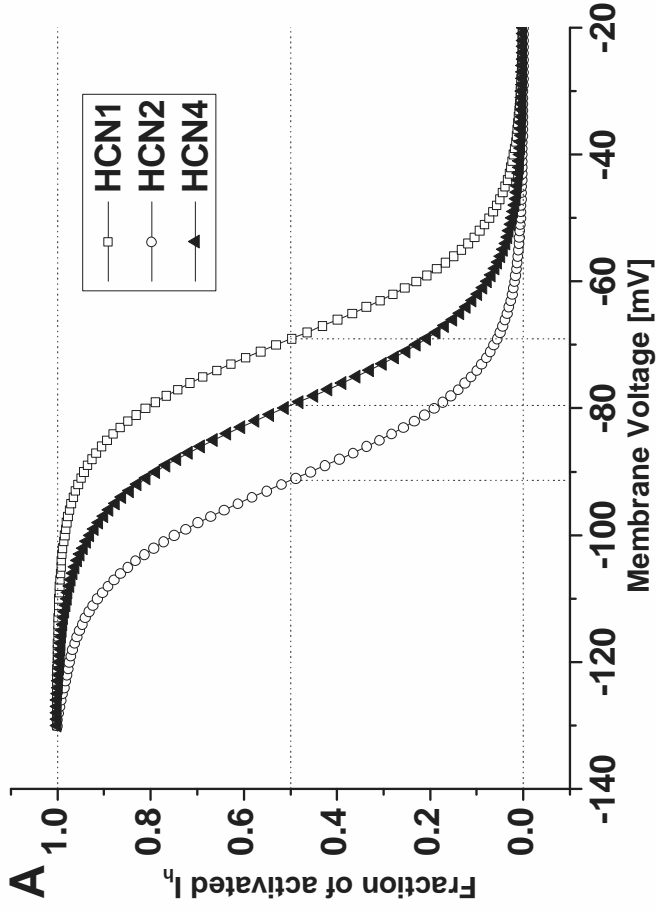


Fig. S3



	variable	unit	TC cell with stable membrane potential (Fig. 5)	TC cell template	Pacemaking TC cell (Fig. 7)	NRT cell (Fig. 7)
pas	number of compartments	nseg	1	1	1	1
	number of segments	diam	1	1	1	1
	diameter	μm	96	96	96	70
	length	L	96	96	96	64.86
	membrane capacitance	cm	1	1	1	1
	axial resistance	Ra	100	100	100	100
	area	μm^2	28,953	28,953	28,953	14,263
	temperature	celsius	36	36	36	36
	initial membrane voltage	v_init	-60	-70	-70	-70
	Passive membrane channel	e_pas	mV	-44	-70	-70
reversal potential leak current	g_pas	S / cm^2	1e-5	1e-5	1e-5	5e-5
specific membrane conductance						
Kleak	Leak potassium current	Erev_kleak	mV	-100	-100	-100
	reversal potential potassium channel	kl_gmax	μS	0.003	0.004	0.005
	maximum conductance					
hh2	Hippocampal HH channels	ek	mV	-100	-100	-100
	reversal potential potassium channel	ena	mV	50	50	50
	reversal potential sodium channel	vtraub_hh2	mV	-25	-25	-25
	threshold adjustment (Traub & Miles 1991)	gkbar_hh2	S / cm^2	0.01	0.01	0.01
	specific membrane conductance	gnabar_hh2	S / cm^2	0.09	0.09	0.09
	specific membrane conductance					
it	Low threshold calcium current (TC)	gcabar_it	S / cm^2	0.002	0.002	0.002
	specific membrane conductance	shift_it	mV	2	2	2
	shift for screening charge	cai	mM	2.4e-4	2.4e-4	2.4e-4
	calcium concentration inside	cao	mM	2	2	2
	calcium concentration outside	eca	mV	120	120	120
	reversal potential calcium channel					

it2	Low threshold calcium current (RE)										
	specific membrane conductance	gcabar_it2	S / cm ²							0.003	
	shift for screening charge	shift_it2	mV							2	
	kinetic adjustment to 36°C using Q10	qm_it2								2.5	
	kinetic adjustment to 36°C using Q10	qh_it2								2.5	
	calcium concentration inside	cai	mM							2.4e-4	
	calcium concentration outside	cao	mM							2	
	reversal potential calcium channel	eca	mV							120	
	ih	Anomalous rectifier channel									
		reversal potential lh channel	eh	mV	-40	-40					-40
number of binding sites of ca++		nca_iar		4	4					4	
inverse of time constant		k2_iar	1 / ms	0.0004	0.0004					0.0004	
half-activation of calcium dependence		cac_iar	mM	0.002	0.002					0.002	
number of binding sites on lh channels		nexp_iar		1	1					1	
backward binding on lh		k4_iar	1 / ms	0.001	0.001					0.001	
half-activation of CB protein dependence		Pc_iar		0.01	0.01					0.01	
augmentation of conductance with Ca++		ginc_iar		1	2					1	
specific membrane conductance		ghbar_iar	S / cm ²	1e-5	2e-5					1e-5	
shift of lh voltage-dependence		shift_iar	mV	0	0					0	
cad		Fast mechanism for submembranal Ca++ concentration (cai)									
		depth of shell	depth_cad	µm	1	1					1
		rate of calcium removal	taur_cad	ms	5	5					5
		equilibrium concentration of calcium	cainf_cad	mM	2.4e-4	2.4e-4					2.4e-4
		parameter specific to the pump	kt_cad	mM / ms	0	0					0
		parameter specific to the pump	kd_cad	mM	0	0					0

Summary (English)

Computational modeling can be used in a variety of different scenarios and scientific disciplines. Within the presented work this multipurpose tool was used to investigate the influence of alterations in one or several ion channels on the functional behavior of thalamic inter- and relay neurons. The thalamus is a brain region that is involved in the sleep-wake-cycle as well as in several neurological pathologies. Its neurons show two distinct firing modes during wakefulness and sleep. In comparison to the tonic firing behavior during wakefulness, the action potentials generated in the burst mode are of higher frequency and crown a low-threshold spike. This spike is mediated by the T current and follows an H current driven depolarization of the cell membrane. Whether a neuron shows tonic or burst firing depends on its resting membrane potential, which is stabilized by the interaction of the H current and a potassium current named I_{TASK} .

In summary the presented work reveals the following neuroscience results:

- (1) Multiple ion channels including I_{NaP} , I_h , I_{IR} , and non-inactivating I_{KV} channels contribute to the resting membrane potential of thalamocortical relay (TC) neurons.
- (2) Extracellular acidification blocks about 25% of I_h and 90% of I_{TASK} in TC neurons.
- (3) The functional interaction between the depolarizing I_h and the hyperpolarizing I_{TASK} most likely accounts for the TC cell's resistivity against extracellular acidification.
- (4) The inhalational anesthetic halothane functions via the specific modulation of I_h and I_{TASK} .
- (5) The voltage sags of TC neurons, caused by hyperpolarizing voltage steps, increase during the postnatal development and can be clearly attributed to the increasing I_h .
- (6) Thalamocortical oscillations stop in case the I_h density falls below a critical threshold.
- (7) Maturing animals compensate the initial lack of I_h by right-shifting the corresponding I/V relationship via high levels of cAMP.
- (8) The functional differences in the burst behavior of thalamic inter- and relay neurons cannot be explained by location-dependent differences in the I_T channel distribution, but are caused by differences in the T current density and I/V relationship.
- (9) Regarding the three different thalamic nuclei lateral geniculate nucleus, centrolateral nucleus and reticular nucleus, the LTS onset potential primarily depends on the I/V relationship of I_T , whereas the number of LTS associated action potentials as well as the minimum stimulation strength necessary for eliciting a LTS mainly depends on the T current density.
- (10) Clinically relevant concentrations of the anti-absence substance ethosuximide function via the parallel reduction of I_T , I_{KCa} and I_{NaP} .

By developing the software package named TNT in the course of the presented work the original NEURON simulation environment got extended by the following features:

- (1) Intuitive and compact simulation description of an arbitrary number of simulations
- (2) Extension of the modularization principle to network components and network connectivity
- (3) Powerful parser and error handling engine
- (4) Automated conversion to / build up of NEURON standard hoc simulations
- (5) Automated integration and compilation of all simulation required NMODL mechanisms
- (6) Unsupervised simulation execution and data recording

Summary (German)

Computer Modeling kann bei einer Vielzahl von unterschiedlichen Szenarien und Wissenschaftsdisziplinen eingesetzt werden. In der vorliegenden Arbeit wurde dieses Mehrzweckwerkzeug benutzt, um den funktionalen Einfluss von Veränderungen in einem oder mehreren Ionenkanälen in thalamischen Inter- und Schaltneuronen zu untersuchen. Der Thalamus ist eine Hirnregion, die sowohl im Schlaf-Wach-Zyklus als auch in mehreren Neuropathien involviert ist. Die Neurone des Thalamus zeigen zwei unterschiedliche Feuermodi während der Wachheit und des Schlafens. Im Vergleich zum tonischen Feuerverhalten während der Wachheit, besitzen die Aktionspotenziale, die im *Burst* Modus generiert werden eine höhere Frequenz und reiten auf einem LTS. Dieser LTS wird durch den T Strom mediiert und folgt einer durch den H Strom getriebenen Depolarisation der Zellmembran. Ob ein Neuron tonisches Feuern oder *Bursten* zeigt, hängt von dessen Membranruhepotenzial ab, das wiederum durch die Interaktion von I_h und dem Kaliumstrom I_{TASK} stabilisiert wird.

Zusammengefasst ergab die vorliegende Arbeit die folgenden neurowissenschaftlichen Ergebnisse:

- (1) Viele verschiedene Ionenkanäle sind an der Festsetzung des Membranruhepotenzials von thalamokortikalen (TC) Schaltneuronen beteiligt. Darunter zählen I_{NaP} , I_h , I_{IR} und der nicht-inaktivierende I_{KV} Kanal.
- (2) Extrazelluläre Ansäuerung blockiert ca. 25% des I_h und 90% des I_{TASK} in TC Zellen.
- (3) Die funktionale Interaktion zwischen dem depolarisierenden I_h und dem hyperpolarisierenden I_{TASK} ist die wahrscheinlichste Erklärung für die Widerstandskraft von TC Zellen gegenüber extrazellulärer Ansäuerung.
- (4) Das Inhalationsanästhetikum Halothan wirkt über die spezifische Modulation von I_h und I_{TASK} .
- (5) Die durch hyperpolarisierende Spannungssprünge evozierten *voltage sags* in TC Neuronen werden im Laufe der postnatalen Entwicklung stetig größer und können eindeutig dem wachsenden I_h zugeordnet werden.
- (6) Thalamokortikale Oszillation stoppen, sobald die I_h Dichte unter einen bestimmten Schwellwert fällt.
- (7) Heranwachsende Tiere kompensieren den initialen I_h Mangel durch eine über einen hohen cAMP Level verursachte Rechtsverschiebung der zugehörigen Strom-/Spannungsbeziehung.
- (8) Die funktionalen Unterschiede im *Burst* Verhalten von thalamischen Inter- und Schaltneuronen können nicht durch positionsabhängige Unterschiede in der I_T Kanalverteilung erklärt werden, sondern beruhen auf unterschiedlichen I_T Stromdichten und Strom-/Spannungsbeziehungen.
- (9) Betrachtet man die drei verschiedenen Thalamuskern lateral geniculate nucleus, centro-lateral nucleus und den reticular nucleus, hängt das LTS Startpotenzial primär von der I_T Strom-/Spannungsbeziehung ab, während die Anzahl an LTS assoziierten Aktionspotenzialen sowie die minimale Stimulationsstärke für die Auslösung eines LTS hauptsächlich von der I_T Stromdichte abhängt.
- (10) Klinisch relevante Dosen des Antiepileptikums Ethosuximid wirken über die parallele Reduktion der Ströme I_T , I_{KCa} und I_{NaP} .

Das im Verlauf dieser Arbeit entwickelte Softwarepaket namens TNT erweitert die bislang erhältliche NEURON Simulationsumgebung um die folgenden Fähigkeiten:

- (1) intuitive und kompakte Beschreibung einer beliebigen Anzahl von Simulationen

- (2) Erweiterung des Modularisierungsprinzips auf Netzwerkkomponenten und Netzwerkverbindungen
- (3) leistungsfähiger *Parser* mit umfangreicher Fehlerprävention
- (4) automatisierte Konvertierung einer TNT Simulationsbeschreibung in eine standardkonforme NEURON hoc Simulation
- (5) automatisierte Integration und Compilierung aller von einer Simulation benötigten NMODL Mechanismen
- (6) unbeaufsichtigte Simulationsausführung und Datenspeicherung

Danksagung

Meinem Mentor Prof. Thomas Budde danke ich für seine uneingeschränkte Unterstützung in allen Lebenslagen. In den langen Jahren unserer Zusammenarbeit ist er mir nicht nur ein geachteter Ratgeber sondern auch ein guter Freund geworden.

Ein besonderer Dank gilt auch Prof. Martin Burger und Prof. Markus Müller-Olm für die umfangreiche Unterstützung meines Promotionsvorhabens.

Prof. Matthias Löwe danke ich für seine Bereitschaft diese interdisziplinäre Arbeit zu fördern und die Perspektiven, die sich aus dieser Zusammenarbeit ergeben haben.

Ein besonderer Dank gilt meiner Familie für Ihre Liebe, Geduld und Unterstützung.

Aus wissenschaftlicher Sicht ist aus dem Kreis meiner Familie mein Bruder Prof. Sven Meuth hervorzuheben, der schon zu meinen Studienzeiten den Weitblick besaß, mich für den neuro-wissenschaftlichen Sektor zu begeistern.

Danken möchte ich auch Frau Bernadette Reinecke und Herrn Thomas Westhoff für Ihre umfassende Unterstützung im wissenschaftlichen Alltag sowie ihr generell außergewöhnliches Engagement.

Mein Dank gilt auch Frau Dr. Petra Ehling für die produktiven Brainstormings in den letzten Jahren.

Ich danke Prof. Hans-Christian Pape für die finanzielle Unterstützung zum Besuch des Kurses „Methods in Computational Neuroscience“ in Woods Hole, MA, USA.

Prof. John White gilt mein besonderer Dank für die hervorragende Zeit in den USA im ersten Jahr meiner Promotion, durch die ich wissenschaftlich wie menschlich viel gewonnen habe.

Tabellarischer Lebenslauf

Vor- und Zuname: Patrick Meuth

geboren am: 09.10.1979 in Bad Schwalbach

Staatsangehörigkeit: deutsch

Familienstand: verheiratet

Name des Vaters,
Name der Mutter, geb.: Hubert Peter Meuth, Rita Rosina Meuth, geb. Becker

Schulbildung: Grundschule: von 1985 bis 1989 in Bad Camberg
Gymnasium: von 1989 bis 1998 in Bad Camberg und Idstein

Hochschulreife: am 22.06.1998 in Idstein

Ersatzdienst: von Juli 1998 bis Juli 1999

Studium: Informatik, Technische Universität Darmstadt
von Oktober 1999 bis Januar 2007

Promotionsstudiengang: Informatik

Prüfungen: Diplom im Fach Informatik am 08.01.2007 an der TU Darmstadt

Tätigkeiten: wissenschaftlicher Mitarbeiter vom 01.02.2007 bis 31.03.2010 am
Universitätsklinikum Münster, Institut für Physiologie I, Münster

wissenschaftlicher Mitarbeiter vom 01.04.2010 bis 30.06.2010 an der
Rheinisch-Westfälischen Technischen Hochschule Aachen, Fakultät
für Mathematik, Informatik und Naturwissenschaften, Aachen

wissenschaftlicher Mitarbeiter vom 01.07.2010 bis 31.01.2011 an der
Universität Münster, Institut für Mathematische Statistik, Münster

seit 01.02.2011 wissenschaftlicher Mitarbeiter am Universitätsklini-
kum Münster, Institut für Physiologie I, Münster

Beginn der Dissertation: im Februar 2007 am Institut für Physiologie I, Universitätsklinikum
Münster

Betreuer: Prof. Dr. Thomas Budde
Kobetreuer: Prof. Dr. Martin Burger

.....
(Unterschrift)